

Structure formation in binary polymer systems: Short-time dynamics and dynamics of crosslinked systems

DISSERTATION

zur Erlangung des mathematisch-naturwissenschaftlichen Doktorgrades

"Doctor rerum naturalium"

der Georg-August-Universität Göttingen

im Promotionsstudiengang Physik

der Georg-August University School of Science (GAUSS)

vorgelegt von

Gaoyuan Wang

aus Jiangsu, China

Göttingen, 2021

Betreuungsausschuss

Prof. Dr. Marcus Müller, Institut für Theoretische Physik, Universität Göttingen

Prof. Dr. Reiner Kree, Institut für Theoretische Physik, Universität Göttingen

Prof. Dr. Stefan Klumpp, Institut für Dynamik komplexer Systeme, Universität Göttingen

Mitglieder der Prüfungskommission

Referent:

Prof. Dr. Marcus Müller, Institut für Theoretische Physik, Universität Göttingen

Korreferent:

Prof. Dr. Reiner Kree, Institut für Theoretische Physik, Universität Göttingen

Weitere Mitglieder der Prüfungskommission:

Prof. Dr. Stefan Klumpp, Institut für Dynamik komplexer Systeme, Universität Göttingen

Prof. Dr. Peter Sollich, Institut für Theoretische Physik, Universität Göttingen

Prof. Dr. Annette Zippelius, Institut für Theoretische Physik, Universität Göttingen

Prof. Dr. Philipp Vana, Institut für Physikalische Chemie, Universität Göttingen

Tag der mündlichen Prüfung: 22.09.2021

Abstract

Structure evolution in multicomponent polymer melts and in their network equivalents is investigated. In the first part, particle-based simulations reveal that on short length and time scales, the collective kinetics of structure formation and relaxation of polymeric systems is influenced by the sub-diffusive single-chain dynamics. D-RPA and D-SCFT are employed to describe the collective behavior in the simulation. D-RPA successfully captures the observed time evolution of density fluctuations on short time scales, whereas D-SCFT fails to provide an appropriate description on time scales much shorter than the Rouse relaxation time. In addition, a modified D-SCFT that accounts for the non-locality of Onsager coefficient in time is developed. In the second part, the structure and structure formation in 2D networks with a fixed topology and in 3D randomly crosslinked networks made of symmetric diblock copolymers are studied combining analytical approaches and particle-based simulations. The phase behavior of 2D regular networks comprised of square-shaped unit cells is found to depend strongly on the side lengths of the unit cells measured in the unit of the end-to-end distance of the constituent polymer strands and the number of unit cells belonging to the network. In 3D random networks, the crosslinks stabilize and partially memorize the structure existing at the time of their formation. The phase behavior of random networks is determined by the crosslink density and the strength of the repulsion between unlike species at crosslinking.

Contents

1	Introduction	1
1.1	Outline	3
2	Theoretical concepts	5
2.1	The bead-spring model	5
2.2	Rouse model	7
2.3	Phase separation	9
2.3.1	SCFT of diblock copolymer melts	12
2.3.2	RPA of diblock copolymer melts	14
2.3.3	Microphase separation of diblock copolymer melts	16
2.4	Particle-based, coarse-grained simulations	17
2.4.1	Single chain in mean field algorithm	18
I	Collective short-time dynamics in multicomponent polymer melts	23
3	Collective short-time dynamics: Analytical aspects	25
3.1	D-SCFT and Onsager Coefficients	26

3.2	Static RPA	27
3.3	Dynamic RPA	31
3.3.1	Response to external fields	32
3.3.2	Quench from disordered state	34
3.4	Analytical form of $S_{\vec{q},\alpha\beta}(t)$	36
3.4.1	Temporal behavior of $g_{\vec{q}}(t)$	39
3.4.1.1	Ultimate short-time regime	39
3.4.1.2	Intermediate regime	41
3.4.1.3	Long-time regime	42
3.5	Dynamics of symmetric diblock copolymer	42
3.5.1	Dynamics of a chain fraction	42
3.6	Generalized model-B	46
3.6.1	Response of density fields to an external field at $\chi = 0$	47
3.6.2	Spinodal decomposition	49
3.6.3	Symmetric binary homopolymer blends	50
3.6.3.1	Ultimate short-time regime	50
3.6.3.2	Intermediate regime	51
3.6.3.3	Classical regime	52
3.6.4	Symmetric diblock copolymers	52
3.6.4.1	Ultimate short-time regime	53
3.6.4.2	Intermediate regime	54

3.6.4.3	Classical regime	55
4	Collective short-time dynamics: Simulation results	57
4.1	Decay of density fluctuations in symmetric binary homopolymer blends . . .	58
4.2	Decay of density fluctuations in asymmetric homopolymer blends	61
4.3	Spinodal decomposition in binary homopolymer blends: single density mode	63
4.4	Growth rate during spinodal decomposition in binary homopolymer blends: Collective structure factor	67
4.5	Decay of density fluctuations in symmetric diblock copolymer melts	70
4.6	Response to external fields in symmetric diblock copolymer melts	72
4.7	Summary	75
II	Structure formation in copolymer networks	77
5	Structure and structure formation in 2D, regular polymer networks	79
5.1	Theoretical background of polymer networks	82
5.2	Model and analytical considerations	84
5.2.1	Mean-field approximation	85
5.2.2	Phonon model	88
5.3	The structure of 2D polymer networks	95
5.3.1	Diblock strand length	96
5.3.2	Block distance distribution	97
5.4	Structure factor	100

5.4.1	Crosslink structure factor	100
5.4.2	Total structure factor	104
5.5	Phase behavior	108
5.5.1	Macrophase coexistence	109
5.5.2	Order-disorder transition	115
5.6	Summary	121
6	Phase behavior of random copolymer networks	125
6.1	Theoretical background	127
6.1.1	Sol-gel transition	127
6.1.1.1	Finite-size problem	128
6.1.1.2	Gel fraction	129
6.1.1.3	Localization length	129
6.1.2	Order-disorder transition	130
6.2	Percolation threshold	132
6.3	Localization length	133
6.3.1	Universal scaling behavior around p_c	135
6.3.2	Mean MSD as a function of p	136
6.4	Stability of ordered random networks upon heating	137
6.5	Order-disorder transition	142
6.5.1	Disordered preparation state	144

6.5.2	Ordered preparation state	145
6.5.3	Phase diagram	146
6.6	Summary	149
7	Conclusion	151
7.1	Collective short-time dynamics in multicomponent polymer melts	151
7.1.1	Future perspectives	152
7.2	Structure and structure formation in regular polymer networks	153
7.2.1	Future perspectives	154
7.3	Phase behavior of random copolymer networks	155
7.3.1	Future perspectives	156

Chapter 1

Introduction

Polymers are popular and essential materials synthesized by linking a large number of repeating units, the so-called monomers, by covalent bonds. Polymeric materials possess a broad spectrum of unique properties regarding their resilience, strength, toughness, the ability of self-assembly, etc. This variety of features has its origin in the countless possibilities in the selection of monomers and the construction of the chain architecture.

Polymers formed from identical monomers, such as polyethylene (PE) and polystyrene (PS) are called homopolymers. Polymer chains made of monomers from different species are called copolymers [1, 2]. They can be engineered to combine properties owned by different materials. Copolymer chains comprised of two or more homopolymer subunits are called block copolymers. Depending on the number of sequences, block copolymers can be further categorized into diblock, triblock copolymers, etc. Polymers formed from the same chemical composition may also differ in their chain architecture and, thus, show very different physical behavior. Known chain architectures range from linear chains to more elaborate ones, such as rings, stars and networks. The large number of tunable properties that can be achieved during synthesis makes this kind of material very attractive for various applications.

Characteristic for multicomponent copolymer systems is the repulsion between monomers of different chemical species. This results in a microphase separation below a certain temperature. The origin of the self-assembly is the reduction of energetically unfavored contacts between blocks made of different monomer types. Above the critical temperature, the entropy dominates and the system is found to be a homogeneous mixture. This is called the disordered

phase. Below the critical temperature, the polymer melt forms spatially modulated regions. This spatial segregation is restricted by the chain connectivity of block copolymers, leading to microphase separation with domain sizes comparable to the size of a molecule. Most of the applications of block copolymers stem from their ability to build microdomains. Currently, their commercial application can be found in thermoplastic elastomers [3] and compatibilization of polymer blends [4]. On top of that, block copolymers have enormous potential in fields such as microelectronics [5], nanolithography [6–8], batteries [9] and controlled drug delivery [10].

The focus of this study, diblock copolymers, are the simplest copolymers formed from a sequence of A-type monomers attached to a sequence of B-type monomers. Depending on the volume fraction of the two monomer blocks f_A and $f_B = 1 - f_A$, diblock copolymer melts microphase separate into various ordered topologies. The following phases appear with increasing asymmetry in the volume fraction: the lamellar phase (if $f_A \approx f_B$), gyroid phase, hexagonal phase and the cubic phase. One of the major goals of this thesis is to study the dynamics during the early stage of structure formation and the interplay between the single-chain dynamics and collective behavior in non-equilibrium polymer systems. Diblock copolymers are ideal subjects because of their well understood equilibrium phase diagram, straightforward chain architecture and a known accurate free-energy functional provided by Self-Consistent Field Theory (SCFT).

Another focus of this thesis is polymer networks formed by crosslinking polymer chains. This type of novel macromolecules exhibits great potential from both theoretical and industrial perspectives because of their advantageous properties such as elasticity, controllable mechanical strength and deformability. Their applications range from the conventional products like rubber, membranes and sorbents, to more advanced ones including drug delivery [11], catalysis [12, 13] and electronic materials [14]. I will concentrate on the phase behavior of this class of fascinating materials made of symmetric diblock copolymers and perform studies on regular networks with a fixed topology and on randomly crosslink polymer networks.

From a theoretical physics point of view, understanding the fundamental physical properties is essential for the design and synthesis of polymer materials with desired features. On the one hand, the mean-field approximation can be applied to dense polymeric systems because

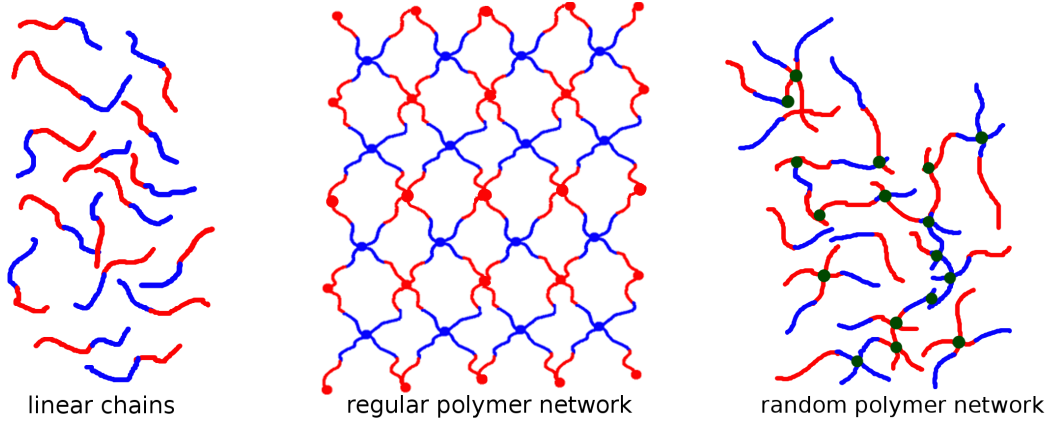


FIGURE 1.1: An illustration of the three main subjects of this thesis.

of the high number of interacting neighbors in the surrounding. On the other hand, the fractal nature of polymer systems enables coarse-grained descriptions. These useful features allow me to employ computer simulations and analytical approaches to investigate polymer systems.

1.1 Outline

This thesis is divided into two parts. I will start with the dynamics of linear chains and proceed with studies of regular polymer networks and random polymer networks made of symmetric diblock copolymers. The three subjects are illustrated in [Figure 1.1](#).

In the first part of this thesis, the collective kinetics of structure formation in polymer melts at short length and time scales is investigated. In [chapter 3](#), I present the key analytical methods Dynamical Random Phase Approximation (D-RPA) and Dynamical Self-Consistent Field Theory (D-SCFT), which are often used to describe the dynamics of structure formation. A modified D-SCFT with a time-dependent Onsager coefficient will also be presented. The predictions of the models are compared with the results obtained from the particle-based Monte-Carlo simulation program SOft coarse grained Monte-Carlo Acceleration (SOMA) in [chapter 4](#). The central goal of this part is to investigate the impact of sub-diffusive single-chain dynamics on short time and length scale.

In the second part of the thesis, I concentrate on the structure and structure formation of crosslinked polymer networks made of symmetric diblock copolymers. In [chapter 5](#), I

study regular two-dimensional polymer networks comprised of square-shaped repeating units (unit cells). A two-dimensional phonon model is applied to describe the structural properties of the regular networks. Then, the accuracy of the phonon model will be compared with a simplified Monte-Carlo (MC) simulation consisting of only junction points and with SOMA simulations. With the simplified description for the molecular structure provided by the phonon model, I continue to investigate the structure factor of the networks. Finally, the order-disorder transition (ODT) of the regular networks is measured as a function of the number of unit cells in the network and the size of the unit cells. In [chapter 6](#), the study of structure formation is extended to randomly crosslinked 3D polymer networks. The particle-based simulation program SOMA is applied to carry out the simulation studies. First, the percolation threshold that separates the sol and gel state of the network is measured. Then, the stabilization effect of the crosslinks on the existing structure at their time of formation will be studied in the simulation and compared to analytical predictions. At the end, the ODT of the random networks is investigated as a function of the crosslink density and the strength of the repulsion between unlike species in the preparation ensemble.

Chapter 2

Theoretical concepts

The major subject of this thesis is melt of the simplest diblock copolymers comprised of *A*- and *B*-type monomers and their network equivalents. Homopolymers and multiblock copolymers will also be discussed in this thesis mainly for comparisons with diblock copolymers and for studies of universal properties. I will combine analytical calculations with simulation studies to investigate the structure and structure formation of copolymer systems during self-assembly. This chapter is organized as follows: First, a brief summary of existing relevant theories and elementary methods for the dynamics of polymer chains will be provided. After that, well-known theories for self-assembly and phase separation are presented. At the end, the simulation program SOMA, applied in the simulation part of this thesis, will be introduced. More detailed background information and theoretical aspects regarding each specific copolymer system can be found in the corresponding parts of this thesis.

2.1 The bead-spring model

The bead-spring model is one of the most popular models developed to describe polymer systems. In this model, a polymer chain is simplified to a string with N beads connected via $N - 1$ harmonic springs. The length of such a spring, which is also called a bond, is the statistical segment length b . The orientations of the spring vectors are assumed to be independent from each other. In the following, polymer chains that are fully described by the bead-spring model without other types of interaction will be referred to as ideal chains. An illustration of an ideal chain with 8 beads and 7 bonds is shown in [Figure 2.1](#).

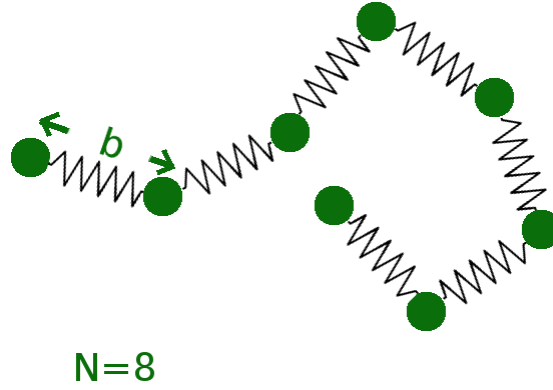


FIGURE 2.1: Illustration of a simplified polymer chain with $N = 8$ monomers and $N - 1 = 7$ bonds in the bead-spring model.

The elastic energy stored in the bonds of such a simplified chain can be expressed with the chain conformation represented by the set of position vectors $\{\vec{r}\}$ of the beads in space

$$U = \sum_{i=2}^N \frac{3k_B T}{2b^2} (\vec{r}_i - \vec{r}_{i-1})^2, \quad (2.1)$$

with $i = 1, \dots, N$ the indices of the beads. The probability distribution of the bond vectors $\vec{R}_i = \vec{r}_i - \vec{r}_{i-1}$ results directly from the harmonic potential [Equation 2.1](#)

$$P(|\vec{R}_i|) = \left(\frac{3}{2\pi b^2} \right)^{3/2} \exp \left(-\frac{3\vec{R}_i^2}{2b^2} \right). \quad (2.2)$$

The joined probability distribution of the positions of all beads in the chain can be written as

$$P(\{\vec{r}\}) = \left(\frac{3}{2\pi b^2} \right)^{3N/2} \exp \left(-\frac{3}{2b^2} \sum_{i=1}^N (\vec{r}_i - \vec{r}_{i-1})^2 \right). \quad (2.3)$$

The most important length scale of ideal chains is the end-to-end distance

$$R_e = \sqrt{\langle (\vec{r}_1 - \vec{r}_N)^2 \rangle},$$

where \vec{r}_1 and \vec{r}_N stand for the positions of the beads at the two ends of the polymer chain. The end-to-end distance of an unconstrained ideal chain obeys random walk and depends on

N according to

$$\vec{R}_e = 0 \quad \text{and} \quad R_e^2 = \langle (\vec{r}_1 - \vec{r}_N)^2 \rangle = (N - 1)b^2. \quad (2.4)$$

The extent of an ideal chain is described by another frequently used quantity called the radius of gyration defined as

$$R_G^2 \equiv \frac{1}{N} \sum_{i=1}^N \left(\vec{r}_i - \langle \vec{r} \rangle \right)^2, \quad (2.5)$$

with $\langle \vec{r} \rangle = \frac{1}{N} \sum_{i=1, \dots, N} \vec{r}_i$ the center of mass. For an ideal linear chain, the radius of gyration is

$$R_G^2 = \frac{(N - 1)b^2}{6} = \frac{R_e^2}{6}. \quad (2.6)$$

Because of the self-similarity of long, flexible polymer chains, the degrees of freedom of such a complex system can often be reduced by using one bead to represent not only one individual monomer but a group of monomers. Therefore, R_e and R_G are often used as a reference to express the length scale in polymer studies. In the following, all lengths will be measured in the unit of R_e if not specified otherwise.

2.2 Rouse model

The Rouse model was introduced in [15] to describe the dynamics of ideal chains in the melt state. During the last decades, Rouse model and Rouse dynamics have been applied and reviewed repeatedly in the literature. This section is based on the fourth chapter “Dynamics of Flexible Polymers in Dilute Solution” from [16].

In the Rouse model, the beads along the molecular backbones are described by the bead-spring model and are subject to thermal fluctuations. The Rouse model does not consider other types of interaction such as excluded volume interaction, hydrodynamic interactions and entanglement effects, which are covered by more complicated models. In Rouse dynamics, the motion of the beads is described by the Langevin equation. In the Langevin equation, the beads experience a viscous force generated by the dense surrounding polymers. This restoring force is proportional to the velocity via a coefficient of friction ζ and acts in the

opposite direction of the velocity. Thermal noises resulting from collision with molecules in the surrounding give rise to a fluctuation term $\eta(t)$. The Langevin equation reads [16]

$$\zeta \frac{d\vec{r}}{dt} = -\frac{\partial \mathcal{U}}{\partial \vec{r}} + \eta(t), \quad (2.7)$$

where \mathcal{U} is the bonded elastic energy of the segments described by the bead-spring model. In a linear chain, the two end segments ($n = 1$ and N) have only one neighbor. Their equations of motion read

$$\zeta \frac{d\vec{r}(n=1)}{dt} = -\frac{3k_B T}{b^2} [\vec{r}(n=1) - \vec{r}(n=2)] + \eta(n=1, t) \quad (2.8)$$

and

$$\zeta \frac{d\vec{r}(N)}{dt} = -\frac{3k_B T}{b^2} [\vec{r}(n=N) - \vec{r}(n=N-1)] + \eta(n=N-1, t). \quad (2.9)$$

For a segment n in the middle of a linear chain with two neighbors, the equation reads

$$\zeta \frac{d\vec{r}(n)}{dt} = -\frac{3k_B T}{b^2} [2\vec{r}(n) - \vec{r}(n-1) - \vec{r}(n+1)] + \eta(n, t). \quad (2.10)$$

In the continuous limit, Equation 2.10 takes the form

$$\zeta \frac{d\vec{r}}{dt} = -\frac{3k_B T}{b^2} \left(\frac{\partial^2 \vec{r}}{\partial n^2} \right) + \eta(n, t). \quad (2.11)$$

According to [16], the Langevin equation can be solved by decoupling a polymer chain into independent Rouse modes. The Rouse modes with wavenumber $p = 0, 1, 2, \dots$ are defined as [16]

$$\vec{X}_p = \frac{1}{N} \int_{i=0}^N \vec{r}_i \cos(ip\pi/N) di. \quad (2.12)$$

And its inverse transform is

$$\vec{r}_n = \vec{X}_0 + 2 \sum_{p=1}^{\infty} \vec{X}_p \cos\left(\frac{p\pi n}{N}\right). \quad (2.13)$$

The Langevin equation of independent Rouse modes takes the form [16]

$$\zeta_p \frac{\partial \vec{X}_p}{\partial t} = -k_p \vec{X}_p + \eta_p, \quad (2.14)$$

with $k_p = \frac{6\pi^2 k_B T}{Nb^2} p^2$, $\zeta_0 = N\zeta$ and $\zeta_p = 2N\zeta$. For $p = 0$, the cosine function collapses to 1. This means that the lowest mode describes the motion of the center of mass of the chain, which is denoted by \vec{r}_c . The higher modes $p = 1, \dots, N - 1$ correspond to fractions of the chain at certain length scales. By introducing the Rouse modes description, the motion of a polymer chain is decoupled into a series of independent functions that describe the dynamics at different length scales.

Within the Rouse model, the self-diffusion constant D_R can be obtained with the center of mass of individual chains [16]

$$D_R = \lim_{t \rightarrow \infty} \frac{1}{6t} \left\langle (\vec{r}_c(t) - \vec{r}_c(0))^2 \right\rangle = \frac{k_B T}{N\zeta}. \quad (2.15)$$

The Rouse time, which is the relaxation time required to equilibrate the polymer chains can be directly expressed in terms of the self-diffusion constant via

$$\tau_R = \frac{R_e^2}{3\pi^2 D_R} = \frac{\zeta N^2 b^2}{3\pi^2 k_B T}. \quad (2.16)$$

The relaxation time of higher Rouse modes can be computed directly from τ_R according to

$$\tau_p = \tau_R / p^2. \quad (2.17)$$

The Rouse time characterizes the important time scale on which the individual polymer chains have displaced their own extent and can thus be considered completely independent from the original conformations.

2.3 Phase separation

Many unique properties of multicomponent polymer systems stem from the repulsion between different segment species, which leads to a separation of the system into multiple regions with different compositions. The Flory-Huggins theory [17, 18] deals with the thermodynamics of binary polymer systems during mixing. In the following paragraph, I provide a brief summary of this well-known theory based on Ref. [19].

The Flory-Huggins theory is a lattice theory based on the assumption that each interaction unit occupies one or more lattice nodes and the volume fraction of them stays constant during mixing. Consider a binary homopolymer blend comprised of n_A A -homopolymers made of N_A monomers and n_B B -homopolymers made of N_B monomers. In the homogeneous state, an A -type polymer can occupy any lattice node in the system, whereas in the demixed state, the number of possible positions is reduced by a factor of ϕ_A , which is the volume fraction of A -type polymers. Thus, the entropy change of one A polymer during mixing is given by

$$\Delta S_A = -k_B \ln \phi_A. \quad (2.18)$$

Accounting for the entropy change of B polymers, the total entropy change of mixing per lattice site is [19]

$$\Delta S = -k_B \left(\frac{\phi_A}{N_A} \ln \phi_A + \frac{\phi_B}{N_B} \ln \phi_B \right). \quad (2.19)$$

The other contribution to the free energy stems from the interaction of the monomers with their surroundings. In the homogeneous state, the probability of any polymer to have a neighbor of type α is given by the corresponding volume fraction ϕ_α . In the demixed state, polymers only have neighbors of the same type of themselves. The energy difference between the homogeneous and the demixed state can be expressed as

$$\Delta U = \chi k_B T \phi_A \phi_B \quad (2.20)$$

with χ the Flory-Huggins parameter. In a dense system, the incompressibility assumption implies $\phi_B = 1 - \phi_A$. The excess free energy of mixing is (see also [19])

$$\begin{aligned} \Delta \mathcal{F} &= \Delta U - T \Delta S \\ &= k_B T \left(\frac{\phi_A}{N_A} \ln \phi_A + \frac{(1 - \phi_A)}{N_B} \ln (1 - \phi_A) + \chi \phi_A (1 - \phi_A) \right). \end{aligned} \quad (2.21)$$

The entropic part (first two terms in the above expression) favors mixing while the repulsive force (the last term) between unlike species increases during mixing for positive χ . The magnitude of the repulsion is controlled by the Flory-Huggins parameter χ . Although χ is called a parameter, it actually depends on quantities such as temperature, molar mass distribution and concentration [19]. This is because the expression introduced above is the

free energy of a coarse-grained description. There exists an empirical law to describe the dependence of χ on the temperature T

$$\chi = \alpha/T + \beta, \quad (2.22)$$

with α and β material specific constants that can be determined in experiments. The excess free energy as a function of ϕ_A given in Equation 2.21 is plotted assuming several different values of χ . If χ is small, the free energy is a concave curve with only one minimum. In this case, the free energy increases with inhomogeneity and there will be no phase separation. If χ is large, the free energy has two local minima, phase separation at the coexisting concentrations will result in a lower free energy than the homogeneous state. In this case, the system undergoes a spontaneous phase transition into A/B -rich domains, the so-called macrophase separation.

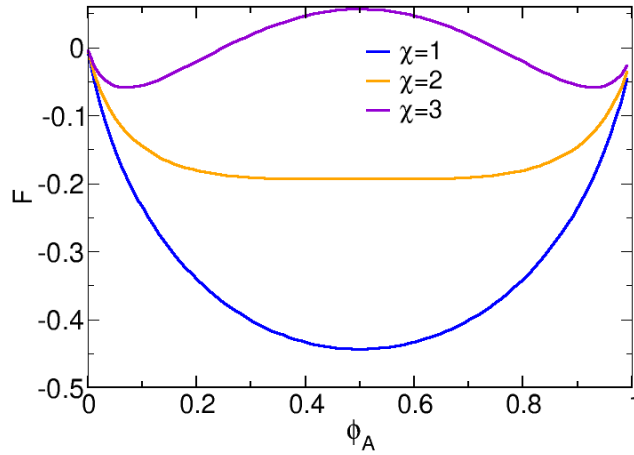


FIGURE 2.2: The free energy of a binary polymer mixture is illustrated for three χ values. If the free energy has only one minimum, the equilibrium state will be a homogeneous one. The free energy curve has two minima if χ is large enough. In this case, the equilibrium state is spatially segregated into domains with corresponding coexisting concentrations.

In diblock copolymers, the connectivity between the blocks prevents a macrophase separation as in the mixture of homopolymers. Instead, the strong repulsion between unlike sequences leads to microphase separation into smaller A/B -rich domains on the level of molecular dimensions. More complex models are required in order to describe the microphase separation of diblock copolymers, for they must take into account the long-range interaction resulting from the connectivity.

2.3.1 SCFT of diblock copolymer melts

In the limit of infinite invariant degree of polymerization, *i.e.* $\sqrt{N} = \frac{\rho_0}{N} R_e^3 \rightarrow \infty$, an accurate free-energy functional can be calculated within the framework of SCFT. The content of this section does not result from my own calculations but summarizes other literature [20–22].

In SCFT, chains are continuous and the system is strictly incompressible everywhere. Consider a system consisting of n molecules with monomer discretization N and the fraction of A -block is denoted as f_A . Normalized density operators are used to express the segment concentration. They are defined as

$$\hat{\phi}_A(\vec{r}) = \frac{N}{\rho_0} \sum_{\alpha=1}^n \int_0^{f_A} ds \delta(\vec{r} - \vec{r}_\alpha(s)) \quad (2.23)$$

$$\hat{\phi}_B(\vec{r}) = \frac{N}{\rho_0} \sum_{\alpha=1}^n \int_{f_A}^1 ds \delta(\vec{r} - \vec{r}_\alpha(s)), \quad (2.24)$$

where $\vec{r}_\alpha(s)$ is the space curve of the α 'th diblock and s the parameter used to label the monomers. The bonded energy of the chain α can be expressed by its trajectory

$$\frac{E_b[\vec{r}_\alpha(s)]}{k_B T} = \frac{3}{2Nb^2} \int_0^1 \left| \frac{d\vec{r}_\alpha(s)}{ds} \right|^2 ds. \quad (2.25)$$

The non-bonded repulsive energy between unlike species is:

$$\frac{E_{nb}[\hat{\phi}_A, \hat{\phi}_B]}{k_B T} = \chi \rho_0 \int d\vec{r} \hat{\phi}_A \hat{\phi}_B, \quad (2.26)$$

with χ the Flory-Huggins incompatibility parameter and $\rho_0 = \frac{nN}{V}$ the number density of particles in the system. Assuming incompressibility for a dense diblock copolymer melt leads to the constraint

$$\hat{\phi}_A(\vec{r}) + \hat{\phi}_B(\vec{r}) = 1. \quad (2.27)$$

The partition function of the diblock copolymer melt is given by [20]

$$\mathcal{Z}_{SCFT} \propto \frac{1}{n!} \int \prod_{\alpha=1}^n \mathcal{D}[\{\vec{r}\}_{\alpha}] \exp \left\{ -\chi \rho_0 \int d\vec{r} \hat{\phi}_A \hat{\phi}_B \right\} \quad (2.28)$$

$$\times \delta[1 - \hat{\phi}_A - \hat{\phi}_B] \exp \left\{ -\frac{3}{2Nb^2} \int_0^1 ds \left[\frac{d\vec{r}_{\alpha}(s)}{ds} \right]^2 \right\}. \quad (2.29)$$

with $\mathcal{D}[\{\vec{r}\}_{\alpha}]$ the path integral that runs over all segments on polymer α . The partition function \mathcal{Z}_{SCFT} cannot be solved directly. It is necessary to apply the Hubbard–Stratonovich transformation, which decouples the pairwise interaction via fluctuating auxiliary fields. This exact reformulation enables the subsequent mean-field approximation. For diblock copolymers, auxiliary fields W_A, W_B, ϕ_A, ϕ_B and Ξ are introduced by establishing the unity conditions [20]

$$1 = \int \mathcal{D}\Xi \exp \left\{ \int d\vec{r} \frac{\rho_0}{N} \Xi (1 - \hat{\phi}_A - \hat{\phi}_B) \right\}, \quad (2.30)$$

$$1 = \int \mathcal{D}\phi_A \delta[\phi_A - \hat{\phi}_A], \quad (2.31)$$

$$1 = \int \mathcal{D}\phi_B \delta[\phi_B - \hat{\phi}_B], \quad (2.32)$$

$$1 = \int \mathcal{D}W_A \int \mathcal{D}\phi_A \exp \left\{ \int d\vec{r} \frac{\rho_0}{N} W_A (\phi_A - \hat{\phi}_A) \right\}, \quad (2.33)$$

$$1 = \int \mathcal{D}W_B \int \mathcal{D}\phi_B \exp \left\{ \int d\vec{r} \frac{\rho_0}{N} W_B (\phi_B - \hat{\phi}_B) \right\}. \quad (2.34)$$

Inserting the identities into the partition function one obtains

$$\mathcal{Z}_{SCFT} \propto \int \mathcal{D}\Xi \int \mathcal{D}\phi_A \int \mathcal{D}\phi_B \int \mathcal{D}W_A \int \mathcal{D}W_B \exp \left\{ -\frac{\mathcal{F}_{SCFT}}{k_B T} \right\}. \quad (2.35)$$

The free-energy functional $\mathcal{F}_{SCFT}[\phi_A, \phi_B, W_A, W_B, \Xi]$ acquires the expression [20]

$$\begin{aligned} \frac{\mathcal{F}_{SCFT}}{k_B T} = & -\ln \mathcal{Q} + \frac{1}{V} \int d\vec{r} \left\{ \chi N \phi_A(\vec{r}) \phi_B(\vec{r}) \right. \\ & \left. - W_B \phi_B(\vec{r}) - W_A \phi_A(\vec{r}) - \Xi [1 - \phi_A(\vec{r}) - \phi_B(\vec{r})] \right\}, \end{aligned} \quad (2.36)$$

with V denoting the volume. \mathcal{Q} is the partition function of a single Gaussian chain in external fields W_A and W_B

$$\begin{aligned} \mathcal{Q}[W_A, W_B] \propto & \int \mathcal{D}[\{\vec{r}\}_i] \exp \left\{ - \int_0^{f_A} ds W_A(\vec{r}_i(s)) - \int_{f_A}^1 ds W_B(\vec{r}_i(s)) \right\} \\ & \times \exp \left\{ - \frac{3}{2Nb^2} \int_0^1 ds \left[\frac{d\vec{r}_i(s)}{ds} \right]^2 \right\}. \end{aligned} \quad (2.37)$$

In the mean-field approximation, the equilibrium free-energy functional is obtained by replacing the auxiliary fields by the most probable ones. Minimizing the free energy with respect to $\phi_A, \phi_B, W_A, W_B, \Xi$ leads to self-consistent equations [20]

$$\phi_A + \phi_B - 1 = 0 \quad (2.38)$$

$$\frac{V}{\mathcal{Q}} \frac{\delta \mathcal{Q}}{\delta W_A} + \phi_A = 0 \quad (2.39)$$

$$\frac{V}{\mathcal{Q}} \frac{\delta \mathcal{Q}}{\delta W_B} + \phi_B = 0 \quad (2.40)$$

$$\Xi - W_A + \chi N \phi_B = 0 \quad (2.41)$$

$$\Xi - W_B + \chi N \phi_A = 0. \quad (2.42)$$

Back-substituting the solutions of the above equations $\phi_A^*, \phi_B^*, W_A^*, W_B^*, \Xi^*$ into \mathcal{F}_{SCFT} provides the free energy of the equilibrium state in the absence of thermal fluctuations.

2.3.2 RPA of diblock copolymer melts

In case the local density deviates only little from its mean value, the free energy can be expanded in terms of the order parameter by means of Random Phase Approximation (RPA). Here, I provide a brief overview of the static RPA of diblock copolymers. More detailed aspects on the structure factor and RPA can be found in [chapter 3](#). In the weak segregation regime, Leibler [23] introduced the RPA formalism of microphase separation in diblock copolymers. Because of the incompressibility constraint, the local density fluctuation of A -type segments $\phi(\vec{r}) = \phi_A(\vec{r}) - f_A$ is sufficient to parametrize the density field. $\phi(\vec{r})$ is used as an order parameter for the free energy near the phase transition. The free energy of copolymers in the weak segregation regime can be expressed by a fourth-order Taylor

expansion in the Fourier modes of ϕ [23]

$$\begin{aligned} \frac{\mathcal{F}[\phi]}{k_B T} = & \frac{1}{2!} \int \frac{d\vec{q}}{(2\pi)^3} \gamma_2(\vec{q}) \phi(\vec{q}) \phi(-\vec{q}) \\ & + \frac{1}{3!} \int \frac{d\vec{q}_1 d\vec{q}_2}{(2\pi)^6} \gamma_3(\vec{q}_1, \vec{q}_2) \phi(\vec{q}_1) \phi(\vec{q}_2) \phi(-\vec{q}_1 - \vec{q}_2) \\ & + \frac{1}{4!} \int \frac{d\vec{q}_1 d\vec{q}_2 d\vec{q}_3}{(2\pi)^9} \gamma_4(\vec{q}_1, \vec{q}_2, \vec{q}_3) \phi(\vec{q}_1) \phi(\vec{q}_2) \phi(\vec{q}_3) \phi(-\vec{q}_1 - \vec{q}_2 - \vec{q}_3) \\ & + \dots \end{aligned} \quad (2.43)$$

with

$$\phi(\vec{q}) = \frac{1}{V} \int [\phi_A(\vec{r}) - f_A] \exp(i\vec{r} \cdot \vec{q}) d\vec{r} \quad (2.44)$$

the Fourier transformed order parameter.

For symmetric diblock copolymers, the third-order vertex vanishes. The fourth-order vertex γ_4 is found to be only weakly dependent on \vec{q} and can be approximated by a wavevector-independent constant [23, 24]. The second-order vertex function γ_2 is given by the inverse structure factor $S_{\vec{q}}$ via

$$\gamma_2(\vec{q}) = 1/S_{\vec{q}} - 2\chi. \quad (2.45)$$

The structure factor takes the form [23]

$$S_{\vec{q}} = N \frac{g(x, f)g(x, 1-f) - 1/4 [g(x, 1) - g(x, f) - g(x, 1-f)]^2}{g(x, 1)} \quad (2.46)$$

where $g(x, f)$ is the Debye-function defined as

$$g(x, f) = \frac{2}{x^2} [fx + \exp(-fx) - 1] \quad \text{with} \quad x = \frac{\vec{q}^2 R_e^2}{6}. \quad (2.47)$$

The second-order term contribution to the free energy is

$$\frac{\mathcal{F}_2[\phi]}{k_B T} \propto \int d\vec{q} \phi(\vec{q}) \phi(-\vec{q}) (1/S_{\vec{q}} - 2\chi). \quad (2.48)$$

For $1/S_{\vec{q}} - 2\chi > 0$, the second-order contribution to the free energy is positive. In this case, any density fluctuation around the homogeneous state increases the free energy and

thus will be suppressed. For large χ such that $1/S_{\bar{q}} - 2\chi$ becomes smaller than zero, the second-order contribution to the free energy becomes negative. This suggests that large density fluctuations are energetically favored and indicates the formation of domains with very different compositions. In this case, the fourth-order term in the Taylor-expansion of the free energy must be considered in order to describe the spatially modulated equilibrium state.

2.3.3 Microphase separation of diblock copolymer melts

At high χN , Equation 2.48 suggests ordered morphology of diblock copolymers. Depending on the volume fraction of the block components, diblock copolymers form different equilibrium morphologies, such as body-centered cubic, hexagonal or lamellar microphase structure in the ordered state. In Figure 2.3, a phase diagram with the equilibrium morphologies of diblock copolymer melts in microphase separated phases is shown as a function of the volume fraction of A -type block f_A . The ODT of diblock copolymers is controlled by the Flory-Huggins parameter χN .

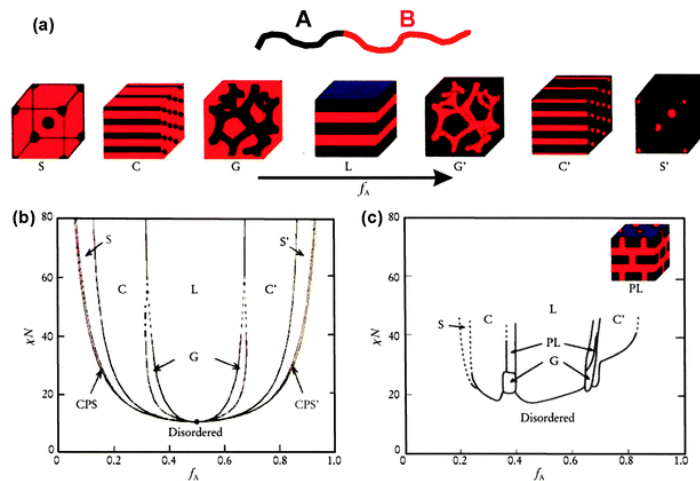


FIGURE 2.3: The phase diagram of diblock copolymers as a function of the volume fraction of A -type block f_A is shown. The multitude of morphologies in the corresponding ordered states is illustrated. The figures are republished with permission of [25]; permission conveyed through Copyright Clearance Center, Inc. And with permission from [20] Copyright 2021 by the American Physical Society.

In this thesis, the focus is the lamella-forming symmetric diblock copolymers, *i.e.* $f_A = 1/2$. As χN is increased, the system undergoes a transition from a disordered state, where the composition field is homogeneous, to an ordered state with long-range order characterized by

a dominant scattering vector q^* . RPA predicts a structure factor singularity at $q^*R_e \approx 3.79$ which corresponds to the length scale of $1.32R_e$. The ODT of symmetric diblock copolymers is predicted to be a second-order one and occurs at $\chi_c N \approx 10.495$ [23].

To account for the correction to the mean-field approximation caused by fluctuation effects, one could apply a universal class of models first considered by Brazovskii [26]. These systems exhibit an instability against fluctuations and has an isotropic fluctuation spectrum with a maximum near a shell of non-zero wavevectors $|\vec{q}| = q^*$ (instead of one single wavevector). For this type of systems, Brazovskii suggests a fluctuation-induced first-order transition instead of a continuous second-order one. Fredrickson and Helfand [27] studied fluctuation corrections to Leibler's theory on critical behavior of diblock copolymers. They explained the fluctuation-induced first-order phase transition of symmetric diblock copolymers and predicted the location of the ODT to be increased to

$$\chi_c N = 10.495 + 41.022\bar{N}^{-1/3}$$

with \bar{N} the invariant degree of polymerization. In case of symmetric diblock copolymers with infinite molecular weight, the result of Leibler is recovered.

2.4 Particle-based, coarse-grained simulations

Although many well developed analytical models such as RPA exist for polymer systems, the accuracy of their predictions are often limited to a certain regime (weak segregation limit, strong segregation limit, etc.). To overcome the limitation of analytical calculations as well as to verify their correctness, computational simulations are applied to draw conclusions about complex systems directly. For polymeric simulations, the entities involved in the calculation range from atomic length scale (*e.g.* atoms) to micrometers (*e.g.* macromolecules). With the current computational capacity, there exist no efficient way to capture the behavior of such a system at all length scales for large system sizes and simulation time scales. Various models [28, 29] were proposed to describe polymer systems at different levels of granularity. Atomistic simulations handle atoms or molecules and their interactions explicitly.

They provide insights on monomer-level phenomena on length scales much shorter than the polymer chain contour length. This type of simulation is computationally very expensive if one is interested in phenomena occurring on the length scales of polymer chains and on large time scales. Coarse-grained models [30, 31] were introduced to speed up large-scale simulations by replacing atomistic descriptions with coarse-grained ones. They make use of the fractal nature of a macromolecule on mesoscopic length scales to reduce the degrees of freedom. The effective interaction centers, or the so-called segments, are obtained by integrating out the degrees of freedom inside the segment using underlying microscopic models. In this type of simulations, each interaction center can represent multiple monomeric repeating units. During this process, information below the coarse-grained scale is lost. Thus, the coarse-graining level should be adjusted according to the scientific goal.

2.4.1 Single chain in mean field algorithm

The thermodynamics and the kinetics of diblock copolymers during structure formation is governed by a large degree of universality with respect to the polymerization N as a result of their self-similar structure. Coarse-grained models can be applied in the simulation of the self-assembly of diblock copolymer systems. In this thesis, the main part of the simulations are based on the Single Chain in Mean Field (SCMF) algorithm [32] developed for dense polymer systems by Daoulas and Müller. In SCMF, a large number of monomeric repeating units are grouped into an effective coarse-grained interaction center (segment) to reduce the degrees of freedom. Henceforth, the terms monomer, bead and segment will be used interchangeably.

The chain architecture and the interactions in SCMF are encoded by a few invariant parameters. The basic length scale is the mean-squared end-to-end distance of a free, non-interacting molecule R_e . A configuration composed of n indistinguishable molecules, each discretized into N segments, has an invariant degree of polymerization $\sqrt{\bar{N}} = \frac{n}{V} R_e^3$, which is the number of polymers in a cubic box with side length equal to the reference chain length. \bar{N} reflects the number of neighbors one polymer chain interacts with and is also an experimentally relevant quantity. The coarse-grained description of a polymer chain is invariant under variation of the contour segment discretization N . The resolution of the

coarse-grained model is constrained by the smallest length scale $b = \frac{1}{\sqrt{N-1}}$ *i.e.* the statistical segment length. The statistical segment lengths of all components are assumed to be identical in this work.

The particles in SCMF simulation experience a bonded interaction, provided by the connectivity between segments along the molecular backbone, and non-bonded monomer interactions.

The *bonded interaction* is described by the discretized bead-spring model from [section 2.1](#). The effective Hamiltonian of the bonded interaction for all segments on a single polymer chain is given by

$$\frac{\mathcal{H}_b}{k_B T} = \sum_{i=1}^n \sum_{(s,s')} \frac{3(N-1)}{2R_e^2} \left[\vec{r}_i(s) - \vec{r}_i(s') \right]^2, \quad (2.49)$$

where (s, s') are pairs of segments that are connected via a bond. For a linear chain, (s, s') follows $s' = s + 1$.

$\hat{\phi}_\alpha(\vec{r})$ is used to denote the density of a given component α after coarse-graining. In the simulation, the discrete density field is computed for each type of particles in each simulation cell c . This density is denoted by $\hat{\phi}_\alpha(c)$ and computed as

$$\hat{\phi}_\alpha(c) = \int_{\Delta V} \frac{d^3\vec{r}}{\Delta V} \hat{\phi}_\alpha(\vec{r}), \quad (2.50)$$

with ΔV the volume of a simulation cell.

In order to accelerate the simulation, the non-bonded interactions are simplified into computational less demanding soft potentials that mimic the relevant interactions between the segments. There are two types of non-bonded interactions in SCMF: the incompressibility constraint that limits fluctuations of the total density and the repulsive force between segments from different species.

The *incompressibility constraint* keeps the fluctuation of the total density around the average density small. The strength of the total density fluctuation is restrained by the parameter κ which is related to the inverse isothermal compressibility. The *incompatibility* is the repulsion between monomers from different species. In SCMF, the strength of the

thermodynamic incompatibility is controlled by the Flory-Huggins parameter χ . The non-bonded part of the discretized effective Hamiltonian reads [32]

$$\frac{\mathcal{H}_{nb}[\hat{\phi}_A(c), \hat{\phi}_B(c)]}{k_B T} = \frac{\rho_0 \Delta V}{N} \sum_{c \in \text{cells}} \left\{ \frac{\kappa N}{2} [\hat{\phi}_A(c) + \hat{\phi}_B(c) - 1]^2 - \frac{\chi N}{4} [\hat{\phi}_A(c) - \hat{\phi}_B(c)]^2 \right\}. \quad (2.51)$$

The potentials can be described by auxiliary external fields $\mathcal{W}_A(c)$ and $\mathcal{W}_B(c)$ [32]. The external fields are functional derivatives of the non-bonded part of the Hamiltonian with respect to the corresponding density field

$$\begin{aligned} \mathcal{W}_A(c) &= \frac{N}{k_B T \rho_0 \Delta V} \frac{\delta \mathcal{H}_{nb}}{\delta \hat{\phi}_A(c)} \\ &= \kappa N [\hat{\phi}_A(c) + \hat{\phi}_B(c) - 1] - \frac{\chi N}{2} [\hat{\phi}_A(c) - \hat{\phi}_B(c)] \end{aligned} \quad (2.52)$$

$$\begin{aligned} \mathcal{W}_B(c) &= \frac{N}{k_B T \rho_0 \Delta V} \frac{\delta \mathcal{H}_{nb}}{\delta \hat{\phi}_B(c)} \\ &= \kappa N [\hat{\phi}_A(c) + \hat{\phi}_B(c) - 1] - \frac{\chi N}{2} [\hat{\phi}_B(c) - \hat{\phi}_A(c)]. \end{aligned} \quad (2.53)$$

During the simulation, the external fields are kept constant during each simulation step. Because of this, they are also called quasi-instantaneous external fields. Instead of pairwise interactions, the molecules in the simulation are in constant interaction with $\mathcal{W}_A(c)$ and $\mathcal{W}_B(c)$. This allows all particles that are not directly connected with each other to be treated simultaneously and thus enables a parallel implementation of the SCMF algorithm for large-scale simulations on high-performance computers. The calculation of the quasi-instantaneous fields requires a sufficient number of segments in each simulation cell. Hence, the method is rather appropriate for dense polymer melts. SCMF includes fluctuation effects to achieve an accurate description in vicinity of *e.g.* phase transitions [33, 34]. In the simulation, $\bar{\mathcal{N}}$ controls the strength of the fluctuations. In the limit $\sqrt{\bar{\mathcal{N}}} \rightarrow \infty$, fluctuations are strongly suppressed and the mean-field results are recovered.

The MC sampling technique is applied to update the positions of the particles. To be more precise, a smart MC procedure [35] that uses stiff bonded forces [36] is implemented to mimic the Rouse-type dynamics. The procedure of the algorithm can be divided into four

parts:

- The density $\hat{\phi}_\alpha(c)$ of each simulation cell is calculated from the position vectors $\{\vec{r}\}$ of the segments.
- The external quasi-instantaneous fields $\mathcal{W}_\alpha(c)$ are computed from $\hat{\phi}_\alpha(c)$.
- Changes to positions are suggested (smart Monte-Carlo move) to segments that are not directly connected with each other via bonds. Segments that depend on each other are treated successively.
- The energy difference between the new and old configuration is calculated. The proposed attempts are accepted according to the Metropolis acceptance rate [37].

During the simulation, this cycle of calculation will be repeated and each round is called one MC-step.

The SCMF method is a suitable tool to perform large-scale polymer simulations because of its high parallel capability as a result of the application of quasi-instantaneous fields to decouple the molecules. The features of SCMF have been well investigated and verified since it was proposed. The simulated evolution of polymer chains successfully recovers the diffusive behavior of Rouse-type dynamics [35]. The thermodynamics including fluctuations is also correctly captured by the algorithm [38]. SOMA [38] is a software for polymer simulations based on the SCMF algorithm implemented in C with the option to be executed in parallel on multi-core central processing units and graphics processing units. The simulation study of polymer systems throughout this thesis will be carried out with SOMA if not stated otherwise.

Part I

Collective short-time dynamics in multicomponent polymer melts

Chapter 3

Collective short-time dynamics: Analytical aspects

Some content of this chapter 3 has been published in *Macromolecules* with the title “Collective Short-Time Dynamics in Multicomponent Polymer Melts” [39]. Some parts of this chapter are results of close collaboration with Marcus Müller and Yongzhi Ren.

Diblock copolymers microphase separate into diverse stable and metastable morphologies when they experience a sudden change of thermodynamic control parameters (quench). The condition for the phase transition as well as the equilibrium states are described by static SCFT and static RPA as introduced in [chapter 2](#). Despite the progress made in this field, the fabrication of morphologies for experimental and engineering purposes still faces the difficulty that the polymer systems often become stuck in a metastable state without reaching the target thermodynamical equilibrium state. In order to invent and fabricate desired complex morphologies, one needs to develop a strategy that allows guidance of the structure formation. Studies on process-directed self-assembly [40–42] suggest that the early stage structure evolution provides a template for the development of the morphology in the later stage. Hence, to tailor the relaxation process after quenching, it is important to understand the short-time dynamics that occurs spontaneously after the initial equilibrium state becomes unstable.

In this part of the thesis, the dynamics of multicomponent polymer systems from an unstable initial state to the next free-energy local minimum is investigated with a focus on the structure formation on very short length and time scales. The length scale shall remain small

compared to the typical mean-squared end-to-end distance R_e . The time scale will be kept short compared to the single-chain relaxation time τ_R .

Two popular techniques, D-SCFT [43–55] and D-RPA [56–60] are applied to explore the collective short-time dynamics of polymer melts. In this chapter, the basics of both methods will be introduced. Equations of dynamics within the corresponding models, which can be found in the literatures mentioned above, are used as the starting point of the calculations. Then, time evolutions of specific systems of our interest are derived. In the next chapter, the predictions made by the analytical models are compared with simulation results carried out by SOMA. Since the dynamics at this time and length scale is very unique, common analytical models might break down at this scale because the sub-diffusive dynamics become the dominant factor.

3.1 D-SCFT and Onsager Coefficients

D-SCFT was introduced to describe the structure evolution in an incompressible binary polymer melt. Incorporating the SCFT free-energy expression \mathcal{F} , it searches for the dynamics of the normalized density fields $\phi_A(\vec{r})$ and $\phi_B(\vec{r}) = 1 - \phi_A(\vec{r})$. During the spatial decomposition of multicomponent polymer systems, the exchange chemical potential μ acts as the driving force for the density evolution.

In the absence of fluctuations, the thermodynamical force is given by the gradient of the exchange chemical potential [61]

$$\mathbf{J}(\vec{r}, t) = - \int_{\mathbf{V}} \Lambda(\vec{r} - \vec{r}') \nabla \frac{\mu(\vec{r}', t)}{k_B T}. \quad (3.1)$$

Inserting the above equation into the continuity equation

$$\frac{\partial \phi_A(\vec{r}, t)}{\partial t} = - \nabla \cdot \mathbf{J}(\vec{r}, t) \quad (3.2)$$

with $\phi_A(\vec{r}, t)$ the segment density of particles of type A , a model-B type [56, 62, 63] time evolution is obtained

$$\frac{\partial \phi_A(\vec{r}, t)}{\partial t} = \nabla \cdot \int d\vec{r}' \Lambda(\vec{r} - \vec{r}') \nabla' \frac{\mu(\vec{r}', t)}{k_B T}. \quad (3.3)$$

The integral kernel Λ , that connects the gradient of the chemical potential with the dynamics of the collective densities, is called the Onsager Coefficient. According to SCFT, the exchange chemical potential is given by [64]

$$\mu(\vec{r}) = \frac{N}{\rho_0} \frac{\delta \mathcal{F}[\phi_A, \phi_B = 1 - \phi_A]}{\delta \phi_A(\vec{r})}. \quad (3.4)$$

Performing Fourier transformation on Equation 3.3, the wavevector-dependent form of Equation 3.3 reads

$$\frac{\partial \phi_{\vec{q}, A}(t)}{\partial t} = -\vec{q}^2 \Lambda_{\vec{q}} \frac{\mu_{\vec{q}}[\phi_{\vec{q}, A}]}{k_B T}. \quad (3.5)$$

The structure evolution predicted by D-SCFT may break down on short time and length scales because the displacement of segments, which corresponds to higher internal Rouse modes, is rather sub-diffusive and hence much faster than the diffusive one of the molecule's center of mass [55]. Moreover, the Onsager Coefficient is assumed to be time independent in D-SCFT but there is no physical evidence behind this assumption. In the latter part of this study, a modified D-SCFT (also called generalized model-B) that uses a time-dependent Onsager Coefficient is explored as an attempt to overcome some shortcomings of the original D-SCFT, such as the inability to describe short-time dynamics.

3.2 Static RPA

In this section, I apply static RPA to calculate the equilibrium state of an incompressible multicomponent polymer system depending on the Flory-Huggins parameter χ and external fields if applicable. I will leave the dynamical aspects of structure evolution to section 3.3 and concentrate only on the static results in this section. The partition function of polymers in

canonical ensemble [20, 23] assuming ideal gas within the linear response regime is given by

$$\begin{aligned}\mathcal{Z}[V_{\vec{q},A}, V_{\vec{q},B}] &= \prod_i \frac{1}{n_i! \Lambda_T^{3n_i N_i}} \int \prod_{i_p=1}^{n_i} \mathcal{D}[\{\vec{r}\}_{i,i_p}] \mathcal{P}[\{\vec{r}\}_{i,i_p}] \exp \left[-\rho_0 V \sum_{\alpha} \sum_{\vec{q}} \phi_{\vec{q},\alpha} V_{-\vec{q},\alpha} \right] \\ &= \prod_i \frac{\left\{ \mathcal{Q}_i[V_{\vec{q},A}, V_{\vec{q},B}] \right\}^{n_i}}{n_i! \Lambda_T^{3n_i N_i}}\end{aligned}\quad (3.6)$$

with $V_{\vec{q},A}$ and $V_{\vec{q},B}$ the constant potentials acting on A and B segments. Λ_T stands for the thermal de-Broglie wavelength. The path integral $\mathcal{D}[\{\vec{r}\}_{i,i_p}]$ runs over all segments on polymer i_p of type i . $\mathcal{P}[\{\vec{r}\}_{i,i_p}]$ is the Boltzmann factor of the corresponding chain conformation. The single-chain partition function of a polymer of type i takes the form [21, 65]

$$\begin{aligned}\mathcal{Q}_i[V_{\vec{q},A}, V_{\vec{q},B}] &= \int \mathcal{D}[\{\vec{r}\}_i] \mathcal{P}[\{\vec{r}\}_i] \exp \left[-\rho_0 V \sum_{\vec{q}} \left(\phi_{\vec{q},A,i} V_{-\vec{q},A} + \phi_{\vec{q},B,i} V_{-\vec{q},B} \right) \right] \\ &\approx \mathcal{Q}_i^{(0)} \left[1 + \frac{(\rho_0 V)^2}{2} \sum_{\vec{q}, \vec{q}'} \sum_{\alpha, \beta} V_{-\vec{q},\alpha} V_{\vec{q}',\beta} \left\langle \phi_{\vec{q},\alpha,i} \phi_{-\vec{q}',\beta,i} \right\rangle_0 + \dots \right] \\ &\approx \mathcal{Q}_i^{(0)} \exp \left[\frac{N_i}{2} \sum_{\vec{q}} \sum_{\alpha, \beta} S_{\vec{q},\alpha\beta,i} V_{-\vec{q},\alpha} V_{\vec{q},\beta} \right]\end{aligned}\quad (3.7)$$

where $\mathcal{Q}_i^{(0)}$ denotes the single-chain partition function of a polymer of type i in the absence of external fields. N_i stands for the polymerization of the polymer chain of type i . In the last step, the structure factor of polymers of type i is defined as

$$S_{\vec{q},\alpha\beta,i} \equiv \langle \phi_{\vec{q},\alpha,i} \phi_{-\vec{q},\beta,i} \rangle_0. \quad (3.8)$$

In the equation above, $\langle \dots \rangle_0$ is the average over all single-chain conformations in the absence of external fields. Alternatively, in particle-based simulations, $S_{\vec{q},\alpha\beta,i}$ can be computed directly from particles positions via

$$S_{\vec{q},\alpha\beta,i} = \frac{1}{N_i} \left\langle \sum_{a \in \alpha, b \in \beta}^{N_i} e^{i\vec{q}(\vec{r}_a - \vec{r}_b)} \right\rangle_{i_p} \quad (3.9)$$

where the average is performed over an ideal gas of polymers of the type i .

Inserting the single-chain partition function [Equation 3.7](#) into the canonical ensemble partition function [Equation 3.6](#) leads to

$$\mathcal{Z}_{\text{RPA}}[V_{\vec{q},A}, V_{\vec{q},B}] = \prod_i \frac{\left\{ \mathcal{Q}_i^{(0)} \right\}^{n_i}}{n_i! \Lambda_T^{3n_i N_i}} \exp \left[\sum_i \frac{n_i N_i}{2} \sum_{\vec{q}} \sum_{\alpha, \beta} S_{\vec{q}, \alpha \beta, i} V_{-\vec{q}, \alpha} V_{\vec{q}, \beta} \right]. \quad (3.10)$$

The average density of species α can be derived as the functional derivative of the partition function with respect to the corresponding field [\[65\]](#)

$$\langle \phi_{\vec{q}, \alpha} \rangle_{\text{RPA}} = -\frac{1}{\rho_0 V} \frac{\partial \ln \mathcal{Z}[V_{\vec{q},A}, V_{\vec{q},B}]}{\partial V_{-\vec{q}, \alpha}} \quad (3.11)$$

$$= -\sum_i \sum_{\beta} \frac{n_i N_i}{\rho_0 V} S_{\vec{q}, \alpha \beta, i} V_{\vec{q}, \beta} \quad (3.12)$$

$$= -\sum_{\beta} S_{\vec{q}, \alpha \beta} V_{\vec{q}, \beta} \quad (3.13)$$

with

$$S_{\vec{q}, \alpha \beta} = \sum_i \frac{n_i N_i}{\rho_0 V} S_{\vec{q}, \alpha \beta, i} \quad (3.14)$$

the concentration-weighted, static single-chain structure factor.

For a binary system $\alpha = A, B$, the external fields can be replaced by effective potentials defined as $V_{\vec{q},A} = \frac{W_{\vec{q}} + U_{\vec{q}}}{2}$ and $V_{\vec{q},B} = \frac{-W_{\vec{q}} + U_{\vec{q}}}{2}$ for simplicity. $U_{\vec{q}}$ acts as a pressure field that enforces the incompressibility constraint. I make use of the incompressibility constraint to eliminate $U_{\vec{q}}$:

$$\begin{aligned} 0 &= -\langle \phi_{\vec{q},A} \rangle_{\text{RPA}} - \langle \phi_{\vec{q},B} \rangle_{\text{RPA}} \\ &= \sum_i \frac{n_i N_i}{2\rho_0 V} \left\{ S_{\vec{q},AA,i} [W_{\vec{q}} + U_{\vec{q}}] + S_{\vec{q},AB,i} [-W_{\vec{q}} + U_{\vec{q}}] + \right. \\ &\quad \left. S_{\vec{q},BA,i} [W_{\vec{q}} + U_{\vec{q}}] + S_{\vec{q},BB,i} [-W_{\vec{q}} + U_{\vec{q}}] \right\} \\ &= W_{\vec{q}} \sum_i \frac{n_i N_i}{2\rho_0 V} [S_{\vec{q},AA,i} - S_{\vec{q},BB,i}] + \\ &\quad U_{\vec{q}} \sum_i \frac{n_i N_i}{2\rho_0 V} [S_{\vec{q},AA,i} + 2S_{\vec{q},BA,i} + S_{\vec{q},BB,i}]. \end{aligned} \quad (3.15)$$

One solution that guarantees the equality above is

$$\begin{aligned}
 U_{\vec{q}} &= -\frac{\sum_i \frac{n_i N_i}{\rho_0 V} [S_{\vec{q},AA,i} - S_{\vec{q},BB,i}]}{\sum_i \frac{n_i N_i}{\rho_0 V} [S_{\vec{q},AA,i} + 2S_{\vec{q},BA,i} + S_{\vec{q},BB,i}]} W_{\vec{q}} \\
 &= -\frac{S_{\vec{q},AA} - S_{\vec{q},BB}}{S_{\vec{q},AA} + 2S_{\vec{q},BA} + S_{\vec{q},BB}} W_{\vec{q}}.
 \end{aligned} \tag{3.16}$$

From this follows

$$\begin{aligned}
 V_{\vec{q},A} &= \frac{S_{\vec{q},AB} + S_{\vec{q},BB}}{S_{\vec{q},AA} + 2S_{\vec{q},BA} + S_{\vec{q},BB}} W_{\vec{q}} \\
 V_{\vec{q},B} &= -\frac{S_{\vec{q},AB} + S_{\vec{q},AA}}{S_{\vec{q},AA} + 2S_{\vec{q},BA} + S_{\vec{q},BB}} W_{\vec{q}}.
 \end{aligned} \tag{3.17}$$

Implementing Equation 3.17 into Equation 3.13 leads to the static RPA prediction for the equilibrium density field in response to effective potentials

$$\begin{aligned}
 \langle \phi_{\vec{q},A} \rangle_{\text{RPA}} &= -S_{\vec{q},AA} \frac{S_{\vec{q},AB} + S_{\vec{q},BB}}{S_{\vec{q},AA} + 2S_{\vec{q},BA} + S_{\vec{q},BB}} W_{\vec{q}} \\
 &\quad + S_{\vec{q},AB} \frac{S_{\vec{q},AB} + S_{\vec{q},AA}}{S_{\vec{q},AA} + 2S_{\vec{q},BA} + S_{\vec{q},BB}} W_{\vec{q}} \\
 &= -\underbrace{\frac{S_{\vec{q},AA}S_{\vec{q},BB} - (S_{\vec{q},AB})^2}{S_{\vec{q},AA} + 2S_{\vec{q},BA} + S_{\vec{q},BB}}}_{=S_{\vec{q}}} W_{\vec{q}} \equiv -S_{\vec{q}} W_{\vec{q}}.
 \end{aligned} \tag{3.18}$$

In case of the presence of a “real” external field $H_{\vec{q}}$ that contributes additionally to the monomer interaction controlled by χN , the effective potential $W_{\vec{q}}$ takes the form

$$W_{\vec{q}} = H_{\vec{q}} - \chi \left[\langle \phi_{\vec{q},A} \rangle_{\text{RPA}} - \langle \phi_{\vec{q},B} \rangle_{\text{RPA}} \right] = H_{\vec{q}} - 2\chi \langle \phi_{\vec{q},A} \rangle_{\text{RPA}}. \tag{3.19}$$

And the resulting collective density field in equilibrium state is

$$\langle \phi_{\vec{q},A} \rangle_{\text{RPA}} = -\frac{H_{\vec{q}}}{\frac{1}{S_{\vec{q}}} - 2\chi} = -S_{\vec{q}}^{\text{coll}} H_{\vec{q}} \tag{3.20}$$

$$\text{with } \frac{1}{S_{\vec{q}}^{\text{coll}}} \equiv \frac{1}{S_{\vec{q}}} - 2\chi, \tag{3.21}$$

with $S_{\vec{q}}^{\text{coll}}$ defined as the collective static structure factor. One should note that the expressions $S_{\vec{q},\alpha\beta}$, $H_{\vec{q}}$, $W_{\vec{q}}$, etc. are time independent. In the next section on D-RPA, these quantities will become dynamical and acquire explicit time dependency denoted as *e.g.* $S_{\vec{q},\alpha\beta}(t)$. The static structure factors are equivalent to the dynamical ones measured at reference time $t = 0$. The quantities without signified explicit time dependency should be assumed static. Occasionally, I will also address the static quantities explicitly with the argument (0), like in the case $S_{\vec{q},\alpha\beta}(0)$, to underline their difference to the dynamical ones.

3.3 Dynamic RPA

In this section, the dynamical RPA [56–60] is applied in order to derive the time evolution towards the equilibrium state. In this case, time-dependent effective external potentials $V_{\alpha}(\vec{r}, t)$ are used to mimic the relevant interactions.

The general starting point of D-RPA is a time-dependent structure factor, also called the dynamical structure factor $S_{\vec{q}}(t)$, and a response function $\chi_{\vec{q}}(t)$ [56] that connects the effective external potentials with the density field. The difference between the dynamical structure factor and the static one is the time delay between the measurements of the positions of the two beads. In the static structure factor, the positions of the two beads are measured simultaneously, whereas the dynamical structure factor is defined as a function of this time delay t [16]

$$S_{\vec{q},\alpha\beta}(t) = \frac{1}{N} \sum_{a \in \alpha, b \in \beta}^N e^{i\vec{q} \cdot [\vec{r}_a(t) - \vec{r}_b(0)]}. \quad (3.22)$$

The time-dependent linear response functions in Fourier space $\chi_{\vec{q},\alpha\beta}(t)$ is given by the dynamical structure factor of the reference system according to

$$\chi_{\vec{q},\alpha\beta}(t) = -\frac{\partial S_{\vec{q},\alpha\beta}(t)}{\partial t} \theta(t) \quad \text{with} \quad \theta(t) = \begin{cases} 1, & \text{for } t > 0 \\ 0, & \text{for } t < 0 \end{cases}. \quad (3.23)$$

$$(3.24)$$

I calculate the Laplace transform (denoted by a tilde) defined as the one-sided temporal Fourier transform of the response function

$$\tilde{\chi}_{\alpha\beta}(\omega) = \int_0^\infty dt \chi_{\alpha\beta}(t) e^{-i\omega t} = S_{\vec{q},\alpha\beta}(0) - i\omega \tilde{S}_{\vec{q},\alpha\beta}(\omega) \quad (3.25)$$

with $S_{\vec{q},\alpha\beta}(0)$ the static single-chain structure factor. The collective density field can be obtained according to

$$\begin{aligned} \phi_{\vec{q},\alpha}(t) &= - \sum_{\beta} \int_{-\infty}^t d\tau \chi_{\vec{q},\alpha\beta}(t-\tau) V_{\vec{q},\beta}(\tau) \\ \text{or} \\ \tilde{\phi}_{\vec{q},\alpha}(\omega) &= - \sum_{\beta} \tilde{\chi}_{\vec{q},\alpha\beta}(\omega) \tilde{V}_{\vec{q},\beta}(\omega). \end{aligned} \quad (3.26)$$

In the following, I will demonstrate detailed calculations on the time evolution of the density field (i) in response to external fields and (ii) after a quench from disordered state. For the purpose of clarity, I drop the explicit (ω) dependency in expression $\tilde{S}_{\vec{q}}(\omega)$, $\tilde{S}_{\vec{q},\alpha\beta}(\omega)$ and $\tilde{\chi}_{\vec{q},\alpha\beta}(\omega)$ hereafter. The $\tilde{}$ symbol per se is an indication of the (ω) dependency of the corresponding quantity.

3.3.1 Response to external fields

In this section, the response of density fields to a time periodic external field $H_{\vec{q}}(t) = H_{\vec{q}}^{(0)} \cos(\Omega t)$ is calculated. To start with, I write down the Laplace transform of the real external field, which repels A segments and favors B segments,

$$\tilde{H}_{\vec{q}}(\omega) = \pi H_{\vec{q}}^{(0)} [\delta(\omega - \Omega) + \delta(\omega + \Omega)]. \quad (3.27)$$

The effective potential can be written as

$$V_{\vec{q},A}(t) = \frac{-\chi [\phi_{\vec{q},A}(t) - \phi_{\vec{q},B}(t)] + H_{\vec{q}}^{(0)} \cos(\Omega t) + U_{\vec{q}}(t)}{2} \quad (3.28)$$

$$V_{\vec{q},B}(t) = \frac{+\chi [\phi_{\vec{q},A}(t) - \phi_{\vec{q},B}(t)] - H_{\vec{q}}^{(0)} \cos(\Omega t) + U_{\vec{q}}(t)}{2}, \quad (3.29)$$

where the field $U_{\vec{q}}(t)$ enforces the incompressibility constraint. The Laplace transformed effective potentials take the form

$$\tilde{V}_{\vec{q},A}(\omega) = \frac{-\chi \left[\tilde{\phi}_{\vec{q},A}(\omega) - \tilde{\phi}_{\vec{q},B}(\omega) \right] + \tilde{H}_{\vec{q}}(\omega) + \tilde{U}_{\vec{q}}(\omega)}{2} \quad (3.30)$$

$$\tilde{V}_{\vec{q},B}(\omega) = \frac{+\chi \left[\tilde{\phi}_{\vec{q},A}(\omega) - \tilde{\phi}_{\vec{q},B}(\omega) \right] - \tilde{H}_{\vec{q}}(\omega) + \tilde{U}_{\vec{q}}(\omega)}{2}. \quad (3.31)$$

Inserting this into [Equation 3.26](#), the density fields can be expressed as:

$$\begin{aligned} -2\tilde{\phi}_{\vec{q},A}(\omega) &= \left(\tilde{\chi}_{\vec{q},AA} - \tilde{\chi}_{\vec{q},AB} \right) \left(-\chi \left[\tilde{\phi}_{\vec{q},A}(\omega) - \tilde{\phi}_{\vec{q},B}(\omega) \right] + \tilde{H}_{\vec{q}}(\omega) \right) \\ &\quad + \left(\tilde{\chi}_{\vec{q},AA} + \tilde{\chi}_{\vec{q},AB} \right) \tilde{U}_{\vec{q}}(\omega) \end{aligned} \quad (3.32)$$

$$\begin{aligned} -2\tilde{\phi}_{\vec{q},B}(\omega) &= \left(\tilde{\chi}_{\vec{q},BA} - \tilde{\chi}_{\vec{q},BB} \right) \left(-\chi \left[\tilde{\phi}_{\vec{q},A}(\omega) - \tilde{\phi}_{\vec{q},B}(\omega) \right] + \tilde{H}_{\vec{q}}(\omega) \right) \\ &\quad + \left(\tilde{\chi}_{\vec{q},BA} + \tilde{\chi}_{\vec{q},BB} \right) \tilde{U}_{\vec{q}}(\omega). \end{aligned} \quad (3.33)$$

Note that $\tilde{\chi}_{\vec{q},AB} = \tilde{\chi}_{\vec{q},BA}$ and the incompressibility constraint $\tilde{\phi}_{\vec{q},A}(\omega) + \tilde{\phi}_{\vec{q},B}(\omega) = 0$ can be applied to eliminate $\tilde{U}_{\vec{q}}(\omega)$

$$\begin{aligned} \tilde{U}_{\vec{q}}(\omega) &= -\frac{\tilde{\chi}_{\vec{q},AA} - \tilde{\chi}_{\vec{q},BB}}{\tilde{\chi}_{\vec{q},AA} + 2\tilde{\chi}_{\vec{q},AB} + \tilde{\chi}_{\vec{q},BB}} \times \\ &\quad \left(-\chi \left[\tilde{\phi}_{\vec{q},A}(\omega) - \tilde{\phi}_{\vec{q},B}(\omega) \right] + \tilde{H}_{\vec{q}}(\omega) \right) \\ &= 2\chi \frac{\tilde{\chi}_{\vec{q},AA}\tilde{\phi}_{\vec{q},A}(\omega) + \tilde{\chi}_{\vec{q},BB}\tilde{\phi}_{\vec{q},B}(\omega)}{\tilde{\chi}_{\vec{q},AA} + 2\tilde{\chi}_{\vec{q},AB} + \tilde{\chi}_{\vec{q},BB}} - \\ &\quad \frac{\tilde{\chi}_{\vec{q},AA} - \tilde{\chi}_{\vec{q},BB}}{\tilde{\chi}_{\vec{q},AA} + 2\tilde{\chi}_{\vec{q},AB} + \tilde{\chi}_{\vec{q},BB}} \tilde{H}_{\vec{q}}(\omega). \end{aligned} \quad (3.34)$$

Replacing $\tilde{U}_{\vec{q}}(\omega)$ in the expression of density fields leads to

$$\tilde{\phi}_{\vec{q},A}(\omega) = -\frac{\tilde{\chi}_{\vec{q},AA}\tilde{\chi}_{\vec{q},BB} - \left(\tilde{\chi}_{\vec{q},AB} \right)^2}{\underbrace{\tilde{\chi}_{\vec{q},AA} + 2\tilde{\chi}_{\vec{q},AB} + \tilde{\chi}_{\vec{q},BB}}_{=\tilde{S}_{\vec{q}}}} \tilde{W}_{\vec{q}}(\omega) \quad (3.35)$$

$$\text{with } \tilde{W}_{\vec{q}}(\omega) = -2\chi\tilde{\phi}_{\vec{q},A}(\omega) + \tilde{H}_{\vec{q}}(\omega). \quad (3.36)$$

Equation 3.35 is the time-dependent generalization of the static RPA. I rewrite this equation similar to Equation 3.21

$$\tilde{\phi}_{\vec{q},A}(\omega) = -\frac{\tilde{H}_{\vec{q}}(\omega)}{\frac{1}{\tilde{S}_{\vec{q}}} - 2\chi} = -\tilde{S}_{\vec{q}}^{\text{coll}} \tilde{H}_{\vec{q}} \quad \text{with} \quad \frac{1}{\tilde{S}_{\vec{q}}^{\text{coll}}} = \frac{1}{\tilde{S}_{\vec{q}}} - 2\chi. \quad (3.37)$$

3.3.2 Quench from disordered state

I continue with the dynamics in a quenched polymer mixture. At time $t < 0$, the external field $V_{\vec{q},\alpha}(t)$ is set to a constant $V_{\vec{q},\alpha}^{(-)}$ to match the starting morphology $\phi_{\vec{q},\alpha}^{(-)}$. The density field is related to the effective external potential via (see static RPA)

$$V_{\vec{q},A}^{(-)} = -\frac{S_{\vec{q},AB} + S_{\vec{q},BB}}{S_{\vec{q},AA}S_{\vec{q},BB} - (S_{\vec{q},AB})^2} \phi_{\vec{q},A}^{(-)}, \quad (3.38)$$

$$V_{\vec{q},B}^{(-)} = +\frac{S_{\vec{q},AA} + S_{\vec{q},AB}}{S_{\vec{q},AA}S_{\vec{q},BB} - (S_{\vec{q},AB})^2} \phi_{\vec{q},A}^{(-)}. \quad (3.39)$$

For $t > 0$, monomers from unlike species start to repel each other. That gives rise to the effective potential of the form

$$V_{\vec{q},\alpha}(t) = -\chi \phi_{\vec{q},\alpha}(t) + U_{\vec{q}}(t) \quad (3.40)$$

where $U_{\vec{q}}(t)$ enforces the incompressibility constraint. Recalling Equation 3.26, the Laplace transformed density field in the linear response regime can be obtained via

$$\tilde{\phi}_{\vec{q},\alpha}(\omega) = -\sum_{\beta} \int_0^{\infty} dt \int_{-\infty}^t d\tau \chi_{\vec{q},\alpha\beta}(t-\tau) V_{\vec{q},\beta}(\tau) e^{-i\omega t} \quad (3.41)$$

$$= -\sum_{\beta} \tilde{S}_{\vec{q},\alpha\beta}(\omega) V_{\vec{q},\beta}^{(-)} - \sum_{\beta} \tilde{\chi}_{\vec{q},\alpha\beta}(\omega) \tilde{V}_{\vec{q},\beta}(\omega). \quad (3.42)$$

Implementing the expression for external fields into the above equation, the density field of A species is obtained

$$\begin{aligned} \tilde{\phi}_{\vec{q},A}(\omega) = & \frac{\tilde{S}_{\vec{q},AA}(\omega) [S_{\vec{q},AB} + S_{\vec{q},BB}] - \tilde{S}_{\vec{q},AB}(\omega) [S_{\vec{q},AA} + S_{\vec{q},AB}]}{S_{\vec{q},AA}S_{\vec{q},BB} - (S_{\vec{q},AB})^2} \phi_{\vec{q},A}^{(-)} \\ & + \chi \left[\tilde{\chi}_{\vec{q},AA} \tilde{\phi}_{\vec{q},A} + \tilde{\chi}_{\vec{q},AB} \tilde{\phi}_{\vec{q},B} \right] - [\tilde{\chi}_{\vec{q},AA} + \tilde{\chi}_{\vec{q},AB}] \tilde{U}_{\vec{q}}. \end{aligned} \quad (3.43)$$

$\tilde{U}_{\vec{q}}$ can be eliminated using the incompressibility constraint $\tilde{\phi}_{\vec{q},A}(\omega) + \tilde{\phi}_{\vec{q},B}(\omega) = 0$:

$$\begin{aligned} \tilde{U}_{\vec{q}} = & \chi \frac{\tilde{\chi}_{\vec{q},AA} - \tilde{\chi}_{\vec{q},BB}}{\tilde{\chi}_{\vec{q},AA} + 2\tilde{\chi}_{\vec{q},AB} + \tilde{\chi}_{\vec{q},BB}} \tilde{\phi}_{\vec{q},A} \\ & + \left\{ \frac{\tilde{S}_{\vec{q},AA} [S_{\vec{q},AB} + S_{\vec{q},BB}]}{[\tilde{\chi}_{\vec{q},AA} + 2\tilde{\chi}_{\vec{q},AB} + \tilde{\chi}_{\vec{q},BB}] [S_{\vec{q},AA}S_{\vec{q},BB} - (S_{\vec{q},AB})^2]} \right. \\ & - \frac{\tilde{S}_{\vec{q},AB} [S_{\vec{q},AA} - S_{\vec{q},BB}]}{[\tilde{\chi}_{\vec{q},AA} + 2\tilde{\chi}_{\vec{q},AB} + \tilde{\chi}_{\vec{q},BB}] [S_{\vec{q},AA}S_{\vec{q},BB} - (S_{\vec{q},AB})^2]} \\ & \left. - \frac{\tilde{S}_{\vec{q},BB} [S_{\vec{q},AA} + S_{\vec{q},AB}]}{[\tilde{\chi}_{\vec{q},AA} + 2\tilde{\chi}_{\vec{q},AB} + \tilde{\chi}_{\vec{q},BB}] [S_{\vec{q},AA}S_{\vec{q},BB} - (S_{\vec{q},AB})^2]} \right\} \phi_{\vec{q},A}^{(-)}. \end{aligned} \quad (3.44)$$

Inserting $\tilde{U}_{\vec{q}}$ into [Equation 3.43](#) leads to the D-RPA prediction for the structure evolution after a quench from the initial configuration $\phi_{\vec{q},A}^{(-)}$

$$\left(\frac{\tilde{\chi}_{\vec{q},AA} + 2\tilde{\chi}_{\vec{q},AB} + \tilde{\chi}_{\vec{q},BB}}{\tilde{\chi}_{\vec{q},AA}\tilde{\chi}_{\vec{q},BB} - (\tilde{\chi}_{\vec{q},AB})^2} - 2\chi \right) \tilde{\phi}_{\vec{q},A}(\omega) = \frac{\phi_{\vec{q},A}^{(-)}}{\tilde{S}'_{\vec{q}}(\omega)} \quad (3.45)$$

with

$$\begin{aligned} \frac{1}{\tilde{S}'_{\vec{q}}(\omega)} = & \frac{-i\omega \left(\tilde{S}_{\vec{q},AA} \tilde{S}_{\vec{q},BB} - \left(\tilde{S}_{\vec{q},AB} \right)^2 \right) \left(S_{\vec{q},AA} + 2S_{\vec{q},BA} + S_{\vec{q},BB} \right)}{\left(\tilde{\chi}_{\vec{q},AA} \tilde{\chi}_{\vec{q},BB} - \left(\tilde{\chi}_{\vec{q},AB} \right)^2 \right) \left(S_{\vec{q},AA} S_{\vec{q},BB} - \left(S_{\vec{q},AB} \right)^2 \right)} \\ & + \frac{\tilde{S}_{\vec{q},AA} \left[S_{\vec{q},AB} + S_{\vec{q},BB} \right]^2 + \tilde{S}_{\vec{q},BB} \left[S_{\vec{q},AB} + S_{\vec{q},AA} \right]^2}{\left(\tilde{\chi}_{\vec{q},AA} \tilde{\chi}_{\vec{q},BB} - \left(\tilde{\chi}_{\vec{q},AB} \right)^2 \right) \left(S_{\vec{q},AA} S_{\vec{q},BB} - \left(S_{\vec{q},AB} \right)^2 \right)} \\ & - \frac{2\tilde{S}_{\vec{q},AB} \left[S_{\vec{q},AB} + S_{\vec{q},AA} \right] \left[S_{\vec{q},AB} + S_{\vec{q},BB} \right]}{\left(\tilde{\chi}_{\vec{q},AA} \tilde{\chi}_{\vec{q},BB} - \left(\tilde{\chi}_{\vec{q},AB} \right)^2 \right) \left(S_{\vec{q},AA} S_{\vec{q},BB} - \left(S_{\vec{q},AB} \right)^2 \right)}. \end{aligned}$$

3.4 Analytical form of $S_{\vec{q},\alpha\beta}(t)$

So far, I have derived a relation between the dynamical single-chain structure factor $S_{\vec{q},\alpha\beta}(t)$ and the time evolution of the density field without specifying the exact form of $S_{\vec{q},\alpha\beta}(t)$. Numerically, one can measure $S_{\vec{q},\alpha\beta}(t)$ in the simulation with [Equation 3.22](#). However, in order to explore the underlying nature of the dynamics and to make predictions that can be generalized to other polymer systems, an analytic expression for $S_{\vec{q},\alpha\beta}(t)$ is essential.

In many simple cases, the dynamical structure factor $S_{\vec{q},\alpha\beta}(t)$ of an ideal gas of polymers is related to a normalized structure factor $g_{\vec{q}}(t)$ defined as

$$g_{\vec{q}}(t) \equiv \frac{1}{N^2} \sum_{i,j} \left\langle \exp [i\vec{q}(\vec{r}_i(t) - \vec{r}_j(0))] \right\rangle. \quad (3.46)$$

The expression of $g_{\vec{q}}(t)$ is very similar to that of $S_{\vec{q},\alpha\beta}(t)$ but independent of monomer types. Instead of computing an analytic expression for the time dependence of $S_{\vec{q},\alpha\beta}(t)$ for each specific type of polymer, I will first explore the temporal behavior of $g_{\vec{q}}(t)$. Then, $g_{\vec{q}}(t)$ will be used as an intermediate quantity to compute $S_{\vec{q},\alpha\beta}(t)$ for specific chain architectures. The advantages of this procedure are (i) $g_{\vec{q}}(t)$ has been studied for many decades and (ii) the transition from $g_{\vec{q}}(t)$ to $S_{\vec{q},\alpha\beta}(t)$ is straightforward for the systems of my interest.

The summands in $g_{\vec{q}}(t)$ can be calculated as [16]

$$\left\langle \exp [i\vec{q}(\vec{r}_i(t) - \vec{r}_j(0))] \right\rangle = \left\langle \exp \left[\sum_{\alpha=x,y,z} i q_{\alpha} (r_{i\alpha} - r_{j\alpha}) \right] \right\rangle \quad (3.47)$$

$$\begin{aligned} &= \prod_{\alpha=x,y,z} \exp \left(-\frac{1}{2} q_{\alpha}^2 \left\langle (r_{i\alpha}(t) - r_{j\alpha}(0))^2 \right\rangle \right) \\ &= \exp \left[-\frac{\vec{q}^2}{6} \left\langle (\vec{r}_i(t) - \vec{r}_j(0))^2 \right\rangle \right]. \end{aligned} \quad (3.48)$$

Using the Rouse modes expression in Equation 2.13 leads to [16]

$$\begin{aligned} \left\langle (\vec{r}_i(t) - \vec{r}_j(0))^2 \right\rangle &= \left\langle \left([X_0(t) - X_0(0)] \right. \right. \\ &\quad \left. \left. + 2 \sum_{p=1}^{\infty} \left[\cos \left(\frac{p\pi i}{N} \right) X_p(t) - \cos \left(\frac{p\pi j}{N} \right) X_p(0) \right] \right)^2 \right\rangle. \end{aligned} \quad (3.49)$$

Since the correlation between different modes vanishes, the above equality can be rewrite into

$$\begin{aligned} \left\langle (\vec{r}_i(t) - \vec{r}_j(0))^2 \right\rangle &= \left\langle \left([X_0(t) - X_0(0)] \right)^2 \right\rangle \\ &\quad + \left\langle \left(2 \sum_{p=1}^{\infty} \left[\cos \left(\frac{p\pi i}{N} \right) X_p(t) - \cos \left(\frac{p\pi j}{N} \right) X_p(0) \right] \right)^2 \right\rangle \end{aligned} \quad (3.50)$$

where the last term can be simplified to [16]

$$\sum_{p=1}^{\infty} \left[\cos \left(\frac{p\pi i}{N} \right) X_p(t) - \cos \left(\frac{p\pi j}{N} \right) X_p(0) \right]^2 = \frac{\pi^2}{2N} |i - j|. \quad (3.51)$$

Making use of the above equation, one obtains [16]

$$\begin{aligned} \left\langle (\vec{r}_i(t) - \vec{r}_j(0))^2 \right\rangle &= 6Dt + |i - j| b^2 + \frac{4Nb^2}{\pi^2} \sum_{p=1}^{\infty} \frac{1}{p^2} \cos \left(\frac{p\pi i}{N} \right) \\ &\quad \times \cos \left(\frac{p\pi j}{N} \right) \left(1 - \exp \left(-p^2 t / \tau_R \right) \right). \end{aligned} \quad (3.52)$$

Thus, $g_{\vec{q}}(t)$ can be calculated numerically by solving the following integral

$$g_{\vec{q}}(t) = \int_0^1 ds \int_0^1 ds' \exp \left\{ -\frac{(\vec{q}R_e)^2 |s - s'|}{6} - \frac{(\vec{q}R_e)^2 t}{3\pi^2 \tau_R} - \frac{2(\vec{q}R_e)^2}{3\pi^2} \sum_{p=1} \frac{1 - e^{-p^2 t / \tau_R}}{p^2} \cos(\pi p s) \cos(\pi p s') \right\}. \quad (3.53)$$

The relation between $S_{\vec{q},\alpha\beta}(t)$ and $g_{\vec{q}}(t)$ can be worked out analytically for simple chain architectures [63]. For homopolymer blends, the dynamical single-chain structure factor is linked to $g_{\vec{q}}(t)$ according to

$$S_{\vec{q},\alpha\beta}(t) = \bar{\phi}_\alpha N \delta_{\alpha\beta} g_{\vec{q}}(t) \quad (3.54)$$

$$\tilde{\chi}_{\vec{q},\alpha\beta}(\omega) = \bar{\phi}_\alpha N \delta_{\alpha\beta} \left[g_{\vec{q}}(0) - i\omega \tilde{g}_{\vec{q}}(\omega) \right]. \quad (3.55)$$

For diblock copolymers with A -fraction given by f_A , the structure factor is given by

$$S_{\vec{q},AA}(t) = N g_{\vec{q},f}(t) \quad (3.56)$$

$$S_{\vec{q},BB}(t) = N g_{\vec{q},1-f}(t) \quad (3.57)$$

$$S_{\vec{q},AB}(t) = \frac{N}{2} \left[g_{\vec{q}}(t) - g_{\vec{q},f}(t) - g_{\vec{q},1-f}(t) \right]. \quad (3.58)$$

In case of symmetric diblock copolymers *i.e.* $f_A = 1/2$, the Laplace transformed response function is found to be

$$\tilde{\chi}_{\vec{q},AA} = \tilde{\chi}_{\vec{q},BB} = N \left[g_{\vec{q},1/2}(0) - i\omega \tilde{g}_{\vec{q},1/2}(\omega) \right] \quad (3.59)$$

$$2\tilde{\chi}_{\vec{q},AB} = N \left[g_{\vec{q}}(0) - 2g_{\vec{q},1/2}(0) - i\omega \tilde{g}_{\vec{q}}(\omega) + 2i\omega \tilde{g}_{\vec{q},1/2}(\omega) \right]. \quad (3.60)$$

$g_{\vec{q}}(0)$ is the well known Debye-function [66]:

$$g_{\vec{q}}(0) = \frac{2}{x^2} (e^{-x} - 1 + x) \quad \text{with} \quad x = \frac{(\vec{q}R_e)^2}{6}. \quad (3.61)$$

For $(\vec{q}R_e)^2 \ll 1$, the exponential term e^{-x} in Equation 3.61 can be Taylor expanded around zero. In this regime, the Debye-function can be approximated by

$$g_{\vec{q}}(0) = \frac{2}{x^2}(1 - x + x^2/2 - x^3/6... - 1 + x) \quad (3.62)$$

$$\approx \frac{2}{x^2}\left(\frac{x^2}{2} - x^3/6\right) = (1 - x/3) \quad (3.63)$$

$$= 1 - (\vec{q}R_e)^2/18. \quad (3.64)$$

For $(\vec{q}R_e)^2 \gg 1$, the linear term x is the dominant term and the Debye-function can be approximated by

$$g_{\vec{q}}(0) \approx \frac{2}{x} = \frac{12}{(\vec{q}R_e)^2}. \quad (3.65)$$

3.4.1 Temporal behavior of $g_{\vec{q}}(t)$

With an accurate expression for $g_{\vec{q}}(t)$ and $S_{\vec{q}}(t)$, the time evolution of collective quantities, such as the density field, can be “easily” calculated within the linear response regime. Unfortunately, an accurate analytic form of the dynamical single-chain structure factor is not available even for the simplest linear chains. Approximations must be made in order to perform calculations with the dynamical structure factor. Typically, the structure evolution after a sudden change of control parameters can be separated into a sub-diffusive regime, an intermediate regime and a diffusive regime. Here, I introduce several approximations proposed to describe the time dependence of $g_{\vec{q}}(t)$ on different time scales. The approximations discussed in this section are visualized in Figure 3.1.

3.4.1.1 Ultimate short-time regime

The ultimate short-time behavior of the dynamic, single-chain structure factor deals with the short time limit where structure on small length scales *i.e.* $(\vec{q}R_e)^2 \gg 1$ is important. In this limit, the segments in polymer chains move only very little from their original position. The dynamics on this scale are dominated by free particle motion and the chain connectivity has

almost no impact. The time dependence of $g_{\vec{q}}(t)$ can be approximated by [16, 67]

$$\begin{aligned} g_{\vec{q}}(t) &= g_{\vec{q}}(0) \left[1 - \frac{t}{\tau_{\vec{q}}} + \mathcal{O}(t^{3/2}) \right] \\ &= g_{\vec{q}}(0) e^{-t/\tau_{\vec{q}}} + \mathcal{O}(t^{3/2}) \\ \text{with } \frac{1}{\tau_{\vec{q}}} &= \frac{(\vec{q}R_e)^2}{3\pi^2\tau_R g_{\vec{q}}} = \frac{(\vec{q}R_e)^4}{36\pi^2\tau_R}. \end{aligned} \quad (3.66)$$

$g_{\vec{q}}(t)$ adopts the scaling form

$$g_{\vec{q}}(t) = g_{\vec{q}}(0) \varphi \left(\frac{(\vec{q}R_e)^4 t}{36\pi^2\tau_R} \right), \quad (3.67)$$

with φ the scaling function with argument $\tau = \frac{(\vec{q}R_e)^4 t}{36\pi^2\tau_R}$. The Laplace transformed form of this scaling behavior reads

$$\frac{\tilde{g}_{\vec{q}}(\omega)}{g_{\vec{q}}(0)} = \frac{\Omega}{\omega} \tilde{\varphi}(\Omega), \quad (3.68)$$

$$\text{with } \tilde{\varphi}(\Omega) = \int_0^\infty dx e^{-i\Omega\tau} \varphi(\tau) \quad \text{and} \quad \Omega = \frac{36\pi^2\omega\tau_R}{(\vec{q}R_e)^4}. \quad (3.69)$$

The behavior of the scaling function $\varphi(\tau)$ in the limit $t \lesssim \frac{36\pi^2\tau_R}{(\vec{q}R_e)^4}$ is [67]

$$\varphi(\tau) = 1 - \tau + \frac{4\sqrt{2}}{3\sqrt{\pi}} \tau^{3/2} + \dots. \quad (3.70)$$

Or simply

$$\varphi(\tau) \approx \exp(-\tau). \quad (3.71)$$

In this limit, the important length scales are the very short ones and the Onsager coefficient can be treated as spatial-independent. This gives rise to the \vec{q} -independent “local” Onsager coefficient, $\Lambda_{\vec{q}}^{\text{local}} = \bar{\phi}_A \bar{\phi}_B D$. The Laplace representation of the exponential function in Equation 3.71 yields

$$\tilde{\varphi}(\Omega) \approx 1/(1 + i\Omega). \quad (3.72)$$

3.4.1.2 Intermediate regime

I consider the intermediate regime $\frac{36\pi^2\tau_R}{(\bar{q}R_e)^4} \ll t \ll \tau_R$ between the ultimate short-time scale and the classical long-time scale. In this regime, the dynamics is dominated by the sub-diffusive motion. The single-chain dynamics in this region can be approximated by [68, 69]

$$\varphi(\tau) \approx \frac{\pi^{3/4}}{\sqrt{2}} \tau^{1/4} \exp\left(-\sqrt{\frac{4\tau}{\pi}}\right). \quad (3.73)$$

A popular alternative expression for this regime is given by

$$\varphi(\tau) \approx 4.2 \exp\left(-\sqrt{\frac{4\tau}{\pi}}\right). \quad (3.74)$$

For large Ω , the Laplace transformation of Equation 3.73 is

$$\tilde{\varphi}(\Omega) = \frac{\pi^{3/4}}{\sqrt{2}} \sum_{n=0}^{\infty} \left(-\frac{2}{\sqrt{\pi}}\right)^n \frac{\Gamma(\frac{2n+5}{4})}{n!} \left(\frac{1}{i\Omega}\right)^{\frac{2n+5}{4}}. \quad (3.75)$$

The above expression for $\tilde{\varphi}$ can be numerically approximated over the entire Ω -regime by

$$\tilde{\varphi}(\Omega) \approx \frac{1}{i\Omega + 1 - \frac{\Omega_0(\tilde{\varphi}(0)-1)}{\tilde{\varphi}(0)(i\Omega+\Omega_0)}}. \quad (3.76)$$

with $\Omega_0 \approx 3.619$ and $\tilde{\varphi}(0) = \int_0^\infty dx \varphi(x) \approx 3.47$. Another advantage of this simplified expression is that it recovers the ultimate short-time scale limit for $\Omega \rightarrow 0$. The Taylor-expansion this expression in $z = \frac{1}{i\Omega}$ is

$$\begin{aligned} \tilde{\varphi}(\Omega) = z - z^2 + & \frac{(1 - \Omega_0)\tilde{\varphi}(0) + \Omega_0}{\tilde{\varphi}(0)} z^3 \\ & + \frac{(\Omega_0^2 + 2\Omega_0 - 1)\tilde{\varphi}(0) - (\Omega_0 + 2)\Omega_0}{\tilde{\varphi}(0)} z^4 + \dots. \end{aligned} \quad (3.77)$$

In time representation, this expression reads

$$\begin{aligned} \varphi(t) = 1 - t + & \frac{(1 - \Omega_0)\tilde{\varphi}(0) + \Omega_0}{2\tilde{\varphi}(0)} t^2 \\ & + \frac{(\Omega_0^2 + 2\Omega_0 - 1)\tilde{\varphi}(0) - (\Omega_0 + 2)\Omega_0}{6\tilde{\varphi}(0)} t^3 + \dots. \end{aligned} \quad (3.78)$$

The first two terms in Equation 3.78 match the exact ultimate short-time expansion. This expression gives rise to a time-dependent Onsager coefficient $\Lambda_{\vec{q}}(t)$ and provides a better approximation than D-SCFT.

3.4.1.3 Long-time regime

The structure evolution on long-time scale $t \gg \tau_R$, $\vec{q}R_e \ll 1$ (the classical regime) is governed by diffusive dynamics which can be described by an exponential decay

$$g_{\vec{q}}(t) = g_{\vec{q}}(0)e^{-\vec{q}^2 D t}. \quad (3.79)$$

The Laplace transformed structure evolution in the classical regime is

$$\tilde{g}_{\vec{q}}(\omega) = \frac{g_{\vec{q}}(0)}{i\omega + \vec{q}^2 D} = \frac{g_{\vec{q}}\tau_R}{i\omega\tau_R + \frac{(\vec{q}R_e)^2}{3\pi^2}}. \quad (3.80)$$

3.5 Dynamics of symmetric diblock copolymer

In the previous section, I computed an analytic expression for $g_{\vec{q}}(t)$ of a linear chain without further specification. In this section, I will perform this study on a fraction of a chain in order to describe the dynamics of block copolymers.

3.5.1 Dynamics of a chain fraction

Many mechanical and dynamical properties of polymer systems are governed by universal scaling behavior which has its origin in the fractal nature of polymer chains. Therefore, one would naturally expect a fragment of a chain to be described by the same dynamical behavior as an entire chain requiring only proper scaling. However, the dynamical single-chain structure factor of a chain fraction obeys, despite the self-similarity, a non-trivial decay law on certain length scales.

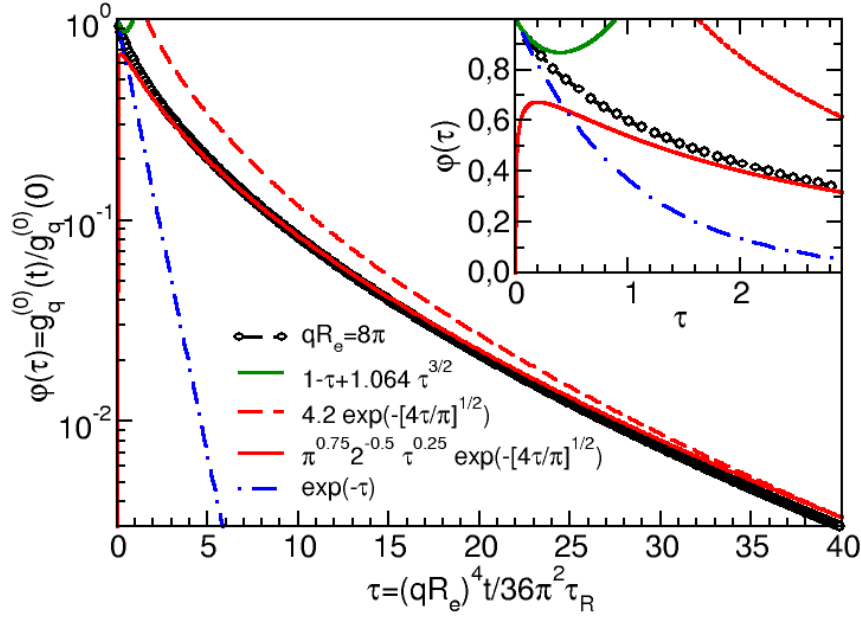


FIGURE 3.1: Time evolution of the single-chain structure factor $\phi \equiv \frac{g_{\vec{q}}(t)}{g_{\vec{q}}}$ measured in simulation (black dots) is shown for $qR_e = 8\pi$. One Rouse time τ_R corresponds to $\tau \approx 1123$ for this wavevector. The analytic approximations discussed in this section are shown for comparison. Equation 3.74 (red dashed) and Equation 3.73 (red solid) are popular approximation for the intermediate time scale. For the ultimate short-time scale, appropriate approximations are Equation 3.71 (blue dashed) and Equation 3.70 (green solid). The inset enlarges the small- τ regime. The figure is reprinted with permission from [39].
Copyright 2021 American Chemical Society.

The scale-free behavior in the limit $(\vec{q}R_e)^2 \gg 1$ and $t \ll \tau_R$ relates the dynamical structure factor of a block of a chain with fraction f to that of the entire chain according to

$$g_{\vec{q},f}(t) = f^2 g_{\sqrt{f}\vec{q}}(t/f^2) = f^2 g_{\sqrt{f}\vec{q}}(0) \phi\left(\frac{(\vec{q}R_e)^4 t}{36\pi^2 \tau_R}\right). \quad (3.81)$$

However, for a wide range of length scales, the scale-free universality is not the dominating effect. The dynamics of a chain fraction f for small \vec{q} is derived in the following

$$\begin{aligned}
g_{\vec{q},f}(t) &= \int_0^f ds \int_0^f ds' \exp \left\{ -\frac{(\vec{q}R_e)^2 |s-s'|}{6} - \vec{q}^2 Dt - \right. \\
&\quad \left. \frac{2(\vec{q}R_e)^2}{3\pi^2} \sum_{p=1} \frac{1 - e^{-p^2 t/\tau_R}}{p^2} \cos(\pi p s) \cos(\pi p s') \right\} \\
&\approx e^{-\vec{q}^2 Dt} \int_0^f ds \int_0^f ds' \left\{ 1 - \frac{(\vec{q}R_e)^2 |s-s'|}{6} - \right. \\
&\quad \left. \frac{2(\vec{q}R_e)^2}{3\pi^2} \sum_{p=1} \frac{1 - e^{-p^2 t/\tau_R}}{p^2} \cos(\pi p s) \cos(\pi p s') \right\} + \mathcal{O}\left((\vec{q}R_e)^4\right) \\
&\approx e^{-\vec{q}^2 Dt} \left\{ f^2 - \frac{(\vec{q}R_e)^2}{18} f^3 - \right. \\
&\quad \left. \frac{2(\vec{q}R_e)^2}{3\pi^2} \sum_{p=1} \frac{1 - e^{-p^2 t/\tau_R}}{p^2} \int_0^f ds \int_0^f ds' \cos(\pi p s) \cos(\pi p s') \right\} \\
&\quad + \mathcal{O}\left((\vec{q}R_e)^4\right) \\
&= e^{-\vec{q}^2 Dt} f^2 \left\{ 1 - \frac{f(\vec{q}R_e)^2}{18} - \right. \\
&\quad \left. \frac{2(\vec{q}R_e)^2}{3\pi^2 f^2} \sum_{p=1} \frac{1 - e^{-p^2 t/\tau_R}}{p^2} \left[\frac{\sin(\pi p f)}{p\pi} \right]^2 \right\} + \mathcal{O}\left((\vec{q}R_e)^2\right) \\
&= g_{\vec{q},f}(0) e^{-\vec{q}^2 Dt} e^{-(\vec{q}R_e)^2 h_f(t)} + \mathcal{O}\left((\vec{q}R_e)^4\right). \tag{3.82}
\end{aligned}$$

In the last step, a new function $h_f(t)$ defined as

$$h_f(t) \equiv \frac{2}{3\pi^2} \sum_{p=1} \frac{1 - e^{-p^2 t/\tau_R}}{p^2} \left[\frac{\sin(\pi p f)}{\pi p f} \right]^2 \tag{3.83}$$

is introduced to characterize the deviation of the dynamics of a block of a Rouse chain from the diffusive motion. The difference between the dynamics of a block of a chain with $f = 1/2$ and that of an entire chain is demonstrated in [Figure 3.2](#).

For $f = 1$, $h_f(t)$ vanishes and the diffusive decay of an entire chain is recovered. For symmetric diblock polymers, *i.e.* $f = 0.5$, there exists no closed analytical expression for $h_{1/2}(t)$. However, such an expression is needed in order to compute the Laplace transformation of the dynamical structure factor $\tilde{g}_f(\omega)$. To overcome this difficulty, I explore the

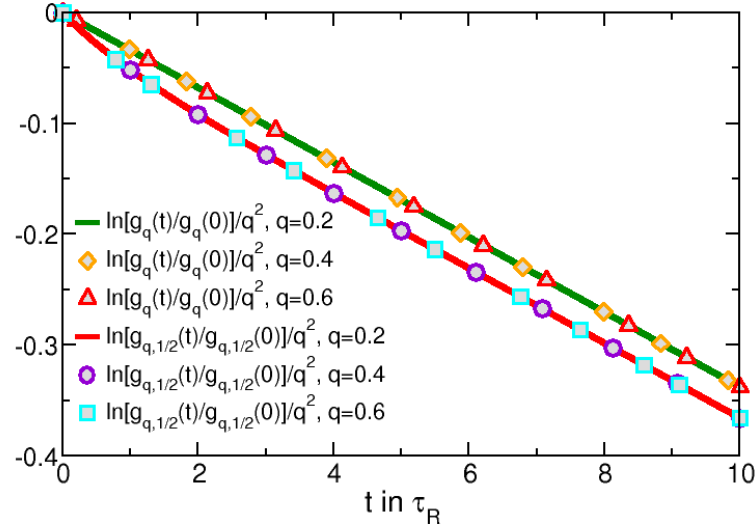


FIGURE 3.2: The decay of $g_{\vec{q},f}(t)$ of an entire Rouse chain is compared with that of a fraction of a chain $g_{\vec{q},f}(t)$ for three wavevectors, $|\vec{q}|R_e = 0.2, 0.4$, and 0.6 . For $|\vec{q}|R_e \ll 1$, the time dependence of the dynamic, single-chain structure can be described by a master curve. The figure is reprinted with permission from [39]. Copyright 2021 American Chemical Society.

asymptotic behavior of $h_{1/2}(t)$ and find for $t \ll \tau_R$

$$(\vec{q}R_e)^2 h_{1/2}(t) \approx (\vec{q}R_e)^2 t / (3\pi^2 \tau_R) = \vec{q}^2 D t \quad (3.84)$$

and for large t

$$h_{1/2}(\infty) = \frac{2}{3\pi^4 \frac{1}{4}} \cdot \frac{\pi^4}{96} = \frac{1}{36}. \quad (3.85)$$

I approximate $h_{1/2}(t)$ by a much simpler function $h_{1/2}^{\text{eff}}(t) = t / (3\pi^2 \tau_R + 36t)$. This approximation is illustrated in Figure 3.3. With this, the Laplace transformed dynamical structure factor in the limit of $(\vec{q}R_e)^2 \ll 1$ can be computed

$$\begin{aligned} \tilde{g}_{\vec{q},f}(\omega) \approx & \frac{f^2 \left\{ 1 - \frac{f(\vec{q}R_e)^2}{18} - (\vec{q}R_e)^2 h_f(\infty) \right\}}{\vec{q}^2 D + i\omega} \\ & + \frac{2(\vec{q}R_e)^2}{3\pi^4} \sum_{p=1} \frac{\left(\frac{\sin(\pi p f)}{p^2} \right)^2}{\vec{q}^2 D + \frac{p^2}{\tau_R} + i\omega}. \end{aligned} \quad (3.86)$$

One should keep in mind that the calculation in this section and the impact of the auxiliary

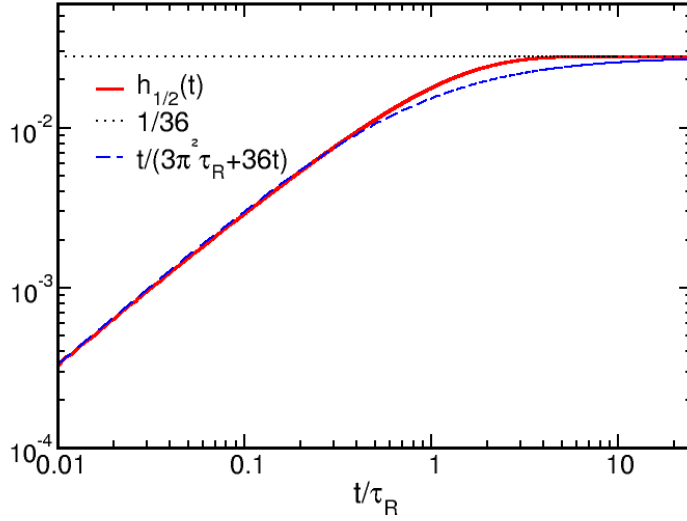


FIGURE 3.3: The correction factor $h_{1/2}(t)$ for the dynamical structure factor for a block of a symmetric copolymer is shown. The figure is reprinted with permission from [39]. Copyright 2021 American Chemical Society.

function $h_f(t)$ is not restricted to any regime. In fact, the calculation suggests a correction term to $g_{\vec{q},f}(t)$ of a block of a chain at all length scales. In the classical diffusive regime *i.e.* $t \gg \tau_R$, this correction factor becomes time independent and shifts $g_{\vec{q},f}(t)$ only by a constant factor, while for $t \ll \tau_R$, the correction factor speeds up the decay. This extensive understanding of the dynamics of chain fractions is important for the application of D-SCFT and D-RPA on diblock copolymers.

3.6 Generalized model-B

In the previous sections, I worked out some essential formulas for the dynamical single-chain structure factor. The single-chain structure factor can be applied within the framework of D-RPA to describe the time evolution of collective quantities such as the density field. Another approach towards dynamical behavior of polymer systems was provided by D-SCFT which predicts a pure diffusive motion (see [section 3.1](#)). As mentioned before, modifications of D-SCFT have been developed to also include non-diffusive motion at, for instance, short time scales. In this section, I test a generalization of the model-B dynamics by introducing a

time-dependent Onsager coefficient $\Lambda_{\vec{q}}(t)$. The generalized model-B dynamics, originally proposed by Semenov in [58], read

$$\frac{\partial \phi_{\vec{q},A}(t)}{\partial t} = -\vec{q}^2 \int_{-\infty}^t d\tau \Lambda_{\vec{q}}(t-\tau) \frac{\mu_{\vec{q}}[\phi_{\vec{q},A}(\tau)]}{k_B T} \quad (3.87)$$

$$(3.88)$$

or in the Laplace transformed form

$$i\omega \tilde{\phi}_{\vec{q},A}(\omega) - \phi_{\vec{q},A}^{(-)} = -\vec{q}^2 \tilde{\Lambda}_{\vec{q}}(\omega) \frac{\tilde{\mu}_{\vec{q}}(\omega)}{k_B T} \quad (3.89)$$

with $\phi_{\vec{q},A}^{(-)} \equiv \phi_{\vec{q},A}(t=0)$ the initial configuration at reference time $t=0$. The chemical potential can be derived from the functional derivative of the free energy according to

$$\mu_{\vec{q}}[\phi_{\vec{q},A}] = \frac{N}{\rho_0 V} \frac{\partial \mathcal{F}[\phi_{\vec{q},A}]}{\partial \phi_{-\vec{q},A}}. \quad (3.90)$$

In order to derive an expression for the frequency-dependent Onsager coefficient $\tilde{\Lambda}_{\vec{q}}(\omega)$, Equation 3.89 is matched with the D-RPA results. Within the framework of D-RPA, I have solved the time evolution of the density field in two scenarios, namely in response to a time periodic external field and during spinodal decomposition after a quench. In the following, $\tilde{\Lambda}_{\vec{q}}(\omega)$ is derived by comparing generalized model-B with D-RPA within the linear regime for both cases.

3.6.1 Response of density fields to an external field at $\chi = 0$

In this case, the chemical potential is given by

$$\frac{\tilde{\mu}_{\vec{q}}}{k_B T} = \frac{\tilde{\phi}_{\vec{q},A}}{S_{\vec{q}}^{\text{coll}}} + \tilde{H}_{\vec{q}}. \quad (3.91)$$

Inserting the chemical potential expression into Equation 3.89, the generalized model-B equation of motion is obtained

$$\begin{aligned} i\omega\tilde{\phi}_{\vec{q},A} &= -\vec{q}^2\tilde{\Lambda}_{\vec{q}}\left(\frac{\tilde{\phi}_{\vec{q},A}}{S_{\vec{q}}^{\text{coll}}} + \tilde{H}_{\vec{q}}\right) \\ \tilde{\phi}_{\vec{q},A} &= -\frac{S_{\vec{q}}^{\text{coll}}\tilde{H}_{\vec{q}}}{1 + \frac{i\omega S_{\vec{q}}^{\text{coll}}}{\vec{q}^2\tilde{\Lambda}_{\vec{q}}}}. \end{aligned} \quad (3.92)$$

Recall the D-RPA prediction for density field evolution in response to an external potential in Equation 3.37

$$\tilde{\phi}_{\vec{q},A} = -\frac{\tilde{H}_{\vec{q}}}{\frac{1}{\tilde{S}_{\vec{q}}} - 2\chi} = -\tilde{S}_{\vec{q}}^{\text{coll}}\tilde{H}_{\vec{q}} \quad \text{with} \quad \frac{1}{\tilde{S}_{\vec{q}}^{\text{coll}}} = \frac{1}{\tilde{S}_{\vec{q}}} - 2\chi. \quad (3.93)$$

Comparing Equation 3.93 with Equation 3.92 leads to

$$\vec{q}^2\tilde{\Lambda}_{\vec{q}}\tau_R = -\frac{i\omega\tau_R}{\frac{1}{S_{\vec{q}}^{\text{coll}}} + \frac{\tilde{H}_{\vec{q}}}{\tilde{\phi}_{\vec{q},A}}} = -\frac{i\omega\tau_R}{\frac{1}{S_{\vec{q}}^{\text{coll}}} - \frac{1}{\tilde{S}_{\vec{q}}^{\text{coll}}}} = -\frac{i\omega\tau_R}{\frac{1}{\tilde{S}_{\vec{q}}} - \frac{1}{\tilde{S}_{\vec{q}}}} \quad (3.94)$$

$$= -\frac{i\omega\tau_R}{\frac{S_{\vec{q},AA} + 2S_{\vec{q},BA} + S_{\vec{q},BB}}{S_{\vec{q},AA}S_{\vec{q},BB} - (S_{\vec{q},AB})^2} - \frac{\tilde{\chi}_{\vec{q},AA} + 2\tilde{\chi}_{\vec{q},AB} + \tilde{\chi}_{\vec{q},BB}}{\tilde{\chi}_{\vec{q},AA}\tilde{\chi}_{\vec{q},BB} - (\tilde{\chi}_{\vec{q},AB})^2}}. \quad (3.95)$$

Thus, an expression for $\tilde{\Lambda}_{\vec{q}}(\omega)$ is obtained

$$\frac{i\omega}{\vec{q}^2\tilde{\Lambda}_{\vec{q}}} = \frac{\tilde{\chi}_{\vec{q},AA} + 2\tilde{\chi}_{\vec{q},AB} + \tilde{\chi}_{\vec{q},BB}}{\tilde{\chi}_{\vec{q},AA}\tilde{\chi}_{\vec{q},BB} - (\tilde{\chi}_{\vec{q},AB})^2} - \frac{S_{\vec{q},AA} + 2S_{\vec{q},BA} + S_{\vec{q},BB}}{S_{\vec{q},AA}S_{\vec{q},BB} - (S_{\vec{q},AB})^2}. \quad (3.96)$$

3.6.2 Spinodal decomposition

I perform the same type of calculation in the case of spinodal decomposition. An accurate expression of the free-energy functional and the chemical potential after a quench is [23]

$$\begin{aligned} \frac{\mathcal{F}^{(\text{RPA})}[\phi_A]}{k_B T} &= \frac{\rho_0 V}{2} \sum_{\vec{q}} \phi_{-\vec{q},A} \left[\frac{1}{S_{\vec{q}}} - 2\chi \right] \phi_{\vec{q},A} \\ \text{and } \frac{\mu_{\vec{q}}^{(\text{RPA})}}{k_B T} &= \left[\frac{N}{S_{\vec{q}}} - 2\chi N \right] \phi_{\vec{q},A} \\ \text{with } S_{\vec{q}} &\equiv \frac{S_{\vec{q},AA} S_{\vec{q},BB} - (S_{\vec{q},AB})^2}{S_{\vec{q},AA} + 2S_{\vec{q},BA} + S_{\vec{q},BB}}. \end{aligned} \quad (3.97)$$

Inserting this chemical potential into Equation 3.89 gives

$$\begin{aligned} i\omega \tilde{\phi}_{\vec{q},A}(\omega) - \phi_{\vec{q},A}^{(-)} &= -\vec{q}^2 \tilde{\Lambda}_{\vec{q}}(\omega) \frac{\tilde{\mu}_{\vec{q}}(\omega)}{k_B T} \\ &= -\vec{q}^2 \tilde{\Lambda}_{\vec{q}}(\omega) \left(N/S_{\vec{q}} - 2\chi N \right) \tilde{\phi}_{\vec{q},A}(\omega). \end{aligned} \quad (3.98)$$

Rearranging the terms in the above equation leads to

$$\begin{aligned} \left(i\omega + \vec{q}^2 \tilde{\Lambda}_{\vec{q}}(\omega) \frac{N}{S_{\vec{q}}} \right) \tilde{\phi}_{\vec{q},A}(\omega) - \phi_{\vec{q},A}^{(-)} &= 2\chi N \vec{q}^2 \tilde{\Lambda}_{\vec{q}}(\omega) \tilde{\phi}_{\vec{q},A}(\omega) \\ \left(1 - \frac{2\chi N \tilde{\Lambda}_{\vec{q}}(\omega) \vec{q}^2}{i\omega + \vec{q}^2 \tilde{\Lambda}_{\vec{q}}(\omega) N/S_{\vec{q}}} \right) \tilde{\phi}_{\vec{q},A}(\omega) &= \frac{1}{i\omega + \vec{q}^2 \tilde{\Lambda}_{\vec{q}}(\omega) N/S_{\vec{q}}} \phi_{\vec{q},A}^{(-)}. \end{aligned} \quad (3.99)$$

Recall Equation 3.45

$$\left(\frac{\tilde{\chi}_{\vec{q},AA} + 2\tilde{\chi}_{\vec{q},AB} + \tilde{\chi}_{\vec{q},BB}}{\tilde{\chi}_{\vec{q},AA} \tilde{\chi}_{\vec{q},BB} - (\tilde{\chi}_{\vec{q},AB})^2} - 2\chi \right) \tilde{\phi}_{\vec{q},A}(\omega) = \frac{\phi_{\vec{q},A}^{(-)}}{\tilde{S}'_{\vec{q}}(\omega)}. \quad (3.100)$$

Comparing the Equation 3.45 with Equation 3.99, I identify the generalized time-dependent Onsager coefficient also for this scenario

$$\frac{i\omega}{\vec{q}^2 \tilde{\Lambda}_{\vec{q}}(\omega)} = N \frac{\tilde{\chi}_{\vec{q},AA} + 2\tilde{\chi}_{\vec{q},AB} + \tilde{\chi}_{\vec{q},BB}}{\tilde{\chi}_{\vec{q},AA} \tilde{\chi}_{\vec{q},BB} - (\tilde{\chi}_{\vec{q},AB})^2} - N \frac{S_{\vec{q},AA} + 2S_{\vec{q},BA} + S_{\vec{q},BB}}{S_{\vec{q},AA} S_{\vec{q},BB} - (S_{\vec{q},AB})^2}. \quad (3.101)$$

With the above-mentioned definition for $\tilde{\Lambda}_{\vec{q}}(\omega)$ in Equation 3.96, model-B type dynamics that match the result of D-RPA in the linear-response regime is received. Moreover, this model is not restricted to the linear-response theory, but can be applied for any given chemical potential of arbitrary order. In the following, I will take a closer look at the formalism of generalized model-B dynamics for two simple examples: homopolymer blend and diblock copolymer melt. I will also investigate the limiting behavior of generalized model-B and examine its crossover to the original D-SCFT.

3.6.3 Symmetric binary homopolymer blends

I first calculate the time-dependent Onsager coefficient for symmetric binary homopolymer blends. For homopolymers, the single-chain cross-correlations $\tilde{\chi}_{\vec{q},AB}(\omega)$ and $S_{\vec{q},AB}$, between monomers of different types vanish. The Onsager coefficient can be simplified to

$$\tilde{\Lambda}_{\vec{q}}(\omega) = \bar{\phi}_A \bar{\phi}_B D g_{\vec{q}}(0) \frac{3\pi^2}{(\vec{q}R)^2} \left[\frac{g_{\vec{q}}(0)\tau_R}{\tilde{g}_{\vec{q}}(\omega)} - i\omega\tau_R \right]. \quad (3.102)$$

The first four factors are the original Onsager coefficient in D-SCFT [46]

$$\Lambda_{\vec{q}}^{\text{D-SCFT}} = \bar{\phi}_A \bar{\phi}_B D g_{\vec{q}}(0). \quad (3.103)$$

I define for the following

$$\tilde{\Delta}_{\vec{q}}(\omega) \equiv \frac{3\pi^2}{(\vec{q}R)^2} \left[\frac{g_{\vec{q}}(0)\tau_R}{\tilde{g}_{\vec{q}}(\omega)} - i\omega\tau_R \right]. \quad (3.104)$$

3.6.3.1 Ultimate short-time regime

Recalling Equation 3.69 in the limit referred to as the ultimate short-time scale for small length scales $qR_e \gg 1$ and small time scales $\omega\tau_R \gg 1$ gives

$$\tilde{\Delta}_{\vec{q}}(\omega) = \frac{(\vec{q}R)^2}{12 \tilde{\phi}(\Omega)} - i \frac{3\pi^2 \omega \tau_R}{(\vec{q}R)^2} \approx \frac{1}{g_{\vec{q}}(0)} \frac{1 - i\Omega \tilde{\phi}(\Omega)}{\tilde{\phi}(\Omega)}. \quad (3.105)$$

Using the large- Ω approximation $\tilde{\varphi}(\Omega) \approx \frac{1}{1+i\Omega}$ results in a frequency-independent $\tilde{\Delta}_{\vec{q}} \approx \frac{1}{g_{\vec{q}}(0)}$ and

$$\Lambda_{\vec{q}}(t) = \underbrace{\bar{\varphi}_A \bar{\varphi}_B D}_{\Lambda_{\vec{q}}^{\text{local}}} \delta(t) \quad \text{for } \frac{t}{\tau_R} \rightarrow 0 \text{ and } (\vec{q}R_e)^2 \gg 1. \quad (3.106)$$

This recovers the “local” Onsager coefficient [46] in the ultimate short-time limit.

3.6.3.2 Intermediate regime

Within the intermediate sub-diffusive regime, *i.e.* $\frac{36\pi^2}{(\vec{q}R_e)^2} \ll \frac{t}{\tau_R} \ll 1$, the approximation of [Equation 3.76](#)

$$\tilde{\varphi}(\Omega) \approx \frac{1}{i\Omega + 1 - \frac{\Omega_0(\tilde{\varphi}(0)-1)}{\tilde{\varphi}(0)(i\Omega + \Omega_0)}} \quad (3.107)$$

can be applied. In this case, the approximation leads to

$$\tilde{\Delta}_{\vec{q}}(\omega) \approx \frac{1}{g_{\vec{q}}(0)} \left[1 - \frac{\Omega_0(\tilde{\varphi}(0) - 1)}{\tilde{\varphi}(0)[i\omega + \Omega_0]} \right] \quad (3.108)$$

$$= \frac{1}{g_{\vec{q}}(0)} \left[1 - \frac{\tilde{\varphi}(0) - 1}{\tilde{\varphi}(0) \frac{36\pi^2\tau_R}{(\vec{q}R_e)^4\Omega_0}} \frac{1}{i\omega + \frac{(\vec{q}R_e)^4\Omega_0}{36\pi^2\tau_R}} \right]. \quad (3.109)$$

This gives a time-dependent Onsager coefficient

$$\Lambda_{\vec{q}}(t) = \bar{\varphi}_A \bar{\varphi}_B D \left[\delta(t) - \frac{\tilde{\varphi}(0) - 1}{\tilde{\varphi}(0) \frac{36\pi^2\tau_R}{(\vec{q}R_e)^4\Omega_0}} \exp\left(-\frac{(\vec{q}R_e)^4\Omega_0 t}{36\pi^2\tau_R}\right) \right]. \quad (3.110)$$

Applying the Markovian approximation leads to

$$\Lambda_{\vec{q}}(t) \approx \bar{\varphi}_A \bar{\varphi}_B D \left[\delta(t) - \frac{\tilde{\varphi}(0) - 1}{\tilde{\varphi}(0)} \delta(t) \right] \quad (3.111)$$

$$= \frac{\bar{\varphi}_A \bar{\varphi}_B D}{\tilde{\varphi}(0)} \delta(t) \approx 0.288 \bar{\varphi}_A \bar{\varphi}_B D \delta(t). \quad (3.112)$$

3.6.3.3 Classical regime

For large length scales $(\vec{q}R_e)^2 \ll 1$ and all time scales, the diffusive approximation in [Equation 3.80](#) can be used

$$\begin{aligned}\tilde{g}_{\vec{q}}(\omega) &= \frac{g_{\vec{q}}\tau_R}{i\omega\tau_R + \frac{(\vec{q}R_e)^2}{3\pi^2}} \\ \frac{g_{\vec{q}}(0)\tau_R}{\tilde{g}_{\vec{q}}(\omega)} &= i\omega\tau_R + \frac{(\vec{q}R_e)^2}{3\pi^2}.\end{aligned}\quad (3.113)$$

This gives

$$\tilde{\Delta}(\omega) \approx 1 \quad \text{and} \quad \tilde{\Lambda}_{\vec{q}}(\omega) = \Lambda_{\vec{q}}^{\text{D-SCFT}}. \quad (3.114)$$

In this regime, the time-dependent Onsager coefficient from the generalized model-B dynamics recovers the constant Onsager coefficient [\[46\]](#) from the original D-SCFT

$$\Lambda_{\vec{q}}(t) \approx \bar{\phi}_A \bar{\phi}_B D g_{\vec{q}}(0) \delta(t) = \Lambda_{\vec{q}}^{\text{D-SCFT}} \delta(t) \quad \text{for } (\vec{q}R_e)^2 \ll 1. \quad (3.115)$$

3.6.4 Symmetric diblock copolymers

For symmetric diblock copolymer melts, the Onsager coefficient in [Equation 3.101](#) can be simplified to

$$\begin{aligned}\tilde{\Lambda}_{\vec{q}}(\omega) &= D \left(g_{\vec{q},1/2}(0) - \frac{1}{4}g_{\vec{q}}(0) \right) \times \\ &\quad \frac{3\pi^2}{(\vec{q}R)^2} \left[\frac{\left(g_{\vec{q},1/2}(0) - \frac{1}{4}g_{\vec{q}}(0) \right) \tau_R}{\tilde{g}_{\vec{q},1/2}(\omega) - \frac{1}{4}\tilde{g}_{\vec{q}}(\omega)} - i\omega\tau_R \right].\end{aligned}\quad (3.116)$$

3.6.4.1 Ultimate short-time regime

On short length and time scales, $(\vec{q}R_e)^2 \gg 1$ and $t \ll \tau_R$, I use the approximation

$$\begin{aligned} g_{\vec{q}} &= \frac{2}{x^2} (e^{-x} - 1 + x) \\ &\approx \frac{2}{x^2} x = \frac{2}{x} = \frac{12}{(\vec{q}R_e)^2}. \end{aligned} \quad (3.117)$$

The Debye-function of a chain fraction $f = 1/2$ can be approximated by

$$\begin{aligned} g_{\vec{q},1/2}(0) &= \frac{1}{4} g_{\vec{q}/\sqrt{2}}(0) \approx \frac{6}{(\vec{q}R_e)^2} \\ g_{\vec{q},1/2}(0) &- \frac{1}{4} g_{\vec{q}}(0) \approx \frac{3}{(\vec{q}R_e)^2}. \end{aligned} \quad (3.118)$$

In Laplace representation, the normalized dynamical structure factor takes the form

$$\begin{aligned} \tilde{g}_{\vec{q},1/2}(\omega) - \frac{1}{4} \tilde{g}_{\vec{q}}(\omega) &\approx \left(g_{\vec{q},1/2}(0) - \frac{1}{4} g_{\vec{q}}(0) \right) \frac{36\pi^2 \tau_R}{(\vec{q}R)^4} \tilde{\varphi}(\Omega) \\ &\approx \frac{108\pi^2 \tau_R}{(\vec{q}R)^6} \tilde{\varphi}(\Omega). \end{aligned} \quad (3.119)$$

with $\Omega = \frac{36\pi^2 \tau_R}{(\vec{q}R)^4} \omega$. Inserting this expression into [Equation 3.116](#), the Onsager coefficient for generalized model-B dynamics of symmetric diblock copolymers is obtained

$$\tilde{\Lambda}_{\vec{q}}(\omega) \approx D \left(g_{\vec{q},1/2}(0) - \frac{1}{4} g_{\vec{q}}(0) \right) \frac{(\vec{q}R_e)^2}{12} \left[\frac{1}{\tilde{\varphi}(\Omega)} - i\Omega \right] \quad (3.120)$$

$$\approx \frac{D}{4} \left[\frac{1}{\tilde{\varphi}(\Omega)} - i\Omega \right]. \quad (3.121)$$

I use again the large- Ω approximation $\tilde{\varphi}(\Omega) \approx \frac{1}{1+i\Omega}$ for the ultimate short-time scale. For the limit $\frac{t}{\tau_R} \rightarrow 0$ and $(\vec{q}R_e)^2 \gg 1$, the dynamical Onsager Coefficient takes the form

$$\begin{aligned} \tilde{\Lambda}_{\vec{q}}(\omega) &\approx D \left(g_{\vec{q},1/2}(0) - \frac{1}{4} g_{\vec{q}}(0) \right) \frac{(\vec{q}R_e)^2}{12} \\ \Lambda_{\vec{q}}(t) &\approx D \left(g_{\vec{q},1/2}(0) - \frac{1}{4} g_{\vec{q}}(0) \right) \frac{(\vec{q}R_e)^2}{12} \delta(t) \approx \frac{D}{4} \delta(t). \end{aligned} \quad (3.122)$$

Here, the “local” Onsager Coefficient $\Lambda_{\vec{q}}(t) \approx \Lambda_{\vec{q}}^{\text{local}} \delta(t)$ is recovered.

3.6.4.2 Intermediate regime

The numerical approximation of $\varphi(\Omega)$ in Equation 3.76 is used again for the sub-diffusive region

$$\tilde{\varphi}(\Omega) \approx \frac{1}{i\Omega + 1 - \frac{\Omega_0(\tilde{\varphi}(0)-1)}{\tilde{\varphi}(0)(i\Omega+\Omega_0)}}. \quad (3.123)$$

I obtain for this limit

$$\begin{aligned} \Lambda_{\vec{q}}(t) &\approx D \left(g_{\vec{q},1/2}(0) - \frac{1}{4} \tilde{g}_{\vec{q}}(0) \right) \times \\ &\quad \frac{(\vec{q}R_e)^2}{12} \left[\delta(t) - \frac{\tilde{\varphi}(0) - 1}{\tilde{\varphi}(0) \frac{36\pi^2\tau_R}{(\vec{q}R_e)^4\Omega_0}} \exp \left(-\frac{(\vec{q}R_e)^4\Omega_0 t}{36\pi^2\tau_R} \right) \right] \\ &\approx \frac{D}{4} \left[\delta(t) - \frac{\tilde{\varphi}(0) - 1}{\tilde{\varphi}(0) \frac{36\pi^2\tau_R}{(\vec{q}R_e)^4\Omega_0}} \exp \left(-\frac{(\vec{q}R_e)^4\Omega_0 t}{36\pi^2\tau_R} \right) \right]. \end{aligned} \quad (3.124)$$

For $\frac{36\pi^2}{(\vec{q}R_e)^2} \ll \frac{t}{\tau_R} \ll 1$, the Markovian approximation leads to

$$\Lambda_{\vec{q}}(t) = \frac{D}{4\tilde{\varphi}(0)} \delta(t) \approx 0.072 D \delta(t). \quad (3.125)$$

This result is identical to the Onsager coefficients of homopolymers computed in the previous section. This is because this limit is within the scale-free Gaussian coil on very short time scales $t \ll \tau_R$. In this case, the Onsager coefficient depends only on \vec{q} and is given by

$$\Lambda_{\vec{q}}(t) = \Lambda_{\vec{q}}^{\text{local}} \delta(t) / \tilde{\varphi}(0) = \frac{\Lambda_{\vec{q}}^{\text{D-SCFT}}}{g_{\vec{q}}(0) \tilde{\varphi}(0)} \delta(t). \quad (3.126)$$

3.6.4.3 Classical regime

For $(qR_e)^2 \ll 1$, the Debye-function $g_{\vec{q}}(0)$ can be approximated by

$$\begin{aligned} g_{\vec{q}}(0) &= \frac{2}{x^2} (e^{-x} - 1 + x) \quad \text{with} \quad x = \frac{(\vec{q}R_e)^2}{6} \\ &= \frac{2}{x^2} \left(1 - x + \frac{x^2}{2} - \frac{x^3}{6} + \mathcal{O}((\vec{q}R_e)^4) - 1 + x \right) \\ &= 1 - \frac{x}{3} \end{aligned} \tag{3.127}$$

$$= 1 - \frac{(\vec{q}R_e)^2}{18} + \mathcal{O}((\vec{q}R_e)^4). \tag{3.128}$$

And for a chain fraction of $f = 1/2$, the relation reads

$$g_{\vec{q},1/2}(0) = \frac{1}{4}g_{\vec{q}/\sqrt{2}}(0) = 1 - \frac{(\vec{q}R_e)^2}{144} + \mathcal{O}((\vec{q}R_e)^4) \tag{3.129}$$

$$g_{\vec{q},1/2}(0) - \frac{1}{4}g_{\vec{q}}(0) = \frac{(\vec{q}R_e)^2}{144} + \mathcal{O}((\vec{q}R_e)^4). \tag{3.130}$$

I consider the correction factor $h_{1/2}(t)$ as discussed before and compute with [Equation 3.86](#) for small qR_e

$$\tilde{g}_{\vec{q},1/2}(\omega) - \frac{1}{4}\tilde{g}_{\vec{q}}(\omega) \approx \frac{2(\vec{q}R_e)^2}{3\pi^4} \sum_{p \text{ odd}} \frac{1}{p^4(\vec{q}^2 D + \frac{p^2}{\tau_R} + i\omega)}. \tag{3.131}$$

Inserting this into [Equation 3.116](#), the frequency-dependent Onsager coefficient for symmetric diblock copolymers is obtained

$$\tilde{\Lambda}_{\vec{q}}(\omega) \approx \frac{\pi^6 D}{4608} \left[\frac{1}{\sum_{p \text{ odd}} \frac{1}{p^4(\vec{q}^2 D + \frac{p^2}{\tau_R} + i\omega)}} - i\omega\tau_R \right]. \tag{3.132}$$

This Onsager coefficient does not diverge for $(\vec{q}R)^2 \rightarrow 0$ implying the relaxation is dominated by internal modes. For the limit $(\vec{q}R_e)^2 \rightarrow 0$ and $\omega\tau_R \rightarrow 0$, it is $\tilde{\Lambda}_{\vec{q}}(\omega) \rightarrow 5D/24$ or $\Lambda_{\vec{q}}(t) \rightarrow 5D\delta(t)/24$.

Chapter 4

Collective short-time dynamics: Simulation results

Some content of this chapter 4 has been published in *Macromolecules* with the title “Collective Short-Time Dynamics in Multicomponent Polymer Melts” [39]. Some parts of this chapter are results of close collaboration with Marcus Müller.

Three analytical models, D-SCFT, D-RPA and generalized model-B, were introduced in the last chapter. Among the three approaches, D-SCFT suggests very different dynamics at small time scales compared to D-RPA. Their predicted time evolution of the density field differ in evolution speed as well as in \vec{q} dependence. Meanwhile, generalized model-B was derived by matching the D-RPA result in the linear regime. In order to validate the three models, I test their predicted time evolution of the density field against the results from the particle-based simulation of a soft, coarse-grained model. In this chapter, the following scenarios are discussed:

- Density fluctuation decay in symmetric homopolymer blends [section 4.1](#)
- Density fluctuation decay in dynamic asymmetric homopolymer blends [section 4.2](#)
- Spinodal decomposition in symmetric homopolymer blends: Single density mode [section 4.3](#)
- Spinodal decomposition in symmetric homopolymer blends: Collective structure factor [section 4.4](#)

- Density fluctuation decay in symmetric diblock copolymer melts [section 4.5](#)
- Response to external field in symmetric diblock copolymer melts [section 4.6](#)

All simulation configurations in this study have an invariant degree of polymerization of $\sqrt{N} = 128$. Periodic boundary condition is applied for all systems. The Rouse time τ_R is used as a reference to translate MC-steps into physical time scales.

4.1 Decay of density fluctuations in symmetric binary homopolymer blends

I consider a binary homopolymer blend in a small cubic simulation box with geometry $1 \times 1 \times 1 R_e^3$. A large chain discretization of $N = 256$ is used to achieve a large relaxation time ($\tau_R \propto N^2$), which allows a finer resolution of the dynamics. The number of A -type homopolymers is set equal to B -type homopolymers, *i.e.* the normalized density is $\bar{\phi}_A = \frac{1}{2}$ and $\bar{\phi}_B = \frac{1}{2}$. In a symmetric binary system, the dynamics of A and B particles are identical. The spatial discretization is set to $\Delta L = 1/64 R_e$. The incompressibility parameter is $\kappa N = 100$ to suppress density fluctuations and the Flory-Huggins parameter is $\chi N = 0$. For $t < 0$, the A segments in the system are exposed to an external field

$$\frac{H(\vec{r})}{2} = \lambda \cos\left(\frac{2\pi}{L}ix\right) \quad \text{with } i = 1, 4 \quad (4.1)$$

and the B segments are exposed to the opposite field $-\frac{H(\vec{r})}{2}$.

The initial spatially modulated morphology $\phi_{\vec{q},A}^{(-)}$ and $\phi_{\vec{q},B}^{(-)}$ is enforced by the given external fields. According to static RPA (see [section 3.2](#)), the equilibrium density field at $\chi N = 0$ can be expressed as

$$\langle \phi_{\vec{q},A} \rangle_{\text{RPA}} = -S_{\vec{q}}^{(0)} H_{\vec{q}} \quad (4.2)$$

$$\langle \phi_A(x) \rangle_{\text{RPA}} - \langle \phi_B(x) \rangle_{\text{RPA}} = -\lambda N g_{\vec{q}} \cos\left(\frac{2\pi}{L}ix\right). \quad (4.3)$$

At $t = 0$, the external field responsible for the initial density variation is switched off. As a consequence of this, the amplitude of density fluctuations starts to decay towards a homogeneous state. I define the density fluctuation amplitude as

$$a(t) \equiv \frac{\langle \phi_A(x, t) \rangle - \langle \phi_B(x, t) \rangle}{\cos\left(\frac{2\pi}{L}nx\right)}. \quad (4.4)$$

and monitor the temporal decay of $a(t)/a(0)$ with $a(0) = -\lambda N g_{\vec{q}}$.

For symmetric homopolymer blends, the cross-correlation vanishes and the dynamical structure factor of A -type homopolymers is equal to that of B -type homopolymers, *i.e.*

$$S_{\vec{q},AB}(t) = 0 \quad \text{and} \quad S_{\vec{q},AA}(t) = S_{\vec{q},BB}(t). \quad (4.5)$$

For $\chi = 0$, this symmetry simplifies the D-RPA equation in [Equation 3.45](#) to

$$\begin{aligned} 2\tilde{\chi}_{\vec{q},AA}\tilde{\phi}_{\vec{q},A}(\omega) &= \frac{-i\omega 2\tilde{S}_{\vec{q},AA}^2 S_{\vec{q},AA} + 2\tilde{S}_{\vec{q},AA} S_{\vec{q},AA}^2}{S_{\vec{q},AA}^2} \phi_{\vec{q},A}^{(-)} \\ &= \left(-i\omega \frac{\tilde{S}_{\vec{q},AA}^2}{S_{\vec{q},AA}\tilde{\chi}_{\vec{q},AA}} + \frac{\tilde{S}_{\vec{q},AA}}{\tilde{\chi}_{\vec{q},AA}} \right) \phi_{\vec{q},A}^{(-)}. \end{aligned} \quad (4.6)$$

One should remember that \tilde{S} indicates the explicit (ω) dependence and $S_{\vec{q},\alpha\beta}$ without further specification denotes the static quantities *i.e.* $S_{\vec{q},\alpha\beta}$ is equivalent to $S_{\vec{q},\alpha\beta}(t = 0)$. From the previous chapter, the following relations are known for homopolymers

$$\frac{\tilde{S}_{\vec{q},AA}}{S_{\vec{q},AA}} = \frac{\tilde{g}_{\vec{q}}(\omega)}{g_{\vec{q}}}, \quad (4.7)$$

$$\tilde{\chi}_{\vec{q},AA} = \left(-i\omega \frac{\tilde{g}_{\vec{q}}(\omega)}{g_{\vec{q}}} + 1 \right) S_{\vec{q},AA}. \quad (4.8)$$

Inserting this into [Equation 4.6](#), I obtain within **D-RPA**

$$\boxed{\phi_{\vec{q},A}(t) = \frac{g_{\vec{q}}(t)}{g_{\vec{q}}} \phi_{\vec{q},A}^{(-)}} \quad (4.9)$$

$$\boxed{\frac{a(t)}{a(0)} = \frac{g_{\vec{q}}(t)}{g_{\vec{q}}}}. \quad (4.10)$$

For this system, **D-SCFT** predicts an exponential density fluctuation decay

$$\frac{a(t)}{a(0)} = \exp(-\bar{q}^2 Dt) = \exp\left(-\frac{(\bar{q}R_e)^2}{3\pi^2} \frac{t}{\tau_R}\right). \quad (4.11)$$

The D-SCFT and D-RPA predictions are tested against simulation results for $qR_e = 2\pi$ and $qR_e = 8\pi$ in [Figure 4.1](#) and [Figure 4.2](#). In both cases, the density evolution differs from an exponential decay. Thus, D-SCFT fails to predict the basic kinetics of fluctuation relaxation. Furthermore, the pure sub-diffusive decay with a square-root approximation as suggested in [Equation 3.74](#) fails to describe the data as well. On the other hand, the D-RPA prediction matches the simulation data very well without using adjustable parameters.

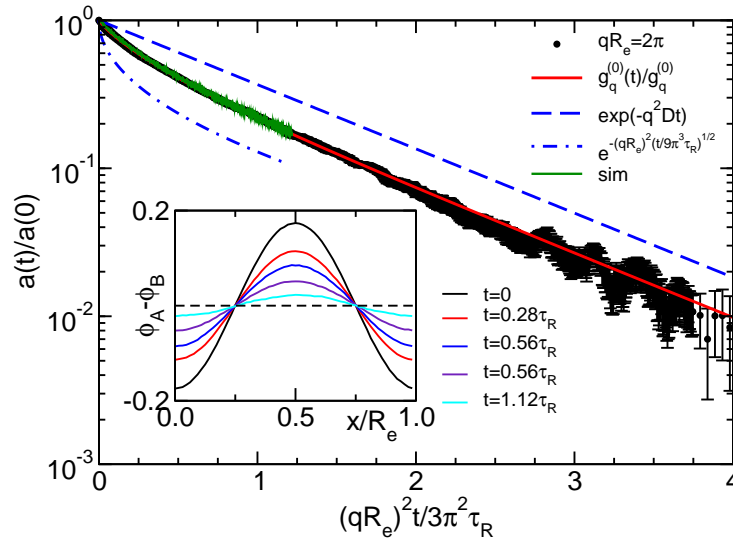


FIGURE 4.1: The density fluctuation relaxation of a symmetric homopolymer blend at $\chi N = 0$ is shown for $qR_e = 2\pi$. The amplitude of density modulation $a(t)$ as a function of time is calculated analytically from the numerical expression of $g_{\bar{q}}(t)$ and compared with the measurement from SOMA (black dots). The asymptotic behaviors in short (dashed-dotted blue line) and long time limit (dashed blue line) are also shown. The inset shows the corresponding density profile measured in the simulation for various t . The strength of the external field is set to $\lambda N = 0.7$. The figure is reprinted with permission from [39]. Copyright 2021 American Chemical Society.

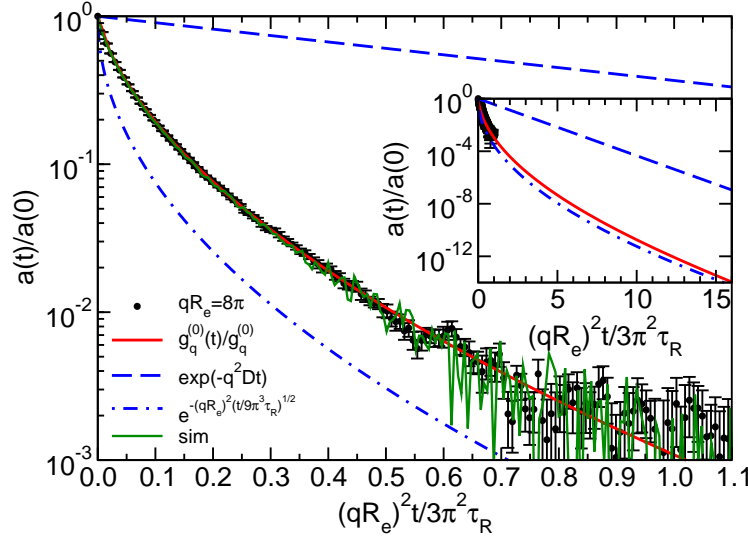


FIGURE 4.2: The same study as in Figure 4.1 for $qR_e = 8\pi$ with $\lambda N = 10$. The inset of this figure shows the decay of the amplitude for longer times. The figure is reprinted with permission from [39]. Copyright 2021 American Chemical Society.

4.2 Decay of density fluctuations in asymmetric homopolymer blends

In addition to the study on the dynamics of symmetric homopolymers, I now consider the density fluctuation decay in more sophisticated dynamically asymmetric homopolymer blends. This means that the diffusion coefficient of A -type and B -type homopolymers, denoted by D_A and D_B , are different. In an asymmetric binary mixture, the structure factors $S_{\vec{q},AA}(t)$ and $S_{\vec{q},BB}(t)$ are no longer equal for $t > 0$. For $\chi = 0$ and $S_{\vec{q},AB}(t) = 0$, Equation 3.45 can be simplified to

$$\frac{\tilde{\chi}_{\vec{q},AA} + \tilde{\chi}_{\vec{q},BB}}{\tilde{\chi}_{\vec{q},AA}\tilde{\chi}_{\vec{q},BB}} \tilde{\phi}_{\vec{q},A}(\omega) = \left\{ -\frac{i\omega \tilde{S}_{\vec{q},AA} \tilde{S}_{\vec{q},BB} [S_{\vec{q},AA} + S_{\vec{q},BB}]}{\tilde{\chi}_{\vec{q},AA}\tilde{\chi}_{\vec{q},BB} S_{\vec{q},AA} S_{\vec{q},BB}} + \frac{\tilde{S}_{\vec{q},AA} S_{\vec{q},BB}^2 + \tilde{S}_{\vec{q},BB} S_{\vec{q},AA}^2}{\tilde{\chi}_{\vec{q},AA}\tilde{\chi}_{\vec{q},BB} S_{\vec{q},AA} S_{\vec{q},BB}} \right\} \phi_{\vec{q},A}^{(-)}. \quad (4.12)$$

Since the two polymer types have identical chain architecture and differ only in their chain mobility, the equality of their static structure factor is still valid, *i.e.* $S_{\vec{q},AA} = S_{\vec{q},BB}$. I define

$$\tilde{\varphi}_{\vec{q},\alpha}(\omega) = \frac{\tilde{S}_{\vec{q},\alpha\alpha}}{S_{\vec{q},\alpha\alpha}} \quad (4.13)$$

and obtain

$$\tilde{\phi}_{\vec{q},A}(\omega) = \frac{\frac{1}{2} [\tilde{\varphi}_{\vec{q},A}(\omega) + \tilde{\varphi}_{\vec{q},B}(\omega)] - i\omega \tilde{\varphi}_{\vec{q},A}(\omega) \tilde{\varphi}_{\vec{q},B}(\omega)}{1 - i\omega \frac{1}{2} [\tilde{\varphi}_{\vec{q},A}(\omega) + \tilde{\varphi}_{\vec{q},B}(\omega)]} \phi_{\vec{q},A}^{(-)}. \quad (4.14)$$

An accurate decay rate can be obtained by solving Equation 4.14. First, I approximate the dynamical structure factor by an exponential decay *i.e.* $\varphi_{\vec{q},\alpha}(t) \approx \exp(-D_\alpha \vec{q}^2 t)$ for simplicity. Inserting

$$\tilde{\varphi}_{\vec{q},\alpha}(\omega) = \frac{1}{D_\alpha \vec{q}^2 + i\omega}$$

into Equation 4.14, an exponential decay of the density field with an effective diffusion coefficient \bar{D} is obtained

$$\begin{aligned} \tilde{\phi}_{\vec{q},A}(\omega) &\approx \frac{1}{\bar{D} \vec{q}^2 + i\omega} \phi_{\vec{q},A}^{(-)} \\ \phi_{\vec{q},A}(t) &\approx \exp(-\bar{D} \vec{q}^2 t) \phi_{\vec{q},A}^{(-)} \\ \text{with } \bar{D} &= 2 \frac{D_A D_B}{D_A + D_B}. \end{aligned} \quad (4.15)$$

As discussed before, this exponential Ansatz is only valid in the classical regime, namely for $qR_e \ll 1$. For this reason, I have to test whether the idea of an effective diffusion coefficient \bar{D} can be generalized to other length scales in the simulation. The simulation setup is, except for the diffusion coefficient, the same as in section 4.1 with $N = 256$, $L = 1R_e$ and $\Delta L = 1/64R_e$. The strengths of the non-bonded energy are set to $\kappa N = 100$ and $\chi N = 0$. For $t < 0$, the segments in the system are exposed to an external field that enforces the starting morphology. The diffusion coefficients are set so that $D_A/D_B \approx 8.5$.

As one can see in Equation 4.15, increasing the diffusion coefficient by a factor is equivalent to reducing t by the same factor. Scaling down t leads to a rescaled time for A polymers $t' = \frac{\bar{D}}{D_A} t \approx t/4.75$. The rescaled dynamical single-chain structure factor is

compared with the simulation results of an asymmetric homopolymer blend for $qR_e = 2\pi$ in Figure 4.3. The dynamics derived from D-RPA with a rescaled t dependence match the simulation data very well. This result suggests that the dynamics of an asymmetric homopolymer blend can be captured by an effective diffusion constant. With this, the underlying dynamics of asymmetric binary homopolymers can be computed analogously to that of symmetric binary homopolymers within the framework of D-RPA or D-SCFT.

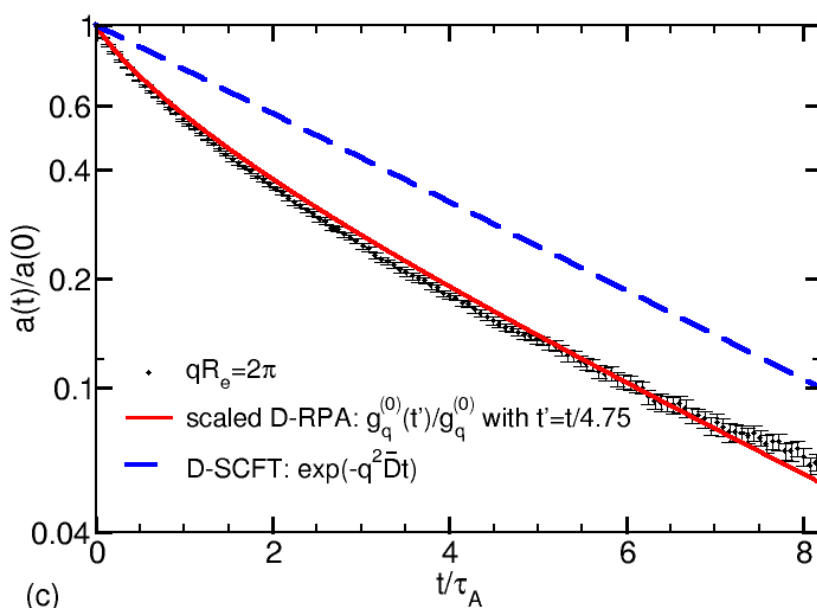


FIGURE 4.3: The density fluctuation relaxation of an asymmetric homopolymer blend is shown for $qR_e = 2\pi$. The simulation data (black points) are compared with the analytical predictions calculated assuming an effective diffusion constant \bar{D} . The time evolution is measured in units of relaxation time τ_A of A -type homopolymers. The figure is reprinted with permission from [39].

Copyright 2021 American Chemical Society.

4.3 Spinodal decomposition in binary homopolymer blends: single density mode

In this section, I study the spinodal decomposition in a symmetric binary homopolymer blend. I will only consider the structure evolution of two modes $qR_e = 2\pi$ and $qR_e = 8\pi$. The phase separation is triggered by a sudden change of the incompatibility χN from 0 to a

finite value. The **D-SCFT** prediction for the temporal growth of density fluctuations after the quench is

$$\boxed{\begin{aligned} \phi_{\vec{q},A}(t) &= \phi_{\vec{q},A}^{(-)} e^{r_{\vec{q}}^{\text{D-SCFT}} \frac{t}{\tau_R}} \\ \text{with } r_{\vec{q}}^{\text{D-SCFT}} &= -\frac{(\vec{q}R_e)^2}{3\pi^2} \left(1 - 2\bar{\phi}_A\bar{\phi}_B\chi N g_{\vec{q}}(0)\right). \end{aligned}} \quad (4.16)$$

D-SCFT predicts an exponential growth of density inhomogeneity for sufficiently large χ .

I continue to calculate the dynamics in the early stage of the spinodal decomposition with D-RPA. For homopolymers, the structure factor is given by

$$S_{\vec{q},\alpha\alpha}(t) = \bar{\phi}_\alpha N g_{\vec{q}}(t) \quad , \quad \tilde{S}_{\vec{q},\alpha\alpha}(\omega) = \bar{\phi}_\alpha N \tilde{g}_{\vec{q}}(\omega) \quad (4.17)$$

$$\tilde{\chi}_{\vec{q},\alpha\alpha} = \bar{\phi}_\alpha N \left[g_{\vec{q}}(0) - i\omega \tilde{g}_{\vec{q}}(\omega) \right]. \quad (4.18)$$

This simplifies [Equation 3.45](#) to

$$\tilde{\phi}_{\vec{q},A}(\omega) = \frac{\tilde{g}_{\vec{q}}(\omega)}{g_{\vec{q}}(0) \left(1 - 2\bar{\phi}_A\bar{\phi}_B\chi_{\text{FH}} N \left[g_{\vec{q}}(0) - i\omega \tilde{g}_{\vec{q}}(\omega) \right] \right)} \phi_{\vec{q},A}^{(-)}. \quad (4.19)$$

For a binary homopolymer blend at $\chi N = 0$, the result in [section 4.1](#) is recovered

$$\phi_{\vec{q},A}(t) = \frac{g_{\vec{q}}(t)}{g_{\vec{q}}(0)} \phi_{\vec{q},A}^{(-)}. \quad (4.20)$$

For $\chi N > 0$, [Equation 4.19](#) can be solved using approximations for $g_{\vec{q}}(t)$.

I restrict the study to short length and time scales and apply the scaling behavior

$$g_{\vec{q}}(t) = g_{\vec{q}}(0) \varphi \left(\frac{(\vec{q}R_e)^4 t}{36\pi^2 \tau_R} \right) \quad (4.21)$$

to rewrite [Equation 4.19](#) and obtain the **D-RPA** prediction

$$\boxed{\begin{aligned} \tilde{\phi}_{\vec{q},A}(\omega) &= \frac{\frac{36\pi^2 \tau_R}{(\vec{q}R_e)^4} \tilde{\varphi}(\Omega)}{1 - 2\bar{\phi}_A\bar{\phi}_B\chi_{\text{FH}} N g_{\vec{q}}(0) [1 - i\Omega \tilde{\varphi}(\Omega)]} \phi_{\vec{q},A}^{(-)} \\ \text{with } \Omega &= \frac{36\pi^2 \omega \tau_R}{(\vec{q}R_e)^4}. \end{aligned}} \quad (4.22)$$

The time dependence of the density field is then obtained by a numerical, inverse Laplace transformation of [Equation 4.22](#).

In the ultimate short time limit, the approximation $\tilde{\phi}(\Omega) \approx 1/(1 + i\Omega)$ is valid. In this case, the density field obeys

$$\tilde{\phi}_{\vec{q},A}(\omega) = \frac{\phi_{\vec{q},A}^{(-)}}{i\omega + \frac{(\vec{q}R_e)^4}{36\pi^2\tau_R} \left(1 - 2\bar{\phi}_A\bar{\phi}_B\chi_{FH}Ng_{\vec{q}}\right)} \quad (4.23)$$

$$\phi_{\vec{q},A}(t) = \phi_{\vec{q},A}^{(-)} \exp \left[-\frac{(\vec{q}R_e)^4}{36\pi^2} \left(1 - 2\bar{\phi}_A\bar{\phi}_B\chi_{FH}Ng_{\vec{q}}\right) \frac{t}{\tau_R} \right]. \quad (4.24)$$

In this case, the growth rate of the structure is by a factor

$$\frac{(\vec{q}R_e)^2}{12} = 1/g_{\vec{q}}$$

faster than the D-SCFT result.

In the intermediate short time regime, the approximation in [Equation 3.76](#) can be applied which leads to

$$\tilde{\phi}_{\vec{q},A}(\omega) = \frac{1}{i\omega + \frac{(\vec{q}R_e)^4}{36\pi^2\tau_R} \left[1 - 2\bar{\phi}_A\bar{\phi}_B\chi_{FH}Ng_{\vec{q}}(0)\right] \left[1 - \frac{\Omega_0(\tilde{\phi}(0)-1)}{\tilde{\phi}(0)[i\Omega+\Omega_0]}\right]} \phi_{\vec{q},A}^{(-)}. \quad (4.25)$$

In the limit $\Omega \ll \Omega_0$, [Equation 4.25](#) can be further approximated by

$$\tilde{\phi}_{\vec{q},A}(\omega) = \frac{1}{i\omega + \frac{(\vec{q}R_e)^4}{36\pi^2\tau_R} \left[1 - 2\bar{\phi}_A\bar{\phi}_B\chi_{FH}Ng_{\vec{q}}(0)\right] \left[\frac{1}{\tilde{\phi}(0)}\right]} \phi_{\vec{q},A}^{(-)}. \quad (4.26)$$

This gives rise to an exponential growth of the density field within the framework of **D-RPA**

$$\phi_{\vec{q},A}(t) = \phi_{\vec{q},A}^{(-)} \exp \left[-\frac{(\vec{q}R_e)^4}{36\pi^2\tilde{\phi}(0)} \left(1 - 2\bar{\phi}_A\bar{\phi}_B\chi_{FH}Ng_{\vec{q}}(0)\right) \frac{t}{\tau_R} \right]. \quad (4.27)$$

The density growth in D-RPA is faster than the D-SCFT result by a factor of

$$\frac{(\vec{q}R_e)^2}{[12\tilde{\phi}(0)]} = \frac{1}{[g_{\vec{q}}(0)\tilde{\phi}(0)]}.$$

I test the analytical prediction of D-SCFT (Equation 4.16) and D-RPA (Equation 4.22) against SOMA simulation results. The simulation setup with $N = 256$ and a cubic simulation box with geometry $1 \times 1 \times 1R_e^3$ is used. The spatial discretization is $\Delta L = 1/64R_e$. Two simulations focusing on the time evolution of the density field at $qR_e = 2\pi$ and $qR_e = 8\pi$ are performed. For $qR_e = 2\pi$, the system is quenched to $\chi N = 32$ and, for $qR_e = 8\pi$, χN is increased to 160 (κN is also increased in this case). The time evolution of density amplitude at $qR_e = 2\pi$ and $qR_e = 8\pi$ predicted by different models are compared with simulation results in Figure 4.4.

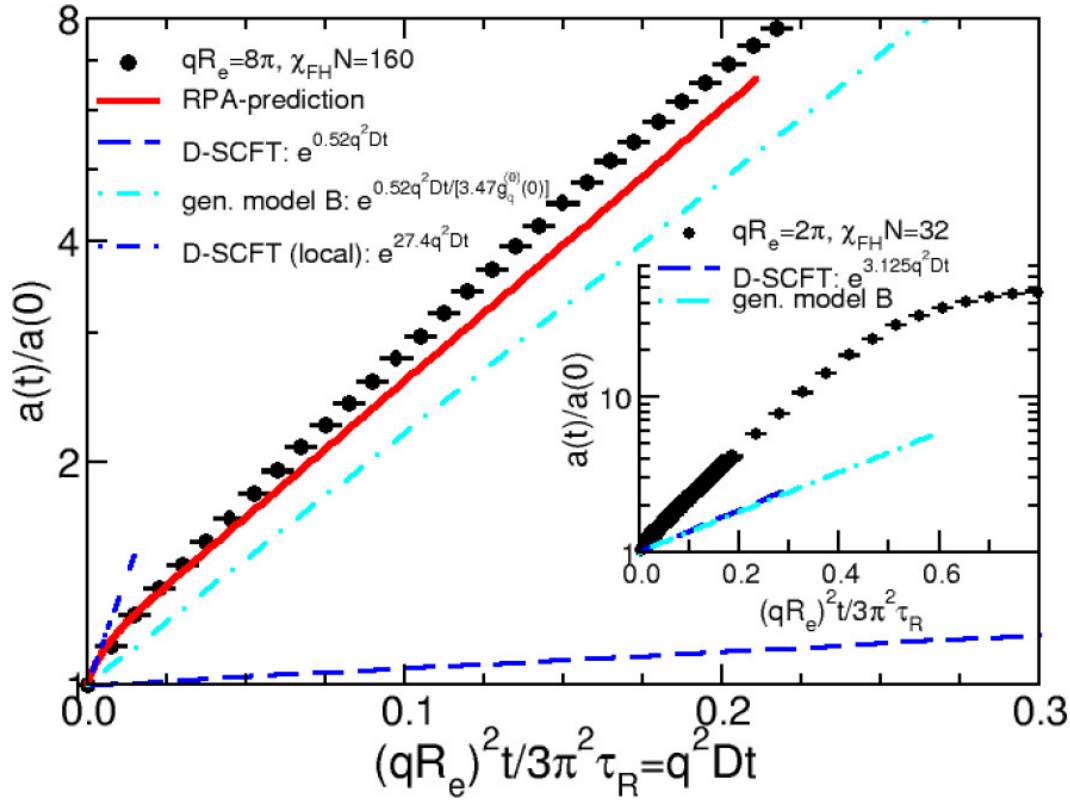


FIGURE 4.4: The density variation growth after increasing χN to 160 and 32 (inset) are shown for $qR_e = 8\pi$ and $qR_e = 2\pi$ (inset). The simulation results for $qR_e = 8\pi$ (black dots) are compared with the exponential growth predicted by D-SCFT (Equation 4.16), the prediction of the generalized model-B (Equation 4.27), D-RPA (the numerical, inverse Laplace transformation of Equation 4.22) and the D-SCFT result with the “local” Onsager coefficient. The figure is reprinted with permission from [39]. Copyright 2021 American Chemical Society.

I restrict the study to small density fluctuations because the linear response theory, which is the assumption in D-RPA, is only valid in this regime. D-SCFT underestimates the growth rate in both cases, and its deviation is much larger on small length scales ($qR_e = 8\pi$) than on intermediate length scales ($qR_e = 2\pi$). On short time scales, D-SCFT using a “local”

Onsager coefficient (as given in Equation 4.26) successfully captures the fast increase of the density variation at $qR_e = 8\pi$. In this case, the temporal decay for $t < 0.01/(q^2D)$ can be well described by a sub-diffusive motion, which is captured by the intermediate short time approximation. For $qR_e = 2\pi$, the sub-diffusive approximation is only modified by a factor of $1/[q_{\vec{q}}^{(0)}\tilde{\varphi}(0)] \approx 0.9$ compared to the original D-SCFT resulting in a similar growth rate in both models. Their predictions deviate considerably from the observation in the simulation indicating that the $qR_e \ll 1$ condition for a scale-free behavior is not fulfilled on this length scale. D-RPA again provides a good match with simulation results without any tunable parameters. However, the D-RPA results were only obtained with a numerical inverse Laplace transformation and a closed analytical expression for the time dependence of the dynamics could not be obtained. The generalized model-B dynamics using a modified Onsager coefficient also provides a qualitative appropriate prediction.

4.4 Growth rate during spinodal decomposition in binary homopolymer blends: Collective structure factor

In this section, I continue the study on spinodal decomposition in homopolymer blends and study the growth rate over the whole wavevector spectrum. Unlike in the previous section, the time resolution of the dynamics of each single mode qR_e is less important and I will focus on the general qR_e dependence of the growth rate. The analytical predictions of different models have already been derived in the previous section.

I perform simulations with SOMA on *A*-type and *B*-type homopolymer mixture with $N = 256$ in a simulation box with geometry $3 \times 3 \times 3R_e^3$. The grid discretization is $\Delta L = 1/64$ and the incompressibility parameter is set to $\kappa N = 100$. At time $t = 0$, the disordered system is quenched from $\chi N = 0$ to $\chi N = 70$. Since this study is restricted to the linear response regime, the density variations must remain small. This is demonstrated by the snapshot in Figure 4.5 showing the density variation of the latest snapshot at $t = 0.0263\tau_R$, which is far below the saturation value of the two coexisting phases $\phi_A \approx 0$ or 1 .

Figure 4.6 shows the growth of the collective structure factor $S_{\vec{q}}(t)$, obtained as the Fourier

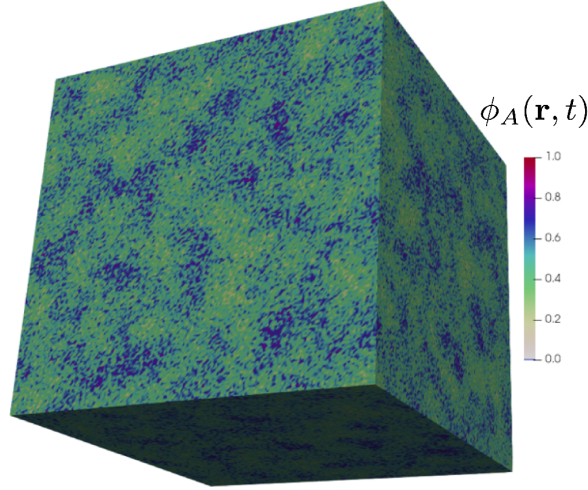


FIGURE 4.5: Snapshot of one configuration at $t = 0.0263\tau_R$ after a quench to $\chi N = 70$. The normalized density fluctuation remains around 0.2 for most of the regions. The figure is reprinted with permission from [39]. Copyright 2021 American Chemical Society.

transformation of the density field, after a deep quench from $\chi N = 0$ to 70. In Figure 4.7, the corresponding growth rate of $S_{\vec{q}}(t)$ is presented. In the simulation, the \vec{q} -dependent growth rate is measured according to

$$2r_{\vec{q}} = \frac{\ln [S_{\vec{q}}(t) / S_{\vec{q}}(0)]}{t / \tau_R}. \quad (4.28)$$

The density variation growth is fast at first and slows down over time. In Figure 4.7, a maximum of growth rate around $qR_e \approx 6\pi$ is measured at very early stage. The peak of the growth rate shifts to lower qR_e with time which is in agreement with prior experiments [70–74] and simulation [46, 75, 76].

The collective structure factor before the quench at $t = 0$ in the disordered state can be obtained with static RPA

$$\frac{S_{\vec{q}}(t)}{N} \equiv \sqrt{\mathcal{N}} \frac{V}{R_e^3} \left\langle |\phi_{\vec{q},A}(t)|^2 \right\rangle = \frac{1}{\frac{N}{S_{\vec{q}}^{(0)}} - 2\chi N} \stackrel{\chi=0; \bar{\phi}_A=\frac{1}{2}}{=} \frac{g_{\vec{q}}(0)}{4}. \quad (4.29)$$

This is plotted as the green dashed line in Figure 4.6. The RPA calculation for the disordered initial state matches the simulation data very well. Starting from the disordered state, the time dependence of the dynamical structure factor according to D-SCFT (see Equation 4.16) is

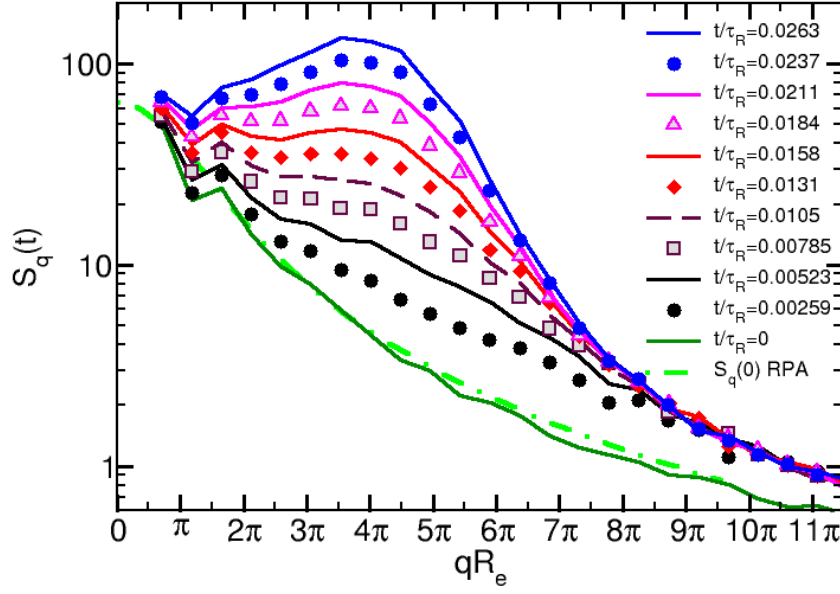


FIGURE 4.6: The collective structure factor $S_{\vec{q}}(t)$ after a quench from the disordered phase to $\chi N = 70$ is shown for multiple timesteps. The data is obtained by averaging over 4 – 8 independent simulation runs. The figure is reprinted with permission from [39]. Copyright 2021 American Chemical Society.

given by

$$S_{\vec{q}}(t) = S_{\vec{q}}(0) e^{2r_{\vec{q}}^{\text{D-SCFT}} \frac{t}{\tau_R}}. \quad (4.30)$$

In the theory, the growth rate can be calculated with Equation 4.16

$$r_{\vec{q}}^{\text{D-SCFT}} = -\frac{(\vec{q}R_e)^2}{3\pi^2} \left(1 - 2\bar{\phi}_A\bar{\phi}_B\chi N g_{\vec{q}}(0) \right).$$

For $1 - 2\bar{\phi}_A\bar{\phi}_B\chi N g_{\vec{q}}(0) < 0$, the growth rate is positive suggesting an exponential growth of density variations. For $1 - 2\bar{\phi}_A\bar{\phi}_B\chi N g_{\vec{q}}(0) > 0$, the theory predicts a negative growth rate *i.e.* the density variation decreases. For the given parameters, this transition occurs at $qR_e \approx 20.5$. I do not expect to observe this effect in this simulation because of the presence of thermal fluctuations. To avoid the influence of such an effect, I only analyze the result for $qR_e < 20.5$. D-SCFT predicts a constant growth rate independent of time (shown as the blue dashed line in Figure 4.7). However, the simulation data in Figure 4.7 suggests a clearly time-dependent growth rate. On top of that, the growth rate measured in the simulation is

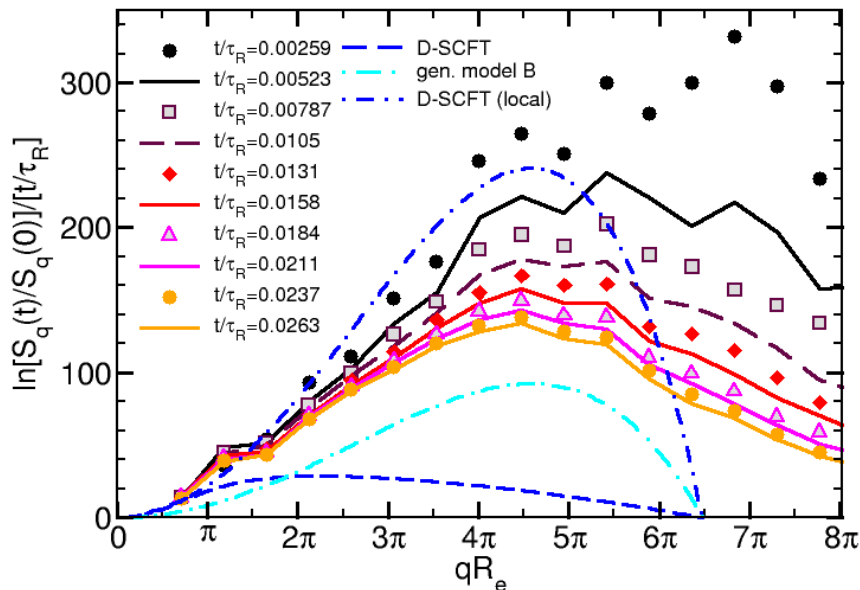


FIGURE 4.7: The measured growth rate of $S_{\vec{q}}(t)$ as a function of qR_e is shown for different times after the quench. The simulation data is compared with predictions of D-SCFT, generalized model-B and D-SCFT with the “local” Onsager coefficient. The figure is reprinted with permission from [39]. Copyright 2021 American Chemical Society.

significantly larger than the D-SCFT prediction for all qR_e . The reason for a smaller growth rate in D-SCFT is the assumption of diffusive dynamics in Rouse-like dynamics. As discussed before, the sub-diffusive motion of segments on length scales much shorter than the extent of the macromolecule is important for large qR_e and leads to faster structure growth than the D-SCFT prediction. In Figure 4.7, the D-SCFT prediction for very short time scales $t/\tau_R \approx 0$ with the “local” Onsager Coefficient is plotted as well.

4.5 Decay of density fluctuations in symmetric diblock copolymer melts

I proceed to study on structure evolution with symmetric diblock copolymer melts. First, I explore the time dependence of the decay of enforced density fluctuations. In this simulation, I set $N = 256$, $\tilde{N} = 51\,200$ and keep $\chi N = 0$. The system geometry is set to $6 \times 1 \times 1R_e^3$

and periodic boundary conditions are applied. For $t < 0$, the system is exposed to an external field that generates initial configurations with a density variation on the length scale of $qR_e = \frac{2\pi}{L}n$ with $L = 6R_e$ and $n = 1, 2$. The external field is switched off at $t = 0$ after the system is equilibrated. The temporal decay of the amplitude $a(t)$ at target qR_e is recorded.

D-SCFT predicts an exponential decay:

$$\boxed{a(t) = a(0) \exp(-D\vec{q}^2 t)}. \quad (4.31)$$

I also apply D-RPA to describe this decay process. For $f_A = 1/2$, earlier results for the dynamical structure factor of a block of a chain gives

$$\begin{aligned} S_{\vec{q},AA}(t) &= S_{\vec{q},BB}(t) = Ng_{\vec{q},1/2}(t) \\ S_{\vec{q},AB}(t) &= \frac{N}{2} [g_{\vec{q}}(t) - g_{\vec{q},f}(t) - g_{\vec{q},1-f}(t)] \\ \tilde{\chi}_{\vec{q},AA} &= \tilde{\chi}_{\vec{q},BB} = N [g_{\vec{q},1/2}(0) - i\omega \tilde{g}_{\vec{q},1/2}(\omega)] \\ 2\tilde{\chi}_{\vec{q},AB} &= N [g_{\vec{q}}(0) - 2g_{\vec{q},1/2}(0) - i\omega \tilde{g}_{\vec{q}}(\omega) + 2i\omega \tilde{g}_{\vec{q},1/2}(\omega)]. \end{aligned} \quad (4.32)$$

Inserting the above equalities into the D-RPA formalism in [Equation 3.45](#) leads to

$$\tilde{\phi}_{\vec{q},A}(\omega) = \frac{\tilde{S}_{\vec{q},AA}(\omega) - \tilde{S}_{\vec{q},AB}(\omega)}{\left(S_{\vec{q},AA}(0) - S_{\vec{q},AB}(0)\right) \left(1 - \chi_{\text{FH}}[\tilde{\chi}_{\vec{q},AA}(\omega) - \tilde{\chi}_{\vec{q},AB}(\omega)]\right)} \phi_{\vec{q},A}^{(-)}, \quad (4.33)$$

which can be simplified to

$$\phi_{\vec{q},A}(t) = \left[g_{\vec{q},1/2}(t) - \frac{g_{\vec{q}}(t)}{4} \right] / \left[g_{\vec{q},1/2}(0) - \frac{g_{\vec{q}}(0)}{4} \right] \phi_{\vec{q},A}^{(-)}. \quad (4.34)$$

For large length scales $qR_e \ll 1$, the temporal dependency of the dynamical structure factor of a block of a chain can be approximated by

$$\begin{aligned} g_{\vec{q},f}(t) &= f^2 \left[1 - \frac{f(\vec{q}R_e)^2}{18} - (\vec{q}R_e)^2 h_f(t) + \mathcal{O}((\vec{q}R_e)^4) \right] e^{-\vec{q}^2 Dt} \\ &\approx g_{\vec{q},f}(0) e^{-\vec{q}^2 Dt - (\vec{q}R_e)^2 h_f(t)}. \end{aligned} \quad (4.35)$$

Inserting Equation 4.35 into Equation 4.34, the **D-RPA** prediction for the density fluctuation decay is obtained

$$\phi_{\vec{q},A}(t) \approx \left[1 - \frac{h_{1/2}(t)}{h_{1/2}(\infty)} \right] e^{-\vec{q}^2 D t} \phi_{\vec{q},A}^{(-)} + \mathcal{O}\left((\vec{q} R_e)^2\right), \quad (4.36)$$

with the long time plateau value $h_{1/2}(\infty) = \frac{1}{36}$.

I continue to study the same problem with generalized model-B dynamics. In the limit $qR_e \rightarrow 0$ and $\omega\tau_R \rightarrow 0$, Equation 3.132 suggests for symmetric diblock copolymers an Onsager coefficient of the form

$$\Lambda_q = \frac{5D}{24} \delta(t). \quad (4.37)$$

Implementing the above expression into the equation of motion of **generalized model-B** leads to an exponential decay

$$a(t) = a(0) \exp\left(-\frac{10t}{\pi^2 \tau_R}\right). \quad (4.38)$$

The simulation results are compared with analytical predictions provided by D-SCFT, D-RPA and modified D-SCFT for $qR_e = \frac{2\pi}{3}$ and $qR_e = \frac{2\pi}{6}$ in Figure 4.8.

The original D-SCFT fails to provide a qualitative prediction for the time evolution of the density fluctuation decay. D-RPA and generalized model-B, on the other hand, predict a temporal decay that matches the simulation data very well.

4.6 Response to external fields in symmetric diblock copolymer melts

I continue the study on symmetric diblock copolymers and investigate how the density field responds to external fields. The geometry of the simulation system is set to $1.32 \times 1 \times 1 R_e^3$. The system length in x -direction $L_x = 1.32 R_e$ corresponds to the maximum of the collective structure factor $qR_e = 4.76 \approx 2\pi R_e / L_x$ at $\chi N = 0$. Periodic boundary conditions are

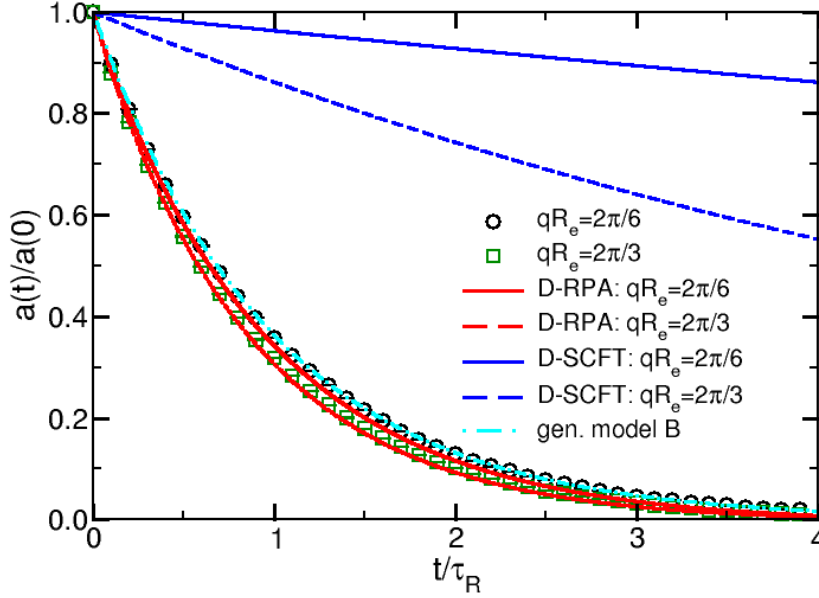


FIGURE 4.8: The decay of density fluctuations at $qR_e = 2\pi/6$ and $2\pi/3$ are shown for a symmetric diblock copolymer melt. The simulation results (circles, squares) are compared with the results of D-RPA, D-SCFT as well as the generalized model-B for the limit $qR_e \rightarrow 0$ and $\omega\tau_R \rightarrow 0$. The figure is reprinted with permission from [39]. Copyright 2021 American Chemical Society.

applied in all directions. For $t < 0$, the diblock copolymer melt is in a disordered state. For $t > 0$, I switched on an external field $H(x)$ for A -type monomers and $-H(x)$ for B -type monomers with

$$\frac{H(x)}{2} = \begin{cases} +\lambda & \text{for } 0 \leq x < L_x/2 \\ -\lambda & \text{for } L_x/2 \leq x < L_x \end{cases}. \quad (4.39)$$

In this study, the strength of the external field is set to $\lambda N = 2$. The Fourier representation of the external field reads

$$H_{\vec{q}} = \pm \frac{4\lambda i}{\pi n} \quad (4.40)$$

for $\vec{q} = (\pm 2\pi n/L)\vec{e}_x$ and $n = \pm 1, \pm 3, \pm 5, \dots$. The time dependency of the composition $\langle \phi_A(x, t) \rangle - \langle \phi_B(x, t) \rangle$ is recorded with the average computed over multiple simulation runs.

Within D-RPA, the temporal evolution of the structure formation is described by [Equation 3.45](#). For symmetric diblock copolymers ($f_A = 1/2$), it can be simplified to

$$\begin{aligned}\tilde{\phi}_{\vec{q},A}(\omega) &= -\frac{\tilde{\chi}_{\vec{q},AA}\tilde{\chi}_{\vec{q},BB} - \tilde{\chi}_{\vec{q},AB}^2}{\tilde{\chi}_{\vec{q},AA} + 2\tilde{\chi}_{\vec{q},AB} + \tilde{\chi}_{\vec{q},BB}}\tilde{H}_{\vec{q}} \\ &= -\frac{\tilde{\chi}_{\vec{q},AA} - \tilde{\chi}_{\vec{q},AB}}{2}\tilde{H}_{\vec{q}}(\omega),\end{aligned}\quad (4.41)$$

with $\tilde{H}_{\vec{q}}(\omega) = H_{\vec{q}}/(i\omega)$. From [Equation 4.32](#) follows the **D-RPA** prediction for the density field response of symmetric diblock copolymers to external fields:

$$\begin{aligned}\tilde{\phi}_{\vec{q},A}(\omega) &= -\left[\frac{g_{\vec{q},1/2}(0)}{i\omega} - \frac{g_{\vec{q}}(0)}{4i\omega} - \tilde{g}_{\vec{q},1/2}(\omega) + \frac{\tilde{g}_{\vec{q}}(\omega)}{4}\right]NH_{\vec{q}} \\ \phi_{\vec{q},A}(t) &= -\left[g_{\vec{q},1/2}(0)\left(1 - \frac{g_{\vec{q},1/2}(t)}{g_{\vec{q},1/2}(0)}\right) - \frac{g_{\vec{q}}(0)}{4}\left(1 - \frac{g_{\vec{q}}(t)}{g_{\vec{q}}(0)}\right)\right]NH_{\vec{q}}.\end{aligned}\quad (4.42)$$

I also calculate the D-SCFT prediction for this case. The time evolution according to **D-SCFT** is

$$\begin{aligned}\phi_{\vec{q},A}(t) &= \phi_{\vec{q},A}(\infty)\left[1 - e^{-\frac{\vec{q}^2\Lambda_{\vec{q}}^{\text{D-SCFT}}}{S_{\vec{q}}}t}\right] \\ &= \phi_{\vec{q},A}(\infty)\left[1 - e^{-\vec{q}^2Dt}\right]\end{aligned}\quad (4.43)$$

with $\phi_{\vec{q},A}(\infty)$ the static RPA prediction of the equilibrium density field given by

$$\phi_{\vec{q},A}(\infty) = -S_{\vec{q}}H_{\vec{q}} = -\left[g_{\vec{q},1/2}(0) - \frac{g_{\vec{q}}(0)}{4}\right]NH_{\vec{q}}.\quad (4.44)$$

The density field profile obtained from the simulation for various times is shown in [Figure 4.9](#). For small t , a novel saddle-shaped profile with two minima and two maxima can be observed. The D-SCFT result is shown as the blue curves in [Figure 4.9](#). It fails to describe the shape of the density profile and predicts a much slower dynamics in general. The D-RPA result is shown in [Figure 4.9](#) as red curves. It agrees with the simulation results very well and successfully captures the characteristic saddle-shape of the density profile.

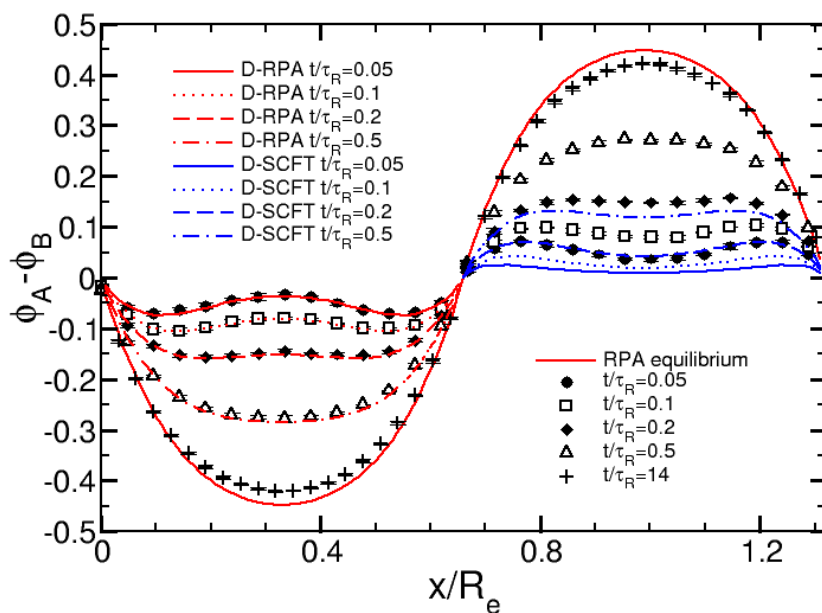


FIGURE 4.9: The density profile growth of a symmetric diblock copolymer melt in an external field is shown for $\chi N = 0$. Symbols represent the simulation results with error bars. The measured data is compared with predictions from D-RPA (Equation 4.42, red curves) and D-SCFT (Equation 4.43, blue curves). The figure is reprinted with permission from [39]. Copyright 2021 American Chemical Society.

4.7 Summary

I investigated the early stage dynamics in multicomponent polymer systems from an unstable initial state to the next (meta)stable state. Two analytical approaches, D-RPA and D-SCFT, were employed to describe the collective kinetics of the structure formation at short length and time scales. D-SCFT makes use of the accurate free-energy functional derived from SCFT and relates the dynamics of the density fields to the exchange chemical potential. D-RPA associates the spatiotemporally dependent density with the external fields via a linear-response function, which can be derived from the dynamic, single-chain structure factors. For diblock copolymers, I introduced a correction term to the dynamic, single-chain structure factor of an entire chain in order to accurately describe the dynamics of a block of the chain. Since D-RPA is only valid in the linear regime, I restricted the scope of this study to early times with small density fluctuations. For binary homopolymer blends, I calculated the structure evolution in the following three scenarios: (i) the decay of the preimposed density fluctuation at $\chi N = 0$,

(ii) the density field growth in response to external fields and (iii) the spinodal decomposition after a deep quench from the disordered state. For symmetric diblock copolymer melts, I studied (i) the decay of preimposed density fluctuations at $\chi N = 0$ and (ii) the density field growth in response to external fields.

Then, I simulated the systems mentioned above using the particle-based simulation program SOMA. The time dependence of the structure formation and relaxation on various length scales was recorded. The measured collective structure factor as a function of time after a quench from the disordered state as well as the time-dependent response of the density field to external fields suggest a fast, sub-diffusive motion in the short-time limit. I compared the simulation data with the analytical predictions. On short time and length scales, D-RPA successfully captures the qR_e dependence and the time dependence of the structure evolution, whereas D-SCFT underestimates the growth rate of the structure formation as a result of not accounting for the fast, sub-diffusive dynamics.

To overcome the shortcomings of D-SCFT, a generalized model-B was developed utilizing a time-dependent Onsager coefficient $\Lambda_{\vec{q}}(t)$. This is achieved by matching the dynamic equations derived in D-RPA and generalized model-B such that generalized model-B reproduces the results of D-RPA in the linear regime. Accurate expressions for $\tilde{\Lambda}_{\vec{q}}(\omega)$ were computed from the structure formation responding to external fields and the self-assembly during the spinodal decomposition. Both processes yield the same expression

$$\frac{i\omega}{\vec{q}^2 \tilde{\Lambda}_{\vec{q}}} = \frac{\tilde{\chi}_{\vec{q},AA} + 2\tilde{\chi}_{\vec{q},AB} + \tilde{\chi}_{\vec{q},BB}}{\tilde{\chi}_{\vec{q},AA}\tilde{\chi}_{\vec{q},BB} - \left(\tilde{\chi}_{\vec{q},AB}\right)^2} - \frac{S_{\vec{q},AA} + 2S_{\vec{q},BA} + S_{\vec{q},BB}}{S_{\vec{q},AA}S_{\vec{q},BB} - \left(S_{\vec{q},AB}\right)^2}.$$

The advantage of generalized model-B over D-RPA is its usage of the accurate exchange chemical potential with validity extended to the nonlinear regime, where D-RPA breaks down.

Part II

Structure formation in copolymer networks

Chapter 5

Structure and structure formation in 2D, regular polymer networks

Some content of this chapter 5 has been published in *Macromolecules* with the title “Phase Separation of Regular, Quasi-Two-Dimensional AB Copolymer Networks” [77]. Some parts of this chapter are results of close collaboration with Marcus Müller.

In the previous part, I focused on the interplay between chain architecture, dynamics and structure formation of linear chains. I will continue the study on structure and structure formation for topologically more complicated polymers networks. Polymer networks are popular subjects of contemporary polymer science [78–81]. Among them, novel class of innovative materials such as interpenetrating polymer networks [82–86] and liquid crystalline polymers [87–91] have drawn much attention because of their promising potential in industrial and biomedical applications [10, 92–95].

Polymer networks are percolating macromolecules obtained by crosslinking linear polymer chains via chemical bonds. They exhibit a large number of unique intrinsic features, such as mechanical elasticity and complex secondary structure (folding). Responsible for these properties is the connectivity of the network brought in by the irreversible crosslinks. This new dimension of varieties of polymer architectures offers a large number of possibilities in the design of polymers with novel properties. Also because of the connectivity, the dynamics and the structure formation of polymer networks are highly non-trivial and must be handled with special attention. How network structure essentially determines physical properties is

important in order to understand the underlying physics of polymer networks and to guide the synthesis of polymer networks with desired properties. Obtaining a detailed understanding and modeling of the structure and structure formation of polymer networks (with or without a fixed topology) has been an active field of research in polymer physics for decades [96–104].

In this part of the thesis, I will concentrate on polymer networks with a fixed topology. To keep the analytical calculations simple and to speed up the simulations in order to reach large-scale networks, the study is performed on 2D networks composed of square shaped repeating units. The repeating units (also called unit cells) are ordered in two perpendicular spatial dimensions x and y , resulting in a quasi two-dimensional network with a planar topology. The exact behaviors of the networks depend on their topology and on their dimensionality. Earlier studies have shown that the physics describing them is qualitatively similar [105].

In this study, the particle-based coarse-grained Monte-Carlo simulation SOMA is applied to carry out the simulation study on the polymer networks made of symmetric diblock copolymers. In SOMA, a multiple number (10 – 700) of quasi 2D molecules are embedded in a 3D simulation box with side length $L_x = L_y = L$ and $L_z = 2R_{db}$. To assure a two dimensional topology and a homogeneous non-bonded energy in the z -direction, only one simulation grid layer is used in the z -direction. The side length L will be varied during the study to enforce different degrees of stretching. The grid discretization in x - and y -direction is set to $\Delta L = 0.1R_{db}$. Periodic boundary conditions are applied on the xy -plane for all sub-projects of this study. The networks extend throughout the whole simulation box and the opposite side are connected via bonds that cross the periodic boundary conditions. In other words, the network is constructed on the surface of a torus. In this way, the molecules are fixed on the length scale given by the geometry of the simulation box. The incompressibility parameter κN_{db} is set to 30 if not stated otherwise. The repulsive interaction between unlike species is controlled by the Flory-Huggins parameter χ and will be varied during the simulation. In addition, I perform the same study with a crudely simplified MC simulation that takes only the junction points into account. The simplified MC simulation is constructed truly two dimensional without extension in the z -direction. A - and B -crosslinks are connected via effective harmonic springs, which are equivalent to the 2D projection of the diblock strands in

SOMA. The statistical segment length of the effective springs is given by

$$B^2 = \frac{2}{3} R_{db}^2.$$

The only interaction in the simplified MC simulation is the bonded interaction given by the harmonic springs. The difference between the simplified MC simulation and SOMA is the monomer discretization and the incompressibility constraint.

I consider square-shaped polymer networks with n_u unit cells arranged in x - and y -directions. The imposed side length of the unit cells is denoted by $l_u = \frac{L}{n_u}$. The networks are generated by end-crosslinking unit cells as illustrated in Figure 5.1 (A). In SOMA simulations, a minimum particle density is required. To fulfill this requirement, several identical networks are overlapped in the z -direction. The number of molecules n_m contained in the system depends on the unit-cell size l_u and is determined so that the total density is constant in all systems. Due to the minimum density requirement, real configurations in the simulation are dense as shown in Figure 5.1 (B).

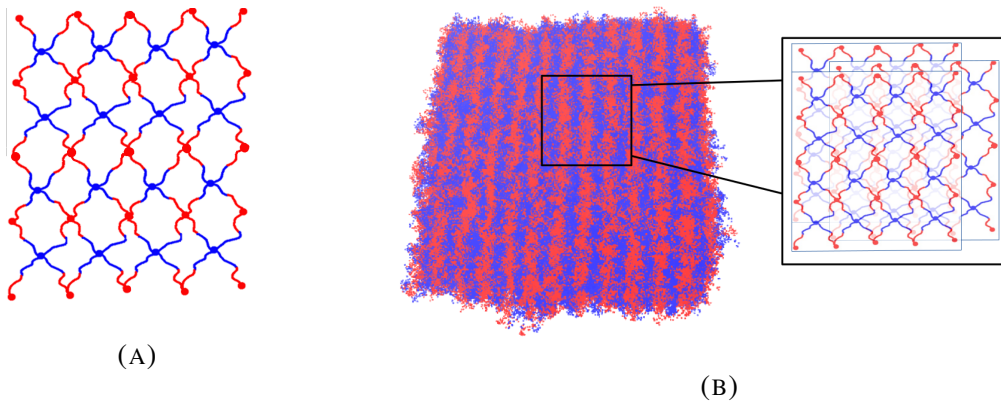


FIGURE 5.1: (A) Illustration of a 2D, regular network with $n_u = 4$ mesh cells in x - and y -direction. A and B segments are colored red and blue. The circles represent the junction points. (B) Snapshot of 16 overlapped 2D copolymer networks from real simulation with mesh size $l_u = 0.5$ and incompatibility $\chi N_{db} = 8$. The enlargement shows three overlapped networks. The figure is reprinted with permission from [77]. Copyright 2022 American Chemical Society.

The main interest of this study is to investigate the structure and structure formation of 2D networks, as well as to describe their phase behavior as a function of l_u and n_u . In this chapter, I will first give a brief summary of the theoretical background of this field in [section 5.1](#). Then in [section 5.2](#), I will provide analytical models that describe the structure of 2D regular networks based on two different approximations. The crosslink distributions derived from the analytical models will be tested against simulations in [section 5.3](#). Then in [subsection 5.4.2](#), the structure factor of 2D networks is studied. At the last, the order-disorder phase transition of 2D polymer networks will be investigated as a function of l_u and n_u in [subsection 5.5.2](#).

5.1 Theoretical background of polymer networks

Crosslinked polymers are macromolecules with extremely complicated molecular architecture if all monomers are considered. Hence, an appropriate model needs to simplify the network conformation in order to reduce the degrees of freedom in the molecular structure. The origin of many universal scaling behaviors of linear polymers is the fractal nature of the polymer chains. This fundamental assumption can be generalized to polymers of arbitrary dimension with fractal connectivity and lead to generalized description on their statistical properties and dynamics [[105](#)] without considering local binary interactions such as the excluded volume. Two of the most important classical models for polymer networks are the affine network model [[106–108](#)] and the phantom network model [[109–111](#)], providing the most simple approaches to describe network's mechanical properties *e.g.* elasticity. More detailed aspects on elasticity models of polymer networks can be found in [[98](#), [112](#), [113](#)].

The *affine model* applies a single-chain approximation where the free energy is simply a linear sum over the contributions from each individual chain. This model assumes that the end-to-end vector of strands deforms in the same way as the macroscopic molecule. Fluctuations are completely suppressed by the dense surrounding chains. The physical properties of networks derived from this theory do not depend on their structure, *e.g.* the crosslink functionality, etc.

In the *phantom model*, the strands are treated as Gaussian chains that are allowed to cross through each other and the crosslink points interact via forces imparted by the strands between

them. The trajectory of each strand depends only on the position of its ends without any impact from the surrounding strands. This results in an affine mean junction point position and a non-affine fluctuation around the mean position of junction points in the phantom model. Their structure can be described by two simple facts:

- The mean position of the crosslink point is affine and depends only on the system's macroscopic overall length.
- The fluctuation of the chain vector connecting two crosslink points follows a normal distribution and can be treated effectively as Gaussian springs as in the bead-spring-model.

In [114], Eichinger studied statistical features of such a regular macroscopic network. The relation between mean-squared fluctuation of the chain length and the second moment of the equilibrium chain length and the crosslink functionality f reads (see also [115])

$$\langle \Delta r^2 \rangle = (2/f) \langle r^2 \rangle_0. \quad (5.1)$$

For tetra-functional crosslinks $f = 4$ (as in my case), the mean-squared distance between two junction points is:

$$\langle \Delta r^2 \rangle = \frac{1}{2} \langle r^2 \rangle_0, \quad (5.2)$$

with $\langle r^2 \rangle_0$ the mean-squared end-to-end distance of a free chain. This shows that the strands in the network are contracted and are clearly distinguishable from the 1D linear chains. The source of this contraction is not only the existence of the direct connection between two crosslink points but also the remaining strands inside the network serving as effective strings that further constrain the fluctuation of junction points.

Up-to-date MC simulations are applied to investigate more realistic (yet more complicated) self-avoiding 2D polymer networks [116–118]. Because of bending rigidity, the 2D polymer sheets are, unlike collapsed linear chains, considered to be flat. Moreover, additional attractive interactions are found to be able to overcome the bending rigidity and lead to crumpled states of 2D polymer networks [119].

5.2 Model and analytical considerations

The calculation in this study will be performed within the framework of phantom-type theories. The unit cells are star polymers made of four end-linked symmetric diblock copolymers as illustrated in Figure 5.2 (A) with a tetra-functional B -type crosslink in the center of each unit cell. A tetra-functional A -type crosslink is attached to one diblock to allow the integration of other star polymers into a network and to assure symmetry in A and B -type monomers. A regular 2D polymer network with $n_u = 4$ is demonstrated in Figure 5.2 (B).

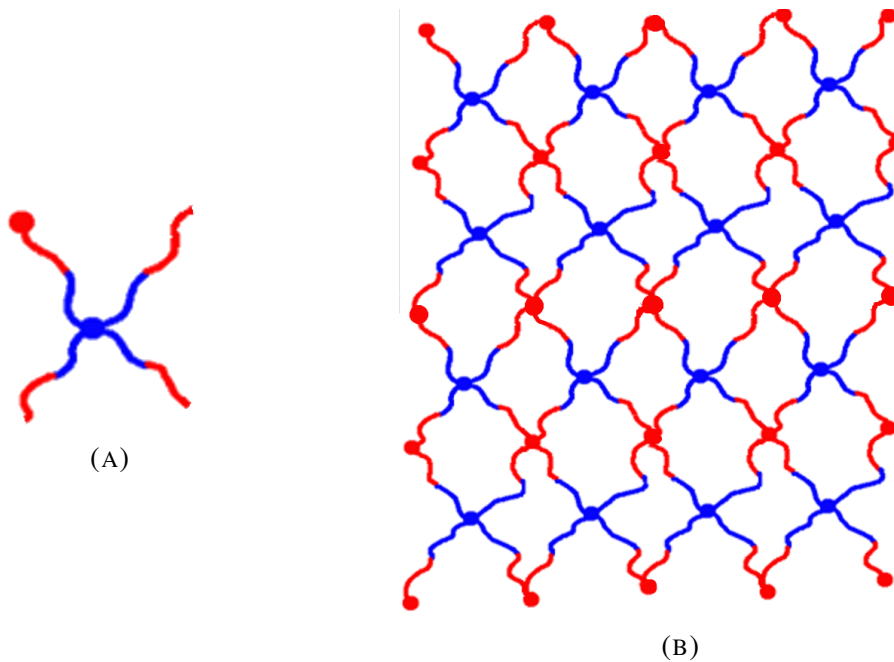


FIGURE 5.2: (A) A star polymer with two junction points serves as the smallest repeating unit in the regular network. (B) Schematic illustration of a 2D polymer network with $n_u = 4$.

In the following, the position distribution of the crosslinks will be derived analytically. The calculation is performed for a general case of n_x and n_y unit cells in x -direction and y -direction. The index difference $\mathbf{M} = (M_x, M_y)$ between two unit cells will be referred to as the *chemical distance*. The *block distance* $\vec{R}_{\mathbf{M}}$ is defined as the spatial distance between two crosslinks of the same type (I use the B -crosslinks in this study) separated by chemical distance $\mathbf{M} = (M_x, M_y)$. The equilibrium positions of the B -crosslinks are homogeneously distributed on the square lattice; thus, the mean block distance between two crosslinks is proportional to their chemical distance. The block distance as a function of chemical distance

will be used as a macroscopic measure for the global structure of the network. The lengths of the diblock strands between the adjacent crosslinks will be referred to as diblock length r_{db} and is determined by the overall parameters of the network. This must be distinguished from the end-to-end distance of a free diblock denoted as R_{db} which serves as the reference length for the distance measurements in this study. The value of R_{db} is given by $R_{db}^2 = b^2 N_{db}$ with N_{db} the monomer discretization of the diblock strands and b the statistical segment length of the bonds between the monomers.

Two approaches are applied to calculate the static structural properties of the networks at $\chi N_{db} = 0$: the *mean-field model* (originally introduced in [120], see also [121, 122]) and the *phonon model* [123]. In the mean-field approach, the fluctuations of the crosslink points around their mean positions are assumed to be uncorrelated. It has the advantage of decoupling a giant network into independent unit cells. The phonon model, on the other hand, takes the correlation between the crosslinks into account. For this reason, the calculation within the framework of the phonon model is far more demanding.

The calculation is performed for d_s spatial dimensions. I use a two-dimensional index \mathbf{i} as illustrated in Figure 5.3 to label the crosslinks in the network regardless of their type. The two axes of the indices (i_x, i_y) are aligned with the x - and y -direction of the spatial dimension. Two junction points are directly connected if $\mathbf{i} - \mathbf{j} = (-1, -1), (-1, 1), (1, -1), (1, 1)$.

5.2.1 Mean-field approximation

Within the mean-field approach, the simplification is achieved by neglecting the correlations between fluctuation of junction points. The vectorial position of the \mathbf{i} -th crosslink, regardless of its type, is denoted as $\hat{\mathbf{r}}_{\mathbf{i}}$. The indices of the four direct neighbors of crosslink \mathbf{i} are denoted by $\mathbf{i}^{\nwarrow}, \mathbf{i}^{\nearrow}, \mathbf{i}^{\swarrow}$ and \mathbf{i}^{\searrow} .

The partition function is:

$$\mathcal{Z} = \prod_{\mathbf{i}} \int d\hat{\mathbf{r}}_{\mathbf{i}} \exp \left(-\frac{d_s}{2R_{db}^2} \sum_{\mathbf{i}} \left[\left(\hat{\mathbf{r}}_{\mathbf{i}^{\nwarrow}} - \hat{\mathbf{r}}_{\mathbf{i}} \right)^2 + \left(\hat{\mathbf{r}}_{\mathbf{i}^{\nearrow}} - \hat{\mathbf{r}}_{\mathbf{i}} \right)^2 \right] \right). \quad (5.3)$$

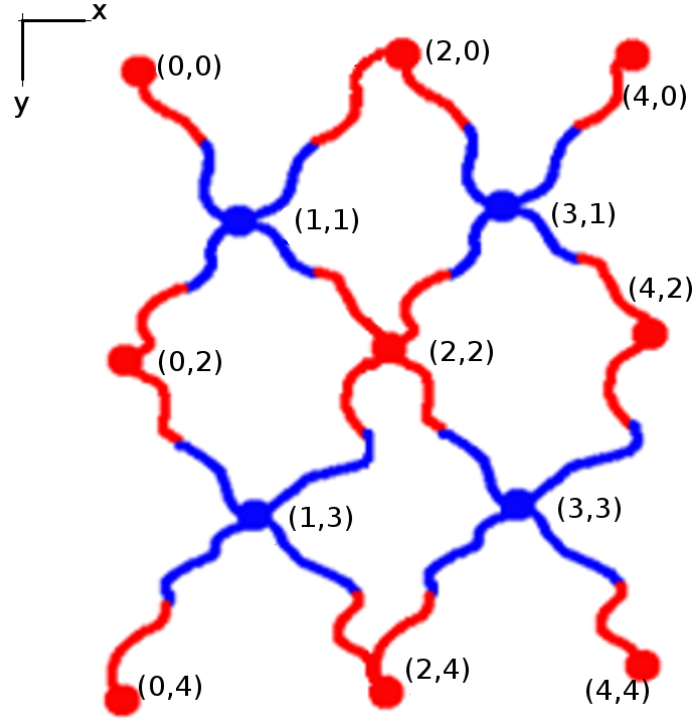


FIGURE 5.3: The definition of the 2D labels of the crosslinks in illustrated.

The crosslink density $\hat{\rho}_i = \delta(\vec{r} - \hat{\vec{r}}_i)$ (*i.e.* the probability that the i 'th crosslink is found at position \vec{r}) and the corresponding self-consistent field h_i are related via

$$1 = \int \mathcal{D}[h_i, \rho_i] \exp \left(\int d\vec{r} h_i(\vec{r}) [\rho_i(\vec{r}) - \hat{\rho}_i(\vec{r})] \right). \quad (5.4)$$

Rewriting $(\hat{\vec{r}}_{i\setminus} - \hat{\vec{r}}_i)^2 = \int d\vec{r} d\vec{r}' \hat{\rho}_{i\setminus}(\vec{r}') \hat{\rho}_i(\vec{r}) [\vec{r} - \vec{r}']^2$, the partition function becomes

$$\begin{aligned} \mathcal{Z} &= \prod_i \int \mathcal{D}[h_i, \rho_i] \exp \left\{ -\frac{d_s}{2R_{db}^2} \sum_i \int d\vec{r} d\vec{r}' [\hat{\rho}_{i\setminus}(\vec{r}') + \hat{\rho}_{i\setminus}(\vec{r}')] \right. \\ &\quad \left. \times \hat{\rho}_i(\vec{r}) [\vec{r} - \vec{r}']^2 + \sum_i \int d\vec{r} h_i(\vec{r}) [\rho_i(\vec{r}) - \hat{\rho}_i(\vec{r})] \right\}, \\ &= \prod_i \int \mathcal{D}[h_i, \rho_i] \exp \left\{ -\frac{\mathcal{F}}{kT} \right\} \end{aligned} \quad (5.5)$$

where the free energy takes the form

$$\frac{\mathcal{F}}{kT} = \frac{d_s}{2R_{db}^2} \sum_{\mathbf{i}} \int d\vec{r} d\vec{r}' [\rho_{\mathbf{i}\nwarrow}(\vec{r}') + \rho_{\mathbf{i}\nearrow}(\vec{r}')] \rho_{\mathbf{i}}(\vec{r}) [\vec{r} - \vec{r}']^2 - \sum_{\mathbf{i}} \int d\vec{r} h_{\mathbf{i}}(\vec{r}) \rho_{\mathbf{i}}(\vec{r}) - \sum_{\mathbf{i}} \ln Q_{\mathbf{i}} \quad (5.6)$$

with

$$Q_{\mathbf{i}} = \int d\hat{r}_{\mathbf{i}} \exp \left(-h_{\mathbf{i}}(\hat{r}_{\mathbf{i}}) \right). \quad (5.7)$$

Now, the saddle point approximation is applied, which is justified by the vanishing correlation.

The mean-field equations read

$$\frac{\delta \mathcal{F}}{\delta \rho_{\mathbf{i}}(\vec{r})} = \frac{d_s}{2R_{db}^2} \int d\vec{r}' (\vec{r} - \vec{r}')^2 (\rho_{\mathbf{i}\nwarrow}(\vec{r}') + \rho_{\mathbf{i}\nearrow}(\vec{r}') + \rho_{\mathbf{i}\swarrow}(\vec{r}') + \rho_{\mathbf{i}\searrow}(\vec{r}')) - h_{\mathbf{i}}(\vec{r}) = 0 \quad (5.8)$$

$$\frac{\delta \mathcal{F}}{\delta h_{\mathbf{i}}(\vec{r})} = -\rho_{\mathbf{i}}(\vec{r}) + \exp(-h_{\mathbf{i}}(\vec{r})) = 0. \quad (5.9)$$

The following Ansatz for the crosslink distribution is applied

$$\rho_{\mathbf{i}}(\vec{r}) = \frac{1}{(2\pi\sigma_{xlink}^2)^{d_s/2}} \exp \left[-\frac{(\vec{r}_{\mathbf{i}} - \vec{r}_{\mathbf{i}}^{(0)})^2}{2\sigma_{xlink}^2} \right]. \quad (5.10)$$

Solving the two mean field equations for $d_s = 3$, the mean and variance of the position of the crosslink point \mathbf{i} are obtained

$$\vec{r}_{\mathbf{i}}^{(0)} = \begin{pmatrix} i_x L_x / (2n_x) \\ i_y L_y / (2n_y) \\ 0 \end{pmatrix}, \quad \sigma_{xlink}^2 = R_{db}^2 / 12. \quad (5.11)$$

Since the crosslinks are assumed to be uncorrelated, the diblock length distribution follows directly from the crosslink position distribution. Based on the diagonal square topology of the network, the diblock length distribution reads

$$p(\vec{r}_{db}) = \frac{1}{(2\pi\sigma_{db}^2)^{3/2}} \exp \left[-\frac{(\vec{r}_{db} - \langle \vec{r}_{db} \rangle)^2}{2\sigma_{db}^2} \right], \quad (5.12)$$

with

$$\langle \vec{r}_{db} \rangle = \begin{pmatrix} L_x / (2n_x) \\ L_y / (2n_y) \\ 0 \end{pmatrix} \quad \text{and} \quad \sigma_{db}^2 = R_{db}^2 / 6. \quad (5.13)$$

The block distance can be calculated analogously. For chemical distance $\mathbf{M} = (M_x, M_y) = \frac{\mathbf{i}-\mathbf{j}}{2}$, the block distance reads:

$$p(\vec{R}_{\mathbf{M}}) = \frac{1}{(2\pi\sigma_{\mathbf{M}}^2)^{3/2}} \exp \left[-\frac{(\vec{R}_{\mathbf{M}} - \langle \vec{R}_{\mathbf{M}} \rangle)^2}{2\sigma_{\mathbf{M}}^2} \right], \quad (5.14)$$

with

$$\langle \vec{R}_{\mathbf{M}} \rangle = \begin{pmatrix} M_x L_x / (n_x) \\ M_y L_y / (n_y) \\ 0 \end{pmatrix} \quad \text{and} \quad \sigma_{\mathbf{M}}^2 = R_{db}^2 / 6 \quad (5.15)$$

the variance is independent of \mathbf{M} .

In [120], a SCFT approach based on the mean-field result is developed. In the SCFT approach, a unit-cell is constructed by placing end-crosslinked symmetric diblock copolymers between the crosslinks (ideal chains with fixed ends) such that blocks of the same type are joined. The positions of the crosslinks are assumed to be uncorrelated and fluctuate about their mean position with the normal distribution given in Equation 5.11. In this way, a macroscopic polymer network with a large number of degrees of freedom is simplified to individual unit cells and the interactions between crosslinks are decoupled. This method will be called the mean-field model in the following.

5.2.2 Phonon model

I define the connectivity matrix

$$C_{ij} = \begin{cases} 1, & \mathbf{i} \text{ and } \mathbf{j} \text{ are directly connected} \\ 0, & \text{otherwise} \end{cases}.$$

The bonded part of the Hamiltonian can be expressed as:

$$\begin{aligned}
\mathcal{H} &= \frac{d_s}{2B^2} \sum_{\mathbf{i}} \sum_{\mathbf{j} > \mathbf{i}} C_{ij} (\vec{r}_{\mathbf{i}} - \vec{r}_{\mathbf{j}}) \\
&= \frac{d_s}{4B^2} \sum_{\mathbf{i}} \sum_{\mathbf{j}} C_{ij} \left(\vec{r}_{\mathbf{i}}^{(0)} - \vec{r}_{\mathbf{j}}^{(0)} \right)^2 + \frac{d_s}{4B^2} \sum_{\mathbf{i}} \sum_{\mathbf{j}} C_{ij} (\Delta \vec{r}_{\mathbf{i}} - \Delta \vec{r}_{\mathbf{j}})^2 \\
&\quad + \frac{d_s}{2B^2} \sum_{\mathbf{i}} \sum_{\mathbf{j}} C_{ij} \left(\vec{r}_{\mathbf{i}}^{(0)} - \vec{r}_{\mathbf{j}}^{(0)} \right) (\Delta \vec{r}_{\mathbf{i}} - \Delta \vec{r}_{\mathbf{j}}) \\
&= \mathcal{H}_0 + \Delta \mathcal{H}.
\end{aligned} \tag{5.16}$$

Here, the position $\vec{r}_{\mathbf{i}}$ is separated into the equilibrium position $\vec{r}_{\mathbf{i}}^{(0)}$ and the fluctuation around the equilibrium position $\Delta \vec{r}_{\mathbf{i}}$. The last term in the penultimate step vanishes because $\langle \Delta \vec{r}_{\mathbf{i}} - \Delta \vec{r}_{\mathbf{j}} \rangle = 0$. The equilibrium position $\vec{r}_{\mathbf{i}}^{(0)}$ is determined by the overall system size according to

$$\vec{r}_{\mathbf{i}}^{(0)} = \begin{pmatrix} i_x \cdot \frac{L_x}{2n_x} \\ i_y \cdot \frac{L_y}{2n_y} \\ \dots \end{pmatrix}. \tag{5.17}$$

Thus, the constant part of the Hamiltonian becomes

$$\mathcal{H}_0 = \frac{d_s}{4B^2} n_x n_y d \left(\left(\frac{L_x}{2n_x} \right)^2 + \left(\frac{L_y}{2n_y} \right)^2 + \dots \right), \tag{5.18}$$

with $d = \sum_{\mathbf{j}} C_{ij}$. The remaining fluctuation term $\Delta \mathcal{H} = \mathcal{H} - \mathcal{H}_0$ reads:

$$\begin{aligned}
\Delta \mathcal{H} &= \sum_{\mathbf{i}} \sum_{\mathbf{j}} \frac{d_s}{2B^2} C_{ij} \left(\Delta \vec{r}_{\mathbf{i}}^2 + \Delta \vec{r}_{\mathbf{j}}^2 - 2 \Delta \vec{r}_{\mathbf{i}} \Delta \vec{r}_{\mathbf{j}} \right) \\
&= \frac{d_s}{4B^2} \left(\sum_{\mathbf{i}} 2d \Delta \vec{r}_{\mathbf{i}}^2 - 2 \sum_{\mathbf{i}} \sum_{\mathbf{j}} C_{ij} \Delta \vec{r}_{\mathbf{i}} \Delta \vec{r}_{\mathbf{j}} \right) \\
&= \frac{d_s}{4B^2} \sum_{\mathbf{i}} \sum_{\mathbf{j}} D_{ij} \Delta \vec{r}_{\mathbf{i}} \Delta \vec{r}_{\mathbf{j}}
\end{aligned} \tag{5.19}$$

with

$$D_{ij} = 2d\delta_{ij} - 2C_{ij}.$$

The components of the connectivity matrix C_{ij} are determined by the network architecture:

- $C_{ij} = 1$, if $|\mathbf{i} - \mathbf{j}| = (-1, -1), (-1, 1), (1, -1), (1, 1)$.

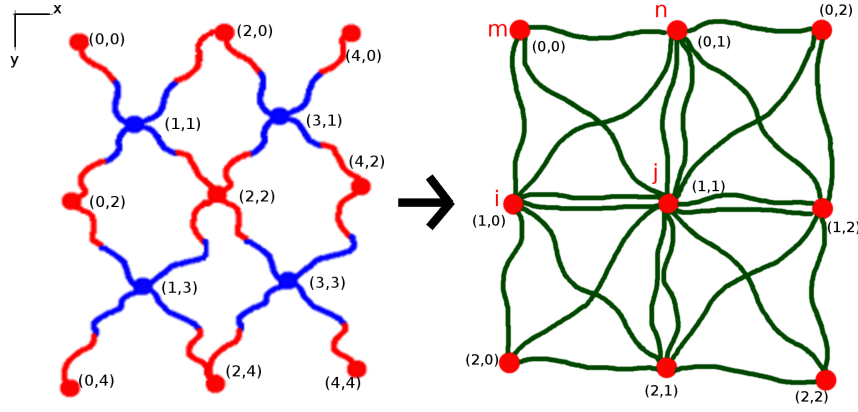


FIGURE 5.4: The blue junction points (B -crosslinks) are integrated out from the configuration.

- $C_{ij} = 0$, else.

The fact that the summation over all indices \mathbf{i} and \mathbf{j} does not include all integer numbers (for instance there exists not crosslink with index $(0,1)$) leads to difficulties in the calculation. For this reason, I will first integrate out all B -crosslinks in the system. I demonstrate this calculation on one unit cell as shown in [Figure 5.4](#). The Hamiltonian of one unit cell is

$$\begin{aligned}
 \mathcal{H}_{\text{unit cell}} &= \frac{d_s}{2B^2} \left(\vec{r}_{\mathbf{n}\mathbf{s}}^2 + \vec{r}_{\mathbf{m}\mathbf{s}}^2 + \vec{r}_{\mathbf{i}\mathbf{s}}^2 + \vec{r}_{\mathbf{j}\mathbf{s}}^2 \right) \text{ (with } \vec{r}_{\mathbf{n}\mathbf{s}} = \vec{r}_{\mathbf{n}} - \vec{r}_{\mathbf{s}}), \\
 &= \frac{d_s}{2B^2} \left[4 \left(\vec{r}_{\mathbf{s}} - \frac{\vec{r}_{\mathbf{n}} + \vec{r}_{\mathbf{m}} + \vec{r}_{\mathbf{i}} + \vec{r}_{\mathbf{j}}}{4} \right)^2 \right. \\
 &\quad \left. - \frac{1}{4} (\vec{r}_{\mathbf{n}} + \vec{r}_{\mathbf{m}} + \vec{r}_{\mathbf{i}} + \vec{r}_{\mathbf{j}})^2 + (\vec{r}_{\mathbf{n}}^2 + \vec{r}_{\mathbf{m}}^2 + \vec{r}_{\mathbf{i}}^2 + \vec{r}_{\mathbf{j}}^2) \right] \\
 &= \frac{2d_s}{B^2} \left(\vec{r}_{\mathbf{s}} - \frac{\vec{r}_{\mathbf{n}} + \vec{r}_{\mathbf{m}} + \vec{r}_{\mathbf{i}} + \vec{r}_{\mathbf{j}}}{4} \right)^2 + \sum_{\alpha, \beta = \text{all pairs}} \frac{d_s}{8B^2} (\vec{r}_{\alpha} - \vec{r}_{\beta})^2. \quad (5.20)
 \end{aligned}$$

In the last term, all pairwise combinations of n, m, i and j are summed up. The effective connections between A -crosslinks after all B -crosslinks are integrated out are shown in [Figure 5.4](#). The strength of the effective bonds is $\frac{d_s}{8B^2}$, smaller than the original bond strength $\frac{d_s}{2B^2}$. The components in the connectivity matrix of the A -crosslinks only network becomes

$$\begin{aligned}
 C_{ij} &= 2, \text{ if } \mathbf{i} - \mathbf{j} = (1,0), (0,1), (-1,0), (0,-1) \\
 C_{ij} &= 1, \text{ if } \mathbf{i} - \mathbf{j} = (1,1), (-1,1), (-1,-1), (1,-1) \\
 C_{ij} &= 0, \text{ else.}
 \end{aligned} \quad (5.21)$$

One should note that the 2D index \mathbf{i} is redefined to label only the remaining A -crosslinks.

The fluctuation part of the Hamiltonian $\Delta\mathcal{H}$ reads

$$\begin{aligned}
 \Delta\mathcal{H} &= \sum_{\mathbf{i}}^n \sum_{\mathbf{j} > \mathbf{i}}^n \frac{d_s}{8B^2} C_{\mathbf{ij}} \left(\Delta\vec{r}_{\mathbf{i}}^2 + \Delta\vec{r}_{\mathbf{j}}^2 - 2\Delta\vec{r}_{\mathbf{i}}\Delta\vec{r}_{\mathbf{j}} \right) \\
 &= \sum_{\mathbf{i}}^n \sum_{\mathbf{j}}^n \frac{d_s}{16B^2} C_{\mathbf{ij}} \left(\Delta\vec{r}_{\mathbf{i}}^2 + \Delta\vec{r}_{\mathbf{j}}^2 - 2\Delta\vec{r}_{\mathbf{i}}\Delta\vec{r}_{\mathbf{j}} \right) \\
 &= \frac{d_s}{16B^2} \left(\sum_{\mathbf{i}}^n 24\Delta\vec{r}_{\mathbf{i}}^2 - 2 \sum_{\mathbf{i}}^n \sum_{\mathbf{j}}^n C_{\mathbf{ij}} \Delta\vec{r}_{\mathbf{i}}\Delta\vec{r}_{\mathbf{j}} \right) \\
 &= \frac{d_s}{16B^2} \sum_{\mathbf{i}}^n \sum_{\mathbf{j}}^n D_{\mathbf{ij}} \Delta\vec{r}_{\mathbf{i}}\Delta\vec{r}_{\mathbf{j}}
 \end{aligned} \tag{5.22}$$

with

$$D_{\mathbf{ij}} = 24\delta_{\mathbf{ij}} - 2C_{\mathbf{ij}}.$$

I apply the plane-wave Ansatz $e_{\mathbf{j}}(\mathbf{q}) = \exp(i\mathbf{q} \cdot \mathbf{j})$ for the eigenvector of the symmetric real matrix $D_{\mathbf{ij}}$ with

$$\mathbf{q} = \begin{pmatrix} \frac{2\pi}{N_x} k_x \\ \frac{2\pi}{N_y} k_y \end{pmatrix}$$

and $k_x = 0, 1, 2, \dots, n_x$ and $k_y = 0, 1, 2, \dots, n_y$. Using the given eigenvectors, the corresponding eigenvalues can be found:

$$\lambda(\mathbf{q}) = 24 - 8 \cos(q_x) - 8 \cos(q_y) - 8 \cos(q_x) \cos(q_y). \tag{5.23}$$

The beads position fluctuation can be written in the plane-wave basis $\Delta\vec{r}_{\mathbf{j}} = \sum_{\mathbf{q}} \vec{a}(\mathbf{q}) e_{\mathbf{j}}(\mathbf{q})$. $\Delta\mathcal{H}$ now reads

$$\begin{aligned}
 \Delta\mathcal{H} &= \frac{d_s}{16B^2} \sum_{\mathbf{i}}^{n_x n_y} \sum_{\mathbf{j}}^{n_x n_y} D_{\mathbf{ij}} \sum_{\mathbf{q}, \mathbf{q}'} \vec{a}(\mathbf{q}) \vec{a}(\mathbf{q}') \exp(i\mathbf{q} \cdot \mathbf{i} + i\mathbf{q}' \cdot \mathbf{j}) \\
 &= \frac{d_s}{16B^2} \sum_{\mathbf{q}, \mathbf{q}'} \vec{a}(\mathbf{q}) \vec{a}(\mathbf{q}') \sum_{\mathbf{i}}^{n_x} \lambda(\mathbf{q}') \exp(i\mathbf{q} \cdot \mathbf{i} + i\mathbf{q}' \cdot \mathbf{i}) \\
 &= \frac{d_s}{16B^2} \sum_{\mathbf{q}} n_x n_y \lambda(\mathbf{q}) |\vec{a}(\mathbf{q})|^2 \\
 &= \frac{d_s}{16B^2} \sum_{\mathbf{q}} n_x n_y \lambda(\mathbf{q}) \left\{ \Re(a_x(\mathbf{q}))^2 + \Im(a_x(\mathbf{q}))^2 + \Re(a_y(\mathbf{q}))^2 + \dots \right\}.
 \end{aligned} \tag{5.24}$$

Making use of the equipartition theorem

$$\langle \Re (a_x(\mathbf{q}))^2 \rangle + \langle \Im (a_x(\mathbf{q}))^2 \rangle = \dots = \frac{16B^2}{2d_s n_x n_y \lambda(\mathbf{q})} \quad (5.25)$$

one obtains

$$\langle \vec{a}(\mathbf{q}) \vec{a}(\mathbf{q}') \rangle = \delta_{\mathbf{q},\mathbf{q}'} \frac{8d_s B^2}{d_s n \lambda(\mathbf{q})}. \quad (5.26)$$

Then, I calculate the correlation function

$$\begin{aligned} \langle \Delta \vec{r}_i \Delta \vec{r}_j \rangle &= \text{Corr}(\mathbf{i} - \mathbf{j}) \\ &= \sum_{\mathbf{q}, \mathbf{q}'} \langle \vec{a}(\mathbf{q}) \vec{a}(\mathbf{q}') \rangle \exp(i\mathbf{q} \cdot \mathbf{i} + i\mathbf{q} \cdot \mathbf{j}) \\ &\quad \text{the real part becomes} \\ &= \sum_{\mathbf{q}} \frac{2d_s B^2}{d_s n \lambda} \cos(\mathbf{q} \cdot \mathbf{i} - \mathbf{q} \cdot \mathbf{j}) \\ &= \sum_{\mathbf{q}} \frac{8B^2}{n \lambda(\mathbf{q})} \cos(\mathbf{q} \cdot \mathbf{i} - \mathbf{q} \cdot \mathbf{j}). \end{aligned} \quad (5.27)$$

The second moment of the block distance reads

$$\begin{aligned} \langle (\vec{r}_i - \vec{r}_j)^2 \rangle &= \langle (\vec{r}_i^{(0)} + \Delta \vec{r}_i - \vec{r}_j^{(0)} - \Delta \vec{r}_j)^2 \rangle \\ &= (\vec{r}_i^{(0)} - \vec{r}_j^{(0)})^2 + \langle \Delta \vec{r}_i^2 \rangle + \langle \Delta \vec{r}_j^2 \rangle - 2\langle \Delta \vec{r}_i \Delta \vec{r}_j \rangle. \end{aligned} \quad (5.28)$$

The mean of the block distance is

$$\langle \vec{r}_i^{(0)} - \vec{r}_j^{(0)} \rangle = \begin{pmatrix} (i_x - j_x) \cdot \frac{L_x}{N_x} \\ (i_y - j_y) \cdot \frac{L_y}{N_y} \\ \dots \end{pmatrix}. \quad (5.29)$$

The B -crosslink position \vec{r}_s can be calculated from the distribution of the A -crosslinks according to [Equation 5.20](#). The equilibrium position of \vec{r}_s is given by the center of the four surrounding A -crosslinks

$$\vec{r}_s^{(0)} = \frac{\vec{r}_n + \vec{r}_m + \vec{r}_i + \vec{r}_j}{4}. \quad (5.30)$$

For $d_s = 3$, the variance of the fluctuation in each spatial dimension is given by Equation 5.20

$$\sigma_x^2 = \sigma_y^2 = \sigma_z^2 = \frac{R_{db}^2}{2 \times 2 \times d_s} = 1/12. \quad (5.31)$$

Thus, \vec{r}_s can be computed as

$$\vec{r}_s = \vec{r}_s^{(0)} + \Delta\vec{r}_s \quad \text{with} \quad \langle \Delta\vec{r}_s \rangle = 0 \quad , \quad \sigma^2(|\Delta\vec{r}_s|) = 1/4. \quad (5.32)$$

The variance of the length of a diblock strand $\vec{r}_s - \vec{r}_n$ can also be computed as

$$\begin{aligned} \sigma^2(|\vec{r}_s - \vec{r}_n|) &= \langle (\vec{r}_s - \vec{r}_n)^2 \rangle - \left(\vec{r}_s^{(0)} - \vec{r}_n^{(0)} \right)^2 \\ &= \langle (\vec{r}_s^{(0)} - \vec{r}_n)^2 \rangle - \left(\vec{r}_s^{(0)} - \vec{r}_n^{(0)} \right)^2 + \langle \Delta\vec{r}_s \rangle^2 \\ &= \frac{1}{16} \left\{ \langle (\vec{r}_m + \vec{r}_i + \vec{r}_j - 3\vec{r}_n)^2 \rangle - \left(\vec{r}_m^{(0)} + \vec{r}_i^{(0)} + \vec{r}_j^{(0)} - 3\vec{r}_n^{(0)} \right)^2 \right\} \\ &\quad + \langle \Delta\vec{r}_s \rangle^2 \\ &= \frac{1}{16} \left\{ \left\langle [(\vec{r}_m - \vec{r}_n) + (\vec{r}_i - \vec{r}_n) + (\vec{r}_j - \vec{r}_n)]^2 \right\rangle - \right. \\ &\quad \left. \left[\left(\vec{r}_m^{(0)} - \vec{r}_n^{(0)} \right) + \left(\vec{r}_i^{(0)} - \vec{r}_n^{(0)} \right) + \left(\vec{r}_j^{(0)} - \vec{r}_n^{(0)} \right) \right]^2 \right\} + \langle \Delta\vec{r}_s \rangle^2 \\ &= \frac{1}{16} \left\{ \langle (\vec{r}_m - \vec{r}_n)^2 \rangle + \langle (\vec{r}_i - \vec{r}_n)^2 \rangle + \langle (\vec{r}_j - \vec{r}_n)^2 \rangle \right. \\ &\quad - \left\langle \left(\vec{r}_m^{(0)} - \vec{r}_n^{(0)} \right)^2 \right\rangle - \left\langle \left(\vec{r}_i^{(0)} - \vec{r}_n^{(0)} \right)^2 \right\rangle - \left\langle \left(\vec{r}_j^{(0)} - \vec{r}_n^{(0)} \right)^2 \right\rangle \\ &\quad + 2 \langle (\vec{r}_m - \vec{r}_n) (\vec{r}_i - \vec{r}_n) \rangle - 2 \left\langle \left(\vec{r}_m^{(0)} - \vec{r}_n^{(0)} \right) \left(\vec{r}_i^{(0)} - \vec{r}_n^{(0)} \right) \right\rangle \\ &\quad + 2 \langle (\vec{r}_m - \vec{r}_n) (\vec{r}_j - \vec{r}_n) \rangle - 2 \left\langle \left(\vec{r}_m^{(0)} - \vec{r}_n^{(0)} \right) \left(\vec{r}_j^{(0)} - \vec{r}_n^{(0)} \right) \right\rangle \\ &\quad + 2 \langle (\vec{r}_i - \vec{r}_n) (\vec{r}_j - \vec{r}_n) \rangle - 2 \left\langle \left(\vec{r}_i^{(0)} - \vec{r}_n^{(0)} \right) \left(\vec{r}_j^{(0)} - \vec{r}_n^{(0)} \right) \right\rangle \right\} \\ &\quad + \langle \Delta\vec{r}_s \rangle^2. \end{aligned} \quad (5.33)$$

Completing the square leads to

$$\begin{aligned}
\sigma^2(|\vec{r}_s - \vec{r}_n|) &= \frac{1}{16} \left\{ \sigma^2(|\vec{r}_m - \vec{r}_n|) + \sigma^2(|\vec{r}_i - \vec{r}_n|) + \sigma^2(|\vec{r}_j - \vec{r}_n|) \right\} \\
&+ \frac{1}{8} \left\{ \langle (\vec{r}_n - \vec{r}_i)^2 \rangle - \langle (\vec{r}_i)^2 \rangle - \left\langle \left(\vec{r}_n^{(0)} - \vec{r}_i^{(0)} \right)^2 \right\rangle + \langle (\vec{r}_i^{(0)})^2 \rangle \right. \\
&\quad + \langle (\vec{r}_n - \vec{r}_m)^2 \rangle - \langle (\vec{r}_m)^2 \rangle - \left\langle \left(\vec{r}_n^{(0)} - \vec{r}_m^{(0)} \right)^2 \right\rangle + \langle (\vec{r}_m^{(0)})^2 \rangle \\
&\quad + \langle (\vec{r}_n - \vec{r}_j)^2 \rangle - \langle (\vec{r}_j)^2 \rangle - \left\langle \left(\vec{r}_n^{(0)} - \vec{r}_j^{(0)} \right)^2 \right\rangle + \langle (\vec{r}_j^{(0)})^2 \rangle \\
&\quad + \langle (\vec{r}_m \vec{r}_i) \rangle + \left\langle \left(\vec{r}_m^{(0)} \vec{r}_i^{(0)} \right) \right\rangle + \langle (\vec{r}_j \vec{r}_i) \rangle + \left\langle \left(\vec{r}_j^{(0)} \vec{r}_i^{(0)} \right) \right\rangle \\
&\quad \left. + \langle (\vec{r}_m \vec{r}_j) \rangle + \left\langle \left(\vec{r}_m^{(0)} \vec{r}_j^{(0)} \right) \right\rangle \right\} + \langle \Delta \vec{r}_s \rangle^2 \\
&= \frac{1}{16} \left\{ \sigma^2(|\vec{r}_m - \vec{r}_n|) + \sigma^2(|\vec{r}_i - \vec{r}_n|) + \sigma^2(|\vec{r}_j - \vec{r}_n|) \right\} \\
&+ \frac{1}{8} \left\{ \sigma^2(|\vec{r}_n - \vec{r}_m|) + \sigma^2(|\vec{r}_n - \vec{r}_i|) + \sigma^2(|\vec{r}_n - \vec{r}_j|) \right\} \\
&- \frac{1}{16} \left\{ \sigma^2(|\vec{r}_i - \vec{r}_m|) + \sigma^2(|\vec{r}_i - \vec{r}_j|) + \sigma^2(|\vec{r}_m - \vec{r}_j|) \right\} + \langle \Delta \vec{r}_s \rangle^2.
\end{aligned} \tag{5.34}$$

$\text{Corr}(m_x - n_x, m_y - n_y)$ will be used to denote the variance $\sigma^2(|\vec{r}_m - \vec{r}_n|)$ in the following equation. This variance can be obtained from [Equation 5.28](#):

$$\begin{aligned}
\sigma^2(|\vec{r}_s - \vec{r}_n|) &= \frac{1}{8} \{ \text{Corr}(1, 0) + \text{Corr}(0, 1) + \text{Corr}(1, 1) \} + \langle \Delta \vec{r}_s \rangle^2 \\
&= \frac{1}{8} \{ \text{Corr}(1, 0) + \text{Corr}(0, 1) + \text{Corr}(1, 1) \} + \frac{3}{12} \\
&\approx \frac{1}{8} (0.7266 + 0.6365 + 0.6365) + 0.25 \\
&= 0.25 + 0.25 = 0.5.
\end{aligned} \tag{5.35}$$

Note that $\sigma^2(|\vec{r}_s - \vec{r}_n|)$ is the variance of the magnitude of the diblock length *i.e.*

$$\sigma^2(|\vec{r}_s - \vec{r}_n|) = 3\sigma_{db}^2$$

and the variance in each independent spatial dimension is $\sigma_{db}^2 = 1/6$. The mean diblock strand length is trivially given by the overall system size

$$\langle \vec{r}_{db} \rangle = \begin{pmatrix} L_x / (2n_x) \\ L_y / (2n_y) \\ 0 \end{pmatrix}. \quad (5.36)$$

This result is in perfect agreement with Flory's prediction for the strand length distribution in regular polymer networks with crosslink functionality equal to four [115] (see Equation 5.2).

The phonon model and the mean-field model both predict trivial mean positions of the crosslinks determined by the overall system parameters. The variance of the block distance derived from the phonon model indicates a correlation between the fluctuations of the crosslinks from their mean position, which is neglected by the mean-field model. The strength of this correlation depends on the number of unit cells. In the following, its impact on the crosslink distribution, the structure factor and the phase behavior will be investigated in simulations for various n_u and l_u .

5.3 The structure of 2D polymer networks

Previously, the mean-field model and the phonon model were introduced to describe the structure of the networks at $\chi N_{db} = 0$. The mean-field model assumes independent crosslinks and predicts a block distance distribution independent of the chemical distance. The phonon model, on the other hand, considers full correlation between the crosslinks and predicts a non-trivial block distance distribution that can be computed numerically for a given n_u . Here, the analytical results will be compared with data measured in the crudely simplified MC simulation and the SOMA simulation. The positions of the monomers in the diblock strands between the crosslinks will not be considered.

5.3.1 Diblock strand length

One important observable related to the structure of the network is the diblock strand length $\vec{r}_{db} = (x_{db}, y_{db})$. In [subsection 5.2.2](#), mean-field approach and the phonon model predicted the same diblock strand length distribution of the form

$$p(x_{db}, y_{db}) = \frac{1}{2\pi\sigma_{db}^2} \exp \left(-\frac{(x_{db} - \langle x_{db} \rangle)^2 + (y_{db} - \langle y_{db} \rangle)^2}{2\sigma_{db}^2} \right), \quad (5.37)$$

with $\langle x_{db} \rangle = L_x / (2n_u)$, $\langle y_{db} \rangle = L_y / (2n_u)$ and $\sigma_{db}^2 = \frac{R_{db}^2}{6}$.

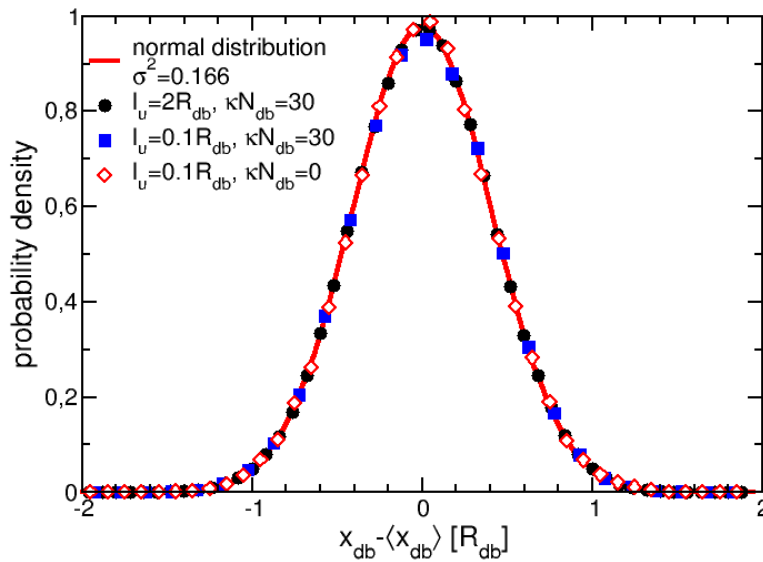


FIGURE 5.5: The strand length distribution in x -direction measured in SOMA matches the analytical predictions very well at $\kappa N_{db} = 0$. At $\kappa N_{db} = 30$, small deviation can be observed. The figure is reprinted with permission from [77].

Copyright 2022 American Chemical Society.

The probability distribution of the strand length in x -direction is measured for $l_u = 0.1 R_{db}$ and $l_u = 2 R_{db}$ in SOMA and compared with the analytical predictions in [Figure 5.5](#). The mean-field model and the phonon model both successfully capture the strand length distribution at $\kappa N_{db} = 0$. The incompressibility constraint shows minor impact on the strand length distribution.

5.3.2 Block distance distribution

First, I measure the block distance distribution with the simplified MC simulation. A network with $n_u = 140$, $l_u = 0.0429 R_{db}$ and $0.1 R_{db}$ is generated according to the connectivity matrix

- $C_{ij} = 1$, if $\mathbf{i} - \mathbf{j} = (1, 0), (1, -1), (-1, 0), (-1, -1)$ and i_x is odd (*A*-crosslinks).
- $C_{ij} = 1$, if $\mathbf{i} - \mathbf{j} = (1, 1), (1, 0), (-1, 1), (-1, 0)$ and i_x is even (*B*-crosslinks).
- $C_{ij} = 0$, else.

The Hamiltonian of the system considering only the crosslinks is given by

$$\mathcal{H} = \frac{1}{B^2} \sum_{\mathbf{i}} \sum_{\mathbf{j} > \mathbf{i}} \left(C_{ij} (\vec{r}_{\mathbf{i}} - \vec{r}_{\mathbf{j}})^2 \right). \quad (5.38)$$

After equilibration, the block distance distribution is obtained by measuring the positions of *B*-crosslinks as a function of the chemical distance \mathbf{M} . This distribution is described by its mean

$$\langle \vec{R}_{\mathbf{M}} \rangle = \langle \vec{r}_{\mathbf{i}+\mathbf{M}} - \vec{r}_{\mathbf{i}} \rangle = \vec{r}_{\mathbf{i}+\mathbf{M}}^{(0)} - \vec{r}_{\mathbf{i}}^{(0)} \quad (5.39)$$

and its variance

$$\begin{aligned} \langle (\vec{r}_{\mathbf{i}+\mathbf{M}} - \vec{r}_{\mathbf{i}})^2 \rangle - \left(\vec{r}_{\mathbf{i}+\mathbf{M}}^{(0)} - \vec{r}_{\mathbf{i}}^{(0)} \right)^2 &= \langle (x_{\mathbf{i}+\mathbf{M}} - x_{\mathbf{i}})^2 \rangle - \left(x_{\mathbf{i}+\mathbf{M}}^{(0)} - x_{\mathbf{i}}^{(0)} \right)^2 \\ &\quad + \langle (y_{\mathbf{i}+\mathbf{M}} - y_{\mathbf{i}})^2 \rangle - \left(y_{\mathbf{i}+\mathbf{M}}^{(0)} - y_{\mathbf{i}}^{(0)} \right)^2 \\ &= 2\sigma_{\mathbf{M}}^2. \end{aligned} \quad (5.40)$$

The average $\langle \dots \rangle$ in the above equation is performed over all *B*-crosslinks \mathbf{i} . The index summation $\mathbf{i} + \mathbf{M}$ is performed across periodic boundary conditions in case $i_{\alpha} + M_{\alpha} > n_u$.

The data from the simplified MC simulation is compared with the analytical prediction from the phonon model. The statistical segment length of the effective springs is set to $B^2 = (2/3) R_{db}^2$ to match the 2D projection of \vec{R}_{db} in 3D SOMA. The results for $M_y = 0$ are shown in [Figure 5.6](#). The mean of the block distances is given by the overall parameter

$\langle \vec{R}_M \rangle = (X_M^0, Y_M^0) = (M_x \frac{L}{n_u}, M_y \frac{L}{n_u})$. The second moment, which characterizes the extent of fluctuation of the crosslinks, provides a more informative comparison with the analytical results. The data from the simplified MC simulation matches the analytical results from the phonon model very well. As the phonon model already predicted, the variance of the block distance is independent of l_u . One can also make use of the result given by Equation 5.26 to generate crosslinks that already have the correct distribution to avoid the equilibration of the configuration. I also show the block distance distribution of one configuration generated with the phonon modes formalism in Figure 5.6 (see Equation 5.26) to demonstrate the reliability of this sampling technique.

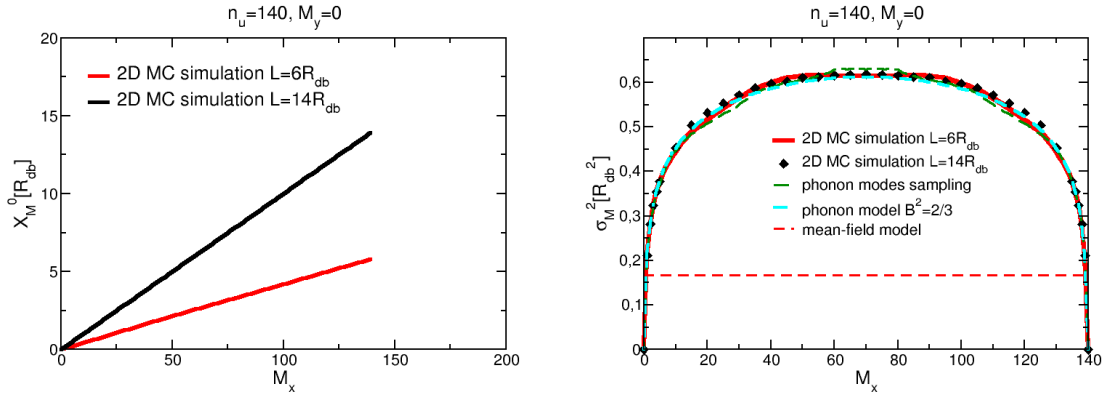


FIGURE 5.6: Left: The mean of the block distance in x -direction is shown as a function of M_x at $M_y = 0$. Right: The variance of the block distance distribution measured in the simplified MC simulation is shown for two system sizes. This is compared with the phonon model prediction (cyan dashed line) from subsection 5.2.2. One configuration generated with the phonon modes sampling technique (green dashed line) is also presented.

Next, I compare the block distance distribution measured in SOMA with the analytical predictions. As mentioned before, the difference between SOMA and the simplified MC simulation is the incompressibility constraint and the monomer discretization of the diblock strands. The network is comprised of 80×80 unit cells and the side length of the simulation box is $L = 8 R_{db}$ (or $l_u = 0.1 R_{db}$). I show the variance of the block distance measured in SOMA at $\kappa N_{db} = 0$, $\kappa N_{db} = 30$ and $\kappa N_{db} = 50$ together with the phonon model prediction and the mean-field prediction in Figure 5.6. The distances in SOMA are computed only with contributions from the x - and y -direction.

The phonon prediction agrees with the simulation results at $\kappa N_{db} = 0$. For systems

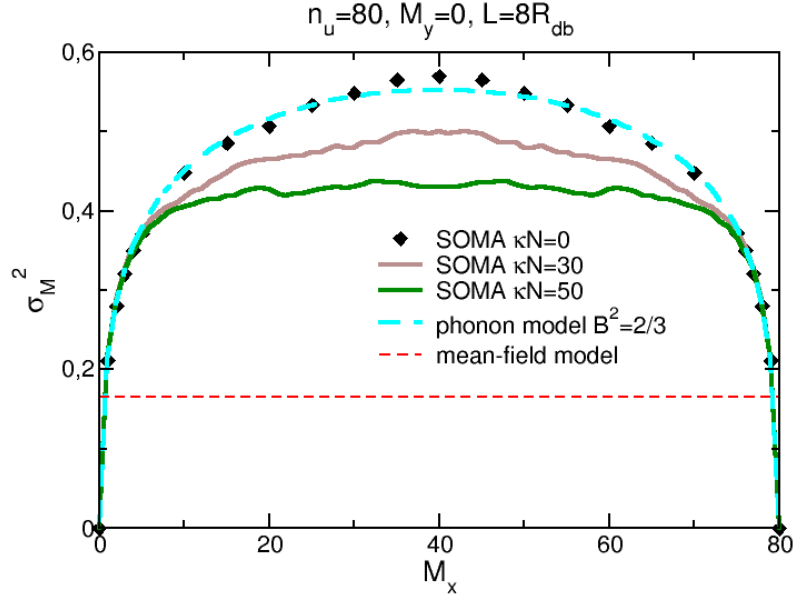


FIGURE 5.7: The variance of the block distance measured in SOMA is compared with the analytical predictions. The phonon model prediction matches the simulation at $\kappa N_{db} = 0$ very well but the fluctuation at large chemical distance is clearly suppressed by κN_{db} . The mean-field predicts a constant variance independent of the chemical distance and is proven to be wrong.

at $\kappa N_{db} = 30$ and $\kappa N_{db} = 50$, the presence of the incompressibility constraint leads to a suppression of fluctuations of more than 30% at the largest length scale. The deviation grows with increasing chemical distance. At small length scales for chemical distances < 5 , the block distance distribution is not affected by this deviation. Fortunately, as will become more clear in the next section, the correlation is only important between nearby crosslinks separated by a few unit cells. Thus, the phonon model is sufficiently good to describe the structure of a 2D regular network at $\chi N_{db} = 0$. The mean-field approach, on the other hand, predicts a constant variance of the block distance independent of the chemical distance. This is a direct consequence of the assumption of uncorrelated crosslinks. The significant deviation between the mean-field result and the simulation proves this simplification to be inappropriate to describe networks with $n_u > 1$.

5.4 Structure factor

Two length scales are of particular importance for understanding the behavior of polymer networks, the typical domain size of segregated constituent diblock strands d_L (the equilibrium lamellar spacing of free diblocks is about $d_L \approx 1.5 R_{db}$ depending on χN_{db} [124–126]) and the imposed unit cell size l_u . In order to describe the networks' novel behavior resulting from the interplay between the two characteristic length scales, I compute the structure factors of the networks with special attention to the two length scales. First, the network specific structure factor around $q_u = 2\pi/l_u$ is computed using only the positions of the A -crosslinks. This will be referred to as crosslink structure factor S_{XLA} and can be calculated analytically based on the block distance distribution derived from the phonon model. Then, the contribution from the diblock strands between the crosslinks is added to the description and provides the total structure factor S_{n_u} .

5.4.1 Crosslink structure factor

The crosslink structure factor considering only the A -type crosslinks is defined as

$$S_{XLA}(\vec{q}, n_u) = \frac{1}{n_u n_u} \sum_{\mathbf{c}} \sum_{\mathbf{c}'} \exp \left(i\vec{q} [\vec{r}_{\mathbf{c}} - \vec{r}_{\mathbf{c}'}] \right). \quad (5.41)$$

$\vec{r}_{\mathbf{c}} - \vec{r}_{\mathbf{c}'}$ denotes the distance between the A -crosslinks labeled by the 2D indices \mathbf{c} and \mathbf{c}' . This distance can be separated into their resting position distance (a deterministic part) and the deviation from their resting position (a fluctuation part).

$$S_{XLA}(\vec{q}, n_u) = \frac{1}{n_u^2} \sum_{c_x=0}^{n_u-1} \sum_{c_y=0}^{n_u-1} \sum_{c'_x=0}^{n_u-1} \sum_{c'_y=0}^{n_u-1} \exp \left(i\vec{q} [\vec{R}_{\mathbf{c}\mathbf{c}'}^0 + \Delta\vec{R}_{\mathbf{c}\mathbf{c}'}] \right) \quad (5.42)$$

with $\vec{R}_{\mathbf{c}\mathbf{c}'}^0$ the resting position distance and $\Delta\vec{R}_{\mathbf{c}\mathbf{c}'}$ the fluctuation distance. Due to spatial translation invariance, the chemical distance $\mathbf{M} = \mathbf{c} - \mathbf{c}'$ is sufficient to parametrize the A -crosslink pairs. The summation can be expressed in terms of chemical distance

$$S_{XLA}(\vec{q}, n_u) = \frac{1}{n_u^2} n_u^2 \sum_{M_x=0}^{n_u-1} \sum_{M_y=0}^{n_u-1} \exp \left(i\vec{q} \vec{R}_{\mathbf{M}}^0 + i\vec{q} \Delta\vec{R}_{\mathbf{M}} \right). \quad (5.43)$$

In the above equation, I make use of the periodic boundary conditions, namely $(c_x - c'_x, c_y - c'_y)$ is equivalent to $(c_x - c'_x + n_u, c_y - c'_y + n_u)$.

The expectation value of $S_{\text{XLA}}(\vec{q}, n_u)$ can be calculated with the block distance distribution $\vec{R}_{\mathbf{M}}$ given by Equation 5.27

$$\begin{aligned}
 \langle S_{\text{XLA}}(\vec{q}, n_u) \rangle &= \sum_{M_x}^{n_u-1} \sum_{M_y}^{n_u-1} \left\{ \exp(i\vec{q} \cdot \vec{R}_{\mathbf{M}}^0) \right. \\
 &\quad \times \int d\Delta \vec{R}_{\mathbf{M}} \left(\frac{1}{\sqrt{2\pi\sigma_{\mathbf{M}}^2}} \right)^{d_s} \exp(i\vec{q} \cdot \Delta \vec{R}_{\mathbf{M}}) \exp\left(-\frac{\Delta \vec{R}_{\mathbf{M}}^2}{2\sigma_{\mathbf{M}}^2}\right) \\
 &= \sum_{(M_x, M_y)=(0,0)}^{(n_u-1, n_u-1)} \left\{ \exp(i\vec{q} \cdot \vec{R}_{\mathbf{M}}^0) \exp\left(-\vec{q}^2 \frac{\sigma_{\mathbf{M}}^2}{2}\right) \right\} \\
 &= 1 + \sum_{(M_x, M_y) \neq (0,0)}^{(n_u-1, n_u-1)} \left\{ \exp(i\vec{q} \cdot \vec{R}_{\mathbf{M}}^0) \exp\left(-\vec{q}^2 \frac{\sigma_{\mathbf{M}}^2}{2}\right) \right\}. \quad (5.44)
 \end{aligned}$$

The variance of the block distance distribution $\sigma_{\mathbf{M}}^2$ has been computed within the phonon model as a function of the chemical distance \mathbf{M} . As demonstrated in Figure 5.8 (left), $\sigma_{\mathbf{M}}^2$ increases with chemical distance and reaches a plateau value already for small \mathbf{M} . Since $\sigma_{\mathbf{M}}^2$ is almost constant everywhere except for very small chemical distances, it can be approximated by its plateau value denoted by σ_p^2 . The numerically calculated value of σ_p^2 is shown in Figure 5.8 (right) as a function of n_u .

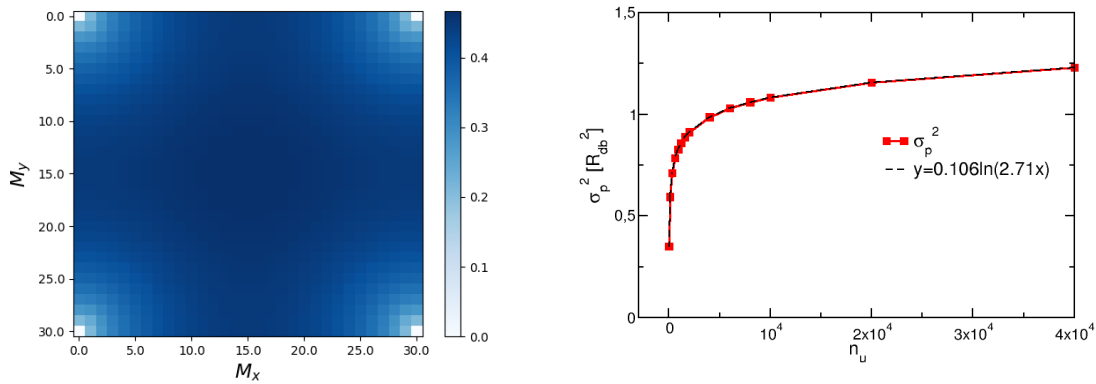


FIGURE 5.8: Left: $\sigma_{\mathbf{M}}^2$ is shown for polymer networks with $n_u = 30$. Right: σ_p^2 as a function of n_u is shown.

This approximation allows me to separate the fluctuation part of the crosslink structure factor from the summation

$$\langle S_{\text{XLA}}(\vec{q}, n_u) \rangle = 1 + \left\{ \sum_{(M_x, M_y) \neq (0,0)}^{(n_u-1, n_u-1)} \exp(i\vec{q} \cdot \vec{R}_{\mathbf{M}}^0) \right\} \exp\left(-\vec{q}^2 \frac{\sigma_p^2}{2}\right). \quad (5.45)$$

The summation term in Equation 5.45 is a system-length-dependent reciprocal lattice with maximal intensity proportional to $n_u^2 - 1$ (number of scattering centers) at

$$q_x^u = \frac{2\pi}{l_u} k_x \quad \text{and} \quad q_y^u = \frac{2\pi}{l_u} k_y, \quad k_x, k_y = 0, 1, 2, \dots$$

The fluctuation part of the structure factor $\propto \exp(-\vec{q}^2 \frac{\sigma_p^2}{2})$ is independent of the system length. It is an exponential decay with a decay constant that depends only slightly on the number of unit cells n_u .

In Figure 5.9, the analytically calculated $S_{\text{XLA}}(\vec{q}, n_u)$ (left) is tested against the structure factor measured in the simplified MC simulation (middle). The crosslink structure factor measured in SOMA at $\kappa N_{db} = 30$ (right) is presented as well in order to address the impact of the incompressibility constraint. In the SOMA simulation, the networks are comprised of 30×30 unit cells. Each diblock strand contains $15 + 1/4$ A -monomers and $15 + 1/4$ B -monomers. The contribution $1/4$ comes from the one A - and the one B -crosslink shared by four strands. The reference number of beads is set to $N_{db} = 32$. The spatial discretization ΔL is $0.1 R_{db}$ in x -direction and y -direction. The simulation results are averaged over at least 100 independent configurations for better statistics. I set the value at $q_x = q_y = 0$ manually to zero for better contrast in the rest of the Fourier space. The crosslink structure factor calculated with the phonon model is in good agreement with the result of the simplified MC simulation and with SOMA. The simulation results confirm the peaks at wavevector $\left(\frac{2\pi k_x}{l_u}, \frac{2\pi k_y}{l_u}\right)$ with $k_x, k_y = 1, 2, \dots$ for $l_u = 1.5 R_{db}$ and $3 R_{db}$.

Apart from $\vec{q} = (0, 0)$, the intensity of the crosslink structure factor has a maximum at the smallest wavevector $q_x^u = \frac{2\pi}{l_u}, q_y^u = 0$ (or equivalently $q_x^u = 0, q_y^u = \frac{2\pi}{l_u}$). Assuming a constant σ_p^2 of order one ($\sigma_p^2 \approx 0.4$ for $n_u = 30$), the intensity of the crosslink structure factor

can be estimated as

$$S_{\text{XLA}}(q_u, n_u) \approx \exp \left[- \left(\frac{2\pi}{l_u} \right)^2 \times \frac{\sigma_p^2}{2} \right] n_u^2. \quad (5.46)$$

For $l_u = 0.5 R_{db}$ ($n_u = 30$), the network's size must be of the order $n_u > 10^7$ to result in an amplitude of order one. Because of this, the peaks are not visible in the simulations with small l_u .

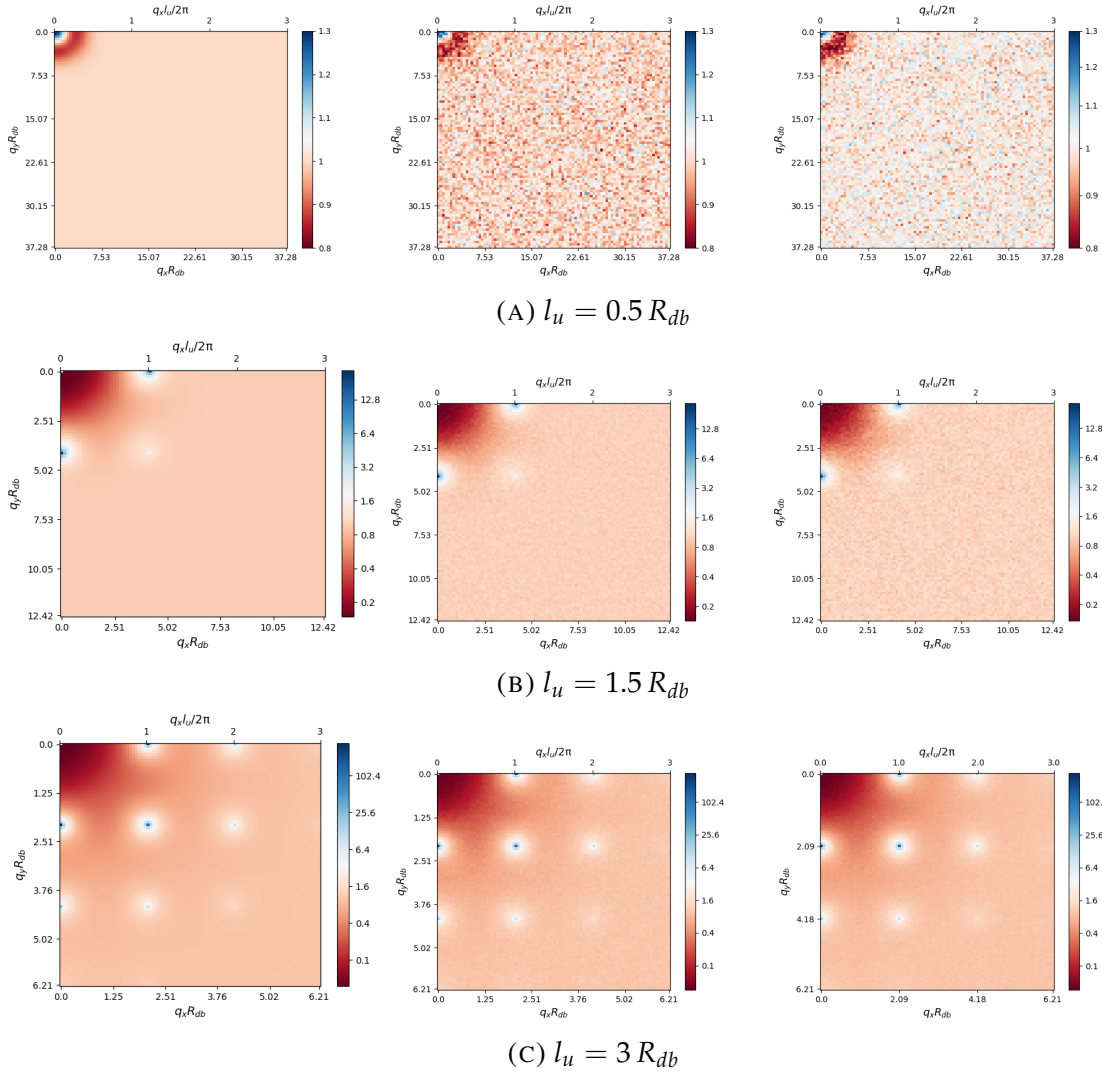


FIGURE 5.9: The expectation value of the crosslink structure factor of a 30×30 regular network at three system lengths $L = 15 R_{db}$ ($l_u = 0.5 R_{db}$), $45 R_{db}$ ($l_u = 1.5 R_{db}$) and $90 R_{db}$ ($l_u = 3 R_{db}$) is calculated analytically (left), measured in the simplified MC simulation (middle) and in SOMA (right). The value at $q_x = q_y = 0$ is set to zero for visibility.

In all the three systems, the incompressibility constraint in SOMA shows no impact on the amplitudes of the peaks. As demonstrated in [Figure 5.7](#), the incompressibility constraint

shows only a significant impact at length scales of the order of the system size and does not affect the structure at the length scale of the unit cell size l_u . Thus, the phonon model provides a reliable description of the crosslink structure factor in the relevant region and predicts an intensity growth given by n_u^2 .

5.4.2 Total structure factor

Now I consider the structure factor of the composition of a (or part of a) network molecule. I measure the total structure factor accounting for all monomers in the (sub-)network defined as

$$S_{total}(\vec{q}, n'_u) = \frac{1}{4n'_u n'_u (4N_{db} - 2)} \left\langle \left| \sum_{\mathbf{n}} \gamma_{\mathbf{n}} \times e^{i\vec{q}\vec{r}_{\mathbf{n}}} \right|^2 \right\rangle. \quad (5.47)$$

and analyze its dependency on l_u and n'_u . $0 < n'_u \leq n_u$ is the number of mesh cells in the sub-network, that are included when calculating the total structure factor. The 2D index \mathbf{n} runs over all monomers in the considered part of the network. The factor $\gamma_{\mathbf{n}}$ is 1 if the monomer \mathbf{n} is of type *A* and 1 if *B*. In the following, I construct a much larger network comprised of $n_u \times n_u$ unit cells and perform the measurements on sub-blocks of $n'_u \times n'_u$ unit cells. I measure the structure factor in two systems. In SOMA, I build 30×30 networks by assigning the crosslinks according to the given topology and equilibrate them. This method allows only for studying of relatively small networks because the equilibration of such giant macromolecules is time-consuming. In the second approach, I first generate crosslink positions according to the phonon model and then construct the strands as Brownian bridges between two fixed ends given by the crosslinks. This process is computationally less expensive and the size of the network reaches 180×180 unit cells. The structure factors are measured using networks constructed with the phonon model unless stated otherwise.

The total structure factor as a function of q_x at $q_y = 0$ is presented for various n'_u and l_u in **Figure 5.10** (left). On the right-hand side, the most characteristic 2D total structure factors are shown. As one can see in **Figure 5.10**, the profile of the total structure factor is a result of the interplay between the structure at the length scale of the diblock strands (diblock characteristics) and the long-range order imposed by the network connectivity at the length scale of l_u (crosslink characteristics) of the network. Although the structure factor of polymer

networks is always dominated by the peak at $q_u = \frac{2\pi}{l_u}$ above a certain n'_u , q_u is not always important. This is because an idealized network with an overwhelming number of unit cells is impractical, for structure irregularities (defects) in the network topology would affect the long-range 2D order. The more realistic ones are networks with a moderate number of unit cells $n'_u = \mathcal{O}(1) - \mathcal{O}(100)$. In this case, the diblock characteristics on the length scale of d_L become important. Whether the network is characterized by the diblock characteristics or by the crosslink characteristics is crucially determined by l_u and n'_u . In [Figure 5.11](#), the peak position q^* of the total structure factor $S_{total}(q, 30)$ is compared with q_u . For small l_u below $\approx 1.3 R_{db}$, $|q^*| R_{db} \approx 5$ is nearly a constant corresponding to a length of $1.26 R_{db}$. The length scale of the unit cell size is not of special importance and q_u is not the dominant wavevector. For $l_u > 1.3 R_{db}$, $q_u = \frac{2\pi}{l_u}$ becomes the dominant wavevector *i.e.* $q^* = q_u$.

I separate the networks into three regimes according to their unit cell size. For compressed networks with $l_u < 0.5 R_{db}$, the intensity of the structure factor increases only slightly with growing n'_u . The impact of the crosslink structure factor is insignificant for the range of n_u that is accessible for this simulation study. The length scale of the crosslink characteristics is much smaller than that of the diblock characteristics. Thus, the ordered structure at periodicity l_u can be ignored here. The total structure factor is dominated by the diblock characteristics and is isotropic as shown in [Figure 5.10 \(A\)](#). In addition to the total structure factor of the network at $l_u = 0.33 R_{db}$, I present the radial averaged total structure factor for $l_u = 0.167 R_{db}$ and $0.5 R_{db}$ in the relevant region in [Figure 5.12 \(left\)](#). In [Figure 5.12 \(right\)](#), the intensity of the peak of the total structure factor is demonstrated as a function of n'_u for several l_u . In this regime, the structure factor increases first with n'_u and reaches a plateau at about $n'_u = 5$. This demonstrates the importance of the correlation between nearby crosslinks and that the correlation can only be neglected if the crosslinks are separated by more than five unit cells. Above $n'_u = 5$, the structure factor and thus the phase behavior of the networks can be considered independent of n'_u .

For intermediate $0.5 R_{db} < l_u \lesssim 1.5 R_{db}$, the diblock characteristics and the crosslink characteristics are similarly important for the structure of the network for the range of n'_u studied in this simulation. As shown in [Figure 5.10 \(B\)](#) for $l_u = 1.167 R_{db}$, the diblock characteristics dominate first at small n'_u where a nearly isotropic structure factor with peaks at $|\vec{q}| R_{db} \approx 4.5$ is observed. With increasing n'_u , the total structure factor becomes more

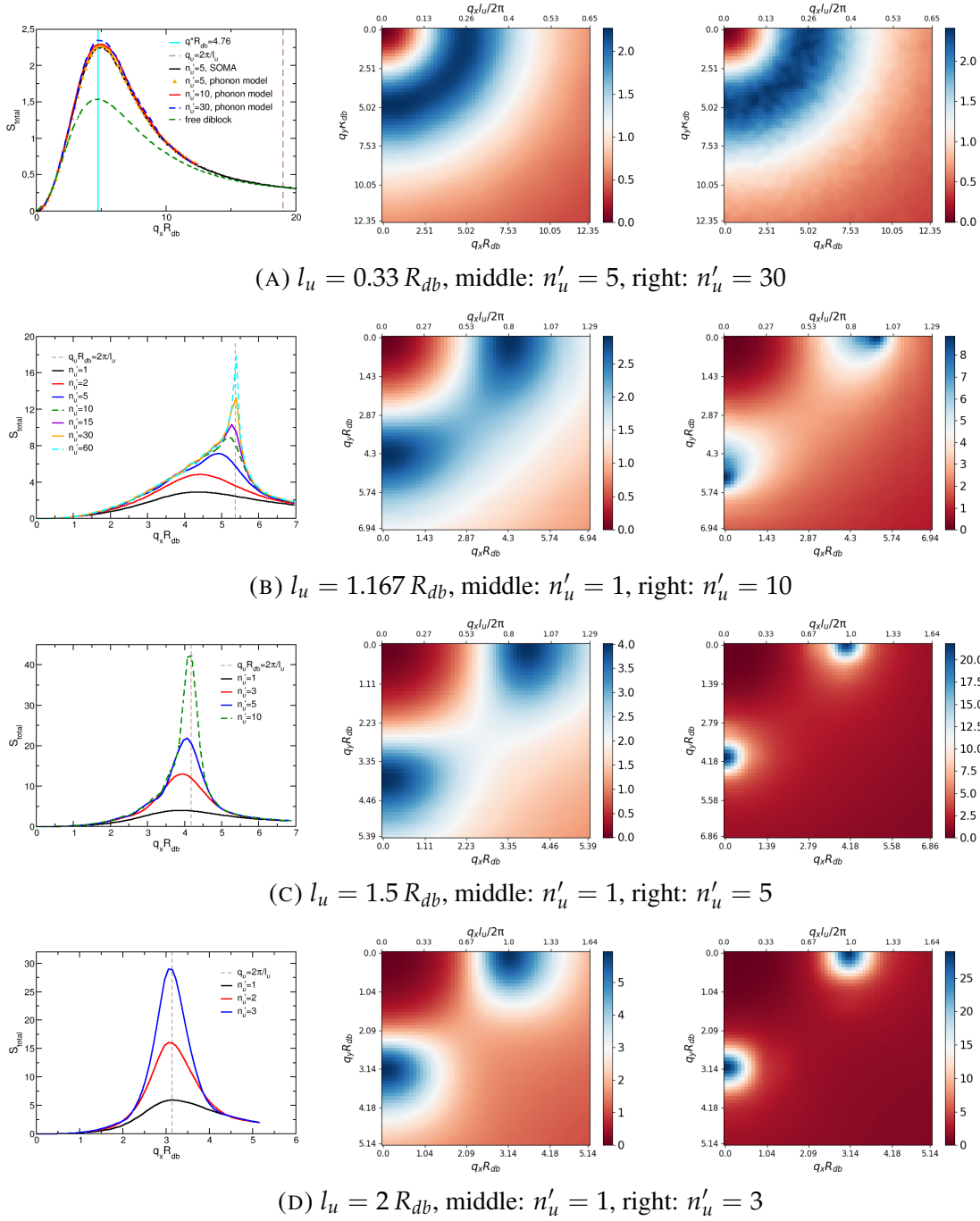


FIGURE 5.10: The total structure factor measured with data generated by the phonon network model is presented for various l_u and n'_u . The size of the network is $n_u = 180$. In (A), $S_{total}(q, 5)$ measured in SOMA is provided to demonstrate that the phonon model and SOMA provide the same results. One should note that the ranges of the colorbars are not identical in the contour plots.

anisotropic and the peak of the structure factor gradually shifts towards larger values until it reaches $\vec{q}R_{db} \approx (5.39, 0)$ and $(0, 5.39)$ close to the length scale of $l_u = 1.167 R_{db}$. The transition occurs at $n'_u \approx 10$, after which the profile of the total structure factor is dominated

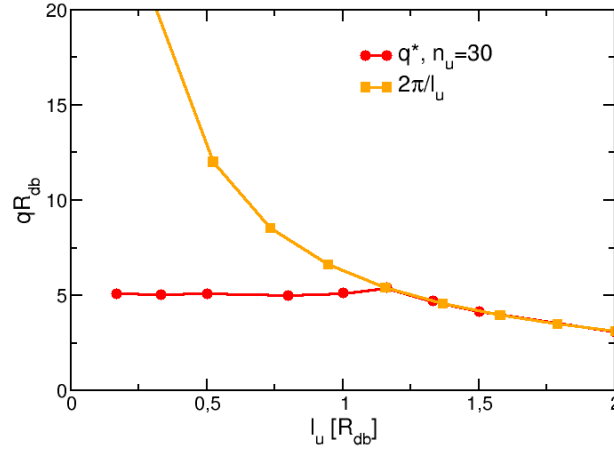


FIGURE 5.11: The peak position q^* of the measured structure factor for $n_u = 30$ is compared with $q_u = 2\pi/l_u$.

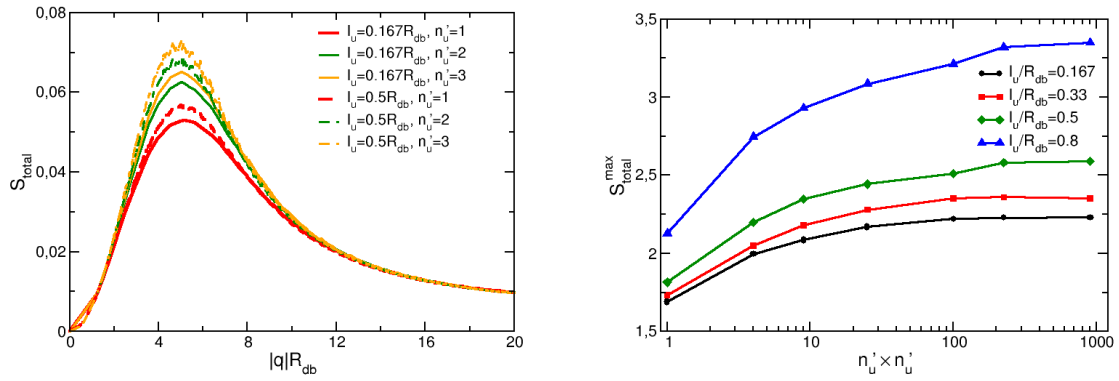


FIGURE 5.12: Left: The radially averaged structure factor (measured in SOMA) for $n'_u = 1$, $n'_u = 2$ and $n'_u = 3$ is shown for networks with $l_u = 0.167 R_{db}$ and $0.5 R_{db}$. Right: The intensity of the structure factor S_{total}^{max} as a function of n'_u (measured in the phonon model) is shown for small l_u .

by the crosslink characteristics and the intensity of the structure factor grows according to $n'_u{}^2$. Similar behavior is observed in [Figure 5.10 \(C\)](#) for $l_u = 1.5 R_{db}$. In this case, the crosslink characteristics dominate the network's structure factor already at much smaller n'_u . In this interesting regime, the structure factor is a result of the complex interplay between the two characteristics that are, only for this range of l_u , at the same length scale. As it can be observed in the 2D structure factor in [Figure 5.10 \(B\)](#) and (C), the dominant wavevector is slightly smaller than q_u . This implies a lamellar spacing marginally above the unit cell size l_u .

The intensity of the total structure factor and crosslink structure factor are shown as a

function of n'_u in Figure 5.13 for $l_u = 2 R_{db}$. The crosslink structure factor (S_{xlink} , measured in the phonon model) dominates the total structure factor (S_{total} , measured in SOMA) already at $n'_u \approx 1$. Above $n'_u \approx 30$, the growth of the structure factor follows n'^2_u indicating that the crosslink characteristics dominate. The maximum of the total structure factor is found at $q_u = 2\pi/l_u$.

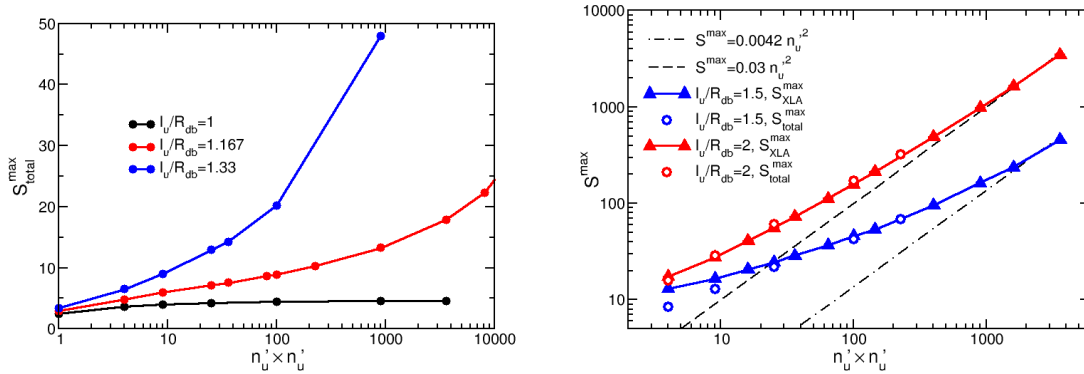


FIGURE 5.13: Left: The intensity of the total structure factor (measured in the phonon model) is shown for intermediate l_u . Right: The structure factor as a function of n'_u is presented for strongly stretched networks at $l_u = 1.5 R_{db}$ and $2 R_{db}$. For n'_u above 30, S^{max} grows like n'^2_u .

5.5 Phase behavior

In [120], the mean-field model was applied in the framework of the standard SCFT to study the phase behavior of regular 2D networks with the topology fixed to a planar square lattice. The main idea of the SCFT approach is to decouple the interaction between the crosslinks. The condition of $\bar{\mathcal{N}} \rightarrow \infty$ in the SCFT approach is imitated by the large number of overlapping 2D networks in SOMA simulations. In the mean-field model, the incompressible homopolymers are found to behave very similar to phantom networks [120]. The key results of the SCFT approach on the phase behavior of regular networks can be summarized as the follows:

- The free energy of the network system as a function of unit cell size l_u possesses two minima for $3 < \chi N_{db} < 10.235$ suggesting a coexistence of two unit cells sizes. The author interprets this as a macrophase coexistence of disordered and ordered state.

- $\chi_c N_{db}$ of the first-order transition gradually decreases as the unit cell size is increased and ends in a critical point at $\chi N_{db} = 3$.

In the following, I first test the predicted macrophase coexistence in [subsection 5.5.1](#). Then, in [subsection 5.5.2](#), the ODT of 2D polymer networks is measured directly in the simulation as a function of l_u and n_u . This will be compared with the RPA prediction making use of the structure factor $S_{total}(q^*, n_u = 30)$. For $\chi N_{db} > 0$, the side lengths of the unit cells perpendicular to the lamellar orientation, denoted by l_u^\perp , are not necessarily equal to the imposed average unit cell size l_u . In the following, it is important to distinguish the two quantities.

5.5.1 Macrophase coexistence

In this section, the macrophase coexistence predicted by the SCFT calculation [[120](#)] will be tested. In Ref. [[120](#)], the free energy per strand is derived for a stretched symmetric diblock copolymer network as a function of the imposed unit cell size l_u for different χN . It is basically the free energy of a deformed network. At $\chi N = 0$, the free energy has a minimum at $l_u = 0$ and increases monotonically with l_u . With χN_{db} increasing above 3, a second local minimum in the free energy apart from zero appears. In this case, the coexisting phases in equilibrium can be obtained by performing the double-tangent construction. The intercepts of the double-tangent line indicate a phase coexistence of two unit cell sizes. For a network with a constant imposed average unit cell size l_u , this suggests the appearance of a lamellar structure with unit cell size $l_u^\perp > 1.3 R_{db}$ in addition to the disordered state with $l_u^\perp < l_u$. Above $\chi N = 10.235$, the second minimum apart from zero dominates, corresponding to a microphase separation with lamellar spacing $\approx 1.33 R_{db}$.

In the following, I search for the predicted macrophase coexistence in the two-phase region, also called the miscibility gap. I choose a relative small imposed unit cell size $l_u = 0.5 R_{db}(1.22 R_g)$. This is because the unit cell sizes l_u^\perp in this system possess the desired bimodal distribution as in the case of the macrophase separation predicted by Ref. [[120](#)]. This will become more clear later when I discuss [Figure 5.15](#). The network is comprised of 30×30 unit cells.

I generate a macrophase-separated system by initializing the polymer networks in an external field to obtain an initial configuration with half of the system equilibrated to the lamellar phase and the other half to the disordered phase. The morphology of the initial configuration is shown in [Figure 5.14 \(A\)](#), it confirms the enforced macrophase-separated state. For $l_u = 0.5 R_{db}$, the macrophase coexistence is predicted for $\chi N_{db} > 6$. If macrophase coexistence is a stable state or a metastable state of the network system, the starting configuration should be able to maintain its structure for a certain range of χN_{db} close to $\chi N = 6$. Because of the presence of the fluctuations in the simulation, the coexistence could be found at a slightly higher value than the prediction of SCFT. After the external potential is removed, I keep l_u constant and increase χN_{db} to 6, 6.5, 7.1, 7.3 and 7.5. In [Figure 5.14](#), the morphology of the network system at various χN_{db} is shown. The typical unit cell size distribution can be found in [Figure 5.15](#). I distinguish between the unit cell size in the direction perpendicular to the lamellar orientation l_u^\perp and parallel to the lamellar orientation l_u^\parallel .

For $\chi N_{db} = 6 - 7.1$, the morphologies suggest isotropic configurations and there exists no direction perpendicular to the lamellar orientation. Identical unit cell distributions are observed in both x - and y -direction, characterized by a single peak center at $l_u = 0.5 R_{db}$. In this range of χN_{db} , the morphologies and the unit cell size distribution indicate disordered states. The macrophase coexistence dissolves after the external field is switched off.

For networks quenched to $\chi N_{db} \geq 7.3$, the morphologies in [Figure 5.14 \(D\)](#) and [Figure 5.19 \(C\)](#) suggest an ordered lamellar structure without disordered regions. In this regime, a bimodal l_u^\perp distribution is observed with one peak close to zero and the second peak at the length scale of the equilibrium lamellar spacing $\approx 1.2 R_{db}$. The lamellar spacing of the ordered structure at $\chi N_{db} = 8$ matches that of the initial configuration. This proves that the lamellar structure in the enforced macrophase separated initial configuration possesses the appropriate lamellar spacing. In the direction parallel to the lamellar orientation, the l_u^\parallel distribution is very similar to that of a disordered state with one peak centered at l_u . Although the predicted simultaneous presence of two unit cell sizes is observed in ordered network systems, there is no hint of macrophase coexistence within the explored range of χN_{db} . In the following, the folded unit cells with $l_u^\perp \approx 0$ will be called the loops and the unfolded unit cells with $l_u^\perp > l_u$ will be called the bridges.

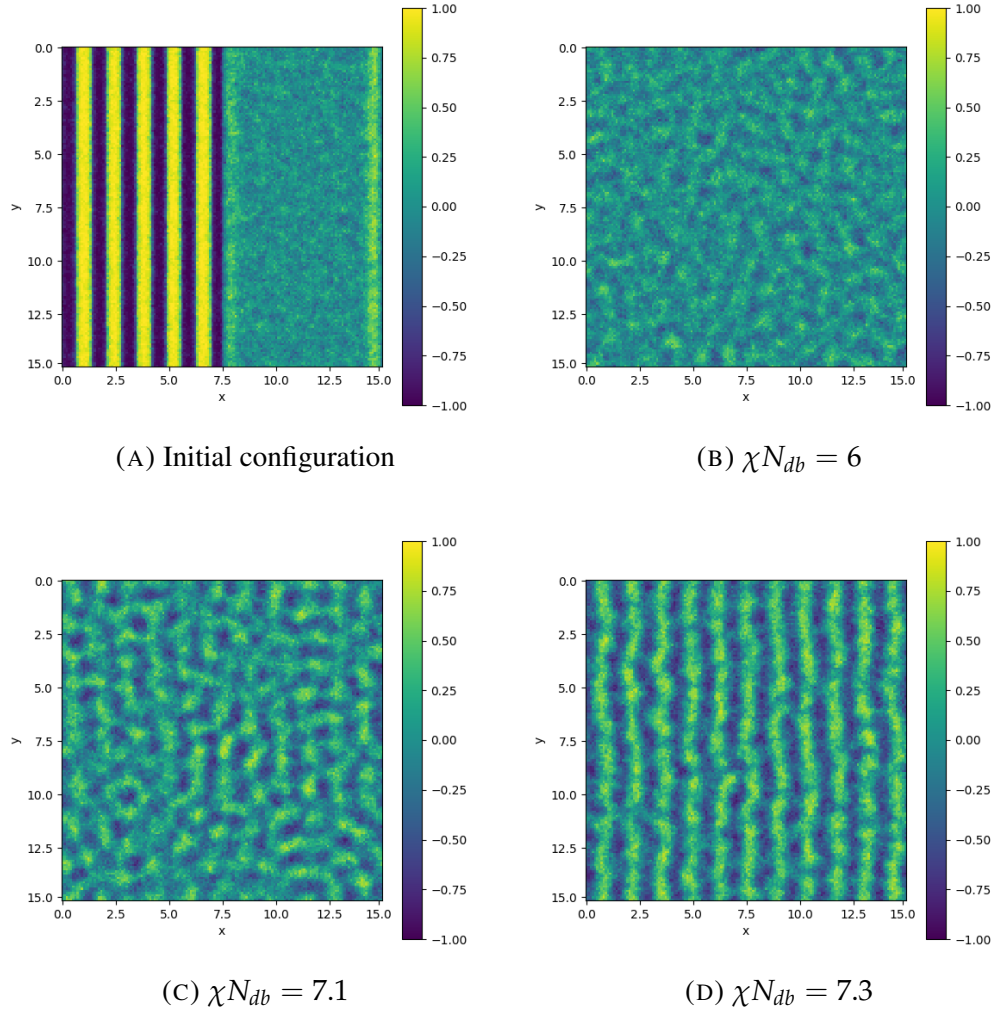


FIGURE 5.14: Density morphologies of macrophase separated copolymer networks with $l_u = 0.5 R_{db}$ are shown for multiple χN_{db} around the predicted macrophase coexistence.

In order to understand the observed simultaneous presence of two unit cell sizes, the spatial correlation between the unit cell sizes is studied as a function of their chemical distance. I consider only the case when the spatial unit cell size and the chemical distance are orthogonal. For the correlation of l_u^\perp (l_u^\parallel), the chemical distance parallel (orthogonal) to the lamellar orientation M_\parallel (M_\perp) is counted. The autocorrelation is defined as the product of l_u^\perp (l_u^\parallel) of two unit cells separated by M_\parallel (M_\perp)

$$C_\perp = \frac{\left\langle l_u^\perp(M_0) \times l_u^\perp(M_0 + M_\parallel) \right\rangle_{M_0}}{\left\langle l_u^\perp(M_0) \times l_u^\perp(M_0) \right\rangle_{M_0}} \quad (5.48)$$

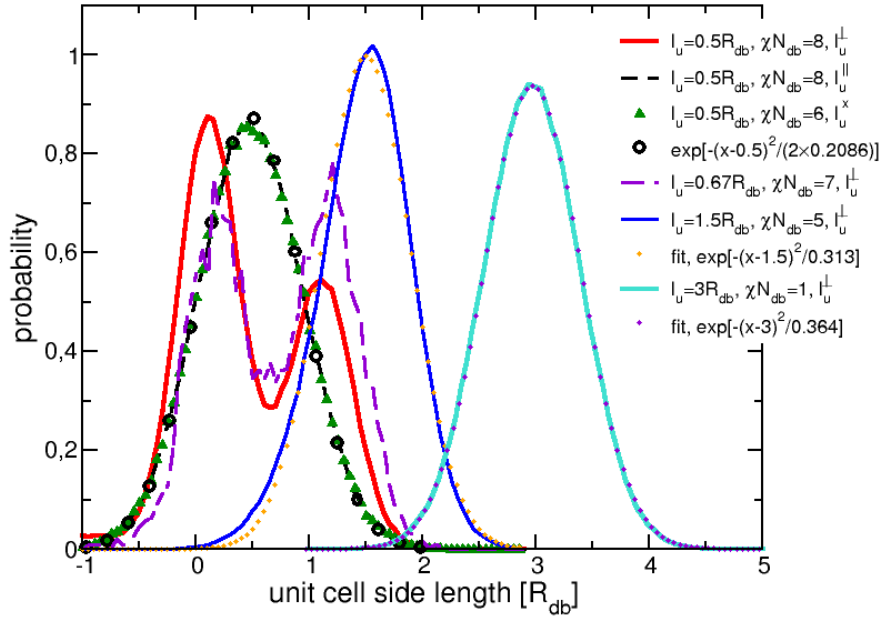


FIGURE 5.15: The unit cell side length distribution of networks with $n_u = 30$ perpendicular (l_u^\perp) and parallel (l_u^\parallel) to the lamellar orientation is shown for $l_u = 0.5 R_{db}$, $l_u = 0.67 R_{db}$, $l_u = 1.5 R_{db}$ and $l_u = 3 R_{db}$. For $l_u = 0.5 R_{db}$ and $l_u = 0.67 R_{db}$ in the ordered state, the unit cells form loops and bridges in the direction perpendicular to the lamellar orientation. At $l_u = 1.5 R_{db}$ and $l_u = 3 R_{db}$, the only peak of the unit cell side length matches the equilibrium lamellar spacing. Two Gaussian distributions with means equal to $1.5 R_{db}$ and $3 R_{db}$ and with fitted variances are shown as well. The figure is reprinted with permission from [77]. Copyright 2022 American Chemical Society.

or

$$C_{\parallel} = \frac{\langle l_u^{\parallel}(M_0) \times l_u^{\parallel}(M_0 + M_{\perp}) \rangle_{M_0}}{\langle l_u^{\parallel}(M_0) \times l_u^{\parallel}(M_0) \rangle_{M_0}}, \quad (5.49)$$

where the average is calculated over all unit cells M_0 in the networks. In the limit of large chemical distance where the unit cells can be considered as uncorrelated, the correlation is given by $l_u^2 = 0.25 R_{db}$. In the disordered state, the autocorrelation can be calculated as a function of the chemical distance M analytically

$$\begin{aligned} C_{\alpha}(M) &= \langle l_u^{\alpha}(M_0) \times l_u^{\alpha}(M_0 + M) \rangle_{M_0} / 0.25 R_{db} \\ &= \frac{2R_{db}^2}{3\pi} \int_0^{\pi/2} dq' \frac{\cos(2q'M)}{1 + \sin(q')}, \end{aligned} \quad (5.50)$$

where α can be x or y .

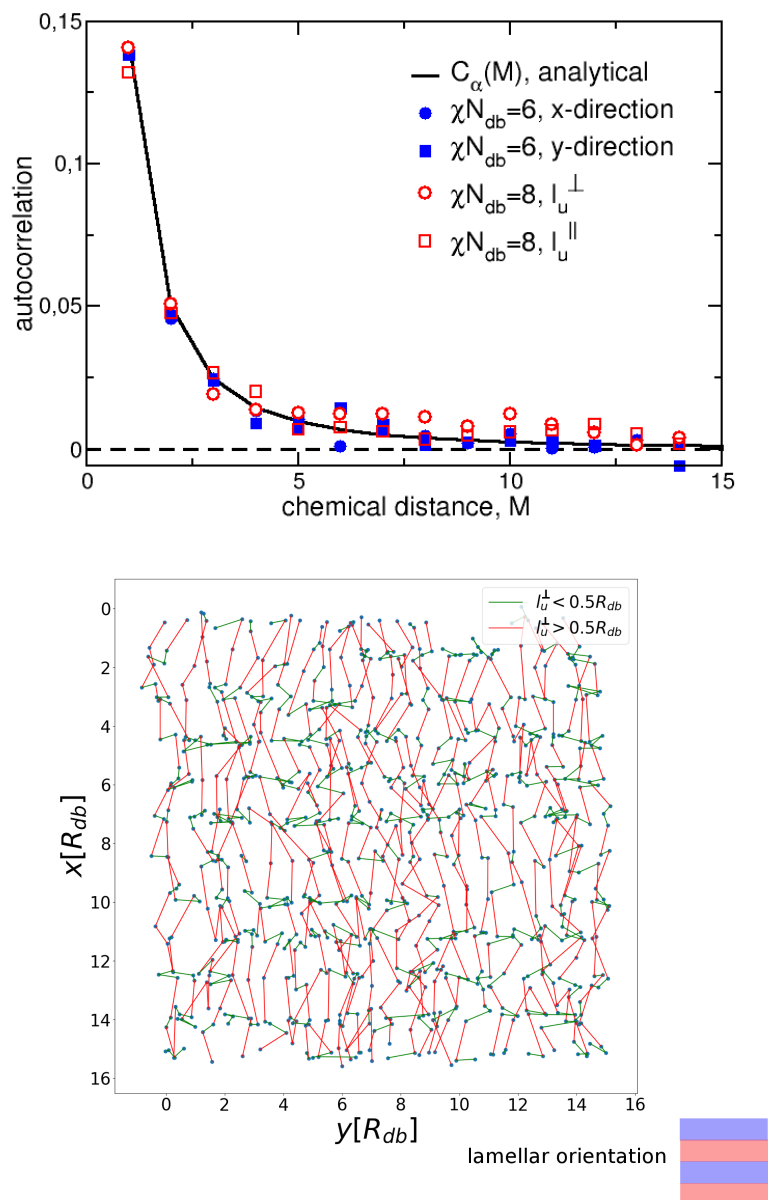


FIGURE 5.16: Top: The autocorrelation between unit cell sizes is shown as a function of their chemical distance. Bottom: The unit cell sizes perpendicular to the lamellar orientation are illustrated for one regular network with $l_u = 0.5 R_{db}$ at $\chi N_{db} = 8$. $l_u^\perp > 0.5 R_{db}$ are shown in red while $l_u^\perp < 0.5 R_{db}$ are shown in green. The figure is reprinted with permission from [77]. Copyright 2022 American Chemical Society.

The correlations are shown in Figure 5.16 (top) for network systems at $\chi N_{db} = 6$ (disordered state) and 8 (lamellar state).

In the disordered state for $\chi N_{db} = 6$, the measured data in both spatial dimensions agrees

with the prediction of the phantom network as given in Equation 5.50. For $\chi N_{db} = 8$ in the ordered state, the networks structure parallel to the lamellar interfaces is unaffected by the lamellae structure because there exists no domains and domain boundaries in this direction. In this case, the autocorrelation function is identical to the disordered system and also agrees with analytical prediction. The unit cell size distributions of these three systems (shown as red square, blue circle and blue square in Figure 5.16 top) have only one peak at the imposed unit cell size.

In the ordered state and in the direction perpendicular to the lamellar orientation (consider l_u^\perp), the unit cell size is characterized by a bimodal distribution with a much larger variance than in the disordered state. Loops and bridges are formed in order to adjust the difference between the imposed average unit cell size and the equilibrium lamellar spacing. According to the simulation data, this autocorrelation also agrees with the data in the disordered state. This indicates that microphase separation does not affect the range of the correlation. The autocorrelation functions drop rapidly with increasing chemical distance and reaches a plateau for $M_\parallel > 4$. This indicates that the typical domain size of the loop-rich area and bridge-rich area is only a few unit cells, suggesting locally formed loops and bridges.

To further address the formation of loops and bridges as a local phenomenon, I show in Figure 5.16 (bottom) the positions of the B -crosslinks as points. l_u^\perp connecting the neighboring unit cells is colored green if it is a loop and red if it is a bridge. As one can see, the loops and bridges are not distributed in macroscopically, spatially separated domains but can be found everywhere with restricted correlation over only a few unit cells.

In addition, the l_u^\perp distributions of ordered networks with imposed unit cell size $l_u = 1.5 R_{db}$ and $l_u = 3 R_{db}$ are also shown in Figure 5.15. For $l_u = 1.5 R_{db}$ and $3 R_{db}$, the l_u^\perp distribution has only one peak at the length scale of l_u . This suggests that the lamellar structure is formed on the template of the imposed A and B -rich domains. Their ordered phase is comprised of unfolded unit cells without the simultaneous presence of two unit cell sizes. I fit the two measured l_u^\perp distributions by a Gaussian distribution

$$f_{l_u}(l_u^\perp) = a_0 \exp \left(- \frac{(l_u^\perp - l_u)^2}{a_1} \right).$$

and obtain for

$$l_u = 1.5 R_{db} : \quad f_{1.5}(l_u^\perp) = \exp \left(- \frac{(l_u^\perp - 1.5)^2}{0.313} \right) \quad (5.51)$$

$$(5.52)$$

and

$$l_u = 3 R_{db} : \quad f_3(l_u^\perp) = \exp \left(- \frac{(l_u^\perp - 3)^2}{0.364} \right). \quad (5.53)$$

In the case of $l_u = 1.5 R_{db}$, the measured l_u^\perp distribution deviates slightly from the Gaussian distribution in the region close to zero. Its peak is found to be slightly above $l_u = 1.5 R_{db}$, which is in good agreement with the peak position of the structure factor $S_{total}(q^*, n_u = 30)$ being slightly below $2\pi/l_u$ as shown in **Figure 5.10** (C). This indicates an equilibrium lamellar spacing larger than l_u and its implication will be discussed in the next section in the context of ODT. For $l_u = 3 R_{db}$, the measured l_u^\perp can be well described by a Gaussian distribution with mean at $l_u = 3 R_{db}$.

Combining these results, I conclude that the macrophase coexistence of ordered and disordered state [120] is not a stable state of 2D regular polymer networks. Instead, I observe the simultaneous presence of unit cells with different side lengths corresponding to locally formed loops and bridges in ordered copolymer networks with small l_u .

5.5.2 Order-disorder transition

Similar to block copolymer melts, copolymer networks microphase separate to avoid disfavored interfaces between A and B segments. Unlike copolymer melts, end-crosslinked networks with the given topology possess an imposed checkerboard pattern with periodicity l_u in x - and y -direction even at $\chi N_{db} = 0$. Once the system undergoes ODT, a lamellar structure with one preferred orientation forms and breaks the symmetry between the two directions.

In this section, the ODT of 2D networks with $n_u = 30$ are directly measured in SOMA. In the simulation, the number of network molecules involved in the simulation grows with increasing l_u to assure a constant density for all simulation systems. I start from configurations

in disordered state and gradually increase the incompatibility in $\Delta\chi N_{db} = 0.1$ steps. The configuration is equilibrated at each χN_{db} stage for 10^6 MC-steps. The ODT in particle simulations can be observed as a discontinuous change of the nonbonded energy per monomer E_{nb} and the composition morphology. An example of an identified ODT during "cooling down" is illustrated in Figure 5.17 for $l_u = 0.33R_e$.

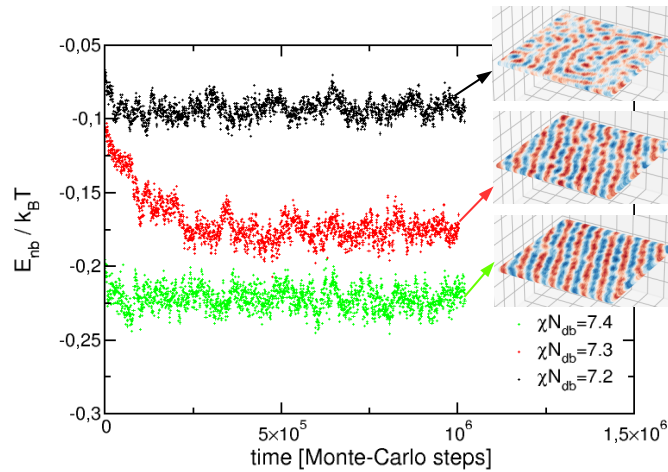


FIGURE 5.17: The nonbonded energy per monomer as a function of MC-steps together with corresponding composition morphologies for $l_u = 0.33R_e$ close to the ODT is shown. $\chi_c N_{db}$ is 7.3 in this example. The figure is reprinted with permission from [77]. Copyright 2022 American Chemical Society.

$\chi_c N_{db}$ as a function of l_u is presented in Figure 5.18. The intensity of the structure factor of the networks can be used to predict χ_c of the ODT according to RPA via

$$\chi_c = \frac{1}{2S_{total}(q^*, n_u)}. \quad (5.54)$$

The SOMA result of ODT (black curve) is compared with the RPA prediction (red curve) using $S_{total}(q^*, n_u)$. The RPA prediction for $n_u = 30$ is qualitatively in good agreement with the simulation result. The measured $\chi_c N_{db}$ is slightly higher than the RPA prediction as a result of the presence of the fluctuations. A reduction of $\chi_c N_{db}$ is observed with increasing l_u . This is caused by the increasing polarization of the system originating from the spatial separation of distance $l_u/2$ imposed between the A - and B -rich domains by end-crosslinking A -blocks with A and B -blocks with B .

In Figure 5.18, I also present the RPA prediction of the ODT using $S_{total}(q^*, 1)$ and $S_{total}(q_u, 1)$ to demonstrate the impact of neglecting correlations between unit cells as assumed by the mean-field model. As shown, assuming $n_u = 1$ results in considerably larger values of $\chi_c N$ of the ODT for all studied l_u . This deviation was already implied by the underestimated structure factor for $n_u = 1$, which corresponds to the case of a single unit cell embedded in a 30×30 network. One should note, that the ODT obtained with RPA in the scenario of $n_u = 1$ is still different from the spinodal curve provided by Ref. [120]. This is because Ref. [120] considers the stability of the free energy with respect to stretching (it is calculated as a function of l_u), whereas in the RPA approach, the free energy is expanded with respect to the composition ϕ .

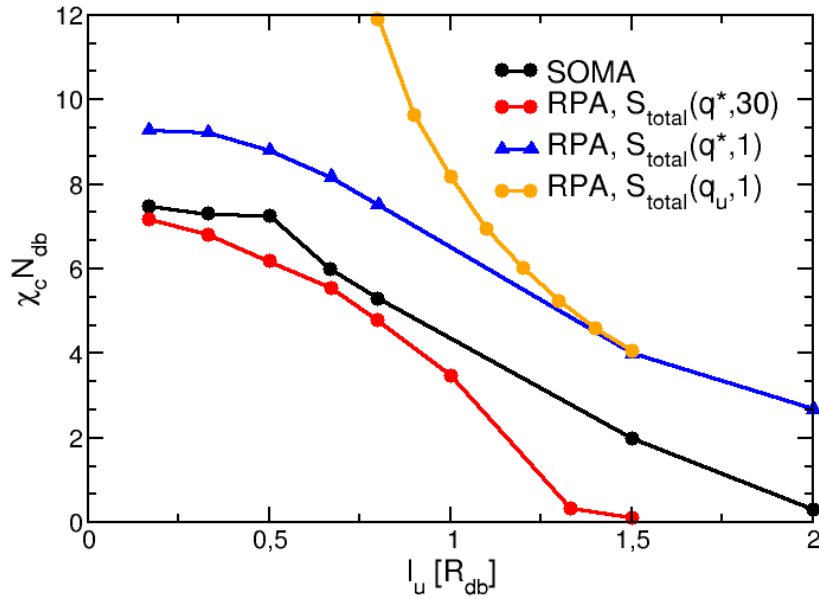


FIGURE 5.18: χN_{db} of the ODT is measured in SOMA and compared with analytical RPA predictions. The simulation data are obtained from the average of five independent runs, which provide nearly identical results. This indicates that the error range is smaller than $\Delta\chi N_{db} = 0.1$.

The morphology of the networks in the ordered state varies with the unit cell size l_u as a result of the interplay between the diblock characteristics and the crosslink characteristics of the network. The analytical models for phantom networks are not able to provide information about morphologies in the ordered state, thus we rely on the SOMA simulation to investigate the local structure underneath the lamellar structure. In accord with the three outlined regimes

of the structure factor, three typical ordered morphologies depending on l_u are shown in [Figure 5.19](#).

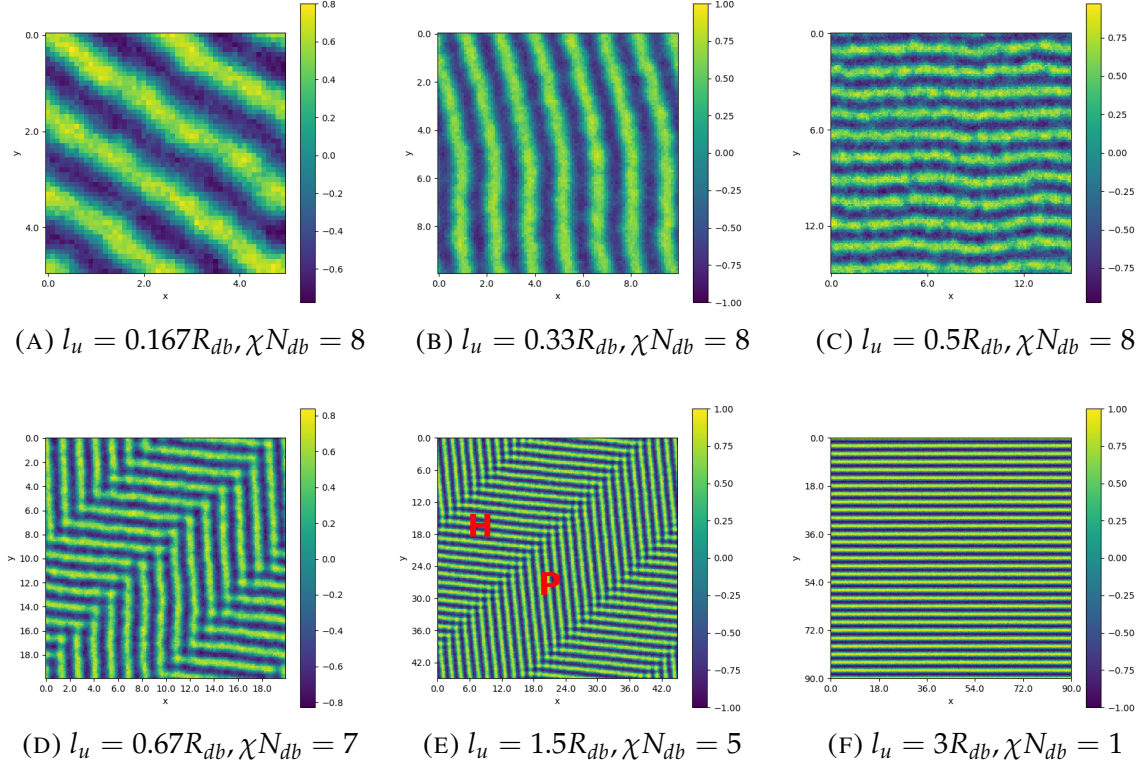


FIGURE 5.19: The composition of the 2D polymer network in ordered state is shown for six unit cell sizes. For compressed polymer networks $l_u \leq 0.5 R_{db}$, the morphology in ordered state is similar to that of a multiblock copolymer melt. For the intermediate range of $0.6 R_{db} < l_u \leq 1.5 R_{db}$, a unique multidomain structure is observed. For strongly stretched polymer networks $l_u > 2 R_{db}$, a lamellar structure is present for any non-zero χN_{db} .

For $l_u \leq 0.5 R_{db}$ and $n_u = 30$, the morphologies are presented in [Figure 5.19](#) (A), (B) and (C). The structure factor as well as the phase behavior of the network is dominated by the diblock characteristics. As observed before, the structure factor of compressed networks at $\chi N_{db} = 0$ is typically isotropic. This corresponds to the fact that the lamellar structure is not necessarily aligned with the unit cell orientation in the network. The ordered morphology is characterized by a lamellar spacing much larger than l_u which leads to a number of lamellae n_L smaller than n_u . The large mismatch between l_u and the lamellar spacing is resolved by the formation of loops and bridges. In this regime, the ordering process is similar to that of a multiblock copolymer melt characterized by two important features [127–130]: (i) the existence of loops and bridges in the ordered state and (ii) $\chi_c N_{db}$ of the ODT converges to ≈ 7.5 for large block numbers. $\chi_c N_{db}$ converges towards a value that is close to 7.5 for

$l_u \rightarrow 0$ and thus confirms their similarity to multiblock copolymer melts. The bimodal l_u^\perp distribution in Figure 5.15 confirms the loops and bridges in ordered polymer networks for small l_u . For the maxima at $l_u^\perp = 0$, the unit cells fold back onto themselves like loops in ordered multiblock copolymer. For the bridges corresponding to the maxima at $l_u^\perp = l_u^*$, the unit cells are flat and stretched across a domain. Furthermore, the network system is able to control the equilibrium lamellar spacing by adjusting the relative weight of loops and bridges. An illustration of loops and bridges can be found in Figure 5.20. As one can see in

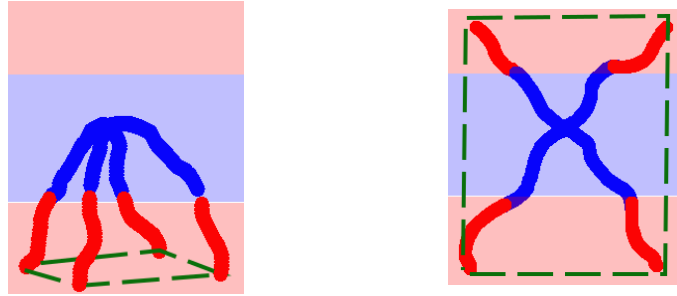


FIGURE 5.20: A loop and a bridge

Figure 5.15, loops are predominately formed for very small l_u . With increasing l_u , the loop fraction decreases.

For strongly stretched networks, the morphology of the ordered state is shown for $l_u = 2 R_{db}$ in Figure 5.19 (F). Only bridges are formed in this regime. The lamellar orientation is found to be aligned with the unit cells orientation in the network. The crosslink characteristics govern the phase behavior in this regime, resulting in a lamellar structure with periodicity l_u . The number of lamellae matches the number of unit cells. The squared shape, size and the orientation of the unit cells retain in this case. The repulsion between A and B monomers reduces the square symmetry of the checkerboard pattern of a single network to a stripe pattern of the collective composition field of multiple networks as demonstrated in Figure 5.21.

Between the two limits $0.5 R_{db} < l_u < 2 R_{db}$, the ordered morphology is characterized by a novel multidomain structure with perpendicular lamellar orientations. The compositions are shown in Figure 5.19 (D) and (E) for $l_u = 0.67 R_{db}$ and $1.5 R_{db}$. In the former case, the two peaks of the bimodal l_u^\perp distribution have similar amplitude, indicating the loops and bridges are formed with comparable probability. In the latter case, the probability of loops is negligible.

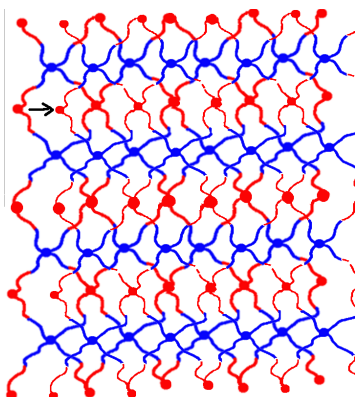


FIGURE 5.21: The incompatibility between unlike species drift overlapping network molecules apart from each other and leads to the formation of *A* and *B* stripes.

In this regime, the unit cells are, in addition to the occasional formation of loops and bridges, slightly deformed with respect to the squared shape affine to the periodic boundary conditions. The equilibrium lamellar spacing is slightly larger than the unit cell size l_u . This small mismatching between the imposed unit cell sizes and the lamellar spacing is resolved by a deformation and rotation of the unit cells. Making use of the positions of the A-crosslinks, the shape of the unit cells can be reconstructed. The measured unit cell shape averaged over unit cells inside each domain is shown in Figure 5.22 (A) for domain *P* and *H* (as denoted in Figure 5.19). The bottom figures illustrate the relation between unit cell shape and the lamellar morphology. The geometry of the unit cells indicate an extension of the unit cell

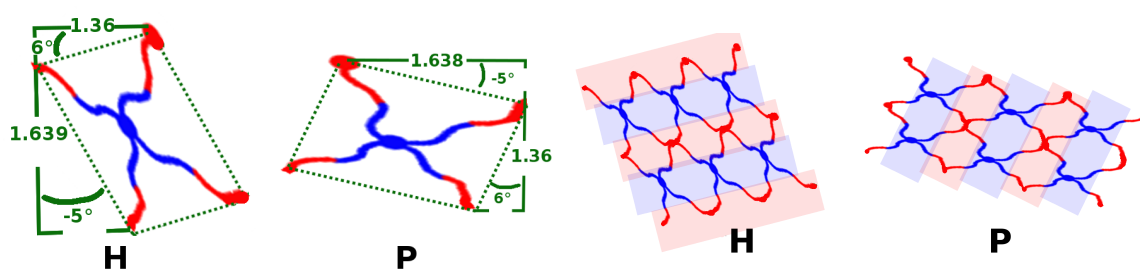


FIGURE 5.22: (A): Geometry of the unit cell shape in two domains *H* and *P*. (B): The underlying arrangement of the unit cells in the lamellar morphology. The figure is reprinted with permission from [77]. Copyright 2022 American Chemical Society.

size perpendicular to the lamellar orientation leading to a reduced number of lamellae and $l_u \lesssim d_L$. The unit cells are compressed horizontally to the lamellar orientation enforced by the incompressibility constraint. Because of the fixed square-shaped boundary conditions, this

deformation cannot be built equally for all unit cells and this is the origin of the multidomain structure. This observation is true for domains with different lamellar orientation.

At this point, I want to briefly address the similarity between the networks in [Figure 5.19 \(D,E\)](#) and liquid-crystalline elastomers. The latter one is a class of materials characterized by unique properties resulting from the interplay between the network elasticity and the liquid-crystalline degrees of freedom. During their ordering process, they deform and rotate to form irregular stripe textures [\[131, 132\]](#). This is similar to the observed unit cell deformations during the microphase separation of regular networks in the presence of elasticity. Within a universal description of nematic elastomers, the free energy of the system can be expressed as a function of the deformation and rotation of the mesogens [\[133\]](#). The free-energy expression in Ref. [\[133\]](#) allows a direct comparison of the free energy of different possible morphologies and thus the prediction of the number of domains as well as the orientations of the lamellar domains.

5.6 Summary

The structure and structure formation in 2D regular networks made of symmetric diblock copolymers were investigated applying two analytical approaches: (i) the 2D phonon model and (ii) the mean-field model (originally introduced in Ref. [\[120\]](#)) and two particle-based simulations. The first simulation program is a truly 2D MC simulation which only accounts for the junction points connected via effective harmonic springs that are equivalent to the polymer strands. The second simulation program is SOMA, where multiple overlapping, quasi-2D polymer networks are embedded in a 3D simulation box. In SOMA, the monomer discretization along the polymer strands as well as the incompressibility constraint are taken into account. In both simulation programs, the opposite sides of the networks are connected via bonds across the periodic boundary conditions.

The phonon model and the mean-field model were applied to compute the distribution of the crosslinks in a 2D polymer network comprised of $n_u \times n_u$ square-shaped unit cells with side length l_u . The phonon model accounts for the full correlation between the crosslinks, whereas the mean-field model assumes independent crosslinks. The advantage gained by the

mean-field approximation is the decoupling of the interactions between different crosslinks. I tested the accuracy of the strand length distribution and the block distance distribution as a function of the chemical distance derived from the two analytical approaches against the simulation results and found the following results: First, the comparison between SOMA at $\kappa N_{db} = 0$ and the MC simulation suggests that the monomer discretization has no effect on the distribution of the crosslinks. Second, the phonon model and the mean-field model predict the same strand length distribution which is also in agreement with my simulation results and with theories [114]. Third, the mean-field model predicts a constant variance of the block distance independent of the chemical distance which deviates significantly from the simulation results for $n_u > 1$, whereas the phonon model successfully describes the non-trivial block distance variance as a function of the chemical distance in the absence of the incompressibility constraint. Fourth, the incompressibility constraint suppresses the amplitude of fluctuations at large length scales of the order of the simulation box size and has only insignificant impact on length scales below five unit cells.

Then, I investigated the structure factor and the phase behavior of 2D networks. The macrophase coexistence of disordered state and lamellar state predicted by the SCFT approach in Ref. [114] was not observed in the simulation. I found that the observed simultaneous presence of two different unit cell sizes for a fixed l_u in fact corresponds to the locally formed loops and bridges. I divided the structure factor into contributions from the crosslink characteristics and the diblock characteristics that are important on two (typically different) length scales. I first computed the crosslink structure factor using the crosslink positions derived from the phonon model. The intensity of the crosslink structure factor was found to be proportional to the number of scattering centers, *i.e.* n_u^2 . The total structure factor and the ODT of 2D diblock copolymer networks were then measured. I found that χN_{db} of the ODT predicted by RPA using the intensity of the total structure factor is in good agreement with the SOMA simulation result. The ODT measured directly in SOMA is slightly higher than the RPA prediction because of the presence of fluctuations. In general, the phase transition in 2D regular networks is associated with the breaking of the square-shaped domains with periodicity l_u in x and y -direction and the formation of lamellae which have a smaller interfacial area compared to the checkerboard pattern. According to their unit cell size l_u , I divided regular networks into three typical classes.

(i) For small unit cell sizes, the diverging contribution ($\propto n_u^2$) from the crosslinks to the total structure factor is minor for the range of moderate n_u covered by the simulations in this study. The intensity of the total structure factor first increases slightly with n_u and reaches a plateau above $n_u > 5$. In this regime, the total structure factor is dominated by the diblock characteristics of the network resulting in a lamellar spacing much larger than l_u and the number of lamellae is much smaller than n_u . The ODT is measured at $\chi N_{db} \approx 7.5$ in SOMA similar to the ODT of multiblock copolymer melts.

(ii) With increasing l_u , the crosslink characteristics become important already at smaller n_u covered by the simulations in this work. In this case, the transition from the diblock characteristics to the crosslink characteristics can be observed as a shift of the nearly isotropic dominant wavevector towards larger values until it reaches the length scale of the imposed unit cell size $\vec{q}_u \approx (\frac{2\pi}{l_u}, 0)$ and $(0, \frac{2\pi}{l_u})$ (anisotropic). For the intermediate l_u and $n_u = 30$ studied here, the complex interplay between the two characteristics leads to an equilibrium lamellar spacing slightly above the unit cell size. The difference between the lamellar spacing and the unit cell size is adjusted by an expansion of the unit cells perpendicular to the lamellar orientation and a compression along the lamellar orientation. This deformation cannot be affine because of the fixed square-shaped boundary conditions. This results in a novel multidomain structure of the ordered morphologies. As I pointed out, this unique morphology bears a resemblance to nematic elastomers.

(iii) For strongly stretched networks, the total structure factor is dominated by the crosslink characteristics already at $n_u = 1$ and the intensity scales according to n_u^2 . An ordered lamellar structure with periodicity l_u is formed already for very small χN_{db} .

Chapter 6

Phase behavior of random copolymer networks

Some content of this chapter has been published in *Macromolecules* with the title “Phase Separation of Randomly Cross-Linked Diblock Copolymers” [134]. Some parts of this chapter are results of close collaboration with Marcus Müller and Annette Zippelius.

In the previous chapter, the structure and structure formation of end-crosslinked 2D regular polymer networks was studied. I discussed interesting mechanical properties such as the elasticity of 2D regular networks and investigated how they affect phase transitions in 2D copolymer networks. The unique structural specialties of copolymer networks studied in the previous chapter are more or less universal. In this part of the thesis, I consider randomly crosslinked 3D polymer networks formed by connecting symmetric diblock chains via covalent bonds. Unlike regular 2D networks with fixed topology, the mechanical strength of random networks can be varied by adjusting the number of crosslinks.

Numerous studies on network structure and elasticity can be found in the literature [81, 99, 101, 135–142]. In this study, I apply the particle-based Monte-Carlo simulation SOMA to study gelation and microphase separation of randomly crosslinked symmetric diblock copolymers for various crosslink densities and preparation conditions. In the simulations, the process of crosslinking is achieved via a stochastic algorithm that assigns irreversible connections to monomer pairs based on their geometrical distance. The added crosslinks are equivalent to the bonds along the molecular backbones and are also described by the

beads-spring model. In this study, the bonds are allowed to cross each other and thus the entanglement effect is not included. The instantaneous formation of crosslinks follows the Deam-Edwards distribution [142] *i.e.*, the probability of a bond being formed between segment i at position \vec{r}_i and segment j at position \vec{r}_j is given by

$$P_{\text{crosslink}} = A \exp \left(-\frac{3}{2b^2} (\vec{r}_i - \vec{r}_j)^2 \right) \quad (6.1)$$

with b the statistical segment length. The entirety of generated crosslinks will be described as the crosslink configuration \mathcal{C} . Because of the stochastic procedure of crosslinking, each network realization is unique and is parametrized by one specific crosslink configuration. The probability of a crosslink configuration can be expressed as

$$P(\mathcal{C}) \propto A \exp \left(-\frac{3}{2b^2} \sum_{\text{all pairs}} (\vec{r}_i - \vec{r}_j)^2 \right). \quad (6.2)$$

Configurations with different crosslink density can be generated by varying the parameter A . The crosslink density p is defined as the total number of crosslinked monomers divided by the total number of polymers n , namely

$$p = \frac{\# \text{crosslinked monomer}}{n}. \quad (6.3)$$

One should note that one established bond is shared by two crosslinked monomers and thus counts as two crosslinks. During crosslinking, the present molecular backbones in the system will not be modified. The crosslinks are allowed to be formed between two neighboring molecules as well as between monomers within the same molecule. The crosslink configuration also depends on the randomly organized structure of the initial linear chains. In the following, the initial crosslink configuration will be referred to as the preparation state. Since the size of the simulation box is always finite, periodic boundary conditions are applied to mimic a macroscopic system and avoid boundary effects. In such a system, chains percolate if their extent reaches both opposing sides of the simulation box and the cluster is connected to itself across periodic boundary conditions. In simulation studies with percolating clusters, the bonds (*i.e.* the distance between monomers) must be evaluated in the minimum image convention.

The phase diagram of interest includes two phase transitions: Gelation, controlled by the crosslink density p , and the ODT, directed by the Flory-Huggins parameter χ . The Flory-Huggins parameter of the measurement ensembles will be referred to as χ_m . Depending on $\chi_p N$ of the preparation state, the random crosslinks enhance the stability of the disordered or the periodically ordered state over a larger range of incompatibilities $\chi_m N$, because the irreversible bonds impart a memory of the structure that existed at their formation. Knowing the amount of crosslinking required to retain a microphase-separated or disordered structure at thermal dynamical conditions that considerably differ from the preparation state is also practically useful for stabilizing the preparation state, which may only be metastable without crosslinks.

This chapter is arranged as follows: In [section 6.1](#), a short summary of the background of the two phase transitions is presented. Then I determine the percolation threshold with finite-size analysis in [section 6.2](#). The localization length ξ is measured in [section 6.3](#) as a function of the crosslink density and its critical behavior at the percolation threshold is examined. Then, I study the stability of crosslinked structure against “warming up” in [section 6.4](#). Lastly, I provide a 3D diagram that shows critical $\chi_c N$ of the ODT as a function of the crosslink density p and the Flory-Huggins parameter $\chi_p N$ in the preparation state in [section 6.5](#).

6.1 Theoretical background

6.1.1 Sol-gel transition

The sol-gel transition or gelation describes the formation of a macroscopic network of polymers which are randomly distributed in space. During this process, components that are free to move in the liquid state (the sol phase) become connected across the entire system and gain elasticity (the gel phase). This technique enables the synthesis of solid phase materials through gelation instead of crystallization or glass formation.

Percolation models [[143–146](#)] have been introduced to describe connectivity in random networks. The application of percolation theory can not only be found in polymer physics

or structural chemistry but also in diverse areas such as sociology and information theory. A network is called percolating (or macroscopic, infinite) if there exists a path that reaches all sides of the system. The extent of clusters and thus the probability of the presence of an infinite network grows with crosslink density. In the theory, there exists a critical crosslink density (denoted by p_c) below which the probability of finding an infinite network is 0 and above which the probability is always 1. Since the clusters generated in this work are finite, the measured sol-gel transition will be smeared out. This difficulty in the measurement of the percolation threshold is known as the finite-size problem.

6.1.1.1 Finite-size problem

Generally, the finite-size problem [147, 148] describes the fact that many physical quantities are size dependent in simulation studies. Only at the limit of infinitely large systems, the measurement of the quantity becomes accurate. This introduces systematic errors in the results since it is impossible to simulate infinitely large systems. This effect often has impact on phase transition studies and causes shifting or scaling on phase transition phenomena. The measurement of the percolation threshold in our particle-based simulation SOMA also suffers from the finite-size problem, so that it is difficult to identify one critical point of phase transition. One approach to extrapolate from finite system size to infinite system size is to perform a finite-size scaling analysis [149, 150] and study the size-dependent scaling behaviors. In the measurement of the percolation threshold, the scaling analysis consists of measuring the percolation probability as a function of crosslink probability and repeating this for several different system sizes. The percolation probability is defined as the probability of a system with crosslink density p to contain at least one percolating cluster. For an infinitely large system, the percolation probability is a step function with respect to the crosslink density. Above p_c , one is certain to have a percolating cluster. When the system size is decreased, the threshold is smeared out. Instead of one critical value, the percolation transition takes place within a range of crosslink densities. In the scaling analysis, the percolation probability of different system sizes cross at a common point which is considered to be an accurate estimation of the percolation threshold.

6.1.1.2 Gel fraction

In the simulation, the gel fraction Q is defined as the fraction of monomers in the percolating macroscopic cluster. In a crosslinked copolymer system, the fraction $(1 - Q)$ of monomers is delocalized, and the remaining fraction of particles Q fluctuates following a Gaussian distribution around a mean position. Especially for small crosslink densities, the fraction of components in the free chains that are not connected to the percolating cluster is significant and has large impact on the mechanical properties and the dynamics of the system. Since the major interest of this study is the unique features of the network which is constrained by the connectivity, the fraction of free chains must be measured in order to estimate their influence on the structure formation. Below the percolation threshold, the gel fraction is zero. In gel phase, the fraction of free chains decreases and the gel fraction grows with increasing crosslink density. In the mean-field model of gelation, the gel fraction can be estimated with the recurrence relation for the probability of a site not connected to the gel [19, 151]. For any crosslink density $p > p_c$, the gel fraction Q can be obtained by solving

$$1 - Q = \exp \left(-\frac{pQ}{p_c} \right). \quad (6.4)$$

6.1.1.3 Localization length

For a weakly crosslinked system in the sol phase, there exists no percolating macroscopic cluster and all monomers, even if small clusters of particles are formed, can diffuse freely in space. For networks above the percolation threshold in the gel phase, monomers belonging to the percolating cluster are localized because the crosslinks restrict their movement and only allow fluctuations around a mean position. The impact of the crosslinks on the structure and structure formation of the network can be outlined by their constraints on the particle mobility captured by the localization length ξ . The localization length is defined as the extent of fluctuations of segments. The localization length of a monomer is calculated in fully equilibrated configurations as

$$2\xi^2 = \lim_{t \rightarrow \infty} g_1(t) = \lim_{t \rightarrow \infty} \left(\vec{r}(t) - \vec{r}(0) \right)^2, \quad (6.5)$$

where $g_1(t)$ is the Mean-Squared Displacement (MSD). Since the center of mass of the entire network can diffuse during the simulation as a result of its finite mass, the positions $\vec{r}(t)$ and $\vec{r}(0)$ must be computed in their center-of-mass frame. The probability distribution of ξ captures the kinematics of the monomers and thus reflects the deformation ability of the crosslinked network. It is an important length scale for describing the structure formation of polymer networks.

In the simulation, the localization length is computed taking only particles belonging to the percolating chain into account. In percolating networks, the confinement of the monomers results in a finite localization length. As for phantom networks, the strands are allowed to pass through each other. For weakly crosslinked systems, the fraction of junction points is small and the strands between junction points remain flexible with large fluctuations retained. In the strongly crosslinked regime, the strands are short and have little possibility to fluctuate. As a result, the localization length declines with increasing crosslink density as will become clear later in this chapter.

Different realizations of random networks can have distinct crosslink configurations even if they are generated with the same crosslink density. Although these networks are very irregular on the length scale of crosslink blocks, they can be considered as homogeneous and isotropic on macroscopic scale. Therefore, the localization lengths exhibit the same distribution at a fixed crosslink density, and the mean localization length can be used to parametrize the topological constraint in a random polymer network without paying attention to the exact crosslink configuration. The measurements I perform will not be restricted to a specific crosslink configuration, but averaged over several realizations at each crosslink density. The exact amount of independent crosslink configurations differs and will be provided in each subproject.

6.1.2 Order-disorder transition

The second phase transition of our interest is the ODT controlled by the Flory-Huggins parameter $\chi_m N$, which is inversely proportional to temperature. The microphase transition of linear diblock, triblock and multiblock copolymers have been repeatedly studied [127, 128,

[152]. In the mean-field treatment, the ODT of symmetric diblock copolymers is known to be a second-order transition at $\chi_{\text{mf}}^{\text{diblock}} N \approx 10.5$. Including composition fluctuation increases the ODT threshold and the phase transition becomes a first-order one [27].

Similar to block copolymer melts, the polymer network microphase separates to mitigate the energetically unfavorable interfaces between *A* and *B* segments. The effect of crosslinks on the phase separation of multicomponent polymer systems was first investigated by de Gennes [153] on homopolymer blends. As he found out, the irreversible crosslinks generated in the disordered state hinders macrophase separation and the homopolymer mixture forms microphase-separated domains. Experimental studies [154] and simulation studies [155] on crosslinked symmetric homopolymer blends revealed that the monomers in the network can rearrange on a considerable length scale and the sizes of microdomains are typically much larger than the extent of the constituent strands of the network. Wald [156] provided a schematic phase diagram of the ODT of crosslinked symmetric homopolymer blends as a function of crosslink density for a fixed preparation condition. His diagram of $\chi_c N$ of the ODT qualitatively suggests the existence of four phases: disordered liquid, disordered gel, ordered liquid and ordered gel. In [102], the properties of diblock copolymer melts that are randomly crosslinked in the ordered state are studied at different $\chi_m N$. The authors point out that a disordered state can be found for a large range of crosslink densities above the percolation threshold when decreasing $\chi_m N$. The findings common to all these studies, which are important for my study can be summarized as follows: (i) the crosslinks enhance the stability of the structure that existed at their formation, (ii) crosslinks only partly fix the structure of the preparation state, even for crosslink densities well above the percolation threshold. Comparable phase states as suggested for homopolymer blends are expected for randomly crosslinked diblock copolymers, but this has never been worked out precisely both for homopolymers and for diblock copolymers. In this study, I aim to measure an accurate phase diagram, quantitatively evaluating $\chi_c N$ of the ODT as a function of the crosslink density and the preparation state.

I apply particle-based simulation tool SOMA to carry out the simulation to determine the ODT of the polymer network. The microphase separation of symmetric diblock copolymer melts has been well investigated in SOMA. For $N = 32, \kappa N = 30$ and $\sqrt{N} = 128$, $\chi_c^{\text{diblock}} N$ of the ODT is measured to be ≈ 14.6 which is in agreement with earlier studies [32].

The equilibrium morphology of symmetric diblock copolymers is a lamellar structure with a characteristic length scale called the lamellar spacing, which parametrizes the periodicity. For crosslinked polymer networks, another important length scale, the localization length, is present because of the connectivity. The interplay between the two length scales plays an important role in the microphase separation of diblock copolymer networks.

In the simulation, I identify the ODT by a change of the non-bonded energy to a lower value when the transition to the ordered phase occurs, as well as a change to a higher value at the transition from ordered to disordered state. For non-zero $\chi_m N$, the incompatibility part of the free energy $\propto \chi_m N [\hat{\phi}_A(c) - \hat{\phi}_B(c)]^2$ decreases to strongly negative values if A/B -rich domains are spatially separated.

6.2 Percolation threshold

To locate the sol-gel phase transition, the probability of a system containing percolated molecules at various crosslink densities is measured. This probability will be referred to as percolation probability in the following. In the simulation, the percolation probability can be determined as the ratio between the number of configurations containing at least one percolating chain and the total number of configurations. In infinite systems, the percolation probability as a function of crosslink density is a step function with transition from zero to one at the percolation threshold p_c . As discussed in [subsection 6.1.1](#), the percolation threshold measurement in real simulations is strongly affected by the finite-size problem. Because of this, the percolation probability curves measured in finite systems are not sharp enough to locate one critical crosslink density p_c . A finite-size analysis is performed to eliminate the impact of the finite system size. This means, the percolation probability is measured for several system sizes and their crossing point is located. I use three system sizes in the simulation: $4 \times 4 \times 4 R_e^3$, $5 \times 5 \times 5 R_e^3$ and $6 \times 6 \times 6 R_e^3$. The invariant degrees of polymerization for all systems are set to $\sqrt{N} = 128$. For each system size, the percolation probability is obtained with 100 – 300 independent crosslink configurations.

I measure the intersection point of the three percolation probability curves and find the percolation threshold is about $p_c \approx 1.12$. The percolation probability at this point is around

1/2. In other simulation studies [139, 155, 157], a similar percolation threshold was estimated. I will use the quantity p/p_c to parametrize the crosslink density in the following.

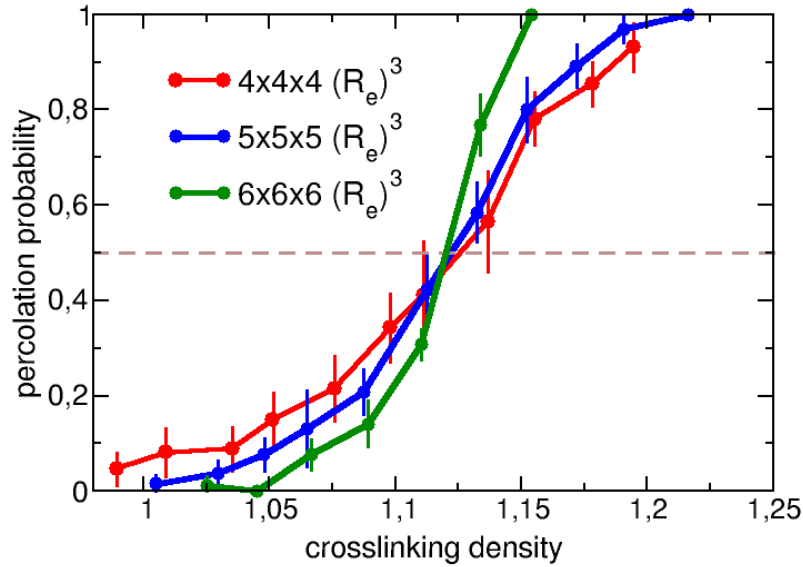


FIGURE 6.1: The percolation probability measured in three different system sizes is shown depending on the crosslink density. The three curves cross at crosslink density $p \approx 1.12$. The percolation probability at this point is about 0.5. The figure is reprinted with permission from [134]. Copyright 2022 American Chemical Society.

6.3 Localization length

In percolating macroscopic molecules, the particles in the cluster are localized and their motion are governed by fluctuations about an equilibrium position \vec{r}_{i0} . In the Gaussian localization model, the probability distribution takes the form

$$P(\vec{r}_i) \propto \exp \left[-\frac{3}{2\tilde{\xi}_i^2} (\vec{r}_i - \vec{r}_{i0})^2 \right]. \quad (6.6)$$

The extent of these fluctuations is described by the localization length $\tilde{\xi}$. According to the theory, the localization distribution can be described by a universal function close to the percolation threshold [136, 151, 158]. One should note that in the literature, the localization length is sometimes defined by a factor three smaller than in our definition. In that case, the

probability distribution of localized particles becomes

$$P(\vec{r}_i) \propto \exp \left[-\frac{1}{2\zeta_i^2} (\vec{r}_i - \vec{r}_{i0})^2 \right]. \quad (6.7)$$

In this study, we stick to the definition of ζ as in Equation 6.6 in accordance with the definition of R_e .

In this simulation study, the localization length is measured with individual monomers connected to the percolating cluster. Since I aim to investigate the collective behavior of random networks (such as the microphase separation), the quantity of interest is the distribution of localization lengths of all monomers in a given polymer network.

Since the gel fraction of weakly crosslinked networks is typically much smaller than one, the size of the networks in the simulation needs to be addressed as well. Close to the percolation threshold, the gel fraction shrinks. Analytically, the gel fraction can be obtained by numerically solving [151]

$$1 - Q = \exp \left(-\frac{pQ}{p_c} \right) \quad (6.8)$$

The gel fraction measured in the simulation as well as the analytical prediction are shown as a function of p/p_c in Figure 6.2. The simulation results match the theoretical prediction very well. This agreement confirms the similarity between the simulated object and the one described by the theory.

I measure the long-time limit of the MSD of segments, $2\zeta_i^2 = \lim_{t \rightarrow \infty} \langle [\mathbf{r}_i(t) - \mathbf{r}_i(0)]^2 \rangle$ in the center-of-mass reference frame. Close to the percolation threshold, the measurement of the localization length distribution is very difficult because of the following reasons. Firstly, the monomers in loosely crosslinked networks are more flexible and are allowed to move in a larger region. This leads to a larger fluctuation of the localization length and a longer evolution time before the maximal displacement is explored. Secondly, the limited amount of monomers in the network results in a smaller sample size and thus further increases the fluctuation of the measured ζ^2 distribution. To overcome these two problems, the localization length distribution is computed from the average of ten snapshots of each configuration.

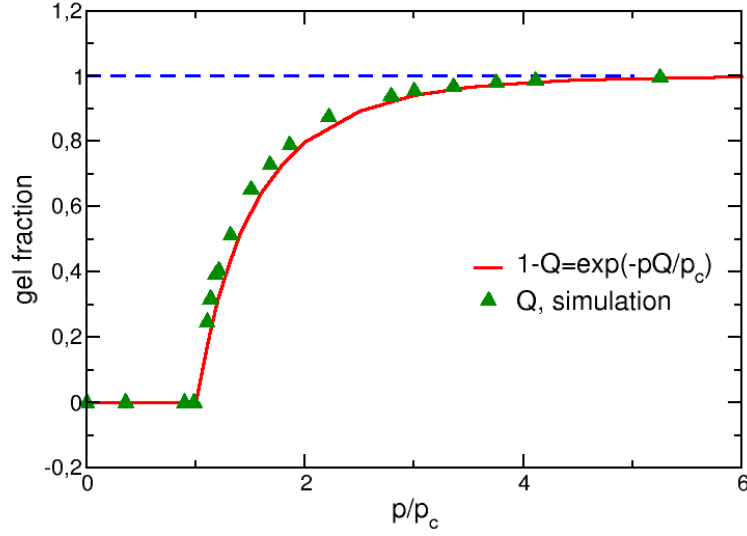


FIGURE 6.2: The gel fraction Q measured in the simulation is shown as a function of p/p_c and compared with the analytical prediction. The figure is reprinted with permission from [134]. Copyright 2022 American Chemical Society.

6.3.1 Universal scaling behavior around p_c

In the vicinity of the percolation threshold p_c , the localization length distribution is governed by universal scaling behavior. According to the calculation in [136], the asymptotic expression of the scaling function is

$$\begin{aligned} \pi(m) &= 4.554 \exp(-2m) \quad \text{for } m \gg 1 \\ \pi(m) &= \frac{3}{m^2} (1.678/m - 3/5) \exp(-1.678/m) \quad \text{for } m \ll 1. \end{aligned} \quad (6.9)$$

In the following, I will probe the universal scaling behavior for $p \gtrsim p_c$ in the simulation. The same system as in the previous section with system size $5 \times 5 \times 5R_e^3$, chain length $N = 32$ and invariant polymer density $\sqrt{N} = 128$ is used. In Figure 6.3, the ξ^2 distribution is shown for two crosslink densities at several time steps to illustrate that the profiles of the distributions have already converged at the measurements. Here, the time is measured in the unit of $\tau_R = R_e^2/D$, where D denotes the self-diffusion coefficient of the uncrosslinked melt with the same system parameters.

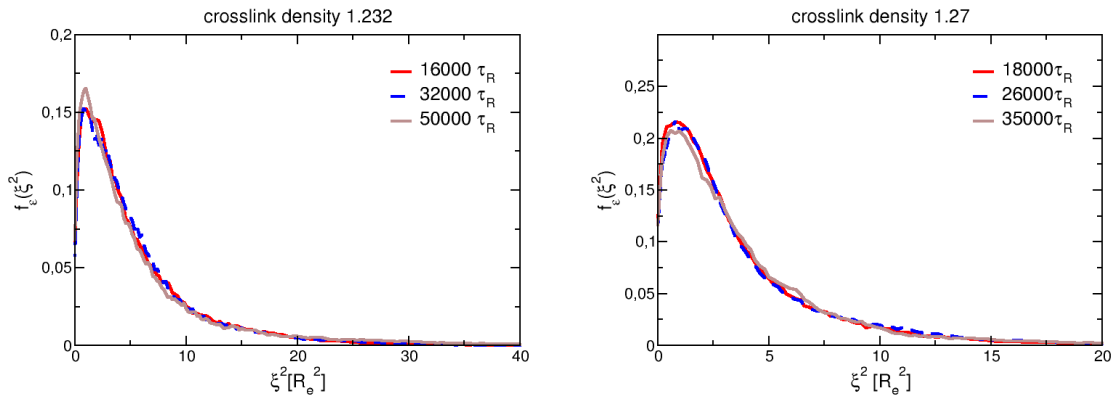


FIGURE 6.3: ξ^2 distribution for $p = 1.232$ (left) and $p = 1.27$ (right) at several time steps are shown to demonstrate their stability.

Then, the averaged ξ^2 denoted as $[\xi^2]$ of each monomer is calculated from ten snapshots and their distribution is computed. I test the scaling behavior of the ξ^2 distribution without making use of the percolation threshold. Instead, the probability distribution of ξ^2 and its first moment will be normalized to one as suggested in [158]. By doing so, a normalized probability density for $\xi^2 / [\xi^2]$ can be obtained. Then I perform the same normalization on the analytical prediction $\pi(m)$. The two asymptotic expressions provided in Equation 6.9 cross at $m = 1.41$ and their derivative is also the same at the crossing point. The two functions can be joined at $m = 1.41$ and the corresponding asymptotic formula is used for $m \gg 1$ and $m \ll 1$. I compare the measured scale-free ξ^2 distribution with the analytical prediction in Figure 6.4. For crosslink densities close to p_c , the measured $\xi^2 / [\xi^2]$ distributions match the scaling function very well, implying the validity of the universal behavior of randomly crosslinked polymers. At $p = 1.27$, the measured distribution deviates slightly from the analytical prediction. This indicates that the networks with crosslink density above $p = 1.14$ do not fall under the description of the universal scaling behavior anymore.

6.3.2 Mean MSD as a function of p

The localization length reflects the length scale of monomer displacement in polymer networks constrained by the spatial connectivity. This length scale is to be compared to the lamellar spacing of unconnected diblock copolymer melts. The equilibrium lamellar spacing of unconnected diblock melts is measured in SOMA to be $d_L \approx 1.52R_e$. The measured $[\xi^2]$ is

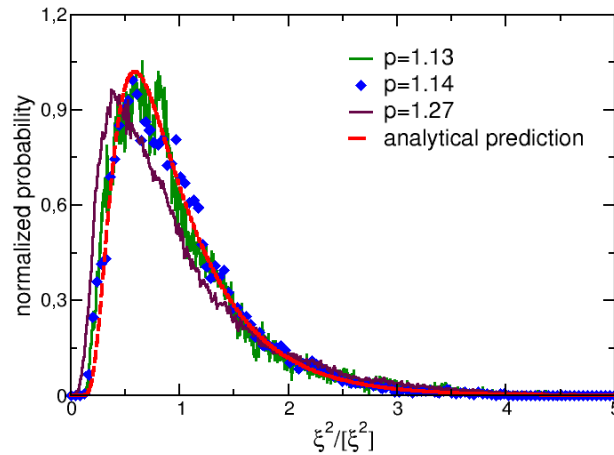


FIGURE 6.4: Normalized MSD distribution measured in the center-of-mass frame compared with the analytical prediction. The figure is reprinted with permission from [134]. Copyright 2022 American Chemical Society.

shown in the unit of d_L^2 as a function of crosslink density in Figure 6.5. As one would expect, $[\zeta^2]$ decreases with growing crosslink density. If $[\zeta^2]$ is much larger than the length scale of diblock lamellar spacing, the constraints introduced by the crosslinks are so small that the network can still be considered flexible. With $[\zeta^2]$ decreasing to the equilibrium lamellar spacing of the constituent diblocks, the microphase separation of diblock polymer networks into lamellar structure becomes more difficult and $\chi_c N$ of the ODT increases. Once $[\zeta^2]$ becomes smaller than the length scale of the lamellar spacing, the mobility of the particles will be too small to allow segregation into domains separated by a distance d_L . The crossover point is measured to be $p/p_c \approx 1.3$.

6.4 Stability of ordered random networks upon heating

For random networks prepared in the lamellar state, the analytical model developed by Annette Zippelius [134] predicts a non-vanishing frozen-in lamellar order for networks with a gel-fraction Q larger than zero (*i.e.* all systems above the percolation threshold). At length scales specified by the wavenumbers kR_e , Annette Zippelius [134] predicts the amplitude of

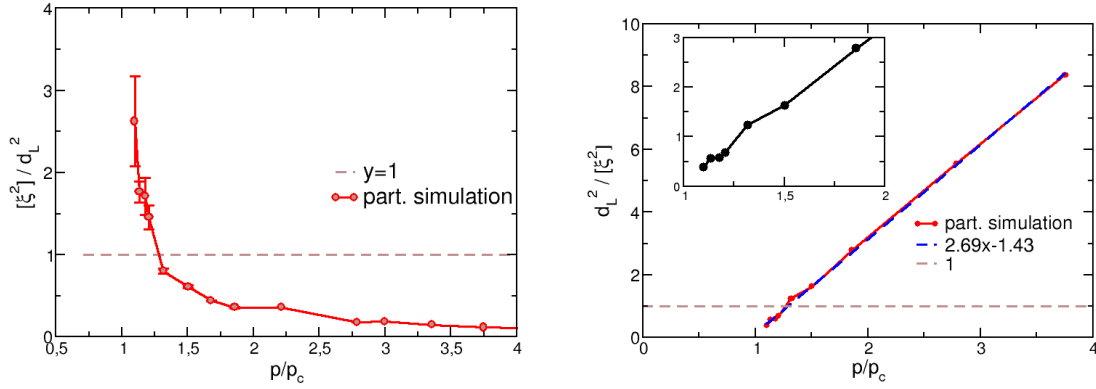


FIGURE 6.5: Left: $[\xi^2]$ is shown in units of d_L^2 . This ratio crosses one at about $p/p_c \approx 1.3$. Right: $d_L^2/[\xi^2]$ is plotted against the crosslink density p/p_c . The inset shows $d_L^2/[\xi^2]$ close to the percolation threshold.

the frozen-in structure σ_k to be

$$\sigma_k = \frac{p}{4p_c} \chi_p N \sigma_k^0 Q e^{-k^2 \xi^2/3} s_{\sigma^2 \Sigma}(k^2, k^2), \quad (6.10)$$

with σ_k^0 the amplitude of the corresponding structure in the preparation state. The lamellar state, which was gradually “cooled down” to $\chi_p N = 25$ during the preparation, has a lamellar spacing $d_L = 1.52R_e$ corresponding to $k_L R_e = 4.13$. The amplitude of the lamellar modulation is found to be one.

In the above equation, $s_{\sigma^2 \Sigma}(k^2, p^2)$ is the three point correlation function defined as

$$s_{\sigma^2 \Sigma}(k^2, p^2) \equiv \int_0^1 \int_0^1 \int_0^1 ds_1 ds_2 ds_3 \gamma(s_1) \gamma(s_2) e^{-k^2 \frac{R_e^2}{6} |s_2 - s_3|} e^{-p^2 \frac{R_e^2}{6} |s_1 - s_3|}. \quad (6.11)$$

The variables s_i in the above equation label the indices of monomers, $\gamma(s_i)$ denotes the particle type and is 1 for *A*-type monomers and -1 for *B*-type monomers. $s_{\sigma^2 \Sigma}(k^2, p^2)$ can be solved numerically as well as analytically. Laborious integral calculation provides an analytical expression for the three point correlation function

$$s_{\sigma^2 \Sigma}(k^2 R_e^2, k^2 R_e^2) = \frac{6^3}{k^6 R_e^6} \left\{ e^{-k^2 \frac{R_e^2}{3}} \left[-1 + 4e^{k^2 \frac{R_e^2}{12}} - 2e^{k^2 \frac{R_e^2}{6}} \left(6 + k^2 \frac{R_e^2}{6} \right) \right. \right. \\ \left. \left. + 4e^{k^2 \frac{R_e^2}{4}} \left(7 + k^2 \frac{R_e^2}{6} \right) + e^{2k^2 \frac{R_e^2}{6}} \left(2k^2 \frac{R_e^2}{3} - 19 \right) \right] \right\}. \quad (6.12)$$

The analytical expression together with the numerically evaluated correlation function is demonstrated in [Figure 6.6](#). At the target wavenumber $k_L R_e = 4.13$, it is $s_{\sigma^2 \Sigma}(k_L R_e, k_L R_e) \approx 0.039$.

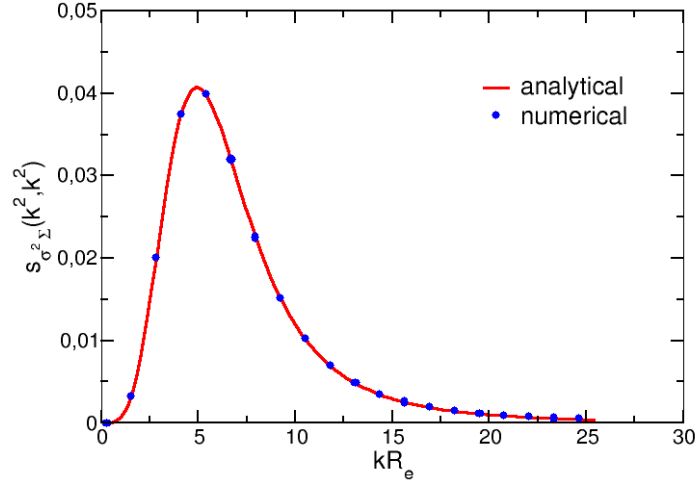


FIGURE 6.6: The result of the analytical expression for $s_{\sigma^2 \Sigma}$ as well as the numerically evaluated value is shown as a function of $k R_e$. The target wavevector corresponds to the peak region of the three point correlation function. The figure is reprinted with permission from [134]. Copyright 2022 American Chemical Society.

In the following, I will estimate the amplitude of the frozen-in structure in the simulation. Consider a polymer network in a simulation box with geometry $5 \times 5 \times 5 R_e^3$, prepared in the lamellar state at $\chi_p N = 25$. I “warm up” the system directly to $\chi_m N = 0$. After equilibration, the amplitude of remaining lamellar order is measured. This amplitude is estimated as the product of the normalized composition fields $\phi(c) = [\phi_A(c) - \phi_B(c)] / [\phi_A(c) + \phi_B(c)]$ of the preparation ensemble $\phi_p(c)$ and the measurement ensemble $\phi_m(c)$ averaged over all simulation cells c

$$C = \left[\frac{1}{V} \sum_c \Delta L^3 \bar{\phi}_p(c) \bar{\phi}_m(c) \right]_C \quad (6.13)$$

The measured lamellar order amplitude is averaged over 10 temporal snapshots for each crosslink configuration to reduce fluctuations. The temporal distance between two measurements is set to 10^5 MC-steps, which is approximately $11 \tau_R$. This time average is indicated by an overbar. For each crosslink density, the result is averaged over five independent crosslink configurations, \mathcal{C} , for better statistics. The lamellar order amplitude $C / \left[\frac{1}{V} \sum_c \Delta L^3 \bar{\phi}_p^2(c) \right]_C$

measured in SOMA is shown as the red curve in [Figure 6.2](#) for multiple crosslink densities. This is compared with the analytical prediction $\sigma_{k_L}/\sigma_{k_L}^0$ (shown as the blue dashed line) provided by [Equation 6.10](#), with the gel fraction, the localization length and percolation threshold measured in the particle-based simulations.

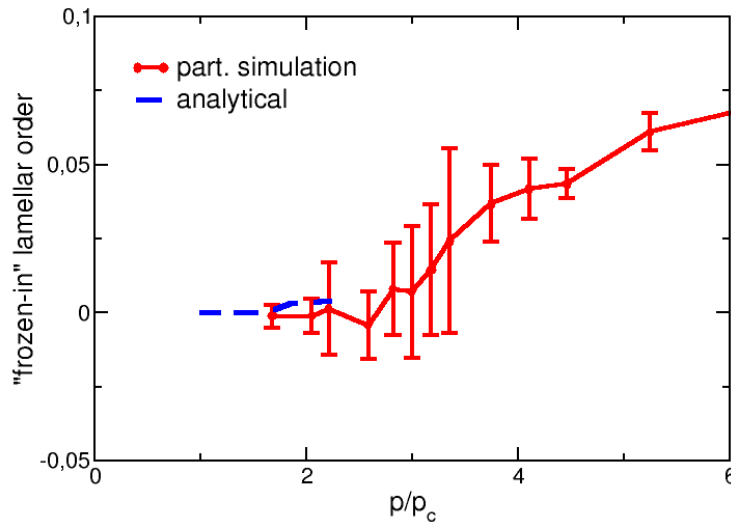


FIGURE 6.7: Networks with ordered preparation state are quenched directly to zero. For large crosslink densities, the non-vanishing lamellar order amplitudes indicate a preserved ordered structure even at $\chi_m N = 0$.

Below $p/p_c \approx 3$, the amplitude of the preserved lamellar order is very close to zero. Above $p/p_c \approx 3$, the amplitude of the remaining lamellar order at $\chi_m N = 0$ grows rapidly. Both the simulation result and the analytical prediction suggest that a noticeable part of the preparation state is preserved. At $p/p_c = 6$, around 7% of the original lamellar order can be measured at $\chi_m N = 0$. One should note that the analytical method applied here is only valid near the percolation threshold $p/p_c \approx 1$. For $p/p_c < 3$, both the theory and the simulation yield a small lamellar-order amplitude which is difficult to distinguish from zero numerically within the range of error. This makes a comparison between the simulation results and the analytical prediction very difficult. Nevertheless, the simulation data is consistent with the theoretical prediction and confirms a very small yet existing fraction of frozen structure in percolating polymer networks.

In [Figure 6.8](#), a network prepared at $\chi_p N = 25$ with $p/p_c = 1.5$ is gradually “warmed

up” (black solid line) to $\chi_m N = 0$ and then “cooled down” back to $\chi_m N = 20$ (red triangles). The intermediate steps in varying $\chi_m N$ is the same in both directions and is demonstrated by the positions of the red triangles. The averaged non-bonded energy is drawn as a function of $\chi_m N$ supplemented by the corresponding morphologies. At $\chi_m N = 0$, the preserved lamellar order is vanishingly small. As expected, an ordered lamellar structure can not be visually recognized in the density field at $\chi_m N = 0$. Nevertheless, “cooling down” the system back to $\chi_m N = 20$ recovers the original ordered structure. This can be seen in the two morphologies at $\chi_m N = 20$ recorded while decreasing $\chi_m N$ (the right one) and while increasing $\chi_m N$ from 0 back to 20 (the left one). The recovered lamellar structure provides an additional evidence for the preserved structure of the preparation state at $\chi_m N = 0$ even though the amplitude of the remaining lamellar order is very small. This observation is in perfect agreement with the study of Lay [102]. For diblock copolymer networks crosslinked in the ordered state, they observed that the lamellar structure is washed away if the repulsion between unlike monomers is switched off but can be re-established once the interaction is switched on again.

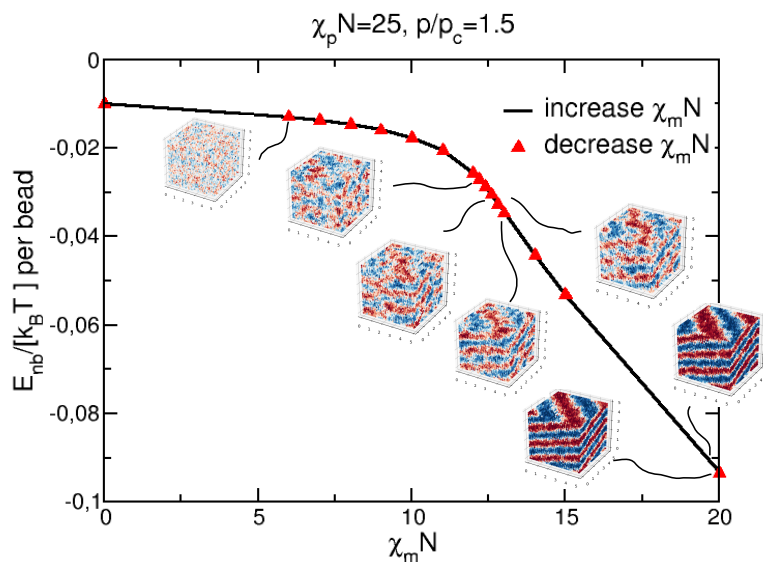


FIGURE 6.8: A network with $p/p_c = 1.5$ and $\chi_p N = 25$ is “warmed up” to $\chi_m N = 0$ and “cooled down” again to $\chi_m N = 20$. The averaged non-bonded energy and the corresponding density fields are shown as a function $\chi_m N$. The original ordered structure of the preparation state is recovered despite a nearly disordered intermediate step at $\chi_m N = 0$. The figure is reprinted with permission from [134]. Copyright 2022 American Chemical Society.

6.5 Order-disorder transition

In this section, I measure $\chi_c N$ of the ODT in random networks as a function of the preparation $\chi_p N$ and the crosslink density p/p_c . As discussed in the previous section, the irreversible crosslinks impart a domain memory of the preparation state. I suggest to capture the impact of the frozen-in structure by an effective field similar to the Ising model in an external field h_i with a Hamiltonian of the form

$$\mathcal{H}_{\text{Ising}} = -J \sum_{\langle i,j \rangle} s_i s_j - \sum_i h_i s_i. \quad (6.14)$$

For networks prepared in the disordered state, the effect of the external field can be understood within the framework of the random field Ising model [159, 160]. For such a system in 3D, Ref. [161] showed that there exists an ordered phase. In the mean-field calculation, the order of the phase transition from the ordered to the disordered state depends on the form of the distribution of the random field. It is predicted to be a second-order one for Gaussian distributed random fields [162] and becomes first-order for any random field distribution with a minimum at zero [163]. In contradiction to the mean-field prediction, later MC studies revealed the universality of the random field Ising model independent of the form of the implemented random-field distribution [164]. The ODT is confirmed to be a first-order transition independent of the form and the strength of the random field distribution [165]. In this scenario, the quenched disorder does not destroy the regular phase separation and a first-order phase transition is expected.

For networks prepared in the lamellar state, the crosslinks are more likely to be formed between monomers of the same species. The alternating A - and B -rich domains result in an external field that is “aligned” with A -monomers in some regions and with B -monomers in other regions. The strength of this external field can be estimated by the amplitude of preserved lamellar order at $\chi_m N = 0$ (see section 6.4). For networks crosslinked below the percolation threshold, the strength of the external field is zero. In this case, a first-order ODT can occur. If the network is crosslinked above the percolation threshold, the symmetry with respect to the composition (which is the order parameter) is locally broken because of the spatially modulated external field. In this regime, a lamellar order as well as a preferred

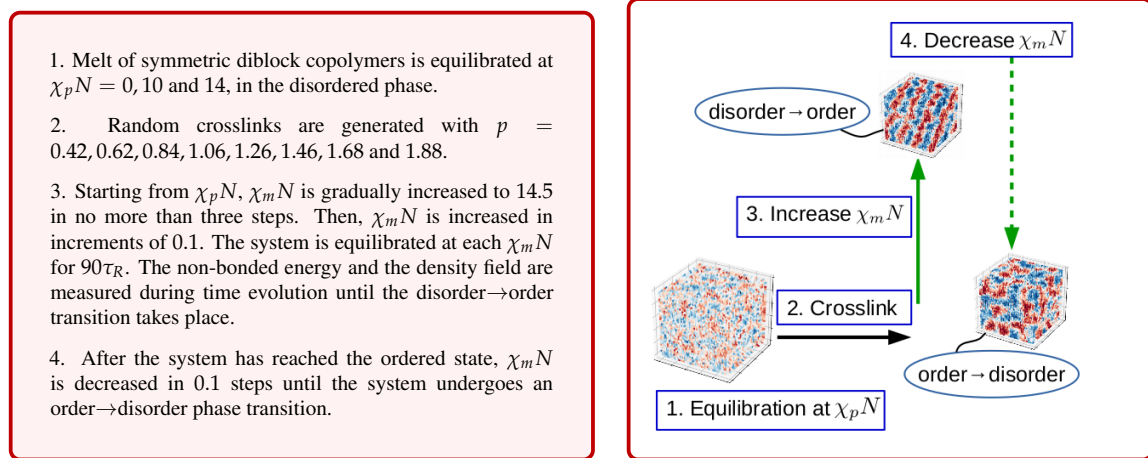


TABLE 6.1: Simulation protocol of systems with disordered preparation states. The figures in this table are reprinted with permission from [134]. Copyright 2022 American Chemical Society.

orientation is present even at $\chi_m N = 0$. Thus, the system can never enter the disordered phase and there exists no phase transition.

I measure the phase transition of randomly crosslinked diblock copolymers in the particle-based simulation program SOMA. The side length of the quadratic simulation box is $L = 5R_e$, the monomer discretization is set to $N = 32$ and the invariant degree of polymerization is $\sqrt{N} = 128$. The incompressibility parameter κN is set to 50 . To avoid confusion while drawing the hysteresis in the following, I will explicitly indicate the direction of the simulation process by an arrow, *e.g.* disorder→order. One should note that $\chi_p N$ and p/p_c are system parameters and only $\chi_m N$ is the tunable variable that is varied during the simulation. For each set of $\chi_p N$ and p/p_c , I study nine independent crosslink configurations to achieve better statistics.

For systems with disordered preparation state, the hysteresis loop around the ODT is obtained according to the simulation protocol described in Table 6.1. The simulation protocol of networks with ordered preparation state can be found in Table 6.2. The average of the hysteresis will be considered an accurate estimate for the ODT and the size of the hysteresis loop provides an estimate for the error interval.

In the following, I will first show the non-bonded energy complemented with the corresponding density morphology to demonstrate the accuracy of the ODT measurement in subsection 6.5.1 and subsection 6.5.2. Then in subsection 6.5.3, a diagram of $\chi_c N$ of the

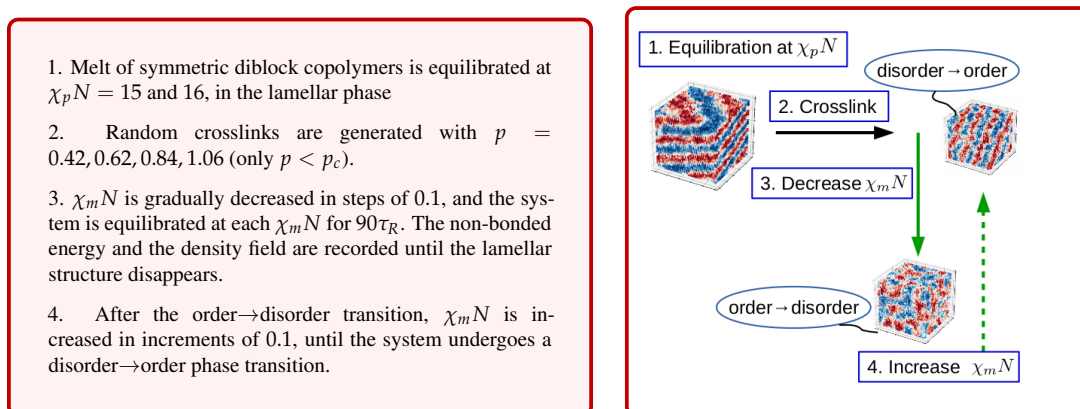


TABLE 6.2: Simulation protocol of systems with ordered preparation states. The figures in this table are reprinted with permission from [134]. Copyright 2022 American Chemical Society.

ODT resulting from extensive simulations will be provided and discussed.

6.5.1 Disordered preparation state

Networks with disordered preparation state experience a first-order transition, which can be observed as a change of the non-bonded energy and the density fields. For large $\chi_m N \lesssim \chi_c N$, a disordered solution of micelles [32] with a small characteristic length exists. During the disordered→ordered phase transition, the non-bonded energy decreases to lower values as a result of the minimized A/B interfacial area after long-range microphase separation. The non-bonded energy of networks with $\chi_p N = 0$ is demonstrated in Figure 6.9 for several crosslink densities.

Then, the ordered final configuration from Figure 6.9 is used as the starting point and $\chi_m N$ is decreased gradually in 0.1 intervals to determine the hysteresis loop. The ordered→disordered phase transition is associated with the destruction of the periodic lamellar structure and can be identified as a growth of the non-bonded energy to higher values as well as by the corresponding density morphologies. In Figure 6.10, I demonstrate the non-bonded energy during the phase transition into the disordered state.

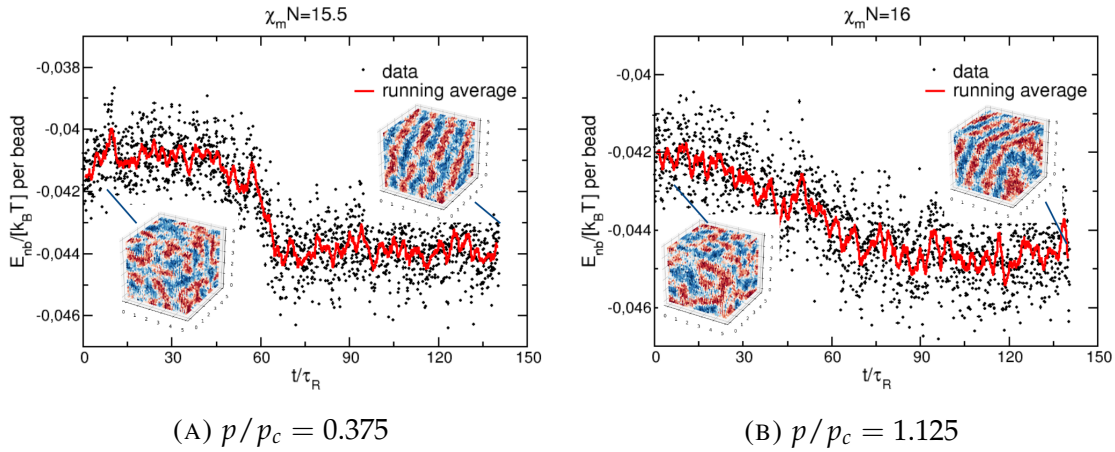


FIGURE 6.9: The disorder→order transition of random networks prepared at $\chi_p N = 0$ is associated with a decline of the non-bonded energy to a lower value. Corresponding density field morphologies of the system before and after the transition are presented as well. The figure is reprinted with permission from [134]. Copyright 2022 American Chemical Society.

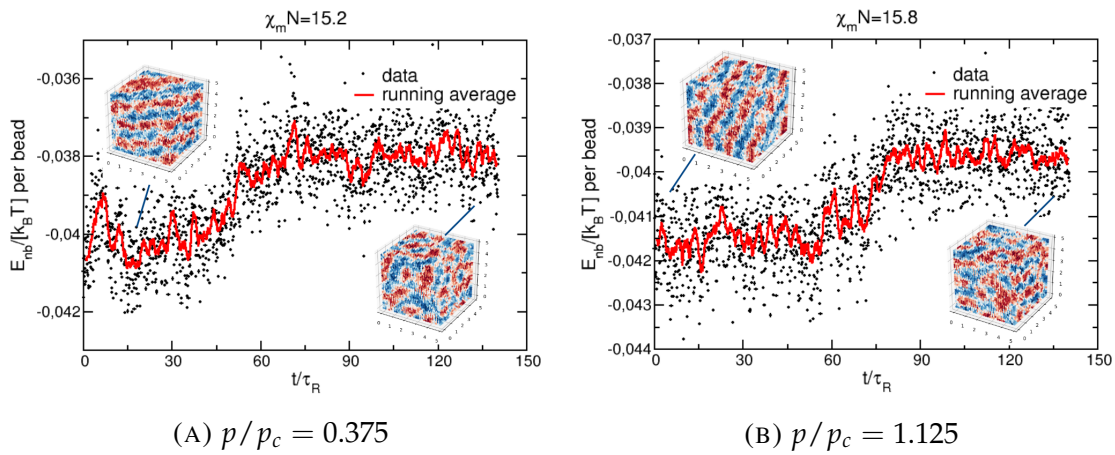


FIGURE 6.10: Order→disorder transition of random networks prepared at $\chi_p N = 0$ are shown. The end configurations from Figure 6.9 are now used as initial configurations. $\chi_m N$ is gradually decreased until the periodic lamellar structure is dissolved. The identified phase transitions are supported by the corresponding density fields before and after the phase transition. The figure is reprinted with permission from [134]. Copyright 2022 American Chemical Society.

6.5.2 Ordered preparation state

In case of an ordered preparation state, only networks with crosslink densities below the percolation threshold undergo a first-order phase transition. Examples of non-bonded energy measured for networks with $\chi_p N = 16$ as a function of time during the order→disorder transition are shown in Figure 6.11.

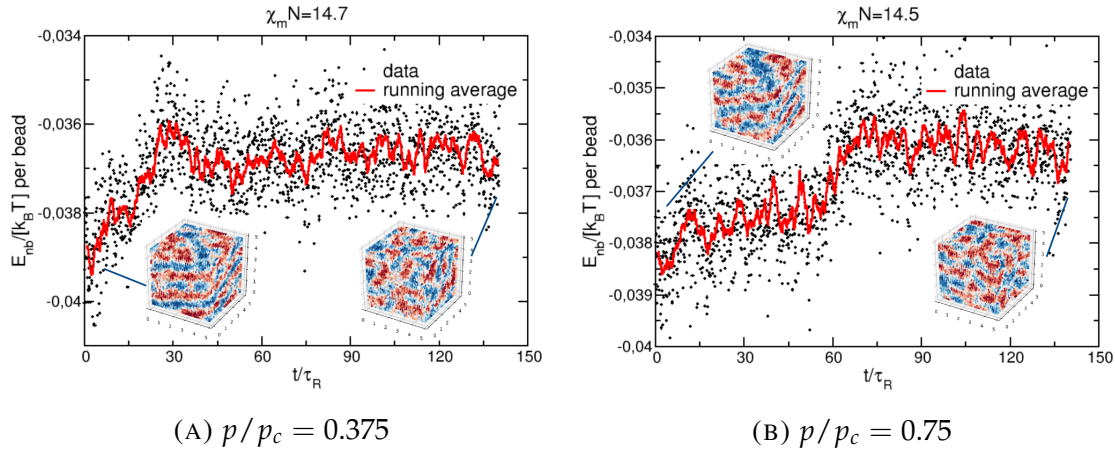


FIGURE 6.11: The non-bonded energy of a network with $\chi_p N = 16$ experiences a change during order \rightarrow disorder transition. The corresponding density fields also indicate phase transitions. The figure is reprinted with permission from [134]. Copyright 2022 American Chemical Society.

The backwards disorder \rightarrow order transition is measured in order to determine the hysteresis loop. The end configurations from Figure 6.11 are used as initial configurations for this measurement. The non-bonded energy measured during this process is shown in Figure 6.12.

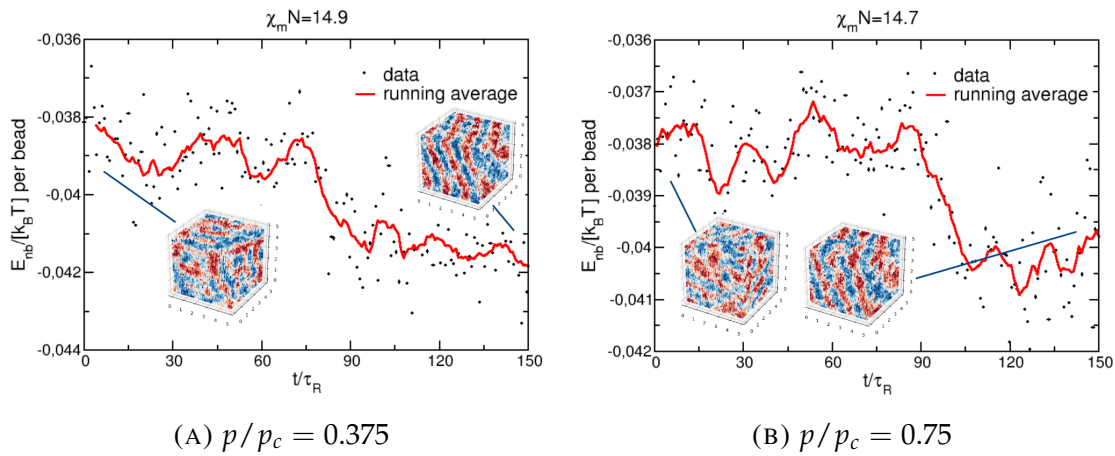


FIGURE 6.12: The non-bonded energy recorded during the disorder \rightarrow order transition of networks prepared at $\chi_p N = 16$ is presented. The corresponding density fields are shown as well. The figure is reprinted with permission from [134]. Copyright 2022 American Chemical Society.

6.5.3 Phase diagram

It is important to mention that the ODT of randomly crosslinked networks are measured at fixed $\chi_p N$ and p/p_c . The phase diagram is in fact one dimensional and depends only on

$\chi_m N$ at the measurement. The diagrams provided here actually show the ODT of different gels. The value of $\chi_m N$ of the ODT obtained following the simulation procedure described above is shown in [Figure 6.13](#), where the curves separate the ordered and disordered state for specific $\chi_p N$. According to the parameters $\chi_p N$ and p/p_c , the results can be discussed as four regimes.

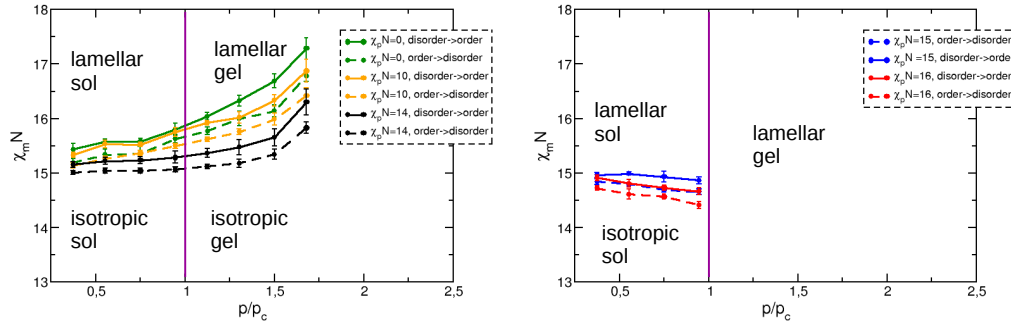


FIGURE 6.13: Phase diagram of random networks in the $\chi_m N - p$ -plane for several $\chi_p N$. The left panel shows the results for networks prepared in the disordered state, $\chi_p N < \chi_c^{\text{diblock}} N$. The right panel shows the location of the ODT for networks prepared in the lamellar state, $\chi_p N > \chi_c^{\text{diblock}} N$. The figure is reprinted with permission from [134]. Copyright 2022 American Chemical Society.

- (A) $p/p_c < 1$, disordered preparation state: Additional AB contacts are inevitably generated in the polymer system during the stochastic crosslinking process in the disordered preparation state. Since only finite clusters are formed in this region, the displacement of the monomers is not constrained. The critical $\chi_c N$ increases slightly with the crosslink density, indicating that large but finite clusters restrain composition modulations. A hysteresis can be observed around the ODT which is strong evidence for a first-order transition.
- (B) $1 < p/p_c$, disordered preparation state: Monomers belonging to the percolating cluster can only fluctuate around their equilibrium position and thus have a finite localization length. The gel fraction grows and the mean localization length drops with growing crosslink density. The limited mobility of the monomers and the frozen-in disorder makes the formation of the lamellar structure more difficult. Nevertheless, a first-order transition exists. In this regime, $\chi_c N$ grows rapidly with increasing crosslink density. For a very large crosslink density, there exist several possible scenarios: (i) The ODT

curve ends at a large p beyond which there is no phase transition, (ii) $\chi_c N$ diverges at a large p or (iii) $\chi_c N$ increases with p but remains finite. Unfortunately, probing these possibilities is beyond the capability of my simulation tool, and the phase behavior of random networks crosslinked far above the percolation threshold will not be discussed in this work.

- (C) $p/p_c < 1$, ordered preparation state: Since there is no frozen-in lamellar order, a first-order phase transition to disordered state takes place. The majority of the crosslinks are established between monomers of the same species. These bonds stabilize the ordered structure over a larger range of $\chi_m N$ and lead to a decreasing $\chi_c N$ with growing crosslink density. The curve that separates the ordered and disordered state ends at the percolation threshold.
- (D) $p/p_c > 1$, ordered preparation state: The frozen-in lamellar order acts as an external field that is beneficial for $A(B)$ -monomers in the original $A(B)$ -rich domains of the preparation ensemble and thus prevents the phase transition. It is worth mentioning that close to the percolation threshold and for small $\chi_p N$, the ratio between the amplitude of the preserved lamellar order is vanishingly small. Thus, a small region of second-order phase transition between region (B) and (D) is possible. This is neither disproved nor confirmed by the current simulation study and provides an interesting topic for future research.

A 3D diagram with $\chi_p N$ and p/p_c serving as x - and y -axes is shown in [Figure 6.14](#) to provide an overview. On the base plane, 4 different preparation states – multiblock liquid with and without lamellar memory, and gel with and without frozen-in lamellar structure – are indicated by colors.

In the 3D diagram, the location of $\chi_c N$ of the ODT is estimated as the average of the hysteresis loop. The error bar indicates the size of hysteresis loop. The surface in the 3D diagram separates the ordered state (above) from the disordered state (below). The irreversible crosslinks enhance the stability of the preparation state over a large range of $\chi_m N$ resulting in the distorted surface of the ODT.

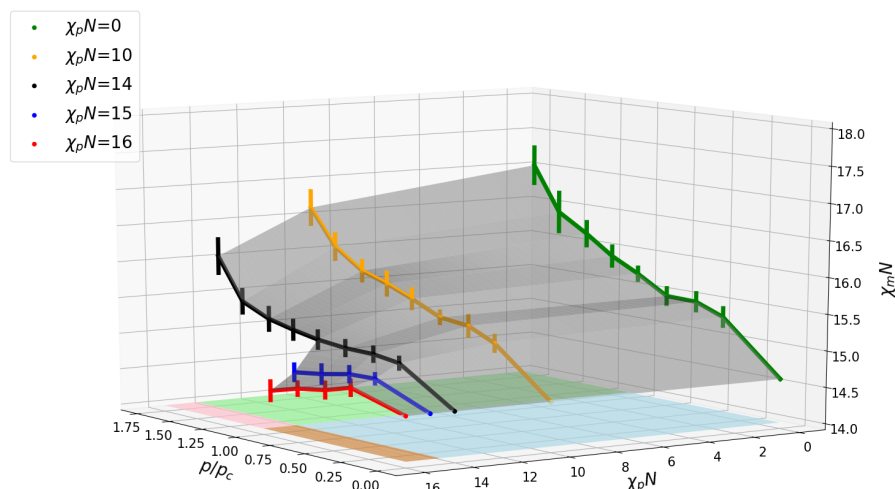


FIGURE 6.14: 3D diagram of the ODT of random networks as a function of $\chi_p N$ and p/p_c . The figure is reprinted with permission from [134]. Copyright 2022 American Chemical Society.

6.6 Summary

Using a particle-based simulation model in conjunction with its efficient and parallel GPU-implementation SOMA, I studied the sol-gel transition and the order-disorder transition in randomly, irreversibly crosslinked networks comprised of symmetric diblock copolymers. The percolation threshold that separates the sol phase from the gel phase is determined with a finite-scaling analysis. To this end, the percolation probability is measured for three crosslinked systems with different sizes and the crossing point of their percolation probability is considered as an accurate estimate of the percolation threshold, $p_c \approx 1.12$.

Then, I investigated the gel fraction and the localization length as a function of the crosslink density p . The two quantities are of special importance because they contain information about the size of the network and the extent of displacements of the monomers in the network. With measurements of the localization length distribution close to p_c , I confirmed that the properties of the networks are governed by a universal scaling behavior in this region. Below p_c , the gel fraction is zero. With increasing p , the gel fraction grows monotonically and

converges to one. At the same time, the mobility of the monomers is increasingly restricted by the densely assigned crosslinks resulting in a decreasing localization length. Above $p/p_c \approx 1.3$, the localization length drops below the length scale of the equilibrium lamellar spacing of free diblocks, indicating that the formation of lamellar structure as in diblock copolymer melts is strongly inhibited.

In general, the crosslinks impart a memory of the domain structure present at their time of formation. Above the percolation threshold, this results in a frozen-in structure of the preparation ensemble, which is preserved even at $\chi_m N = 0$. I measured the preserved lamellar order, originating from the preparation ensemble at $\chi_p N = 25$, in the measurement ensemble at $\chi_m N = 0$. The amplitude of the preserved lamellar order is vanishingly small (yet non-zero) for crosslink densities close to p_c and grows rapidly above $p/p_c = 3$.

Then, I studied the phase behavior of random networks. $\chi_c N$ of the ODT is found to depend strongly on the crosslink density and the Flory-Huggins parameter of the preparation state $\chi_p N$. I obtained an accurate diagram for the ODT as a function of $\chi_p N$ and p from extensive SOMA simulations. For $p < p_c$, a first-order phase transition was observed, independent of the preparation state. $\chi_c N$ of the ODT increases (decreases) slightly with growing p in networks with disordered (ordered) preparation state. For $p > p_c$, there exists no order→disorder phase transition in networks with ordered preparation state as a consequence of the frozen-in ordered lamellar structure. For networks with disordered preparation state and $p > p_c$, $\chi_c N$ increases rapidly with p because of the strongly restricted mobility of the monomers and the increasing amount of frozen-in disorder.

Chapter 7

Conclusion

The design and fabrication of multicomponent polymer materials requires comprehensive understanding of their molecular structure and properties. This work investigated several aspects regarding the structure formation in polymeric systems comprised of two incompatible segment species. In this work, particle-based simulations as well as diverse analytical approaches were applied to uncover the behavior of polymer systems on a broad spectrum of length and time scales, ranging from short-time kinetics of early-stage structure formation in linear chains to equilibrium states of percolating macromolecules.

7.1 Collective short-time dynamics in multicomponent polymer melts

In the first part of this work, I focused on the kinetics of the structure evolution on short time and length scales. I chose binary homopolymer blends and symmetric diblock copolymer melts as subjects of this study because of their well studied equilibrium phase diagram [25, 166]. In the (directed) self-assembly [40, 167, 168] of multicomponent polymer melts, the early stage pattern provides a template for the eventual metastable or equilibrium morphologies. This technique for directing the structure evolution can be applied to tailor the subsequent process of structure formation and enables the fabrication of novel phase-separated morphologies.

I applied two well established theoretical models D-RPA [56, 57, 60] and D-SCFT [43, 44, 46, 63] on several typical cases of structure evolution from unstable initial states and worked out explicit spatiotemporal descriptions for the segment densities. I found that on short time scales, D-RPA is in perfect agreement with the simulation results without the usage of adjustable parameters, whereas D-SCFT underestimates the speed of structure evolution because it does not account for the fast, sub-diffusive motions, which are important on short time scales. Despite the exactness of D-RPA, its application is restricted to the linear regime. To overcome this limitation, a modified D-SCFT that utilizes a time-dependent Onsager coefficient [58] was used to associate the dynamics of density fields with the accurate free-energy functional. The modified D-SCFT reproduces the exact dynamical equations of D-RPA in the linear regime and has the advantage to be a good approximation on all time scales.

7.1.1 Future perspectives

The D-RPA formalism can also be generalized to describe systems with much more complex molecular architectures such as binary polymer networks. For polymer networks with large invariant degree of polymerization, the structure evolution towards equilibrium is protracted and the short-time linear regime can be slowed down to a time scale that can be accurately accessed in experiments. The advantage of the models developed in this work is that they establish a relation between the computationally less demanding single-chain properties and the collective properties. For polymer networks, the system is comprised of only a few macromolecules and the usage of single-chain properties is no longer advantageous. In this case, I suggest to decouple the networks into smaller, uncorrelated blocks and perform the calculation for the kinetics of each individual block in the network. The static aspects of this decoupling scheme are discussed in the second part of this thesis. I expect the combination of the dynamical models and the decoupling scheme demonstrated in this work to be applicable to explore the kinetics of structure formation of various exciting materials with complex architecture.

7.2 Structure and structure formation in regular polymer networks

Irreversibly crosslinked polymer networks are popular materials with applications ranging from rubber industry to biomedical research. Diverse theoretical models have been proposed to describe the structure and elasticity of polymer networks in the disordered state [98, 112]. In multicomponent networks consisting of segment species that repel each other, the microphase-separated structure leads to unique tensile properties with the ability to absorb a large amount of energy during deformation (see Ref. [169, 170] for application).

I focused on networks comprised of symmetric diblock copolymers, the simplest example subjected to the interplay between microscopic domains and network elasticity. An SCFT approach [120] was previously developed for the exact same model system where the interactions of the crosslinks were decoupled. My simulation studies on the same systems show significant deviations from the SCFT prediction in both distribution of crosslinks and phase behavior for $n_u > 1$, where n_u is number of unit cells on each side of the network. To accurately describe the properties of regular networks, I applied the phonon model [123], which accounts for full correlations between the crosslinks, to describe the crosslink position. The calculation was performed for phantom 2D networks but can be generalized to networks with arbitrary dimension and topology. In the comparison to computer simulations, the accuracy of the phonon model was proven for all n_u in the absence of the incompressibility constraint and for $n_u < 5$ in incompressible systems.

Inspired by the results of the phonon model, I found an explanation for the phase behavior of regular diblock copolymer networks by separating contributions to the structure factor into diblock characteristics and crosslink characteristics that occur (typically) on different length scales. The contribution from the respective characteristics, and thus the structure factor as well as the phase behavior of the network system, is crucially determined by the unit cell size l_u and the number of strongly correlated unit cells. For a 2D regular network, the number of correlated unit cells is simply $n_u \times n_u$. For $n_u = 30$, which is studied in this work, three typical types of phase separation are observed. For $l_u \lesssim 0.5 R_{db}$, the network is dominated by the diblock characteristics and $\chi_c N_{db}$ is about 7.5 depending only weakly on l_u . The lamellar

spacing $\approx 1.26 R_{db}$ is much larger than l_u . For $0.5 R_{db} < l_u < 1.5 R_{db}$, the contribution from the two characteristics are comparable resulting in a novel multidomain structure with perpendicular lamellar orientations and a lamellar spacing slightly larger than l_u . For large $l_u \geq 1.5 R_{db}$, the crosslink characteristics dominate and a lamellar structure with spacing l_u is formed already for very small $\chi_c N_{db}$. The phase transition of the 2D regular networks is associated with the breaking of the symmetry of a square (with periodicity l_u in x - and y -direction) and the formation of the lamellar structure. In general, increasing l_u separates the A/B -rich domains imposed by the network topology and thus decreases $\chi_c N_{db}$ of the ODT. According to the relation $S(q_u, n_u) \propto n_u^2$, increasing n_u at a fixed l_u leads to a larger intensity of the structure factor at $q_u = 2\pi/l_u$ and thus a higher significance of the crosslink characteristics with periodicity l_u .

7.2.1 Future perspectives

One obvious extension of this work is to apply the phonon model technique developed here to 3D regular polymers. SCFT suggests, that the phase behavior of 2D and 3D networks are qualitatively similar, but this should be quantitatively validated in future works.

One basic assumption of the phantom network model is that the strands are allowed to pass through each other. However, the crossing of polymer backbones is impossible in experiments. This important factor, the so-called entanglement, affects the properties of polymer networks and was not discussed. Entanglements between polymer strands modify the fluctuation of the crosslinks as well as the stress-strain relationships [171–173]. Their impact on the phase behavior of regular polymer networks is expected to be similar to that of additional crosslinks and should be investigated in future studies in order to make the simulation model better comparable to experimental results.

Furthermore, the opposite sides of the network in the current study are connected via bonds across periodic boundary conditions. This practically fixes the size of the networks to the geometry of the simulation box, which is typically not the case in experiments. Free boundary conditions allow more flexible rearrangement of the monomer positions during the process of structure formation which is beneficial for the ordering process. The influence of

the boundary conditions on the microphase separation behavior of copolymer networks offers an interesting topic for future works.

7.3 Phase behavior of random copolymer networks

Earlier studies provided insights into the phase separation behavior of randomly crosslinked multicomponent polymer melts [154, 156, 174, 175]. Their qualitative findings on the effect of crosslinks in networks up to a crosslink density p well above the percolation threshold suggest the existence of four phases: disordered liquid, disordered gel, ordered liquid and ordered gel. In addition, it is commonly accepted that the crosslinks enhance the stability of the structure at their time of formation and the crosslinked systems are able to maintain their morphology over a larger range of χN .

In this work, I quantitatively studied the effect of crosslinks and the Flory-Huggins parameter of the preparation state $\chi_p N$ on the microphase separation in symmetric diblock copolymers. First, I computed the amplitude of the frozen-in structure originating from preparation configurations at $\chi_p N = 25$ which is maintained at $\chi N = 0$. I found this amplitude to be larger than zero for all percolating networks. For small crosslink densities $p/p_c < 3$, the remaining lamellar order is vanishingly small compared to the original amplitude of the density fluctuation. For strongly crosslinked networks above $p/p_c > 6$, its amplitude reaches 7% of the lamellar structure at $\chi_p N = 25$ and is expected to grow further for larger p .

Furthermore, I provided an accurate diagram, in which $\chi_c N$ of the ODT is shown as a function of the crosslink density and $\chi_p N$ of the preparation state. A first-order transition was identified using the non-bonded energy and the density morphology. For networks crosslinked in the disordered state, $\chi_c N$ increases with p , whereas for networks with ordered preparation state, $\chi_c N$ decreases with p below the percolation threshold. For networks prepared in the ordered state with $p > p_c$, an order-disorder transition is prevented by the frozen-in periodic lamellar structure in contrast to the case of regular networks made from diblock copolymers discussed in the previous chapter. This is because the ordered structure imposed by end-crosslinking, as in the previous chapter, had a checkerboard pattern with periodicity l_u

in both x - and y -direction, which can transition into an energetically more favored lamellar structure, whereas in this chapter, a fixed orientation of the lamellar structure was already imposed by the frozen-in structure. The obtained phase diagram of randomly crosslinked symmetric diblock copolymers serves as a groundwork for more detailed phase behavior studies on polymer networks in the future.

7.3.1 Future perspectives

Further studies can be performed to search for a possible region of second-order transition for $\chi_p N \gtrsim \chi_d N$ and $p \gtrsim p_c$, where a very small amplitude of the preserved lamellar order is measured. For this region, I argued based on a consideration of the random field Ising model that the order \rightarrow disorder transition is prevented by the frozen-in lamellar order. Whereas this is expected if a significant amount of lamellar order is present, the impact of a vanishingly small (yet non-zero) frozen-in structure remains unclear.

Apart from that, one could stretch the network after the crosslinks are generated and study the effect of expansion on the phase behavior of random networks. If the deformation of the network was affine, the stretching would simply shift the peak position of the structure factor. The intensity of the structure factor, and thus χN of the ODT would remain unchanged. However, as calculations on structural properties in regular networks (see the phonon model from the previous chapter) already suggested, the deformation of networks under expansion is not affine. For this reason, the change of the intensity of the structure factor is non-trivial and should be investigated in further works as well as compared with the ODT of stretched random networks.

Bibliography

- [1] L. J. Fetters and M. Morton. “Synthesis and Properties of Block Polymers. I. Poly--methylstyrene-Polyisoprene-Poly--methylstyrene”. In: *Macromolecules* 2.5 (1969), pp. 453–458.
- [2] M. Morton, R. F. Kammereck, and L. J. Fetters. “Synthesis and Properties of Block Polymers. II. Poly(-methylstyrene)-Poly(propylene sulfide)-Poly(-methylstyrene)”. In: *Macromolecules* 4.1 (1971), pp. 11–15.
- [3] W. Wang et al. “Thermoplastic Elastomers Based on Block, Graft, and Star Copolymers”. In: *Elastomers*. InTech, 2017.
- [4] R. J. Spontak and J. J. Ryan. “Chapter 3 - Polymer blend compatibilization by the addition of block copolymers”. In: *Compatibilization of Polymer Blends*. Ed. by A. A.R. and S. Thomas. Elsevier, 2020, pp. 57–102. ISBN: 978-0-12-816006-0.
- [5] M. W. Schulze et al. “High-Modulus, High-Conductivity Nanostructured Polymer Electrolyte Membranes via Polymerization-Induced Phase Separation”. In: *Nano Letters* 14.1 (2014). PMID: 24328570, pp. 122–126.
- [6] C. M. Bates et al. “Block Copolymer Lithography”. In: *Macromolecules* 47.1 (2014), pp. 2–12.
- [7] M. P. Stoykovich et al. “Directed Self-Assembly of Block Copolymers for Nanolithography: Fabrication of Isolated Features and Essential Integrated Circuit Geometries”. In: *ACS Nano* 1.3 (2007). PMID: 19206647, pp. 168–175.
- [8] M. P. Stoykovich and P. Nealey. “Block copolymers and conventional lithography”. In: *Materials Today* 9 (2006), pp. 20–29.

- [9] M. A. Morris et al. “Harnessing the Power of Plastics: Nanostructured Polymer Systems in Lithium-Ion Batteries”. In: *ACS Energy Letters* 2.8 (2017), pp. 1919–1936.
- [10] A. Rösler, G. W. Vandermeulen, and H.-A. Klok. “Advanced drug delivery devices via self-assembly of amphiphilic block copolymers”. In: *Advanced Drug Delivery Reviews* 53.1 (2001). *Polymeric Materials for Advanced Drug Delivery*, pp. 95–108.
- [11] J. Li and D. Mooney. “Designing hydrogels for controlled drug delivery”. In: *Nature Reviews Materials* 1 (2016), p. 16071.
- [12] Y. Zhang and S. N. Riduan. “Functional porous organic polymers for heterogeneous catalysis”. In: *Chem. Soc. Rev.* 41 (6 2012), pp. 2083–2094.
- [13] N. B. McKeown and P. M. Budd. “Polymers of intrinsic microporosity (PIMs): organic materials for membrane separations, heterogeneous catalysis and hydrogen storage”. In: *Chem. Soc. Rev.* 35 (8 2006), pp. 675–683.
- [14] J. A. Rogers, T. Someya, and Y. Huang. “Materials and Mechanics for Stretchable Electronics”. In: *Science* 327.5973 (2010), pp. 1603–1607.
- [15] P. E. Rouse. “A Theory of the Linear Viscoelastic Properties of Dilute Solutions of Coiling Polymers”. In: *J. Chem. Phys.* 21.7 (1953), pp. 1272–1280.
- [16] M. Doi and S. F. Edwards. *The theory of polymer dynamics*. International series of monographs on physics. Oxford: Oxford Univ. Press, 1986.
- [17] P. J. Flory. “Thermodynamics of High Polymer Solutions”. In: *J. Chem. Phys.* 10.1 (1942), pp. 51–61.
- [18] M. L. Huggins. “Thermodynamic Properties of Solutions of Long Chain Compounds”. In: *Annals of the New York Academy of Sciences* 43.1 (1942), pp. 1–32.
- [19] R. Pethrick. “Polymer physics. Edited by Michael Rubinstein and Ralph H Colby Oxford University Press, Oxford, 2003. ISBN 019852059X. pp 440”. In: *Polymer International* 53.9 (2004), pp. 1394–1395.
- [20] M. W. Matsen and M. Schick. “Stable and unstable phases of a diblock copolymer melt”. In: *Phys. Rev. Lett.* 72 (16 1994). DOI:[10.1103/PhysRevLett.72.2660](https://doi.org/10.1103/PhysRevLett.72.2660), pp. 2660–2663.

- [21] M. W. Matsen. “Self-consistent field theory and its applications”. In: *Soft Matter: Polymer Melts and Mixtures*. Ed. by G. Gompper and M. Schick. Vol. 1. Weinheim: Wiley-VCH, 2006, p. 87.
- [22] Y. Ren. “Kinetics of structure formation in block copolymers”. PhD thesis. 2018.
- [23] L. Leibler. “Theory of Microphase Separation in Block Copolymers”. In: *Macromolecules* 13.6 (1980), pp. 1602–1617.
- [24] A. M. Mayes, M. Olvera de la Cruz, and W. E. McMullen. “Asymptotic properties of higher-order random-phase approximation vertex functions for block copolymer melts”. In: *Macromolecules* 26.15 (1993), pp. 4050–4051.
- [25] Y. Mai and A. Eisenberg. “Self-assembly of block copolymers”. In: *Chem. Soc. Rev.* 41 (18 2012). DOI:[10.1039/C2CS35115C](https://doi.org/10.1039/C2CS35115C), pp. 5969–5985.
- [26] S. A. Brazovskii. “Phase transition of an isotropic system to a nonuniform state”. In: *30 Years of the Landau Institute — Selected Papers*, pp. 109–113.
- [27] G. H. Fredrickson and E. Helfand. “Fluctuation effects in the theory of microphase separation in block copolymers”. In: *J. Chem. Phys.* 87.1 (1987), pp. 697–705.
- [28] T. E. Gartner and A. Jayaraman. “Modeling and Simulations of Polymers: A Roadmap”. In: *Macromolecules* 52.3 (2019), pp. 755–786.
- [29] S. C. Glotzer and W. Paul. “Molecular and Mesoscale Simulation Methods for Polymer Materials”. In: *Annual Review of Materials Research* 32.1 (2002), pp. 401–436.
- [30] F. Müller-Plathe. “Coarse-Graining in Polymer Simulation: From the Atomistic to the Mesoscopic Scale and Back”. In: *ChemPhysChem* 3.9 (2002), pp. 754–769.
- [31] C. Peter and K. Kremer. “Multiscale simulation of soft matter systems – from the atomistic to the coarse-grained level and back”. In: *Soft Matter* 5.22 (2009), p. 4357.
- [32] K. C. Daoulas and M. Müller. “Single chain in mean field simulations: Quasi-instantaneous field approximation and quantitative comparison with Monte Carlo simulations”. In: *J. Chem. Phys.* 125.18 (2006), p. 184904.

- [33] M. Müller and G. D. Smith. “Phase separation in binary mixtures containing polymers: A quantitative comparison of single-chain-in-mean-field simulations and computer simulations of the corresponding multichain systems”. In: *Journal of Polymer Science Part B: Polymer Physics* 43.8 (2005), pp. 934–958.
- [34] T. Geisinger, M. Müller, and K. Binder. “Symmetric diblock copolymers in thin films. II. Comparison of profiles between self-consistent field calculations and Monte Carlo simulations”. In: *J. Chem. Phys.* 111.11 (1999), pp. 5251–5258.
- [35] M. Müller and K. C. Daoulas. “Single-chain dynamics in a homogeneous melt and a lamellar microphase: A comparison between Smart Monte Carlo dynamics, slithering-snake dynamics, and slip-link dynamics”. In: *J. Chem. Phys.* 129.16 (2008), p. 164906.
- [36] P. J. Rossky, J. D. Doll, and H. L. Friedman. “Brownian dynamics as smart Monte Carlo simulation”. In: *J. Chem. Phys.* 69.10 (1978), pp. 4628–4633.
- [37] N. Metropolis and S. Ulam. “The Monte Carlo Method”. In: *Journal of the American Statistical Association* 44.247 (1949), pp. 335–341.
- [38] L. Schneider and M. Müller. “Multi-architecture Monte-Carlo (MC) simulation of soft coarse-grained polymeric materials: SOft coarse grained Monte-Carlo Acceleration (SOMA)”. In: *Computer Physics Communications* 235 (2019), pp. 463–476.
- [39] G. Wang, Y. Ren, and M. Müller. “Collective Short-Time Dynamics in Multicomponent Polymer Melts”. In: *Macromolecules* 52.20 (2019). DOI:[10.1021/acs.macromol.9b01709](https://doi.org/10.1021/acs.macromol.9b01709), pp. 7704–7720.
- [40] M. Müller and D. W. Sun. “Process-directed self-assembly of block copolymers: a computer simulation study”. In: *Journal of Physics: Condensed Matter* 27.19 (2015), p. 194101.
- [41] Q. Tang, J. Tang, and M. Müller. “Process-directed self-assembly of multiblock copolymers: Solvent casting vs spray coating”. In: *European Physical Journal Special Topics* 225.8 (2016).
- [42] M. Müller. “Process-directed self-assembly of copolymers: Results of and challenges for simulation studies”. In: *Progress in Polymer Science* 101 (2020), p. 101198.

- [43] J. G. E. M. Fraaije et al. "The Dynamic Mean-Field Density Functional Method and Its Application To the Mesoscopic Dynamics of Quenched Block Copolymer Melts". In: *J. Chem. Phys.* 106 (1997), pp. 4260–4269.
- [44] T. Kawakatsu, M. Doi, and R. Hasegawa. "Dynamic density functional approach to phase separation dynamics of polymer systems". In: *Int. J. Mod. Phys. C* 10 (1999), pp. 1531–1540.
- [45] G. J. A. Sevink et al. "Dynamics of surface directed mesophase formation in block copolymer melts". In: *J. Chem. Phys.* 110 (1999), pp. 2250–2256.
- [46] E. Reister, M. Müller, and K. Binder. "Spinodal Decomposition in a Binary Polymer Mixture: Dynamic Self-Consistent-Field Theory and Monte Carlo Simulations". In: *Phys. Rev. E* 64 (2001), p. 041804.
- [47] H. Morita, T. Kawakatsu, and M. Doi. "Dynamic Density Functional Study on the Structure of Thin Polymer Blend Films with a Free Surface". In: *Macromolecules* 34 (2001), pp. 8777–8783.
- [48] J. G. E. M. Fraaije, A. V. Zvelindovsky, and G. J. A. Sevink. "Computational Soft Nanotechnology with Mesodyn". In: *Molecular Simulation* 30 (2004), pp. 225–238.
- [49] G. H. Fredrickson. "Dynamics and Rheology of Inhomogeneous Polymeric Fluids: a Complex Langevin Approach". In: *J. Chem. Phys.* 117 (2002), pp. 6810–6820.
- [50] E. Reister and M. Müller. "Formation of Enrichment Layers in Thin Polymer Films: the Influence of Single Chain Dynamics". In: *J. Chem. Phys.* 118 (2003), pp. 8476–8488.
- [51] M. Müller and F. Schmid. "Incorporating fluctuations and dynamics in self-consistent field theories for polymer blends". In: *Advances in polymer science* 185 (2005), pp. 1–58.
- [52] X. He and F. Schmid. "Dynamics of Spontaneous Vesicle Formation in Dilute Solutions of Amphiphilic Diblock Copolymers". In: *Macromolecules* 39 (2006), pp. 2654–2662.
- [53] L. Zhang, A. Sevink, and F. Schmid. "Hybrid Lattice Boltzmann/Dynamic Self-Consistent Field Simulations of Microphase Separation and Vesicle Formation in Block Copolymer Systems". In: *Macromolecules* 44 (2011), pp. 9434–9447.

- [54] X. Wan et al. “Ordering kinetics of lamella-forming block copolymers under the guidance of various external fields studied by dynamic self-consistent field theory”. In: *Phys. Chem. Chem. Phys.* 19.9 (2017), pp. 6707–6720.
- [55] S. Qi and F. Schmid. “Dynamic Density Functional Theories for Inhomogeneous Polymer Systems Compared to Brownian Dynamics Simulations”. In: *Macromolecules* 50.24 (2017), pp. 9831–9845.
- [56] F. Brochard and P. de Gennes. “Dynamics of compatible polymer mixtures”. In: *Physica A* 118.1 (1983), pp. 289–299.
- [57] A. Akcasu, M. Benmouna, and H. Benoit. “Application of random phase approximation to the dynamics of polymer blends and copolymers”. In: *Polymer* 27.12 (1986), pp. 1935–1942.
- [58] A. Semenov. “Relaxation of long-wavelength density fluctuations in a concentrated polymer solution”. In: *Journal of Experimental and Theoretical Physics* 63 (1986), p. 1230.
- [59] M. Benmouna et al. “Theory of dynamic scattering from ternary mixtures of two homopolymers and a solvent”. In: *Macromolecules* 20 (1987), pp. 1107–1112.
- [60] M. Benmouna et al. “Theory of dynamic scattering from copolymer solutions using the random phase approximation”. In: *Macromolecules* 20.10 (1987), pp. 2620–2624.
- [61] P. G. de Gennes. “Dynamics of Fluctuations and Spinodal Decomposition in Polymer Blends”. In: *J. Chem. Phys.* 72 (1980), pp. 4756–4763.
- [62] P. C. Hohenberg and B. I. Halperin. “Theory of dynamic critical phenomena”. In: *Rev. Mod. Phys.* 49 (1977), pp. 435–479.
- [63] K. Binder. “Collective Diffusion, Nucleation, and Spinodal Decomposition in Polymer Mixtures”. In: *J. Chem. Phys.* 79 (1983), pp. 6387–6409.
- [64] J. Gunton, M. San Miguel, and P. Sahni. “The Dynamics of First Order Phase Transitions”. In: *Phase Transitions and Critical Phenomena*. Ed. by C. Domb and J. Lebowitz. Vol. 8. Academic Press, 1983, pp. 269–446.
- [65] G. Fredrickson et al. *The equilibrium theory of inhomogeneous polymers*. 134. Oxford University Press on Demand, 2006.

- [66] M. W. Matsen. “The Standard Gaussian Model for Block Copolymer Melts”. In: *J. Phys.: Condens. Matter* 14 (2002), R21–R47.
- [67] J. Farago et al. “Mode-coupling approach to polymer diffusion in an unentangled melt. I. The effect of density fluctuations”. In: *Phys. Rev. E* 85 (2012), p. 051806.
- [68] A. N. Semenov, J. Farago, and H. Meyer. “Length-scale dependent relaxation shear modulus and viscoelastic hydrodynamic interactions in polymer liquids”. In: *J. Chem. Phys.* 136 (2012), p. 244905.
- [69] J. Farago et al. “Hydrodynamic and viscoelastic effects in polymer diffusion”. In: *J. Phys.: Condens. Matter* 24 (2012), p. 284105.
- [70] F. S. Bates and P. Wiltzius. “Spinodal decomposition of a symmetric critical mixture of deuterated and protonated polymer”. In: *J. Chem. Phys.* 91 (1989), pp. 3258–3274.
- [71] H. Jinnai et al. “Time-resolved small-angle neutron scattering study of spinodal decomposition in deuterated and protonated polybutadiene blends. II. Q-dependence of Onsager kinetic coefficient”. In: *J. Chem. Phys.* 99 (1993), pp. 8154–8161.
- [72] G. Müller et al. “Effect of the Onsager coefficient and internal relaxation modes on spinodal decomposition in the high molecular isotopic blend polystyrene/deutero-polystyrene studied with small angle neutron scattering”. In: *J. Chem. Phys.* 104 (1996), pp. 5326–5337.
- [73] T. J. Rappl and N. P. Balsara. “Does coarsening begin during the initial stages of spinodal decomposition?” In: *J. Chem. Phys.* 122 (2005), p. 214903.
- [74] J. T. Cabral and J. S. Higgins. “Spinodal nanostructures in polymer blends: On the validity of the Cahn-Hilliard length scale prediction”. In: *Prog. Polym. Sci.* 81 (2018), pp. 1–21.
- [75] A. Baumgärtner and D. W. Heermann. “Spinodal decomposition of polymer films”. In: *Polymer* 27 (1986), pp. 1777–1780.
- [76] A. Sariban and K. Binder. “Spinodal decomposition of polymer mixtures: a Monte Carlo simulation”. In: *Macromolecules* 24.2 (1991), pp. 578–592.
- [77] G. Wang and M. Müller. “Phase Separation of Regular, Quasi-Two-Dimensional AB Copolymer Networks”. In: *Macromolecules* 55.4 (2022), pp. 1279–1294. URL: <https://doi.org/10.1021/acs.macromol.1c02108>.

- [78] Y. Gu, J. Zhao, and J. A. Johnson. "Polymer Networks: From Plastics and Gels to Porous Frameworks". In: *Angewandte Chemie International Edition* 59.13 (2020), pp. 5022–5049.
- [79] J. Sakamoto et al. "ChemInform Abstract: Two-Dimensional Polymers: Just a Dream of Synthetic Chemists?" In: *Angewandte Chemie (International ed. in English)* 48 (2009), pp. 1030–69.
- [80] P. Payamyar et al. "Two-dimensional polymers: concepts and perspectives". In: *Chem. Commun.* 52 (1 2016), pp. 18–34.
- [81] S. P. O. Danielsen et al. "Molecular Characterization of Polymer Networks". In: *Chemical Reviews* 121.8 (2021). PMID: 33792299, pp. 5042–5092.
- [82] E. S. Dragan. "Design and applications of interpenetrating polymer network hydrogels. A review". In: *Chemical Engineering Journal* 243 (2014), pp. 572–590.
- [83] M. Shivashankar and B. Mandal. "A review on interpenetrating polymer network". In: *International Journal of Pharmacy and Pharmaceutical Sciences* 4 (2012), pp. 1–7.
- [84] A. Lohani et al. "Interpenetrating Polymer Networks as Innovative Drug Delivery Systems". In: *Journal of Drug Delivery* 2014 (2014), pp. 1–11.
- [85] L. H. Sperling. *Interpenetrating polymer networks and related materials*. Springer Science & Business Media, 2012.
- [86] S. Thomas et al. *Micro- and Nano-Structured Interpenetrating Polymer Networks: From Design to Applications*. 2016. ISBN: 978-1-118-13817-5.
- [87] X. Lyu et al. "Liquid crystalline polymers: Discovery, development, and the future". In: *Polymer* 202 (2020), p. 122740.
- [88] C. Ohm, M. Brehmer, and R. Zentel. "Liquid Crystalline Elastomers as Actuators and Sensors". In: *Advanced Materials* 22.31 (2010), pp. 3366–3387.
- [89] M. Warner and E. M. Terentjev. *Liquid crystal elastomers*. Vol. 120. Oxford university press, 2007.
- [90] H. R. Brand, H. Pleiner, and P. Martinoty. "Selected macroscopic properties of liquid crystalline elastomers". In: *Soft Matter* 2 (3 2006), pp. 182–189.

- [91] K. Urayama. “Selected Issues in Liquid Crystal Elastomers and Gels”. In: *Macromolecules* 40.7 (2007), pp. 2277–2288.
- [92] K. Uto, C. A. DeForest, and D.-H. Kim. “5.2 - Soft Shape-Memory Materials”. In: *Biomaterials Nanoarchitectonics*. Ed. by M. Ebara. William Andrew Publishing, 2016, pp. 237–251. ISBN: 978-0-323-37127-8.
- [93] W. B. Liechty et al. “Polymers for drug delivery systems”. In: *Annual review of chemical and biomolecular engineering* 1 (2010), pp. 149–173.
- [94] R. K. O'Reilly, C. J. Hawker, and K. L. Wooley. “Cross-linked block copolymer micelles: functional nanostructures of great potential and versatility”. In: *Chem. Soc. Rev.* 35 (11 2006), pp. 1068–1083.
- [95] J Lub et al. “Formation of optical films by photo-polymerisation of liquid crystalline acrylates and application of these films in liquid crystal display technology”. In: *Molecular Crystals and Liquid Crystals* 429.1 (2005), pp. 77–99.
- [96] P. J. Flory and B. Erman. “Theory of elasticity of polymer networks. 3”. In: *Macromolecules* 15.3 (1982), pp. 800–806.
- [97] H. M. James and E. Guth. “Simple presentation of network theory of rubber, with a discussion of other theories”. In: *Journal of Polymer Science* 4.2 (1949), pp. 153–182.
- [98] P. J. Flory. “Molecular theory of rubber elasticity”. In: *Polymer* 20.11 (1979). Jabtonna Conference on Polymer Networks, pp. 1317–1320.
- [99] S. Panyukov. “Theory of Flexible Polymer Networks: Elasticity and Heterogeneities”. In: *Polymers* 12.4 (2020).
- [100] M. Rubinstein and S. Panyukov. “Elasticity of Polymer Networks”. In: *Macromolecules* 35.17 (2002), pp. 6670–6686.
- [101] R. Everaers and K. Kremer. “Elastic Properties of Polymer Networks”. In: *Journal of Molecular Modeling* 2.9 (1996), pp. 293–299.
- [102] S. Lay, J.-U. Sommer, and A. Blumen. “Comparison of structural properties of different polymer network types as obtained by computer simulation”. In: *J. Chem. Phys.* 110.24 (1999), pp. 12173–12182.

- [103] N. B. Tito, C. Storm, and W. G. Ellenbroek. “Self-Consistent Field Lattice Model for Polymer Networks”. In: *Macromolecules* 50.24 (2017), pp. 9788–9795.
- [104] T. Hölzl, H. L. Trautenberg, and D. Göritz. “Monte Carlo Simulations on Polymer Network Deformation”. In: *Phys. Rev. Lett.* 79 (12 1997), pp. 2293–2296.
- [105] M. E. Cates. “Statics and Dynamics of Polymeric Fractals”. In: *Phys. Rev. Lett.* 53 (9 1984), pp. 926–929.
- [106] P. Flory. *Principles of polymer chemistry*. Cornell University Press: Ithaca, NY, USA, 1953, pp. 1–801.
- [107] F. T. Wall. “Statistical Thermodynamics of Rubber. III”. In: *J. Chem. Phys.* 11.11 (1943), pp. 527–530.
- [108] F. T. Wall and P. J. Flory. “Statistical Thermodynamics of Rubber Elasticity”. In: *J. Chem. Phys.* 19.12 (1951), pp. 1435–1439.
- [109] H. M. James and E. Guth. “Theory of the Increase in Rigidity of Rubber during Cure”. In: *J. Chem. Phys.* 15.9 (1947), pp. 669–683.
- [110] H. M. James. “Statistical Properties of Networks of Flexible Chains”. In: *J. Chem. Phys.* 15.9 (1947), pp. 651–668.
- [111] H. M. James and E. Guth. “Statistical Thermodynamics of Rubber Elasticity”. In: *J. Chem. Phys.* 21.6 (1953), pp. 1039–1049.
- [112] J. Mark. *Physical Properties of Polymers Handbook*. Springer New York, 2007. ISBN: 9780387690025.
- [113] Y. Akagi et al. “Transition between Phantom and Affine Network Model Observed in Polymer Gels with Controlled Network Structure”. In: *Macromolecules* 46.3 (2013), pp. 1035–1040.
- [114] B. E. Eichinger. “Elasticity Theory. I. Distribution Functions for Perfect Phantom Networks”. In: *Macromolecules* 5.4 (1972), pp. 496–505.
- [115] P. J. Flory. “Theory of elasticity of polymer networks. The effect of local constraints on junctions”. In: *J. Chem. Phys.* 66.12 (1977), pp. 5720–5729.
- [116] F. F. Abraham, W. E. Rudge, and M. Plischke. “Molecular dynamics of tethered membranes”. In: *Phys. Rev. Lett.* 62 (15 1989), pp. 1757–1759.

- [117] K. J. Wiese and F. David. “Self-avoiding tethered membranes at the tricritical point”. In: *Nuclear Physics B* 450.3 (1995), pp. 495–557.
- [118] M. Hirata. “Particle scattering function of a two-dimensional flexible macromolecule”. In: *Polymer Journal* 45 (2013), pp. 802–812.
- [119] D. Liu and M. Plischke. “Monte Carlo studies of tethered membranes with attractive interactions”. In: *Phys. Rev. A* 45 (10 1992), pp. 7139–7144.
- [120] F. Schmid. “Self-Consistent Field Approach for Cross-Linked Copolymer Materials”. In: *Phys. Rev. Lett.* 111 (2 2013), p. 028303.
- [121] S. Qi, J. Zhou, and F. Schmid. “Shear Modulus of an Irreversible Diblock Copolymer Network from Self-Consistent Field Theory”. In: *Macromolecules* 52.24 (2019), pp. 9569–9577.
- [122] N. Tito, C. Storm, and W. Ellenbroek. “Self-consistent field lattice model for polymer networks”. English. In: *Macromolecules* 50.24 (2017), pp. 9788–9795.
- [123] Y. F. Zbashta. “Phonons in solid polymers”. In: *Journal of Thermal Analysis* 38.5 (1992), pp. 1047–1060.
- [124] M. W. Matsen. “Thin films of block copolymer”. In: *J. Chem. Phys.* 106.18 (1997), pp. 7781–7791.
- [125] A. B. Croll et al. “Kinetics of layer hopping in a diblock copolymer lamellar phase”. In: *The European Physical Journal E* 27.4 (2008), pp. 407–411.
- [126] Y. Ren and M. Müller. “Kinetics of pattern formation in symmetric diblock copolymer melts”. In: *J. Chem. Phys.* 148.20 (2018), p. 204908.
- [127] T. A. Kavassalis and M. D. Whitmore. “On the theory of linear multiblock copolymers”. In: *Macromolecules* 24.19 (1991), pp. 5340–5345.
- [128] M. W. Matsen and R. B. Thompson. “Equilibrium behavior of symmetric ABA triblock copolymer melts”. In: *J. Chem. Phys.* 111.15 (1999), pp. 7139–7146.
- [129] M. W. Matsen. “Bridging and looping in multiblock copolymer melts”. In: *J. Chem. Phys.* 102.9 (1995), pp. 3884–3887.

- [130] K. Rasmussen et al. “Morphology and bridging properties of (AB)_n multiblock copolymers”. In: *Journal of Polymer Science Part B: Polymer Physics* 41.1 (2003), pp. 104–111.
- [131] M. Warner and E. Terentjev. “Nematic elastomers—A new state of matter?” In: *Progress in Polymer Science* 21.5 (1996), pp. 853–891.
- [132] G. Verwey, M Warner, and E. Terentjev. “Elastic Instability and Stripe Domains in Liquid Crystalline Elastomers”. In: *J. Phys. II (France)* 6 (1998).
- [133] E. M. Terentjev. “Liquid-crystalline elastomers”. In: *Journal of Physics: Condensed Matter* 11.24 (1999), R239–R257.
- [134] G. Wang, A. Zippelius, and M. Müller. “Phase Separation of Randomly Cross-Linked Diblock Copolymers”. In: *Macromolecules* 55.13 (2022), pp. 5567–5580. URL: <https://doi.org/10.1021/acs.macromol.2c00687>.
- [135] R. C. Ball and S. F. Edwards. “Elasticity and Stability of a Dense Gel”. In: *Macromolecules* 13.3 (1980), pp. 748–761.
- [136] P. M. Goldbart, H. E. Castillo, and A. Zippelius. “Randomly crosslinked macromolecular systems: Vulcanization transition to and properties of the amorphous solid state”. In: *Advances in Physics* 45.5 (1996), pp. 393–468.
- [137] P. J. Flory et al. “Statistical thermodynamics of random networks”. In: *Proceedings of the Royal Society of London. A. Mathematical and Physical Sciences* 351.1666 (1976), pp. 351–380.
- [138] V Blavatska, K Haydukivska, and Y. Holovatch. “Shape analysis of random polymer networks”. In: *Journal of Physics: Condensed Matter* 32.33 (2020), p. 335102.
- [139] G. S. Grest and K. Kremer. “Statistical properties of random cross-linked rubbers”. In: *Macromolecules* 23.23 (1990), pp. 4994–5000.
- [140] L. Y. Shy and B. E. Eichinger. “Large computer simulations on elastic networks: Small eigenvalues and eigenvalue spectra of the Kirchhoff matrix”. In: *J. Chem. Phys.* 90.9 (1989), pp. 5179–5189.
- [141] A. A. Gavrilov and A. V. Chertovich. “Computer simulation of random polymer networks: Structure and properties”. In: *Polymer Science Series A* 56.1 (2014), pp. 90–97.

- [142] R. T Deam and S. F. Edwards. “The theory of rubber elasticity”. In: *Philosophical Transactions of the Royal Society of London. Series A, Mathematical and Physical Sciences* 280.1296 (1976), pp. 317–353.
- [143] M. E. Fisher and J. W. Essam. “Some Cluster Size and Percolation Problems”. In: *Journal of Mathematical Physics* 2.4 (1961), pp. 609–619.
- [144] P. J. Flory. “Molecular Size Distribution in Three Dimensional Polymers. I. Gelation”. In: *Journal of the American Chemical Society* 63.11 (1941), pp. 3083–3090.
- [145] D. Stauffer and A. Aharony. *Introduction To Percolation Theory*. Taylor & Francis, 2018.
- [146] E. Dagotto. “An Elementary Introduction to Percolation”. In: *Nanoscale Phase Separation and Colossal Magnetoresistance: The Physics of Manganites and Related Compounds*. Berlin, Heidelberg: Springer Berlin Heidelberg, 2003, pp. 303–312. ISBN: 978-3-662-05244-0.
- [147] “Introduction to Theory of Finite-Size Scaling”. In: *Finite-Size Scaling*. Ed. by J. L. CARDY. Elsevier, 1988, pp. 1–7.
- [148] V. Privman. *Finite Size Scaling and Numerical Simulation of Statistical Systems*. WORLD SCIENTIFIC, 1990.
- [149] P. J. Reynolds, H. E. Stanley, and W. Klein. “Large-cell Monte Carlo renormalization group for percolation”. In: *Phys. Rev. B* 21 (3 1980), pp. 1223–1245.
- [150] G. S. Grest and K. Kremer. “Critical properties of crosslinked polymer melts”. In: *Journal de Physique* 51.24 (1990), pp. 2829–2842.
- [151] A. P. Young. *Spin Glasses and Random Fields*. WORLD SCIENTIFIC, 1997. URL: <https://www.worldscientific.com/doi/abs/10.1142/3517>.
- [152] F. S. Bates et al. “Multiblock Polymers: Panacea or Pandora’s Box?” In: *Science* 336.6080 (2012), pp. 434–440.
- [153] P. de Gennes. “Effect of cross-links on a mixture of polymers”. In: *Journal de Physique Lettres* 40.4 (1979), pp. 69–72.
- [154] R. M. Briber and B. J. Bauer. “Effect of crosslinks on the phase separation behavior of a miscible polymer blend”. In: *Macromolecules* 21.11 (1988), pp. 3296–3303.

- [155] S. Lay, J.-U. Sommer, and A. Blumen. “Monte Carlo study of the microphase separation of cross-linked polymer blends”. In: *J. Chem. Phys.* 113.24 (2000), pp. 11355–11363.
- [156] C. Wald. “Phase behaviour of random copolymers and crosslinked homopolymer blends”. PhD thesis. 2005.
- [157] M. Lang and T. Müller. “Analysis of the Gel Point of Polymer Model Networks by Computer Simulations”. In: *Macromolecules* 53.2 (2020), pp. 498–512.
- [158] M. Plischke and S. J. Barsky. “Molecular dynamics study of the vulcanization transition”. In: *Phys. Rev. E* 58 (3 1998), pp. 3347–3352.
- [159] T. Nattermann. “Theory of the Random Field Ising Model”. In: *Series on Directions in Condensed Matter Physics*. WORLD SCIENTIFIC, 1997, pp. 277–298. ISBN: 978-981-02-3183-5.
- [160] N. G. Fytas et al. “Review of Recent Developments in the Random-Field Ising Model”. In: *Journal of Statistical Physics* 172.2 (2018), 665–672.
- [161] J. Bricmont and A. Kupiainen. “Phase transition in the 3d random field Ising model”. In: *Communications in Mathematical Physics* 116 (1988), pp. 539–572.
- [162] T. Schneider and E. Pytte. “Random-field instability of the ferromagnetic state”. In: *Phys. Rev. B* 15 (3 1977), pp. 1519–1522.
- [163] A. Aharony. “Tricritical points in systems with random fields”. In: *Phys. Rev. B* 18 (7 1978), pp. 3318–3327.
- [164] N. G. Fytas and V. Martín-Mayor. “Universality in the Three-Dimensional Random-Field Ising Model”. In: *Phys. Rev. Lett.* 110 (22 2013), p. 227201.
- [165] A. P. Young and M. Nauenberg. “Quasicritical Behavior and First-Order Transition in the $d = 3$ Random-Field Ising Model”. In: *Phys. Rev. Lett.* 54 (22 1985), pp. 2429–2432.
- [166] R. Riggleman and G. Fredrickson. “Field-theoretic simulations in the Gibbs ensemble”. In: *J. Chem. Phys.* 132 (2010), p. 024104.

- [167] M. Müller and D. W. Sun. “Directing the Self-Assembly of Block Copolymers into A Metastable Complex Network Phase via A Deep and Rapid Quench”. In: *Phys. Rev. Lett.* 111.26 (2013), p. 267801.
- [168] D. W. Sun and M. Müller. “Process-Accessible States of Block Copolymers”. In: *Phys. Rev. Lett.* 118 (6 2017), p. 067801.
- [169] C. Nowak and F. A. Escobedo. “Tuning the Sawtooth Tensile Response and Toughness of Multiblock Copolymer Diamond Networks”. In: *Macromolecules* 49.17 (2016), pp. 6711–6721.
- [170] C. Lorenz et al. “Lateral Subunit Coupling Determines Intermediate Filament Mechanics”. In: *Phys. Rev. Lett.* 123.18 (2019).
- [171] B. Erman. “Rubber Elasticity”. In: *Encyclopedia of Materials: Science and Technology*. Ed. by K. J. Buschow et al. Oxford: Elsevier, 2001, pp. 8227–8237. ISBN: 978-0-08-043152-9.
- [172] J. Oberdisse et al. “Mechanical properties of end-crosslinked entangled polymer networks using sliplink Brownian dynamics simulations”. In: *Rheologica Acta* 46.1 (2006), 95–109.
- [173] Y. Masubuchi et al. “Structure of entangled polymer network from primitive chain network simulations”. In: *J. Chem. Phys.* 132.13 (2010), p. 134902.
- [174] A. von der Heydt and A. Zippelius. “Phase diagram of selectively cross-linked block copolymers shows chemically microstructured gel”. In: *J. Chem. Phys.* 142.5 (2015), p. 054901.
- [175] K. Tietz et al. “Stabilizing the Microphase Separation of Block Copolymers by Controlled Photo-crosslinking”. In: *Macromolecular Chemistry and Physics* 215.16 (2014), pp. 1563–1572.

Acknowledgements

This PhD thesis is a result of efforts from many persons. Without them, I could never have achieved this. I would like to sincerely thank my supervisor Marcus Müller who invested tremendous time and effort to guide me through the four years of polymer research. I want to thank Annette Zippelius and Yongzhi Ren for valuable discussions and collaborations. I also want to thank my second and third supervisor Reiner Kree and Stefan Klumpp for their helpful advice. I had a wonderful time with my colleagues from the institute for theoretical physics. I will remember the happy moments I shared with them. Many thanks to Russell Spencer for proofreading this thesis so carefully. At the end, I want to thank my parents, Jan as well as all of my friends for accompanying and supporting me.

Curriculum Vitae

name: Gaoyuan Wang

date of birth: 13th May 1993

nationality: chinese

2009 - 2012 Abitur, Johann-Vanotti-Gymnasium Ehingen (Donau)

2012 - 2015 Bachelor of Science, Physics, Georg-August-Universität Göttingen

Title of bachelor's thesis:

Aligned Natural Inflation

2015 - 2017 Master of Science, Physics, Georg-August-Universität Göttingen

Title of master's thesis:

Simulation and optimization studies for the measurement of the $t\bar{t}H(b\bar{b})$ process in the semileptonic channel at $\sqrt{s} = 13\text{TeV}$ with the ATLAS detector

2017 - 2021 PhD candidate, Physics, Georg-August-Universität Göttingen